UNIVERSITY OF CALIFORNIA, MERCED

Role of active and elastic forces in cell migration and cytoskeletal shape change

A dissertation submitted in partial satisfaction of the
requirements for the degree
Doctor of Philosophy

in

Physics

by

Subhaya Bose

Committee in charge:

Dr Dustin Kleckner, Chair
Dr Arvind Gopinath
Dr Roberto Carlos Andresen Eguiluz
Dr Kinjal Dasbiswas, Thesis Adviser

2024

The dissertation of Subhaya Bose is approved, and
it is acceptable in quality and form for publication
on microfilm and electronically:

(Dr Arvind Gopinath)

(Dr Roberto Carlos Andresen Eguiluz)

(Dr Kinjal Dasbiswas, Thesis Adviser)

(Dr Dustin Kleckner, Chair)

University of California, Merced

2024

TABLE OF CONTENTS

Signature Page . . . iii

Table of Contents . . . iv

List of Figures . . . vii

List of Tables . . . xxiv

Acknowledgements . . . xxv

Abstract . . . xxix

Chapter 1 Introduction . . . 1
1.1 Motivation . . . 1
1.2 Background . . . 5
1.3 Overview . . . 6

Chapter 2 Matrix stiffness modulates mechanical interactions and promotes contact between motile cells . . . 9
2.1 Introduction . . . 9
2.2 Experimental observations motivate model for cell elastic interactions . . . 12
2.3 Materials and Methods . . . 18
2.3.1 Model for two-cell interactions . . . 18
2.3.2 Dimensionless parameters quantifying cell motion and interactions . . . 19
2.3.3 Numerical solution and tracking cell trajectories . . . 19
2.4 Results . . . 22
2.4.1 Cell-cell contact frequency is controlled by matrix elastic interactions . . . 22
2.4.2 Cell motility characteristics depend on elastic interactions 25
2.4.3 Elastic interactions lead to effective capture of motile cell 27
2.5 Discussion and future extensions to other forms of interactions . 29
2.5.1 Anisotropic cell-cell elastic interactions . . . 29
2.5.2 Extensions to near-contact biochemical or bond interactions 31
2.6 Summary . . . 32

Chapter 3 Collective states of active particles with elastic dipolar interactions . . 35
3.1 Introduction . . . 35
3.2 Model . . . 37
3.3 Results . . . 42
3.3.1 Characteristic states of active dipolar particles: chains, polar bands, clusters and networks . . . 42
3.3.2 Pair correlations reveal spatial organization of active chains 45

3.3.3 Activity and elastic interactions promote orientational order 47
3.3.4 Transport properties of active chains are distinct from single particles . . . 49
3.3.5 Collisions of active chains reveal stable, mobile structures 51
3.3.6 Stronger confinement in narrow channels reveals polar clustering dynamics . . . 52
3.4 Methods . . . 53
3.5 Discussion . . . 57

Chapter 4 Elastic interactions compete with persistent cell motility to drive durotaxis . . . 60
4.1 Introduction . . . 60
4.2 Model for cell motility and elastic cell-boundary interactions . . . 66
4.3 Results . . . 69
4.3.1 Elastic interactions determine steady state distributions near free and clamped elastic boundaries . . . 69
4.3.2 Free elastic (repulsive) boundary induces depletion and prevents anti-durotaxis . . . 74
4.3.3 Clamped (attractive) boundary induces durotactic trapping 76
4.3.4 Comparison with experiment and predicted durotactic phase diagram . . . 80
4.3.5 Clamped (attractive) elastic boundary: escape facilitated by random translational protrusions ($Pe < A$) . . . 84
4.4 Discussion . . . 90

Chapter 5 Analysis of elastic strains reveals shape selection pathways in active gels 95
5.1 Introduction . . . 95
5.1.1 Preparation of intrinsically contractile elastic actomyosin gel discs . . . 96
5.2 Analysis Methods . . . 97
5.2.1 Particle Image Velocimetry . . . 97
5.2.2 Strain tensor obtained from the spatial arrangement of displacement vectors . . . 98
5.3 Results . . . 99
5.3.1 Area strain reveals regions of contraction and stretching . 99
5.3.2 Radial and azimuthal displacement obtained from axisymmetric assumption of gel contraction . . . 100
5.3.3 Radial dependence of displacement reveals a boundary layer 101
5.3.4 Analysis of radial strain profile reveals active stress distribution . . . 102
5.3.5 Predicted contraction phenomenon from analysis of strain 103
5.3.6 Differentiating domes from wrinkled gels . . . 108
5.3.7 Locating wrinkles in gel . . . 109
5.4 Discussion . . . 110

Chapter 6 Conclusions 112

Appendix A 115
A.1 Model for a moving cell interacting with a stationary cell via substrate elasticity 115

Appendix B 118
B.1 Model for substrate mediated cell-interface interactions 118
B.2 Simulation model details 120
B.3 Simulation methodology 121
B.4 Determining escape conditions 123
B.5 Escape of cells from the attractive clamped boundary 124
B.5.1 Adaptation of Kramer's theory to the frequency of orientation flips for spatially localized cells 124
B.5.2 1D and 2D passive case: Escape time without self-propulsion in attractive power-law potentials 127
B.5.3 Activity-assisted escape from the attractive clamped boundary for small and $O(1)$ Pe: Reduced durotaxis 130
B.6 Measurement of tactic indices from simulation 133
B.7 Scattering of motile cells across elastic interface 134

Appendix C 139
C.1 Displacement and strain analysis between frames 139
C.1.1 Central differing scheme to obtain strain from displacements 139
C.1.2 Estimation of local displacements and strains in polar form 140
C.1.3 **2D plots of area strain** 141
C.1.4 2D plots of Eigenvalues 141
C.1.5 Radial and azimuthal displacement and strain obtained from axisymmetric assumption of gel contraction 141
C.1.6 Calculation of center of contraction 142

Appendix D Code Availability 144

Bibliography 145

LIST OF FIGURES

Figure 1.1: (This figure is reproduced with permission from Elsevier.) An illustration of the dynamic interactions between the cell and the matrix during cell migration. While navigating through the matrix, the cell continually integrates physical, biochemical, and mechanical cues from its internal biomolecular regulation, from other cells, and from the matrix. 2

Figure 2.1: Traction forces exerted by motile cells on soft substrates can be modeled as force dipoles. (a) Schematic of an animal cell, *e.g.* an isolated fibroblast in culture [1] adhered to a compliant substrate through focal adhesions comprising of integrins and a host of other mechanosensitive adhesion proteins. Mechanical forces are actively generated by molecular motors of the myosin-II family that put the actin cytoskeleton under tension. Stress fibers are bundles of crosslinked actin filaments with a periodic (sarcomeric) organization of myosin [2] that often span the length of the cell and are anchored at the focal adhesions to the extracellular substrate or matrix (ECM). The contractile forces are transmitted at these sites from the stress fibers to the underlying substrate, which can be strongly deformed if soft. Such deformations are long range (extend up to a few cell lengths away from the cell) and can be measured by Traction Force Microscopy (TMF). This is a common index of cell-substrate mechanical interactions. (b) (i) A simplified top view of the same cell showing the alignment of the stress fibers, and therefore of the contractile forces generated by them. In order to model the effects of the cell on the substrate, we use classical linear elasticity theory with the stress distributions effectively modeled as a contractile force dipole, a pair of equal and opposite forces separated by some distance acting along the dipole axis (marked). (ii) This leads to a very simplified mechanical model of the cell in terms as a contractile force dipole exerted on the substrate along its average axis of orientation defined by the alignment of its stress fibers. 13

Figure 2.2: Schematic of the cell-cell mechanical interactions model: (a) Two cells A and B cultured on the surface of thick elastic substrate can sense each other and interact at long range (when the inter-cell distance r is longer than typical cell sizes, here depicted by dashed red circles) through mechanical deformations of the underlying substrate; here the contractile stresses set up in the substrate yield deformations as indicated by green arrows. The cells are restricted to move on the surface of the substrate. (b) Representative spatial maps of the interaction potential between two dipoles, from the solution of the strain field for the full linear elastic problem of forces exerted on the surface of a semi-infinite medium are shown. The interaction potential corresponds to the work done by a point-like dipole in deforming the substrate in the presence of the strain created by the other. The potential maps shown here are for a pair of contractile force dipoles of fixed orientation. The second dipole is free to translate but held parallel (left) or perpendicular (right) to the central dipole which is placed at the origin and aligned along the x-axis. The contour lines show how the potential decays in space, whereas blue and red regions correspond to attractive and repulsive interactions, respectively. 15

Figure 2.3: We study with our computational model how a motile cell (M, Cell A, pink) moves in the presence of a fixed central cell (Cell B, yellow). This two cell system on a substrate (schematic shown as a top view) also mimics scenarios where a motile cell may encounter an elastic impurity or obstacle on the medium. Shown as blue circles are contours of constant elastic potential (in simplified form) that determine the inter-cell elastic force experienced by the motile cell B as a result of the elastic deformations of the medium by both cells A and B. Also shown (in black) is a representative simulated trajectory of the motile cell which starts outside the area of influence of the stationary cell. 16

Figure 2.4: Number of cell–cell contact events measured in a fixed interval of time depends strongly on the elastic interaction parameter. A contact event is identified as cell A coming within a prescribed contact radius of cell B with cell A initialized randomly in a certain area around cell B. Thus the number of contact is be interpreted as the average number of contacts of the two cells. The number of simulation runs conducted were 50 for each combination of D_T and α. The dashed curves are guides to the eye illustrating the trends seen with increasing values of α. Diffusion is the major factor in governing the number of contacts for low values of α. For higher α, the attractive potential increases the probability of the cell to stay near the contact radius and controls the number of contacts. Trajectories for highlighted data points (1)-(4) are shown on the right. The box plots show the distribution of contact numbers. The lower and upper bounds of the box are the first and the third quartiles respectively, while the line in middle is the median. The lower and upper limits of the dashed lines are the minimum and maximum number of contacts observed for cells for each combination of α and D_T. The simulation was run for a total time of $T = 1000$ and updates in cell position were made every $\delta t = 0.001$. 23

Figure 2.5: Number of cell–cell contact events in a fixed interval of time ($T = 1000$) plotted here as a function of the scaled effective diffusivity, D_T, which represents the random motility of cell B. Here we show how the number of cell–cell contact varies for three different elastic interaction strength values, α, corresponding to substrates with three different stiffness. The highlighted points numbered from (1)-(4), show representative cell trajectories over long times and highlight how varying α and D_T can yield states where the cells are in close proximity most of the time (low D_T, high α) or states where cells interact rarely (high D_T, low α). Interpretation of the box plots is the same as in Fig. 2.3. The simulation was run for a total time of $T = 1000$ and updates in cell position were made every $\delta t = 0.001$. 24

Figure 2.6: **Mean square displacement** (MSD) as a function of the delay time interval τ (calculated from Equation 9), for the motile cell A is shown. Here we explore the variation in the MSD for various values of substrate-mediated elastic interactions, α. The diffusivity D_T is held constant for these simulations with $D_T = 2$. Other diffusivities were explored (results not shown). At low elastic interaction strengths, α, corresponding to stiff substrates, the cell shows a purely diffusive trajectory, whereas at higher values of α, the motile cell is captured by the strong attractive interaction from the stationary cell, resulting in a flattening of the MSD (blue curve). At an intermediate interaction regime (green curve), the motile cell makes repeated contact with the fixed cell but is never fully captured. 26

Figure 2.7: **Capture statistics of motile cell**. (A) Probability that cell B is inside contact radius as a function of time. (B and C) The dependence of steady state capture probability, P_{ss}, *i.e.* the fraction of cells captured within the contact radius after a long time interval, on simulation parameters. (B) shows the dependence on diffusivity,D_T at different values of the elastic interaction parameter, α, whereas (C) shows the dependence on α for different values of D_T. (D) The steady state capture probability, P_{ss}, data can be collapsed into a single master curve, when plotted vs. the key parameter, α/D_T, the strength of the elastic interactions relative to the diffusivity. This is expected since our model steady state is a thermal equilibrium with effective temperature set by the noisy cell motility, D_T, and the competition between attractive interactions and noise dictates the number of cells (cell trajectories) captured vs. the number that escape. 27

Figure 2.8: **Dipolar cell orientation and trajectory** The equilibrium orientation of contractile cells fixed in position, but free to reorient, and that are uniformly distributed in a square box of size 10σ, are depicted by two arrows (red) pointing towards each other. Each cell is influenced by the central stationary cell B (green) and not by each other. Two possible trajectories of cell A (blue and black) are recorded for $D_T = 0.1$, $\alpha = 40$ for total time $T = 500$ with time steps of $dt = 0.001$. The cells did not have any self propulsion or rotational diffusion. The Poisson's ratio ν of the substrate was considered 0.3 for this simulation 30

Figure 3.1: Elastic interactions between model cells on a substrate. (a) Schematic of adherent cell on an elastic substrate. (b) 1D spring model illustrating origin of elastic interaction potential between two contractile dipoles. The elastic energy stored in the medium corresponding to the deformation of springs depends on the relative placement of the dipoles. In particular, placing a contractile dipole in a region where the medium is already expanded by the other dipole can help to reduce the overall deformation of the medium. This leads to a strain-dependent interaction potential between the two dipoles. (c) Representative spatial maps of the interaction potential $W^{\alpha\beta}$ between two dipoles, from the solution of the strain field for the full linear elastic problem of forces exerted on the surface of a semin-infinite medium are showm. The interaction potential corresponds to the work done by a point-like dipole in deforming the substrate in the presence of the strain created by the other. The potential maps shown here are for a pair of contractile force dipoles of fixed orientation. The second dipole is free to translate but held parallel (left) or perpendicular (right) to the central dipole which is placed at the origin and aligned along the x-axis. The contour lines show how the potential decays in space, whereas blue and red regions correspond to attractive ($W^{\alpha\beta} < 0$) and repulsive ($W^{\alpha\beta} > 0$) interactions, respectively. 38

Figure 3.2: Overview of agent based simulations of active Brownian particles (ABPs) moving in the x-y plane and interacting mechanically via elastic deformations induced by contractile, active force dipoles. (a) An elongated cell with traction forces distributed around its long axis is modeled as a disk-like particle endowed with a dipole moment. (b) Each ABP has a dipole axis represented by the bold black line and an in-plane self-propulsion direction represented by the gold arrow. These particles move on a linearly elastic, thick, flat substrate, on which they exert contractile dipolar stresses. Substrate deformation due to one particle is sensed by neighbouring particles. These dipole-dipole elastic interactions are confined to particles within a cutoff distance $r_{\text{cut}} = 7\sigma$ (shown as the dashed red circle). Particle overlap is penalized by a short range steric repulsion. They are confined by steric repulsions along the top and bottom walls shown by the thick lines, while being free to move through periodic boundaries shown by the thin lines. (i) Simulation snapshot shows that weakly interacting particles do not stick to each other and move as independent entities. As the elastic dipolar interaction parameter A increases, the particles self-assemble into long chains ((ii)-(iv), zoomed view shown). The flexibility of the chains and fluctuations in the mean curvature both decrease with increasing values of the interaction parameter. The colors represent the self-propulsion direction of each particle, as indicated by the color wheel. 41

Figure 3.3: Simulation snapshots of active particles with short range steric repulsions and long-range elastic dipole-dipole interactions as a function of effective elastic interaction $A = P^2/E\sigma^3 k_{\text{B}}T_{\text{eff}}$ and Péclet number $Pe = \sigma v_0/D_{\text{T}}$. Particles are confined in the y-direction, while they experience periodic boundary conditions in the x-direction. They are colored according to their self-propulsion direction $\hat{\mathbf{n}}$, and coded based on the color wheel. Motile particles at low effective elastic interaction collect into clusters at the boundaries. Strong elastic interactions promote network formation at low activity. Strong elastic interactions paired with high activity gives rise to active polymers and polar bands. 43

Figure 3.4: Simulation snapshots of active particles at low packing fraction - The interaction parameter $A \equiv P^2/E\sigma^3 k_{\mathrm{B}}T_{\mathrm{eff}}$ and Péclet number $Pe \equiv \sigma v_0/D_{\mathrm{T}}$ define the collective behavior of the particles. Particles are confined in the y-direction, while they experience periodic boundary conditions in the x-direction. They are colored based on the direction of $\hat{\mathbf{n}}$, as indicated by the color wheel. At low interaction parameter $A = 10$, the particles remain isolated and diffuse. At high Pe, more particles get collected at the confining boundary. At higher values of the interaction parameter, A, particles form chains. The typical length of the chains is seen to decrease with increasing Pe. At very high interaction parameter, $A = 200$, networks with multiple branches form at low Pe, while chains aggregate into polar clusters at $Pe = 10$. Although the particles in the cluster are oriented in opposite directions, the cluster is stable and moves in the direction given by its overall polarity. Again at very high Péclet, $Pe = 100$, the particles in the chains are oriented in the same direction. 44

Figure 3.5: Angular dependent pair correlation function is affected by both motility and elastic interactions. Strong elastic interactions promote pair correlation peaks at $(r, \theta) =$ (σ,0) , (σ,π). At $Pe = 1$, these are the only prominent peaks in the pair correlation function. Motile activity gives rise to secondary peaks at roughly $(r, \theta) = (\sigma, \frac{\pi}{3} \bmod \pi)$, $(\sigma, \frac{2\pi}{3} \bmod \pi)$ as the preeminent structures are bundles of offset traveling chains. Weak elastic interactions broaden the pair correlation distribution. In this case, motility breaks head-tail symmetry and peaks can be seen at multiple integers of particle diameter at the head ($\theta = 0$ axis). 46

Figure 3.6: Elastic interactions promote global nematic order and local polar order. (a) Global nematic order, measuring the overall alignment of the particles' dipole axes, vs. time for low effective elastic interaction and high activity. Average global nematic order is negligible for these parameters. (b) Global nematic order vs. time for high effective elastic interaction and high activity. The system quickly gains a persistent global nematic order parameter near unity because the chains align parallel to each other. (c) Spatial distribution of time averaged polar order, where grid size is 3.75σ x 3.75σ, measuring the overall orientation of motility for the particles, for a characteristic run at low effective elastic interaction and high activity. Particles accumulate at the boundary and exhibit polar order along that boundary. This order rapidly decays away from the boundary and there is virtually no polar order observed in the bulk. (d) Spatial distribution of time averaged polar order, where grid size is 3.75σ x 3.75σ, for a characteristic run at high effective elastic interaction and high activity. A polar order near unity is observed at the boundary and persists into the bulk where near the middle of the channel $|p| \approx 0.3$. . 48

Figure 3.7: Mean-Squared Displacement or MSD vs. time interval, for 100 particles in a square simulation box of 30σ. Due to confinement of particles in y-direction, MSD is plotted separately for x and y components of displacement. (a), (b) MSD along unconfined direction: for $A = 10$, particles are super-diffusive at short time scale and diffusive at longer time scale, where the crossover time scale is determined by the Péclet number (Pe) of the particles. At $A = 100$, particles align themselves to form chains or clusters. At low Pe, the particles show sub-diffusive behavior at shorter times and ballistic behavior at longer times. At higher Pe, the ballistic behavior of particles is observed at all time scales. (c), (d) MSD along confined direction: particles reach the confining boundary at shorter times for high Pe number, and also at low elastic interactions A. At higher A, particles chain up and move predominantly parallel to the confining boundary. 49

Figure 3.8: Interaction of two motile chains (Supplementary Movie (Supplementary Movie 8). Two straight chains of 10 particles each are initialized to approach each other at an angle of $\frac{\pi}{3}$ and also π ("head-on") at $Pe = 1$ and 5. At $Pe = 1$, a 'Y' junction forms for an approach angle of $\frac{\pi}{3}$ whereas at $Pe = 5$, an 'eye' (two junctions) occurs. Upon head-on collision, a longer fluctuating chain with negligible net motility results at $Pe = 1$, and a propelling, buckled shape is observed at $Pe = 5$. Insets at the top corners represent the approach of the chains. Color represents angle of orientation of particles. The arrows indicate progression in time and suggest that the configurations are both stable and motile. 51

Figure 3.9: Traveling chains in a narrow channel exhibit cycles of mixing, laning, and collision and remixing. (a) Snapshots of a simulation where channel width has been decreased by a factor of 3. Dynamics of the system are encompassed by three cyclic states: A mixed state shown at an arbitrary initial time t_0, a phase separated laning state shown a short time after t_0, and a collision and remixing state shown a short time after the laning state. (b) Polar order averaged over boxes of width 3σ and height 2.5σ versus time is shown to elucidate the three states described in (a). The polar order for a mixed - laning - collision and remixing cycle are shown in the red circles. When the system is well mixed, the average polar order is small ($p \approx 0.2$). When the particles separate into lanes, the polar order increases rapidly ($p \approx 0.6$). When the lanes then collide and begin remixing, the remnants of the bulk of the lanes provide polar order while mixed particles and the interface between lanes decreases polar order ($p \approx 0.4$). (c) Polar order averaged over boxes of width 3σ and height 2.5σ versus time for three channel widths. Time averaged polar order, shown in dashed horizontal lines, is similar for the $L_y = 20$ and $L_y = 30$ cases when collision dynamics occur in the bulk, but non-interacting traveling chains line the boundaries. Time averaged polar order is smaller for the $L_y = 10$ case as collision dynamics are global phenomena. 54

Figure 3.10: Schematic of two interacting particles with all relevant angles and vectors labeled. $\hat{\mathbf{n}}_i$ are unit vectors of force dipoles. θ_i' are angles of force dipoles with respect to the lab frame x-axis. θ_α and θ_β are angles of force dipoles with respect to their separation vector $\mathbf{r}_{\alpha\beta}$ which has components $\mathbf{r}_{\alpha\beta,x}$ and $\mathbf{r}_{\alpha\beta,y}$. 55

Figure 4.1: **Experimental motivation and model setup.** (a, b) Isolated fibroblasts near interfaces between soft and stiffer regions of a polyacrylamide gel substrate (reproduced with permission from Ref. [3]). (a) A cell approaching the interface from the stiffer side (left) aligns parallel to the interface and remains in the stiffer region. (b) A cell on the softer side aligns normal to the interface and eventually crosses over to the stiffer side. 63

Figure 4.2: **Model setup.** Schematic of a cell moving on a flat linear elastic substrate with uniform stiffness (given by Young's modulus E, and Poisson's ratio ν) near a confining boundary. Clamped or free elastic boundary conditions are employed to distinguish between the cell being on the softer or stiffer region of the substrate, respectively. Unlike the experiment, the simulated cell is not allowed to cross the boundary. Traction forces generated by the cell are reduced to a contractile force dipole of strength $\mathbf{P}$ (red, inward pointing arrows) acting on the substrate. Cells are modeled as circular discs (shown here as red circles) of diameter σ. The direction of propulsion $\mathbf{p}$ is assumed to be along the cell dipole axis and makes an angle θ with the horizontal axis. The cell lies a horizontal distance x from the boundary (the y axis). An excluded region of extent $\sigma/2$ (a lower limit) at the boundary models confinement. 64

Figure 4.3: **Experimental motivation and model setup.** (a,b) The spatial map of the elastic interaction potential experienced by the cell as a function of distance from the boundary and the orientation is shown for free and clamped boundaries, respectively. (c) The potential is plotted as a function of distance for the control case representing pure confinement without elastic interactions (solid black), the repulsive free boundary (dashed, brown) and the attractive clamped boundary (solid, cyan). . . 65

Figure 4.4: **Spatial distribution profiles of single motile cell near free and clamped elastic boundaries.** Spatial distribution map of model cells for (a) free ($A = B = 16$, $Pe = 8$), and (b) clamped boundaries ($A = B = 8$, $Pe = 8$), where the data points represent the occurrence of cells at corresponding positions, sampled at regular intervals from multiple simulation trajectories. Insets show a magnified view close to the boundary, at $x_b = \sigma/2$, with arrows indicating the orientation of the self-propulsion of the cell at each sampled position in its trajectory. In (a), the repulsive potential from the free boundary results in a void region of extent ℓ_{void}, which cells are unable to access. Cells close to the boundary are oriented parallel to it due to elastic torques (see inset). In (b), the attractive potential from the clamped boundary causes accumulation of cells while the elastic torque orients the cells perpendicular to the boundary (inset in (b)). In the inset in (b), the pink dashed line shows the center of all the cells at $x = 0.5\sigma$. 70

Figure 4.5: **Probability of finding motile cell dipoles near free and clamped elastic boundaries.** (a,b) We quantify the localization of particles at the free (a) and clamped (b) boundaries as a function of Pe for various values of $A(= B)$. (a) For the free boundary, the localization at the boundary decreases with A. The value of P_{bound} increases with Pe due to motility induced accumulation at the boundary. At very high A, the particles cannot get close to the boundary leading to $P_{\text{bound}} = 0$. Pe_f^* corresponds to the critical value of Pe at which the cell's motility can overcome the repulsive boundary force and reach the boundary at any specific value of A. Pe_f^* increases with A (only shown for $A = 4$). (b) The localization at a clamped boundary increased with A. At low A, the boundary probability P_{bound} increases with Pe, since faster cells reach the boundaries easily. At higher values of A, cells stay at the boundary until reorientation events occurs. The high speed (high Pe) leads to rapid escape, resulting in a sharp drop in P_{bound}. There is further increase in P_{bound} due to persistence-driven accumulation. At very high A the particles don't leave the boundary leading to $P_{\text{bound}} = 1$. Here, Pe_c^* corresponds to the critical value of Pe at which the cell's motility can overcome the attractive boundary force at any specific value of A. We note that Pe_c^* increases with A, the trend being shown here at $A = 4$). 71

Figure 4.6: **Depletion region near a free boundary, and its dependence on motility and elastic strength interaction parameters.** (a) The probability distribution $\rho(x)$ of a particle is plotted as a function of closest distance x from the boundary for $A = 20$ with $Pe = 0.5, 1, 2, 5, 10$. Increasing Pe leads to a reduction in the length of the void region. (b) The void length scales as $A^{1/4}$, and $Pe^{-1/4}$ (for constant A) as predicted from force balance,see Eq. (4.5). Inset shows the collapse of the $\ell_{\text{void}} + 1$ vs $(A/Pe)^{1/4}$ for $Pe = 0.5, 1, 2, 5, 10$. 75

Figure 4.7: **Cell reorientation (flip) kinetics at clamped (attractive) boundary quantified by barrier crossing theory.** (a) For a clamped boundary, and at very high values of A and B, cells localize at the boundary even at high values of Pe, and are oriented perpendicular to the boundary. (b) Rotational diffusion enables the cell to transition from the parallel to the anti-parallel configuration. These random flips are recorded for a cell stuck at the boundary for $A = B = 20$. (c) The average frequency of these flips is observed as a function of B. The flipping time follows Kramer's theory of barrier crossing and is given by Eq. (4.6). 77

Figure 4.8: **Orientational probability profiles of cells at clamped boundary provides bounds for escape.** The angular probability distribution at the boundary $\rho_{\text{bound}}(\theta)$ is plotted for $A = 0.2$ and $A = 2$. Here we set $B = A$ in both cases. (a) For $A = 0.2$, cells are weakly attracted by the boundary and since $B = 0.2$, the torque due to elastic interaction is low. Under these conditions $\rho_{\text{bound}}(\theta) > 0$ when cells are oriented towards the boundary. Increasing the Pe increases the angle through which the cell can escape from the boundary (inset (a)). θ_{esc} is observed to be 77.4^0, 81^0 and 84.6^0 for $Pe = 1$, 2 and 10 respectively. (b) When $A = B = 2$, we identify 3 distinct regimes that are Pe dependent. For $Pe = 1$, the cells are stuck to the boundary but free to reorient due to rotational diffusion, preferentially orthogonal to the boundary. At $Pe = 10$ the cells can escape the boundary forces when the cell is oriented away from the boundary. At $Pe = 2$, the cells are only able to escape when their orientation lies in the angular pocket between $\theta = 0$ and $\pi/2$, denoted by dotted lines at $\theta_1 = 30.7^0$ and $\theta_2 = 55.8^0$. 78

Figure 4.9: **Comparison of cell migration index with experiment and a predicted durotactic phase diagram.** (a) The forward migration index defined as the ratio of cell displacement towards the boundary and its total path length, FMI $= -\Delta x/\ell_p$, is calculated from simulations at $Pe = 0.1$ and $D = 1$. Simulation results (blue diamonds) compare well with experimental data (orange circles) obtained by DuChez et al. for U-87 gliblastoma cells on an elastic substrate with gradient in stiffness from $2 - 18$ kPa [4]. The substrate had three different stiffness regions with effective Young's modulus of 5 kPa (soft), 10 kPa (medium) and 15 kPa (stiff). (b) To calculate the value of durotactic index (DI, defined in Eq. (4.8)), we simulate and compare the number of cells trapped at a confining boundary for $A \neq 0$ with the corresponding $A = 0$ case at the same Pe value. (c) Simulated phase diagram in $A - Pe$ space classified according to durotactic index and boundary accumulation. The durotactic region (green) corresponds to simulated cells (green pentagrams) with a DI greater than a threshold value (DI$>$ 0.27), which corresponds to the DI value of cells at $A = 1$, escaping through random diffusive motion. The $Pe = A$ line separates the durotactic region into the diffusion-dominated regime (DT1) and motility-dominated regime (DT2). The cells with DI smaller than the $A = 1, Pe = 0$ case (DI$<$ 0.27) are classified as adurotactic, AD1 (purple), or adurotactic with motility-induced accumulation, AD2(MIA) (orange), depending on the boundary localization given by P_{bound}. Experimental data points observed by DuChez et al. [4] are estimated to lie on the $Pe = 0.1$ line in the durotactic region (DT1), marked by the large stars. 81

Figure 4.10: **Diffusive escape from clamped boundary is governed by modified Kramers' theory.** (a) The angle-averaged original potential (black, dashed),given by Eq. (4.3), is modified to a form (orange, solid), given by Eq. (4.9), that introduces an analytical minimum at the boundary ($x = 0$), thus making the potential amenable to analysis in terms of barrier crossing theory. (b) Two trajectories of cells starting of at the boundary ($x = 0$) with random orientation at time $t = 0$ are shown with blue and maroon dashed lines. L_{esc} is the distance beyond which the interaction potential is very low, here $L_{\text{esc}} = 6\sigma$ (c) Average (mean) escape time is plotted for a simplified 1D potential which is orientation angle independent. We observe that the results follow a modified version of Kramer's theory given by Eq. (4.10) for $\tilde{f}_\nu(\theta) = 1$. (d) τ_{esc} for the 2D potential with both spatial and orientation dependence is plotted vs A at $B = 0.1$ and 2, at $Pe = 0$. The dashed lines represent the analytical escape times (purple, for $\tilde{f}_\nu(\theta) = 1$), escape along the direction of least resistance (light blue, escape along $\theta = \pi/2$) and escape along the direction of maximum resistance (brown, escape along $\theta = 0$ or π). . . . 85

Figure 4.11: **Self propulsion-assisted escape from the attractive clamped boundary (at fixed $B = 0.1$).** (a) The normalized mean escape time $\tau_{\text{esc}} D_R$ in simulation for varying Pe (shown by markers) follows the modified exponential relations in Eq. (4.14) with increasing A (shown by dashed lines) by only fitting pre-factor $m(\text{Pe})$ at the given range of values of $\text{Pe} = 0.1 - 0.5$. Here, we assume the coupling between position and orientation results in an effective value of $f^* = 0.651$, which is determined from fitting values for 2D passive particles at the given value of $B = 0.1$. The function m is linear in the Péclet number and is found to be $m(Pe) = 4.13 - 3.17Pe$. (b) Simulation results of the mean escape time (shown by markers) $\tau_{\text{esc}} D_R$ for $A = 4, 6, 8, 10$ also follows the theoretical Ansatz, Eq. (4.14) (dashed lines) with Pe based on the fitting pre-factor $m(Pe)$. 88

Figure 4.12: Cells are more likely to show durotaxis if they have higher escape time. For given Pe and B, increasing A increases mean escape time, corresponding to Fig. (4.11), as well as DI. On the other hand, increasing Pe reduces both mean escape time and DI. 90

Figure 4.13: **Durotaxis across sharp gradient of substrate stiffness** modeled by clamped and free boundary conditions - (a, b) Representative cell trajectories allowed to move across an interface between two regions (distinguished by white and gray) of contrasting substrate stiffness. In this example, they are chosen to have representative values of the Young's modulus of 5 kPa and 25 kPa, corresponding to $A = B = 5$ and 1, respectively. Each plot shows 10 single cell trajectories starting at $x/\sigma = -2$ with $D = 1$ (marked by a yellow disk) and terminating at different end points (marked by filled yellow pentagrams) after a total simulated time of $T = 20$. (a) All cells with lower $Pe = 0.5$ cross over to and spend more time on the stiffer side. (b) A few of the cell trajectories with $Pe = 2$ spend more time on the softer side as compared to the ones at lower values of Pe. (c, d) The steady state probability distribution demonstrates higher probability of finding cells on the stiffer side. The small probability of finding cells on the softer side is less for higher stiffness contrast in (c). It increases with decreased stiffness contrast in (d). The trend is more apparent at higher Pe, which allows cells to escape the attractive boundary force and spend more time on the softer side. Higher Pe also lets the cells overcome the repulsion on the stiffer side, and form the small peak near the interface. 92

Figure 5.1: **ATP activated contraction of actomyosin gel**(a)Schematic shows the formation of actomyosin gel upon mixing g-actin, fascin and myosin motors and contraction upon ATP activation. (b) Formation of different morphologies of gel depends on the intial aspect ratio of the gel, which is controlled by the thickness of the chamber and volume of the solution used. 96

Figure 5.2: **Particle Image Velocimetry (PIV) of active gels obtained from phase contrast images reveals displacements of local regions at short time scales.** The PIV of 8 different analyzed gels is shown here. The green arrows oriented inwards represent displacement vectors and show the direction of contraction. The red circle in the center is the geometric centroid of the gel. 98

Figure 5.3: **Area strain reveals regions of contraction and stretching.** Area strain (trace of the strain tensor) is shown as heatmaps for Gels 1, 3 and 5 for corresponding frames in Fig. 5.2. The red arrows show the PIV displacements after subtracting the rigid body motion of the gel. The inner region of the gels is highly contracted shown by dark blue regions. Close to the boundary there are patches of stretched regions shown by bright yellow spots. (All strains are normalized by their maximum positive and negative values) 100

Figure 5.4: **Azimuthal averaging over annular bins gives radial and azimuthal displacement** (a) Circular annular bins are constructed around the center of contraction. The radial and azimuthal components of the displacements are averaged over all angles from center to the boundary. (b) The angle averaged azimuthal displacement (u_ϕ) does not change with distance from the center of the gel and fluctuates close to 0. The angle averaged radial displacement (u_r) increases linearly in magnitude from the center in the inner region and decreases closer to the boundary in the outer region. 101

Figure 5.5: **Time dependent comparison of radial displacements (u_r) for different gels** (a,b) Radial displacement profiles of gels 1 and 3 respectively at times $t_1 < t_2 < t_3$ are plotted with respect to the normalized distance (r/R_{disk}) from center to the boundary. The magnitude of u_r decreases from that at t_1 to t_3 but the normalized boundary length δ/R_{disk} remains constant for both gels. (c,d) Both the radius of the gel and the boundary length δ decrease exponentially with the same time scale. . . 102

Figure 5.6: **Strain plots reveal a contracting inner region and a stretched outer region** (a) Angle averaged radial and azimuthal strain plots are shown for Gel 1 at times $t_1 < t_2$. Close to the center, the radial and azimuthal strains are constant and equal in both gels, suggesting isotropic contraction. In the transition region, there is a gentle increase in radial strain which becomes positive close to the boundary, suggesting possible stretching. The azimuthal strain increases and approaches 0 close to the boundary. (b) 2D plot of radial strain for gel 1 shows the local strains as estimated from the center of contraction. 103

Figure 5.7: **Gel contracts azimuthally close to the boundary** (a) Confocal image of gel reveals an azimuthally aligned region of actin fibers suggesting azimuthal contraction (b) Eigenvalue and eigenvector analysis of area strain gives the principal directions of contraction and stretching. Azimuthally aligned eigenvectors close to the boundary suggests azimuthal contraction while eigenvectors pointing in random directions close to the center suggest an isotropic contraction core. 104

Figure 5.8: **Proposed contraction model as interpreted from analysis of PIV of gels** (a) This is the proposed schematic for gel contraction with axisymmetry. Each contractile actomyosin unit produces an active stress in the gel, which maybe considered as a force dipole. Close to the boundary, the alignment of stress generated by actin fibers, is represented by contractile force dipoles. These are aligned azimuthally, *i.e.* parallel to the the boundary of the gel. In the inner region there is no specific alignment of force dipoles leading to isotropic contraction. The resulting active forces from the force dipoles at different local regions of the gel are shown by black arrows in the insets. In an overdamped elastic contraction model, these forces direct the local displacement of the gel. (Top inset) Due to isotropic distribution of the force dipoles, the net force at any location in the inner region is 0. But at the edge of the isotropic region, there is an unbalanced force pointing radially inwards (Bottom inset) Due to the azimuthal alignment of the force dipoles, there is an inward pointing unbalanced radial force. The force decreases as $1/r$ from the center, due to the curvature in the direction of alignment of the force dipoles. (b) Analytically calculated radial displacement profile for the model reproduces characteristic "hockey-stick" shape found from the PIV analysis of experimental data. The inner isotropic region shows linear increase in magnitude of displacement. Closer to the boundary, the magnitude of displacement reduces, since the force gets smaller. 105

Figure 5.9: **Differences in radial displacement and strain profiles dictate formation of different gel morphologies**(a,b)The radial displacement profiles obtained from PIV analysis of different gels shows the contrast in curvature between "domes" and "gels" as predicted by the model. (c) The radial strain heatmap of Gel - 1 shows inner radial contraction region and gentle in increase in radial strain close to the boundary in case of "dome". (d) The radial strain heatmap for wrinkles (Gel - 5) shows a sharp increase in radial strain from inner to outer region and then a gentle decrease close to boundary. (All strains are normalized by their maximum positive and negative values) 108

Figure 5.10: **Azimuthal strain reveals formation of wrinkles** (a) Temporal and spatial variations in PIV vectors can lead to high azimuthal strain demarking the onset of formation of wrinkles. (b) Thickening of actin bundles is observed in the phase contrast image of the gel at the locations indicated by the big white arrows. (c) Azimuthal strain at the boundary increases in magnitude at the locations where a wrinkle is forming which is observed at two angular regions between $-\frac{\pi}{3}$ and $\frac{\pi}{3}$ 110

Figure B.1: The force from the boundary and active force orthogonal to the boundary both depend on the angle of orientation with the boundary. We compare the forces at the boundary to graphically estimate the angle of escape of the particles. We compare the force from the boundary (solid blue) at (a) $A = 0.2$ and (b) $A = 2$ with active forces perpendicular to the boundary (dashed) at $Pe = 1, 2, 10$. The particle can escape at angles where the orthogonal component of the active force is greater than the boundary interaction. (a) At $A = 0.2$, for all values of Pe, the particles can escape the boundary through any angle θ such that $cos\theta > 0$. Increasing Pe increases the angle of escape. (b) At $A = 2$ we observe 3 different behaviors. For $Pe = 1$ orthogonal component of active force is always less than the boundary force. At $Pe = 10$, the active force is higher than the boundary force and intersect each other at 1 point. The active force is higher than the boundary force only inside angular pockets for $Pe = 2$. 122

Figure B.2: (a) Schematic of the classical Kramers' Problem for escape from a potential well and across a potential barrier. Particles move in a spatially varying potential $U(z)$, shown as the black curve, that is a function of a general coordinate z. The potential $U(z)$ exhibits two minima: the first at location $z = A$, and a second minimum beyond point $z = C$. Additionally, to get from A to C, particles subject to $U(z)$ have to surmount and pass through a barrier with a local maximum at $z = B$ where $A < B < C$. We analyze an ensemble of particles initially in an equilibrium distribution at the bottom of the cell $z \sim A$, and study the rate at which they escape the barrier at B, and reach C. (b) Schematic of the barrier crossing problem for active self-propelled particle escaping from a potential well. 125

Figure B.3: (a) The mean escape time evaluated from simulation (solid black circles) follows the modified Kramer's theory of barrier crossing for passive particles with $Pe = 0$ moving in the 1D modified potential without the coupling between position and orientation ($\tilde{f} = 1$). In the limiting cases resulting in Eq. B.24, the solid line and dashed line represent the analytical results and the approximation, respectively. (b) Results for the mean escape time from simulations (black circle, red square and blue star symbols) for passive particles in 1D, and with $B = 2, 0.1$ in 2D, respectively. Values of effective f^* averaged over orientational degrees of freedom is by fitting and estimated to be 0.788 and 0.651 for $B = 2, 0.1$, respectively. For larger B, the particles always flip between orientations $\theta = 0$ and $\theta = \pi$, and thus confirm to the 1D situation. Thus, the upper bound of f^* is given by 1 corresponding to 1D case. The lower bound could be estimated by the $f^* \approx \tilde{f}(\theta = \pi/2)$. 128

Figure B.4: (a) The fitting pre-factor $m(Pe)$ (black squares) follows a linear form $m(Pe) = 4.24 - 1.74\, Pe$ (dashed line) for $B = 0.1$. (b) For $f^* = 1$, the magnitude (extent) of the ΔC region increases as A increase, but decreases as Pe increases. 131

Figure B.5: The durotactic index DI as defined in Eq. 8 is plotted here in two ways. In (a), we observe that DI increases with elastic force parameter, A when Pe is held constant and reaches limiting values. (b) For A held fixed, we find that DI decreases with cell motility, Pe. The index is 0 by definition for $A = 0$. 134

Figure B.6: The durotactic index DI as defined in Eq. 4.8 is plotted here in two ways. In (a), we observe that DI increases with elastic force parameter, A when Pe is held constant and reaches limiting values. (b) For A held fixed, we find that DI decreases with cell motility, Pe. The index is 0 by definition for $A = 0$. 135

Figure B.7: The elastic torque from interface between the soft and stiff substrate tries to align the cells perpendicular or parallel to the boundary depending on the direction of approach to the interface. In these trajectories we do not consider any translational or rotational diffusion and also neglect the force from the interface. We observe the effect of elastic torque on the trajectory of cell approaching from the same distance on either side of the interface. (a) When cells are approaching from the softer side of the interface ($x = -5$, $y = 0$, shown by red semicircle) where the interface is at $x = 0$, with $Pe = 2$, the particle trajectories (shown by black lines) get aligned perpendicular to the interface. This kind of behavior is observed in case of refraction when light is traveling from a rarer to a denser medium. Here the refractive index can be realized to be increasing as it approaches the interface. The torque parameter $B = 5$ in the softer substrate region. (b) Cells approaching the interface from the stiffer side of the interface ($x = 5$, $y = 0$, shown by red semicircle) aligns parallel to the interface. This kind of of behavior is observed when light is traveling from a optically denser to a rarer medium. The torque parameter $B = 1$ in the softer substrate region. 136

Figure B.8: The trajectories that are allowed to cross the interface are shown by black lines. The cells approaching the interface (shown by dashed line at $x = 0$) from either side of the interface have motility (a,d) $Pe = 0.5$, (b,e)$Pe = 2$ and (c,f)$Pe = 10$. The soft side of the substrate ($x < 0$) has a Young's modulus of 5kPa ($A = B = 5$), while the stiff side ($x > 0$) of the substrate has a Young's modulus of 25 kPa ($A = B = 1$). 137

Figure C.1: Different components of the strains are obtained from the central difference method. 139

Figure C.2: **Center of contraction to estimate radial profile:** (a) When the gel gets stuck at any point which is not the centroid (r_{CoM}), the center of contraction (r_{CoC}) is shifted to that point. (b) A sample PIV with centroid of the gel shown by a red circle while the center of contraction is shown by a white circle. (c) The PIV changes after subtracting the rigid body motion of the gel. The center of contraction coincides with the centroid shown by the red circle. (d) A very noisy radial profile of the radial displacement is obtained with respect to the centroid of the gel. (e) Noise is reduced when radial profile is obtained from the center of contraction. 143

LIST OF TABLES

Table 2.1: Biophysical parameters characterizing the two-cell (typical values from [5, 6, 7]). 20
Table 2.2: Simulation parameters and their meaning. 20

Table B.1: List of biophysical parameters. 120
Table B.2: List of simulation parameters. 120

ACKNOWLEDGEMENTS

It goes without saying that my experience as a PhD student has been a roller coaster ride, which I believe most of my colleagues can relate to. Without the constant support of my family and friends, I would have lost my mind.

I would like to express my deepest gratitude to my family for their endless love, unwavering support, and encouragement throughout this journey. I am especially grateful to my elder brother for inspiring me to follow the path of Physics. He has been my guiding light for as long as I can remember, always there to help me with academics whenever I needed it. I would like to thank my mother for waking me up every single day, despite living on the opposite side of the globe, for teaching me how to cook over calls, and for ensuring that I maintain my physical and mental health. I am thankful to my father for always having faith in me, trying to understand my research, and keeping me motivated. I deeply appreciate my parents' sacrifices for me, and I can only hope to repay them, starting with my doctorate. Thank you all for being my pillars of support.

I extend my sincere gratitude to my esteemed advisor, Dr. Kinjal Dasbiswas, whose unwavering support, patience, motivation, and profound knowledge have been instrumental throughout my Ph.D. studies and related research. During my Ph.D., there were moments when I doubted my abilities, but Dr. Dasbiswas's faith in me was truly admirable. With his guidance, I managed to publish a paper within a year of starting my work with him.

I would also like to thank Dr. Arvind Gopinath, a collaborator and esteemed member of my committee, for his mentorship, which has greatly contributed to my academic growth. Special gratitude is reserved for Prof. Anne Bernheim-Groswasser from Ben Gurion University, Israel, for her helpful discussions.

In addition to my advisor and collaborators, I express my heartfelt thanks to the other members of my thesis committee: Dr. Dustin Kleckner and Dr. Roberto Andresen Eguiluz. Their insightful comments, encouragement, and challenging questions have spurred me to broaden my research perspectives.

I made wonderful friends over the years, as a PhD student and otherwise. I'd like to give a heartfelt shout-out to a few of them whose presence has truly made a difference in my life. First and foremost, my lab mates (now Dr.) Patrick Noerr, Abhinav Kumar and Arnab Roy have been invaluable companions. I had countless research discussions with them which enriched my understanding, and their expertise in their respective fields

provided valuable insights during our group meetings. I learnt a lot from them, and I hope I had a similar impact on them as well. I would like to extend my gratitude to my collaborator, Dr. Haiqin Wang, for the many insightful discussions we have shared.

My senior and mentor Dr. Niranjan Sarpangala, (formerly from Prof. Ajay Gopinathan's group), stands out as a role model. Not only did he assist me with various research challenges, but he also shared practical advice about postdoc positions and how to look for them. His initiative in starting a writing group significantly aided my academic growth. Another influential mentor during my PhD journey was Dr. Ritwika VPS, another former member of Prof. Gopinathan's team. She patiently guided me through academic writing, which had been a major obstacle for me. I'm grateful for her support. I would also like to thank Dr. Monika Sanoria who encouraged me to step out of my comfort zone and engage in conversations with renowned scientists as I consider future postdoc opportunities. These mentors not only taught me valuable lessons for my research but also became cherished friends. Our shared road trips and potluck gatherings are treasured memories.

I am deeply grateful to my current roommates, Shubham Rohal, Richa Thakur, and Arya Rajan, with whom I have spent countless nights playing card and board games. These moments provided much-needed respite from the rigors of research. I would especially like to thank Arya for her unwavering mental and emotional support during my toughest days. This year has been challenging, but her presence made it significantly more bearable.

I also want to extend my heartfelt thanks to my other friends – Jimmy, Maria, Binod, Anshika, Ekta, Asmitha, Suraj, Anuvetha, Madhuvanthi, Devika, Vignesha, Micah and Albert. Their companionship has made my time as a grad student truly enjoyable.

Lastly, I am thankful to the Center for Cellular and Biomolecular Machines (CCBM) for creating a platform for people working on similar subfields of biophysics to share their research. Being a CCBM scholar I appreciate the opportunity I got to share my research and at this interdisciplinary center. This helped me develop my presentation skills and think more about the physics and biological questions that are expected at scientific meetings and develop as a true researcher.

Subhaya Bose

Education

2019–2024 **Ph. D (Physics)**, *University of California, Merced*, GPA: 3.911/4.
Advanced to candidacy: Summer 2022; Graduation: expected December 2024

Advisor(s): Dr. Kinjal Dasbiswas (Physics, UC Merced).

2014–2019 **Int. B.Tech - M.Tech Dual Degree (Engineering Physics) with Hons. in Condensed Matter Physics**, *Indian Institute of Technology, (BHU), Varanasi (IIT BHU), India*, *GPA: 8.55/10*.

Awards and Other Achievements

2024 **CCBM Travel Award**, *UC Merced*.

2024 **DBIO travel award for APS March Meeting**, *American Physical Society*.

2024 **Physics grad group travel award**, *Physics Department, UC Merced*.

2024 **Graduate Student Supplemental Travel Award**, *UC Merced*.

2020–2024 **CCBM Scholar**, *Center for Cellular and Biomolecular Machines (CCBM), UC Merced*.

2022 **Travel Award for Cargese Summer School**.

2014 **Kishore Vaigyanik Protsahan Yojana (KVPY), India Fellowship**.

Publications

1. **Subhaya Bose**, Haiqin Wang, Xinpeng Xu, Arvind Gopinath, Kinjal Dasbiswas. **Elastic interactions compete with persistent cell motility to drive durotaxis** Biophysical Jornal 10.1016/j.bpj.2024.09.021
2. **Subhaya Bose**, Patrick Noerr, Ajay Gopinathan, Arvind Gopinath, Kinjal Dasbiswas. **Collective States of Active Particles With Elastic Dipolar Interactions** *Frontiers in Physics*. 10.3389/fphy.2022.876126
3. **Subhaya Bose**, Arvind Gopinath, Kinjal Dasbiswas. **Matrix Stiffness Modulates Mechanical Interactions and Promotes Contact between Motile Cells.** *Biomedicines*. 10.3390/biomedicines9040428
4. Devyani Shukla, **Subhaya Bose**, Smarajit P Choudhury, Vinay K. Sharma, Megha Das, Shivesh Sabbarwal, Sanjeev K Yadav, Manoj Kumar, Avanish S Parmar. **Understanding the In Situ Mechanistic Control of Plant-Derived Carbon Quantum Dots on the Synthesis of Gold Nanoparticles***Chemistry Select*. 10.1002/slct.201903634

Manuscripts in Preparation

1. **Subhaya Bose**, Haiqin Wang, Xinpeng Xu, Arvind Gopinath, Kinjal Dasbiswas. **Activity-assisted escape of tactic cells from a confining boundary**
2. **Subhaya Bose**, Arnab Roy, Gefen Livne, Sakshi Chaudhari, Anne Bernheim-Groswasser, Kinjal Dasbiswas. **Analysis of elastic strains reveals shape selection pathways in active gels**

3. Sakshi Chaudhari, **Subhaya Bose**, Kinjal Dasbiswas, Anne Bernheim-Groswasser. **Investigating Fluid Dynamics: Micro Particle Image Velocimetry (Micro-PIV) and its protocol**

Conferences and Seminars

December 2024	ASCB CellBio 2024 (Poster)
May 2024	Bay Area Cytoskeleton Symposium (Poster)
March 2024	APS March Meeting, Minneapolis (Talk)
March 2023	APS March Meeting, Las Vegas (Talk)
March 2022	APS March Meeting, Chicago (Talk)
March 2021	APS March Meeting (Talk, presented virtually)
December 2017	International conference on "Natural and Artificial Molecular Machines" Mumbai India (Attended)
December 2017	International conference on "Current Trends in Intracellular Transport by Molecular Motors" Mumbai, India (Poster)

Workshops and Schools

Summer 2024	Boulder Summer School 2024
August 2023	"Soft and Living Matter - 2023" Summer School in ICTS, Bengaluru, India
Fall 2022	"Active Matter and Complex Media - 202" Summer School in Cargese, France
Summer 2021	UMass Amherst Summer School (held virtually)
Summer 2020	CCBM-CREST Summer Workshop: Introduction to Scientific Computing (held virtually)
Winter 2017	International Workshop on"Modern Biophysical Tools and Technique" - 2017

Technical and Computer Skills

MATLAB, LaTeX, Python, ImageJ, NetLogo, Mathematica

ABSTRACT OF THE DISSERTATION

Role of active and elastic forces in cell migration and cytoskeletal shape change

by

Subhaya Bose

Doctor of Philosophy in Physics

University of California Merced, 2024

Dr Kinjal Dasbiswas, Thesis Adviser

The mechanical micro-environment of cells significantly impacts their structure, function, and motility, influencing essential processes such as tissue development and cellular interactions. The actomyosin cytoskeleton is very important in controlling the shape and migration patterns of the cell.

Cells exert contractile forces on their substrates, leading to deformations that can mediate long-range cell-cell interactions and facilitate coordinated movements. To explore these dynamics, we propose and analyze a minimal biophysical model that integrates cell migration with mutual mechanical deformations of an elastic substrate. Our model evaluates key metrics including the number of cell-cell contacts, dispersion of cell trajectories, and probability of permanent cell contact, examining how these metrics vary with cell motility and substrate stiffness.

Inspired by cell mechanobiology, we model cells as self-propelling particles interacting through substrate-mediated forces. This active matter framework combines motility dynamics with linear elasticity to reveal emergent collective behaviors, such as the formation of flexible, motile chains and larger-scale structures with polar order. By varying elastic interaction strengths and motility, and considering confinement within a channel geometry, we identify different collective states and their implications for cell organization.

Additionally, we introduce a phenomenological model for durotaxis, the directed migration of cells towards stiffer substrate regions, incorporating elastic deformation-mediated interactions and stochastic motility. Our model demonstrates how cells reorient and mi-

grate in response to substrate stiffness, with boundary conditions influencing accumulation or depletion. We quantify the effects of contractility and motility on durotaxis, presenting a phase diagram that characterizes distinct migration regimes.

Finally, we explore how orientational order in actively contractile elastic disks influences strain profiles. We analyze the 2D radial profiles displacement and strains and determine distribution of active stresses in the disk from an analysis of its strain. We also predict the out of plane deformations of active gels from its 2D dynamics. We further developed a simplistic continuum model, which combines elastic displacement with an orientational order parameter, provides analytic solutions for strain-induced alignment in filamentous gels. Comparative analysis with experimental data from actomyosin gel disks validates the model and enhances our understanding of active stress directionality in complex biological systems.

Overall, our work offers a framework for understanding mechanical interactions in cell migration and organization, applicable to both biological and synthetic active matter systems.

Chapter 1

Introduction

1.1 Motivation

Humans have long been captivated by birds gliding through the sky and the graceful movements of swimming fish. Few children are not enchanted by the drifting seeds of a dandelion or mesmerized by a trail of ants. While plants appear stationary, the flow of fluids through their stems and leaves remains unseen, yet is just as essential. To live is to be in constant motion [8].

> "But for anything to be alive, it required motion: the current must run, the record must turn, a person must leave or find another path. Without movement or change, the world became nothing more than a stale copy, it was frozen in time."
>
> – *Madeleine Thien*

In the physicists' view of life, equilibrium is death. To sustain life, organisms absorb energy from their surroundings and use it to remain in a state far from equilibrium, while performing all other essential functions for survival. Starting with 19th-century concerns about the laws of thermodynamics, energy conversion in biological systems has been a continuous source of fascination for physicists.

Organisms need to move in order to stay alive. They move from one place to another to accomplish various things. They move towards sources of food, sometimes over long distances, guided by weak information about the location of the source. The useful signals in the environment and internal signals guide their motion.

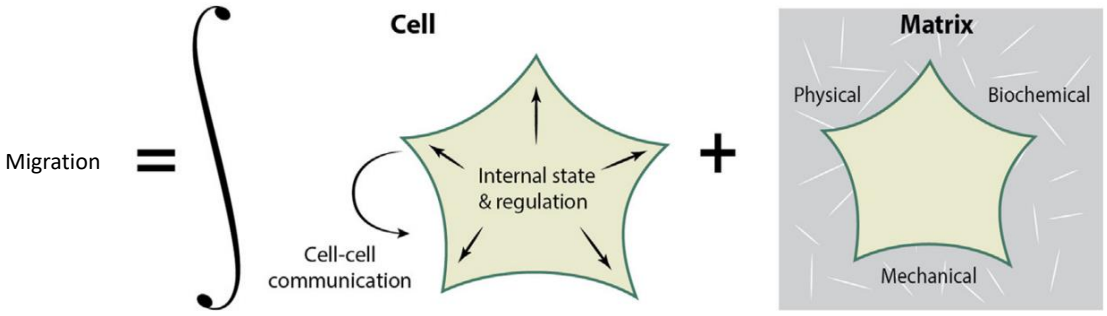

Figure 1.1: (This figure is reproduced with permission from Elsevier.) An illustration of the dynamic interactions between the cell and the matrix during cell migration. While navigating through the matrix, the cell continually integrates physical, biochemical, and mechanical cues from its internal biomolecular regulation, from other cells, and from the matrix.

Growth and motion has been observed in organisms at microscopic scales, extending down to the scale of individual cells. Although cells show a wide variety of migration modes, we can classify them roughly into two categories: migration through liquid medium such as bacterial swimming; and migration through solid ECM, observed in motile animal cells [9]. Animal cell migration is crucial in a number of biological functions, ranging from embryonic development[10, 11], morpho- and organogenesis[12, 13], neuronal guidance[14], and immune response[15, 16], to wound healing[17]. It is also involved in pathophysiological processes such as those occurring in cardiovascular diseases[18, 19] and cancer metastasis [20].

Cell migration is achieved by integrating internal cues within the cell and external cues from the environment (Fig. 1.1) [21]. These cues can be physical/mechanical as well as biochemical. The effect of biochemical cues has been studied extensively. Cell migratory behavior is affected by secreting and receiving various soluble biochemical signals such as chemokines, metalloproteinases (MMPs) and growth factors[22, **?**, 23, 24, 25, 26]. The response of cells under physical/mechanical signals is not completely understood.

Cell migration depends significantly on the geometry of the surroundings. The cells' ability to change shape enables them to travel through 3D porous media [27, 28]. The ability of a cell to do so is determined by the porosity of the medium and stiffness of the cell itself [29, 30]. Low cell stiffness or high cell deformity has been associated with metastasic potential of cells [31, 32]. A cell's ability to travel through porous media is vital in tissue engineering [33, 34]. Although most cells are embedded in 3D medium in organisms,

understanding the underlying mechanism of how substrates interact with the cells is not very straightforward. This is simplified by in-vitro culture of cells on 2D surfaces [35, 36]. The cells on 2D surfaces have a much wider space to explore. The migration is often dominated by broad, flat protrusions called lamellipodia that are driven by the polymerization and treadmilling of branched actin networks [37, 38, 39]. Migration in environments with complex geometries such as tubes, channels, and discontinuous surfaces require more complex machinery that combine effects of cell contractility, substrate topography, and surface adhesion [40, 41].

The viscoelastic properties of the matrix play a major role in cell behavior. The matrix stiffness or elasticity varies from 100 Pa in adipose and brain tissues to MPa or GPa in bones[42]. The stiffness dictates the ability of the cells to migrate in different tissues. Hence, it is expected that alterations in matrix stiffness is associated with progression of diseases including cancer, fibrosis, and atherosclerosis [43]. It has been established that the macroscopic stiffness of breast tumors is strongly correlated with local recurrence and metastasis and can be used as a diagnostic tool [44]. Moreover, it has been shown that the cells show durotaxis, which is a substrate stiffness dependent preferential migration towards a stiffer substrate region [3]. This behavior of cells is suggested to have implications in tissue repair [45].

These eukaryotic cells move by crawling, that is by adhering to and exerting mechanical stresses on their extracellular matrix (ECM) and actively deform it. Animal cells adhere to the elastic substrate by means of a membrane embedded protein called 'integrin'. Actin filaments tether to integrins and molecular motors such as myosin exert force on these filaments by walking along and moving them. Stress fibers are bundles of crosslinked actin filaments with a periodic (sarcomeric) organization of myosin [2] that often span the length of the cell and are anchored at the focal adhesions to the extracellular substrate or matrix (ECM). Cell migration on a 2D surface involves a cascade of events starting with actin polymerization at the leading edge, which generates a force to cause protrusion. The formation of this protrusive edge called the lamellipodium facilitates the formation of new focal adhesions with the substrate [46]. Stress fibers generate contractility in the cell which is mediated by the focal adhesions (FA) and the retrograde flow of actin [47, 48]. The forces produced by the contractile network combined with actin filament and FA disassembly help to retract the trailing edge of the cell.

The contractile forces are transmitted to the underlying elastic substrate [49] and

deform it [50, 51]. Such deformations are long range (extend up to a few cell lengths away from the cell) and can be measured by Traction Force Microscopy (TFM), which is an experimental method to determine the traction forces exerted by a cell on the extracellular matrix by obtaining the displacement fields on the substrate [52, 53]. The cells try to minimize elastic energy by relaxing the elastic strain caused by the deformations. They do so by reorienting the alignment of elastic stress. These substrate deformations can be caused by external sources or neighboring cells or a gradient in substrate stiffness.

Another key aspect I address in my work is active matter. Schrödinger in his book "What is Life?" [54] emphasized that living systems must be kept away from thermodynamic equilibrium to establish order and develop complexity, and do so by continuously consuming energy. This aspect of life is idealized in what we call active matter, namely systems composed of self-driven agents that perform mechanical work on themselves and their environment [55, 56, 57]. Active matter exhibits a wide range of emergent non-equilibrium phenomena, theoretical studies of which often require computer simulations. It encompasses synthetic and living systems, including active gels [58], such as biopolymer networks activated by molecular motors, cells and tissues, and collections of self-propelled nanorobots and microrobots, synthetic and biological microswimmers, animal herds, and flocking birds [59] . In all these cases, mechanical energy is locally generated by the active agents through the conversion of stored or ambient free energy into mechanical work.

The active stresses generated by the actomyosin cytoskeletal network are not just responsible for cell migration and inter-cellular interactions but also the formation of complex 3D shapes during various biologically relevant processes [60, 61]. Living systems can take on different curved shapes [62]. These diverse morphologies appear at many lengthscales, from lamellipodia of cells to structure of tissues and organisms [63] (in hydra [64, 65]). These morphologies modulate intricate processes such as cell migration and tissue morphogenesis [66], [67, 68]. These dynamic shape changes in biological matter are driven primarily by contractile stresses generated by myosin molecular motors. Myosin converts chemical energy into mechanical work by exerting force on the cell's actin cytoskeleton network [69, 70, 71, 72]. These stresses can extend across tissues, affecting the shapes of cells and tissues which are typically organized in two-dimensional thin sheets [60]. Cells and tissues arranged in 2D surfaces tend to show buckling deformations when they are subjected to imbalanced in-plane strains [65, 73, 74, 75].

Due to the complexity of structures of cells and tissues, however, the mechanism by

which these intrinsically active stresses cause shape changes in 3D are poorly understood. A promising approach is to recreate the stress-generating system outside cells using the same building blocks, actin and myosin. By precisely controlling the concentration and activity levels of these microscopic constituents, we can form intrinsically active, cross-linked actomyosin networks. Such networks exhibit spontaneous contraction and self-organization, resulting in various 2D contraction patterns[75, 76, 77, 78, 79, 80] and the spontaneous wrinkling of thin elastic actomyosin gel sheets [81, 60].

1.2 Background

There are several models that study the contractility of cells and the effect of elastic response on the cells. One of the commonly used method is the lattice or cellular Potts model, which have been successfully used to evaluate and predict cell shape and is modeled as a set of lattice points. The natural theoretical framework for studying this situation is continuum mechanics. It is traditionally used to address the mechanics of macroscopic objects like growing tissue [82]. But there are different continuum mechanics approaches that have recently been developed to describe the shapes and forces of adherent cells [83]. In particular, the powerful framework of the finite element method (FEM) was adopted for this purpose. A detailed FEM model integrating mechanical and biochemical aspects was developed that can explain many details of cell adhesion [84, 85, 86]. The Hamiltonian is calculated at each lattice point to determine the size, shape, and motion of the cell.

Another well-established, yet coarse-grained, model that captures the cell dynamics is the molecular clutch model. Cells are thought to probe their environment through the generation of traction by a 'motor-clutch' mechanism where cells utilize molecular clutches to physically link actin bundles to the extracellular substrate at the focal adhesion points [87, 88]. Cells use the motor-clutch system to probe their mechanical environment which is influenced by substrate stiffness[89, 90, 91]. When this model is combined with biochemical responses, it reflects the directionality of cell's propulsion [89, 91].

These models are able to capture cell migration and cell shape, but they are computationally expensive and do not reveal enough statistics about the directionality of cell motility and the effect of combining substrate-based deformation and self-propulsion of the cells.

In this dissertation, we propose a coarse-grained minimal model that combines the

cell's motility with the elastic deformations of the underlying substrate.

There are equal and opposite forces generated at either end of the stress fiber leading to the formation of force dipoles. The force dipoles generate elastic stresses on the substrate and all the neighboring contractile cells respond to this elastic stress and interact with them through substrate mediated forces. These interactions can be coupled to self-propulsion and translational and orientational diffusion of the cell to get a pair of Langevin equations that guide the motion of the cell as shown in eqs. 1.1 and 1.2

$$\frac{d\mathbf{r}}{dt} = \mathbf{v}_0 - \mu_T \left(\mathbf{F}_{elastic}\right) + \sqrt{2D_{\mathrm{T}}}\ \boldsymbol{\eta}_{\mathrm{T}}(t) \tag{1.1}$$

$$\frac{d\theta}{dt} = -\mu_R \left(\tau_{elastic}\right) + \sqrt{2D_{\mathrm{R}}}\ \eta_{\mathrm{R}}(t) \tag{1.2}$$

We model these cells as active Brownian particles,i.e. particles that show persistent motion in addition to diffusive behavior. Persistent motion refers to the tendency of particles to move in a consistent direction for a certain period, while diffusive behavior describes the random motion that occurs over time due to interactions with their environment [92, 93]. These particles are guided by the aforementioned overdamped Langevin equations, where the position update of the cells is shown by $\mathbf{r}$ and orientation update by θ. The self - propulsion of the cells is given by $\mathbf{v}_0$ and elastic force and torque sensed by the cell are given by $\mathbf{F}_{elastic}$ and $\tau_{elastic}$. The form of elastic forces and torques can vary depending on the nature of interaction, i.e. interaction with other cells or interaction with mechanical boundaries. The translational diffusivity and mobility are given by D_{T} and μ_{T} respectively and rotational diffusivity and mobility are given by D_{R} and μ_{R}. $\boldsymbol{\eta}_{\mathrm{T}}$ and η_{R} represent the translational and orientational white noise associated with the cell's migration.

With this method we compromise on the knowledge of details about the cells like their shape and change in size while drastically improving computational efficiency. We can generate statistics over long time scales about cell behaviors like distribution of position and orientation, radial distribution function, as well as mean squared displacement.

1.3 Overview

In this text I present my work on the importance of actomysin cytoskeletal network on cell migration and defining shape in active gels.

In chapter 2, we investigate how elastic substrate stiffness modulates mechanical interactions and facilitates cell-cell contact. Interactions between cells and their mechanical environment influences cell shape and function, including cell motility. Cells can migrate and form contacts which is key in tissue development, wound healing etc. Cells are known to exert contractile forces on the underlying elastic substrate and communicate with other neighboring cells. Here, we propose and analyze a minimal biophysical model for cell migration and long-range cell–cell interactions through mutual mechanical deformations of the substrate. We compute key metrics of cell motile behavior, such as the number of cell-cell contacts over a given time, the dispersion of cell trajectories, and the probability of permanent cell contact. Our investigation explores how these metrics depend on a cell motility parameter and substrate stiffness. These results suggest how cells may sense each other mechanically and generate coordinated movements. Additionally, the metrics also provide an extensible framework to further address both mechanical and short-range biophysical interactions.

In chapter 3, we aim to expand our understanding to collective behavior of group of active particles interacting with elastic dipolar interactions. Cells interacting with long range elastic interactions can often form self-organized structures and show coordinated migration. Here we show that particles self-assemble into flexible, motile chains which can cluster to form diverse larger-scale compact structures with polar order. Focusing on the strong elastic interaction cases in the dilute regime, we study the self-assembly and dynamics of single chains. This study opens door to exploring the bending dynamics of a single active polymer and characterizing how the bending rigidity increases with dipolar interaction strength or decreases with particle motility.

In chapters 4, we investigate how cells tend to migrate preferentially from a soft substrate region to a stiff substrate region. This phenomenon of durotaxis has been associated with morphogenesis, neuronal guidance as well as cancer metastasis. We address single cell durotaxis across a sharp gradient of substrate stiffness. In our model, we considered elastic dipolar interaction with clamped and free boundaries to capture the interaction of cells with a sharp gradient of substrate stiffness. In addition to getting attracted or repelled by the boundaries, cells orient their contractility to minimize elastic energy. We compute metrics such as steady state probability of cells being at the boundary, cell reorientation dynamics and flipping time and study the effect of strength of elastic interaction and cell motility on these metrics. We further compute escape time of cells from the attractive

clamped boundaries as a scenario captured by a modified Kramer's theory of barrier crossing. Our results suggest that escape time is key in determining the extent of durotaxis. Finally, we define metrics quantifying boundary accumulation and durotaxis, and present a phase diagram that identifies three possible regimes: durotaxis, adurotaxis without accumulation and adurotaxis with motility-induced accumulation at a confining boundary.

In chapter 5, we investigate the contraction phenomenon of thin actomyosin gels. Upon contraction these gels buckle to form different morphologies. We explore the mean radial profiles of radial displacement, and radial and azimuthal strain between frames to determine the distribution of active stresses. Moreover, we predict contraction phenomena of different gel morphologies from the radial strain profiles. And finally, from the azimuthal strain profile, we are also able to determine the location at which a wrinkle is forming or getting more pronounced.

Finally in chapter 6, I will summarize my work and present conclusions.

Chapter 2

Matrix stiffness modulates mechanical interactions and promotes contact between motile cells

This chapter is reproduced from our published article in *Biomedicines*.

2.1 Introduction

Many eukaryotic cells move by crawling, that is by adhering to and exerting mechanical stresses and local forces on their extracellular matrix (ECM) that they then actively deform (see for instance [94, 95, 5, 96] and references therein). For these motile cells, that include fibroblasts, endothelial and muscle cells among others, the mechanical properties such as viscosity and elasticity of the environment on or in which the cell moves is known to play crucial roles in determining cell and tissue structure and function [97, 98]. The biological relevance of mechanical signaling between cell and substrate or between two or more cells, as opposed to more extensively studied inter-cellular chemical signaling was dramatically illustrated in [99] where it was shown that the lineage specification of stem cells can be directed by varying only the substrate stiffness. Much recent progress has been made since this pioneering work in understanding the role of mechanical forces in

biology, and how biomolecules especially those in the cellular force-generating and surface-sensing systems and signalling networks respond to mechanical forces through the process of mechanotransduction [100, 101, 102, 103, 104, 105, 106, 97, 107, 108].

Existing approaches to modeling collective cell motility focus on direct (steric and adhesive) cell-cell interactions or focus at the single cell level on cell-substrate interactions [95]. The latter deals with details of focal adhesions that are crucial to generating traction stresses in both adherent and motile cells [1]. Experiments surprisingly and strongly indicate that cells cultured on soft, elastic, bio-compatible substrates can respond to each other even when not in direct contact [5, 96]. Such non-contact and long-range cell-cell interactions arise often when cells are cultured. A common method is to culture cells on the surface of synthetic hydrogels such as polyacrylamide, a linearly elastic polymer. In this instance, cells that are spatially separated may still sense each other through mutual and active deformations of the gel by the cells. These mechanically derived non-contact cell-cell interactions are even more relevant and act over longer ranges in the biological extracellular matrix (ECM) comprising collagen or fibrin, where cells can interact by remodeling and reorienting the fibers in the ECM [109, 110, 111]. Even without such cell-matrix feedback, the presence of matrix or substrate deformations have been shown recently to guide the migration of other cells without requiring chemotactic cues [112].

In this context, it is useful to compare non-contact and long range mechanical signalling as analyzed by these studies to cell-cell interactions that are not mechanical; specifically, chemical signalling such as in immune cell interactions (for instance, see the review by [113] and references therein) or other forms of interactions such as haptotaxis [114, 115, 116, 117, 118, 119], cell stimulation by activating or secretory molecules such as in inflammation and thromboses [120, 121]. Mechanical non-local interactions between cells offer advantages compared to chemical means in terms of rate at which cells can communicate. Mechanical signaling and mechanosensing of neighbouring cells is typically faster and longer-ranged than chemical signaling and concentration field based interactions that are limited by slow diffusion rates. This is because mechanical interactions propagate near instantaneously [122]. This crucially allows cells to not just sense each other, but to also synchronize their behaviour quickly at time scales faster than that seen in diffusive processes. For instance, substrate deformation-mediated long-range interactions has been clearly demonstrated in heart muscle cells that synchronize their beating without direct contact [123, 124], as well as at a subcellular level between myofibrils within a single heart

muscle cell [125]. Cell communications via sensing of substrate or matrix deformation are particularly important in sparse, non-confluent cell cultures or tissue that occur in a number of biologically relevant situations. Apart from beating cardiomyocytes, examples of such situations include wound healing involving fibroblasts [126], sprouting blood vessels comprising endothelial cells [127], and migration of mesenchymal cells in zebrafish embryo before the formation of confluent epithelial tissue [128]. In all these cases, cells are not in direct contact but exert traction forces on the surrounding mechanical medium and concomitantly sense deformations caused by nearby cells. Such interactions therefore crucially depend on the stiffness of the substrate, and can be probed by experiments that vary the stiffness of the hydrogel substrate on which the cells are cultured [129, 97]. These aspects influence not only motility response at the single cell level but also strongly impact collective behavior including directed motility and subsequent spatial self-organization.

While substrate-mediated cell-cell elastic interactions have been considered for the organization of adherent cells in a variety of mechanobiological contexts [130, 131] (the physical basis of such modeling is reviewed in [132]), their effect on collective cell motility, which in principle is always present, have not been carefully modeled. Here, we present a simple biophysical agent–based model and computational results that focus on how substrate mediate mechanical communication allows two cells to sense each other and impacts their collective and relative motility. The focus on mechanical interactions allows us to explore clearly the role of mechanical signaling. By itself, this minimal model can be used to describe cell movements in tissue culture experiments and guide applications that involve varying the mechanical properties of the cellular microenvironment.

Chemical signaling between cells and attendant biochemistry and kinetics is undeniably important in a biological context and is expected to act in concert with mechanical substrate mediated interactions between cells. However, our model provides a foundation for the study of more general cell interactions that include both mechanical and chemical signalling, and generally short-range near-contact and long-range interaction modalities. For instance, we have used a similar methodology to study short range interactions for prokaryotic cells such as bacterial swarms moving on substrates and responding to chemical cues [133]. Our approach also serves as a starting point for studies of mechanical substrate based interactions in multi-cellular systems such as growing tissue and confluent sheets.

2.2 Experimental observations motivate model for cell elastic interactions

Many eukaryotic cells use contractile localized forces generated by their actomyosin cytoskeleton to adhere to and move on their substrates (Fig. 2.1a). Such traction forces typically cause measurable deformations in the underlying substrates in cell culture experiment [1], and have a spatially dipolar pattern [134]. A cell typically acts as a force dipole exerting – a pair of equal and opposite forces – on the elastic medium (Fig. 2.1b). The dipole arrangement arises since no external forces are present on the system (cell + substrate), and the cell therefore moves on its own accord by exploiting the resisting forces exerted by the substrate on the cell. The net effect of traction stresses is to contract or pull in the elastic material comprising the substrate towards the cell (Fig. 2.2a).

Here to focus our discussion, we use experiments on endothelial cells to build the elastic model. In a seminal study [5] studied bovine aortic endothelial cells (BAECs) cells cultured on polyacrylamide based hydrogel substrates of varying stiffness. Endothelial cell migration and traction stresses were directly measured in this study. The number of cell extensions sent out toward an adjacent cell that result in cell-cell contact was also counted for a period of 6 hours as a function of substrate compliance. To investigate the influence of substrate compliance on cell-cell interactions, pairs of cells on varying compliance gels, ranging from very soft (Young's modulus, E = 500 Pa) to very stiff (E = 33,000 Pa) were examined. Three qualitatively different behaviors were observed. On the softest gels (500 Pa), cells were seen to touch and remain in contact for the duration of the experiment. Once in contact, cells were seen to extend additional pseudopodia toward the adjacent cell, but the cells generally did not become significantly spatially separated. Cells on intermediate compliances studied (E = 2500 and 5500 Pa) were observed to contact, separate and retouch repeatedly. Once the cells contacted, they were also observed to generally not migrate significantly far from each other, unless the two-cell interaction was disturbed by a third cell. On the stiffest gels (33,000 Pa), cells contacted and migrated away from each other, without the same repeated contact behavior observed for cells on intermediate compliance substrates. Thus cells made stable contacts on very soft gels (E = 500 Pa), whereas they made repeated contacts and withdrawals on substrates of intermediate compliance (E = 2500-5500 Pa). Tracking of the collective migration of two-cells also showed a strong response to substrate stiffness. Specifically, pairs of endothelial cells could display hindered migration compared

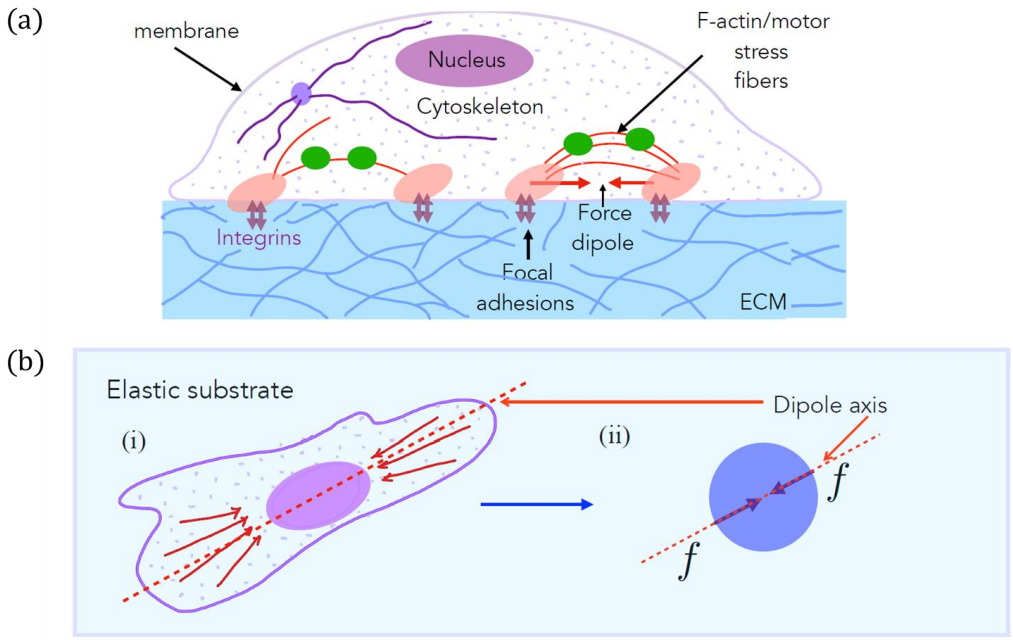

Figure 2.1: Traction forces exerted by motile cells on soft substrates can be modeled as force dipoles. (a) Schematic of an animal cell, *e.g.* an isolated fibroblast in culture [1] adhered to a compliant substrate through focal adhesions comprising of integrins and a host of other mechanosensitive adhesion proteins. Mechanical forces are actively generated by molecular motors of the myosin-II family that put the actin cytoskeleton under tension. Stress fibers are bundles of crosslinked actin filaments with a periodic (sarcomeric) organization of myosin [2] that often span the length of the cell and are anchored at the focal adhesions to the extracellular substrate or matrix (ECM). The contractile forces are transmitted at these sites from the stress fibers to the underlying substrate, which can be strongly deformed if soft. Such deformations are long range (extend up to a few cell lengths away from the cell) and can be measured by Traction Force Microscopy (TMF). This is a common index of cell-substrate mechanical interactions. (b) (i) A simplified top view of the same cell showing the alignment of the stress fibers, and therefore of the contractile forces generated by them. In order to model the effects of the cell on the substrate, we use classical linear elasticity theory with the stress distributions effectively modeled as a contractile force dipole, a pair of equal and opposite forces separated by some distance acting along the dipole axis (marked). (ii) This leads to a very simplified mechanical model of the cell in terms as a contractile force dipole exerted on the substrate along its average axis of orientation defined by the alignment of its stress fibers.

to individual cells, implying strongly that these cells sensed each other through the matrix. Pairs of cells on softer gels, also showed reduced collective migration in comparison to

isolated cells.

Motivated by this experiment, we here model the motility characteristics of a two cell system (schematic in Fig. 2.2) that captures how elastic deformations induced in the substrate allow cells to respond to each other. Our aim is the prediction of signatures of this interaction that are most relevant to biological processes involving cell motility. Specifically, as in experiments we seek to understand the effects of substrate stiffness on cell migration speeds, dispersivity and on the frequency and manner of binary cell contacts. Once mechanical far-field interactions between cells can be modelled, we can in further studies consider additional near-field or contact chemical and bio-chemical interactions. We consider a pair of cells that each adhere to, and exert stresses on the underlying substrate thereby deforming it as shown in Fig. 2.2a. As mentioned above, adherent and motile cells generate contractile stresses on the substrate via focal adhesions. Focal adhesions comprise of integrins and a host of other mechanosensitive adhesion proteins with contractile forces actively generated by actin-myosin aggregates that form stress fibers- bundles of cross-linked actin filaments anchored at the focal adhesions. The contractile forces are transmitted at these sites from the stress fibers to the underlying substrate. While the cell by itself is a soft substrate, studies have indicated that stiffness in the vicinity of the focal adhesion may be regulated and controlled so as to achieve locally large stiffness values in cellular domains involved in the formation of focal adhesions. Therefore, as a first approximation, we treat substrate elasticity as being the controlling parameter and treat the effective (actively maintained) stress fiber stiffness as much larger than the substrate stiffness. Next, the contractility of each cell, is minimally described by a physical model of force dipoles - a pair of equal and opposite forces exerted on the substrate, and is thus a tensorial quantity [130]. Such modeling is inspired by the theory of deformations induced by inclusions in materials [135]. Unlike passive material inclusions, cells can actively regulate their force production in response to external mechano-chemical cues from the substrate, including the presence of other cells. Such complicating feedback effects in cell–cell interactions has also been theoretically considered [136, 137], but we ignore these for simplicity here, and we treat contractility as an intrinsic cell property that is independent of underlying substrate matrix strain and stiffness.

As illustrated in Fig. 2.2a, we start with a model that mimics experimental setups and considers two cell interactions. To simplify our study, we assume that one of the cells is motile (Cell A) and the other is stationary (Cell B). The stationary cell B is nonetheless alive

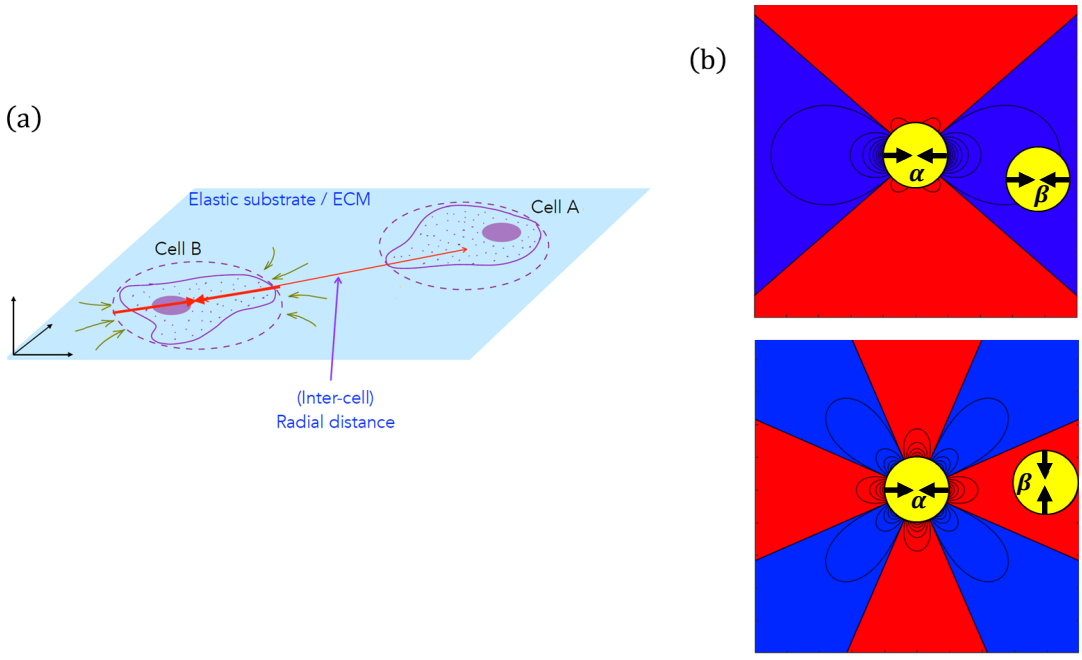

Figure 2.2: Schematic of the cell-cell mechanical interactions model: (a) Two cells A and B cultured on the surface of thick elastic substrate can sense each other and interact at long range (when the inter-cell distance r is longer than typical cell sizes, here depicted by dashed red circles) through mechanical deformations of the underlying substrate; here the contractile stresses set up in the substrate yield deformations as indicated by green arrows. The cells are restricted to move on the surface of the substrate. (b) Representative spatial maps of the interaction potential between two dipoles, from the solution of the strain field for the full linear elastic problem of forces exerted on the surface of a semi-infinite medium are shown. The interaction potential corresponds to the work done by a point-like dipole in deforming the substrate in the presence of the strain created by the other. The potential maps shown here are for a pair of contractile force dipoles of fixed orientation. The second dipole is free to translate but held parallel (left) or perpendicular (right) to the central dipole which is placed at the origin and aligned along the x-axis. The contour lines show how the potential decays in space, whereas blue and red regions correspond to attractive and repulsive interactions, respectively.

and deforms the substrate. The resulting deformation field, or equivalently the substrate mediated elastic potential, is sensed by the other, distant, motile cell A. The interaction potential between the cells in turn creates a mechanical force on the motile cell A. For polarized and elongated cells, the deformations have a dipolar spatial pattern (described in Appendix A). However, here we consider a simplified scenario that is valid when cells reorient

very fast in the time for them to translate and migrate (Appendix A, §3). This implies that the directions of the dipole axis of both cell A and of cell B fluctuate rapidly. This implies that cell A moves and feels an effectively isotropic, attractive interaction potential that decays with distance as $\sim 1/r^3$ (iso–surfaces shown as blue circles in Fig. 2.3).

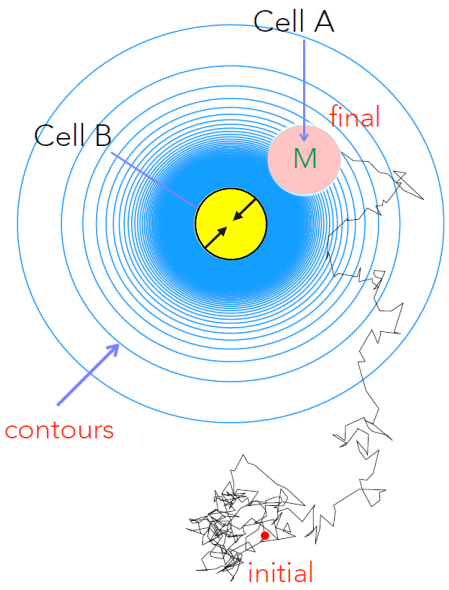

Figure 2.3: We study with our computational model how a motile cell (M, Cell A, pink) moves in the presence of a fixed central cell (Cell B, yellow). This two cell system on a substrate (schematic shown as a top view) also mimics scenarios where a motile cell may encounter an elastic impurity or obstacle on the medium. Shown as blue circles are contours of constant elastic potential (in simplified form) that determine the inter-cell elastic force experienced by the motile cell B as a result of the elastic deformations of the medium by both cells A and B. Also shown (in black) is a representative simulated trajectory of the motile cell which starts outside the area of influence of the stationary cell.

Polarized cells may propel themselves persistently along their body axis; here, we consider cells that are unbiased and thus act in the absence of any orienting chemical

field or signal and therefore extend their pseudopodia in different directions randomly. This response, together with thermal noise, is the origin of the diffusive behaviour observed as the cell moves. Such meandering cell trajectories can be characterized by a diffusion coefficient; similar features hold for cell-pairs in which case one may evaluate dispersion or migration coefficients. In reference to Fig. 2.3, as the motile cell A moves, it is additionally acted upon by an elastic interaction force that arises due to its interaction (via the substrate) with the stationary cell B. The motion of the motile cell (A) may then be described using the Langevin equation. While such an approach has been previously proposed and validated with experiments on elastically coupled motile active particles such as swarming bacteria [138, 133] it has not been studied previously in conjunction with cell-cell dynamics on elastic substrates.

We note that the model can be easily generalized (as derived in Appendix A) to describe a pair of motile cells since the interactions are pairwise and reciprocal. The interaction potential is not isotropic and depends on both the inter-cell distance as well as on the instantaneous alignment of the cells' dipole axes. Thus the force on each cell (related to the gradient of the potential) depends on not just the relative positions of the cells.but additionally on the direction of the contractile dipoles exerted by cells A and B. Truly spherical dipoles embedded in an elastic medium do not interact mechanically [135], unless cell-substrate feedback effects occur [137]. Furthermore, cell-cell interactions in a fibrous, nonlinear elastic medium can be longer ranged [139] and have a power law character, $\sim 1/r^{\alpha}$, where $\alpha < 3$ [140]. The interaction of disk-like cells on top of a thick substrate (semi-infinite geometry) is also more complicated [141]. We choose the isotropic, attractive $1/r^3$ potential as the simplest attractive interaction with the same distance dependence as the dipolar interaction, with the objective of testing how such a potential can affect cell motility. Motivating future work, we show how the conclusions from the simpler potential remain qualitatively valid even as specifics of cell trajectories change when the more general dipolar potential is used. This model highlighted in this work, although very simplified both in its description of cell contractility and motility, can thus capture key aspects of motility and contact formation, as we now describe.

2.3 Materials and Methods

2.3.1 Model for two-cell interactions

The model used to analyze the two-cell system is an agent-based stochastic model. We start with the stochastic Langevin equation for the dynamics of the moving cell A in the presence of a second cell B fixed at the origin as illustrated in Fig. 2.3. Details of the model and the simplifications involved may be found in Appendix A. Starting from the more general model where both cells A and B can move, we now fix cell B and thus set $\mathbf{r}^B = \mathbf{0}$. In other words, we choose the center of cell B to be the origin from which the position of cell A and its distance relative to B is measured. Writing $\mathbf{r} = \mathbf{r}^B - \mathbf{r}^A$, we write the equation for $\mathbf{r}(t)$ where t is the time,

$$\frac{d\mathbf{r}}{dt} = -\mu_T \frac{\partial W}{\partial \mathbf{r}} + \sqrt{2D_{\text{eff}}}\ \boldsymbol{\eta}(t) \tag{2.1}$$

where D_{eff} is the effective translational diffusivity quantifying the random motion of the moving cell in the absence of the fixed cell, and $\boldsymbol{\eta}$ is a random white noise term whose components satisfy

$$\langle \eta_i(t)\eta_j(t')\rangle = \delta(t-t')\delta_{ij}.$$

Note that η - the active noise term - has units of $t^{-1/2}$. The mobility μ_T in equation (1) quantifies the effective friction from the medium and is inversely proportional to the cell size σ and inversely proportional the the viscosity at the surface. Here it is assumed that the cells moving on a wet surface and that the fluid nature of the surface provides a viscous resistance opposing cell motion.

The two-cell potential W derives from the elastic interactions communicated via the linear deformation of the substrate (Appendix A, Equation A5) and is given by,

$$W = \frac{1}{2}k(\sigma - r)^2, \quad \text{when} \quad 0 \le r \le \sigma, \quad \text{and} \tag{2.2}$$

$$= -\frac{P^2}{E}\frac{\phi(\nu)}{r^3}, \quad \text{when} \quad r > \sigma. \tag{2.3}$$

Numerical solutions to equation (1) are obtained with varying initial conditions for cell A as explained subsequently. To ease the computational analysis, we work in scaled dimensionless units. We choose cell size (diameter) σ (see Fig. 2.1b), diffusion time σ^2/D_0, and thermal energy k_BT – with T corresponding to the temperature of the cell/substrate system – as our length, time and energy scales respectively. Equations (1-3) may then be rewritten as

$$\frac{d\mathbf{r}^*}{dt^*} = -\frac{dW^*}{dr^*} + \sqrt{2D_T}\ \boldsymbol{\eta}_T^*, \tag{2.4}$$

where the potential in scaled form is

$$W^* = \frac{1}{2}k_{\text{steric}}(1-r^*)^2, \quad \text{when} \quad 0 \le r^* \le 1, \quad \text{and} \tag{2.5}$$

$$= -\frac{\alpha}{r^{*3}}, \quad \text{when} \quad r^* > 1. \tag{2.6}$$

Superscripts * in equations (4)-(6) denote non-dimensional quantities. Henceforth, we will drop this subscript for clarity. Thus the dynamics may be followed as a function of three dimensionless numbers (parameters)

$$\alpha \equiv \left(\frac{P^2\phi(\nu)}{Ek_BT\sigma^3}\right), \quad D_T \equiv \left(\frac{D_{\text{eff}}}{D_0}\right), \quad \text{and} \quad k_{\text{steric}} \equiv \left(\frac{k\sigma^2}{k_BT}\right). \tag{2.7}$$

2.3.2 Dimensionless parameters quantifying cell motion and interactions

The parameters that emerge in equations (1)-(7) and typical of the two-cell scenario studied here are summarized in Table 1. Following Ref. [5], we are interested in substrates that are linearly elastic with the Young's modulus E ranging from 0.5 kPa to 33 kPa, well within the range of 0.1-100 kPa appropriate for tissues and bio-compatible materials [97]. The effective diffusion coefficients exhibited by cells in experiments [5] include the random noisy motion as the cells explore territory and a contribution due to short-time deterministic motion. We explore values in the range $3\mu\text{m}^2$/minute to 50 μm^2/minute. Time scales are estimated from experiments as well and 250 seconds in real time correspond to a dimensionless time duration of unity.

Scaled non-dimensional parameters relevant to the simulation may be calculated from dimensional quantities as explained earlier. Three scaled parameters determine the dynamics of the two-cell system: D_T, α and k_{steric}. Values used in the computations are listed in Table 2. The self avoidance parameter k_{steric} is chosen such that the cells don't overlap and is computed based on the time step used in the simulations. This allows us to control the stability of the simulation and its accuracy.

2.3.3 Numerical solution and tracking cell trajectories

Equations (4)-(7) are solved for the dynamics of the moving cell with appropriate boundary and initial conditions. The Langevin equation (4) is an example of stochastic differential equations; here we solve this equation using the explicit half-order Euler-Maruyama method one of us has used recently in similar problems involving bacteria cells moving in

light fields [133] and in simulations of active Brownian particles [138]. Given the position of cell A at time t, $\mathbf{r}(t)$, its subsequent location at time $t+\delta t$, $\mathbf{r}(t+\delta t)$, follows,

$$\mathbf{r}(t+\delta t) = \mathbf{r}(t) - \left(\frac{\partial W}{\partial \mathbf{r}}|_{\mathbf{r}(t)}\right)\delta t + \sqrt{2D_T\delta t}\ \mathbf{w}, \tag{2.8}$$

Table 2.1: Biophysical parameters characterizing the two-cell (typical values from [5, 6, 7]).

Quantity	**Interpretation**	**Experimental values**
σ	Cell size	10-100 μm
T	Temperature	25^0 C
D_0	Thermal Diffusivity	25 μm^2/min
D_{eff}	Effective Diffusivity	$3-50$ μm^2/min
E	Young's modulus	$0.5-33$ kPa
ν	Poisson ratio	0.3 - 0.5
P	Contractility	10^{-14} Nm

Table 2.2: Simulation parameters and their meaning.

Parameter	**Interpretation**	**Definition**	**Simulation values**
D_T	Diffusivity	D_{eff}/D_0	0.1-10
α	Cell-cell interaction	$P^2\phi(\nu)/(Ek_BT\sigma^3)$	0.1-100
k_{steric}	Self-avoidance	$k\sigma^2/k_BT$	10^3-10^4

In equation (8), $\mathbf{w}$ is a random two-dimensional vector with components each drawn at every time step from a normal distribution with mean zero and standard deviation of unity.

We simulated several trajectories of cell A ($N = 1000$ trajectories, cells have diameter $\sigma = 1$ in scaled units), under the influence of the central stationary cell B (also having diameter $\sigma = 1$). The simulations were conducted in two different geometries as described below. To study the contact frequency between two-cells and explore the systematically explore the role of the elastic potential, we simulated cell A moving in a confined square box of size 12σ with the stationary cell B at the center of the box. Cells reflect from the

box surface when they encounter it and thus are restricted to remain within the simulation domain.

In order to calculate the number of contact in due course of the simulation, we define a contact radius 1.5σ from the centre of the stationary cell, and we consider a contact if the centre of the test cell lies within the contact radius. The cell can come out of the contact radius and re-enter, increasing the number of contacts. The time step used in these simulations is $dt = 0.0001$ and total number of steps in this simulation is 10^7, i.e. a cell trajectories were followed for a total time of $T = 1000$.

On the other hand for calculating cell dispersivities, and specifically the mean squared displacement (MSD) of cell A, we used periodic boundary conditions and a periodic potential. This corresponds to cell A moving in a periodic domain and interacting with a regular square lattice of multiple stationary cells (images of B) separated uniformly by a distance 12σ. The time step used to integrate equation (7) in these simulations is also $dt = 0.0001$ and total number of steps in this simulation is 10^7, i.e. a cell trajectories were followed for a total time of $T = 1000$. The mean square displacement MSD was calculated by tracking trajectories of cell A (the same as tracking $N = 100$ cells). As before, cell A is initialized randomly inside the same square box of length of 12σ, but outside the contact radius. Cells that move out of the domain are reintroduced into the domain in a manner that respects periodic boundary conditions and the appropriate symmetries.

In this case since $\mathbf{r} \equiv x\mathbf{e}_x + y\mathbf{e}_y$ is the relative distance between the cells, the mean square displacement is calculated by the equation,

$$\mathrm{MSD}(\tau) = \frac{1}{N}\sum_{\alpha=1}^{N}\langle[x_\alpha(t_R+\tau) - x_\alpha(t_R)]^2 + [y_\alpha(t_R+\tau) - y_\alpha(t_R)]^2\rangle \tag{2.9}$$

where τ is the delay time, and the summation is over each cell trajectory (indexed by α) and extends over the full number of trajectories $N = 100$. The delay time is varied and the averages are obtained by choosing different values of the reference time t_R as is normally done.

The MSD is thus an average over time and also an average over realized cell trajectories. We also note that the mean square displacement in (9) is written as a function of the delay time τ that may be interpreted as an effective observation time over which the cell motion is observed.

The mobility of cell A reflects the properties of the microenvironment created by cell B and by the substrate. For instance, a cell that moves with constant speed for small

times (say $\sim T_1$) and undergoes a diffusive random walk when observed over long times (say $\sim T_2$) will exhibit different slopes for $\tau < T_1$ and for $\tau > T_2$. The exponent characterizing the dependence of the MSD on the delay time provides information as to whether the motion is sub-diffusive (exponent < 1), diffusive (exponent $= 1$), or super-diffusive (exponent > 1).

It is constructive to study the expected MSD for cell A in the absence of cell B. In this particular case, since A is purely diffusive, the MSD has the simple form valid for diffusion in two dimensions $\mathrm{MSD}(\tau) = 4D_T\tau$. Deviations from this expression arise due to the mechanically induced inter-cell interaction and thus quantify the extent to which cell B perturbs the dispersion of cell A. For instance transient or persistent trapping of cell A will result in the MSD scaling sub-linearly with τ.

2.4 Results

2.4.1 Cell-cell contact frequency is controlled by matrix elastic interactions

Motivated by experiments which show that two cells make repeated contact and withdrawals on soft substrates, with contact frequency dependent on the substrate stiffness, we measure the total number of contacts of the motile cell (A) with the stationary cell (B) in our model simulations. As indicated earlier, the simulated cells are initialized randomly inside the box, but outside of a pre-defined contact radius around the stationary cell. The total number of contacts between the cells is counted over a fixed period of time i.e. T = 1000. It should be remembered that the cells are confined to stay within the square domain during the course of the simulation.

Cell A's movement is governed by an attractive elastic potential induced by the stationary, central cell and its own random motion, described as an effective diffusion. Additionally when the cell encounters the bounding wall of the square domain, it reflects (moves away) from it. Overall, random noise encapsulated in the diffusion coefficient causes A to move towards or away from B in an unbiased manner. The attractive potential W being isotropic and spatially varying suggests that there is a critical radius of influence (dependent on both α and D_T) within which forces due to the attractive potential dominate diffusion and significantly influence the trajectory of cell A. This effect results in the cell getting closer to cell B, eventually entering this zone of influence.

To carefully study how elastic interactions (α) and random diffusion (D_T) each

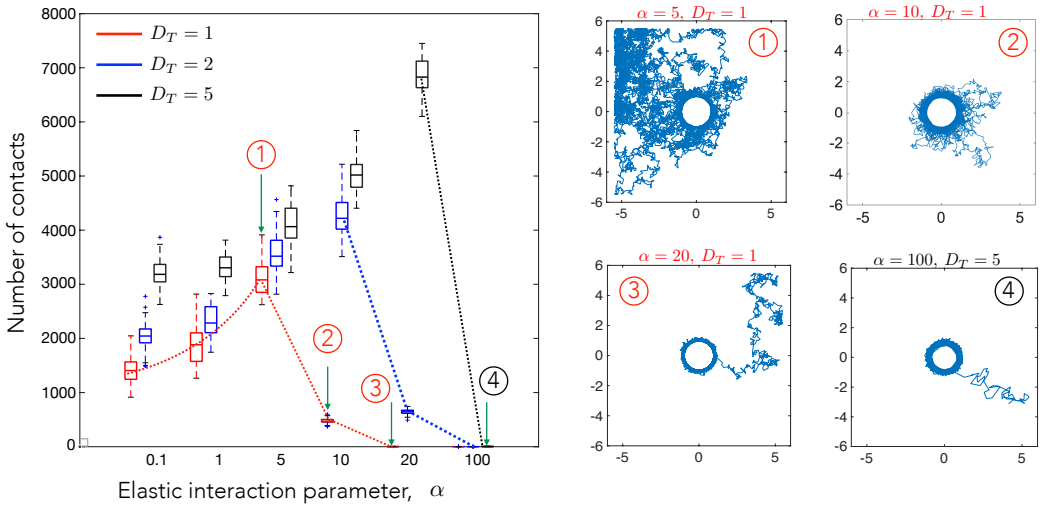

Figure 2.4: Number of cell–cell contact events measured in a fixed interval of time depends strongly on the elastic interaction parameter. A contact event is identified as cell A coming within a prescribed contact radius of cell B with cell A initialized randomly in a certain area around cell B. Thus the number of contact is be interpreted as the average number of contacts of the two cells. The number of simulation runs conducted were 50 for each combination of D_T and α. The dashed curves are guides to the eye illustrating the trends seen with increasing values of α. Diffusion is the major factor in governing the number of contacts for low values of α. For higher α, the attractive potential increases the probability of the cell to stay near the contact radius and controls the number of contacts. Trajectories for highlighted data points (1)-(4) are shown on the right. The box plots show the distribution of contact numbers. The lower and upper bounds of the box are the first and the third quartiles respectively, while the line in middle is the median. The lower and upper limits of the dashed lines are the minimum and maximum number of contacts observed for cells for each combination of α and D_T. The simulation was run for a total time of $T = 1000$ and updates in cell position were made every $\delta t = 0.001$.

influence this process, we first systematically calculated the number of contacts by α, while keeping D_T constant at three different values, $D_T = 1, 2, 5$. (Fig. 2.4). As illustrated by the dotted lines which serve as a guide to the eye, the behavior is highly non-monotonic. For small α, the number of contacts increases with increasing α, then reduces to 1 at high α. The position of the peak increases with increasing D_T. The initial increase in contacts is due to the increased directional movement of the test cells towards the central cell. The decrease in the number of contacts for very high values of α is expected since the attractive

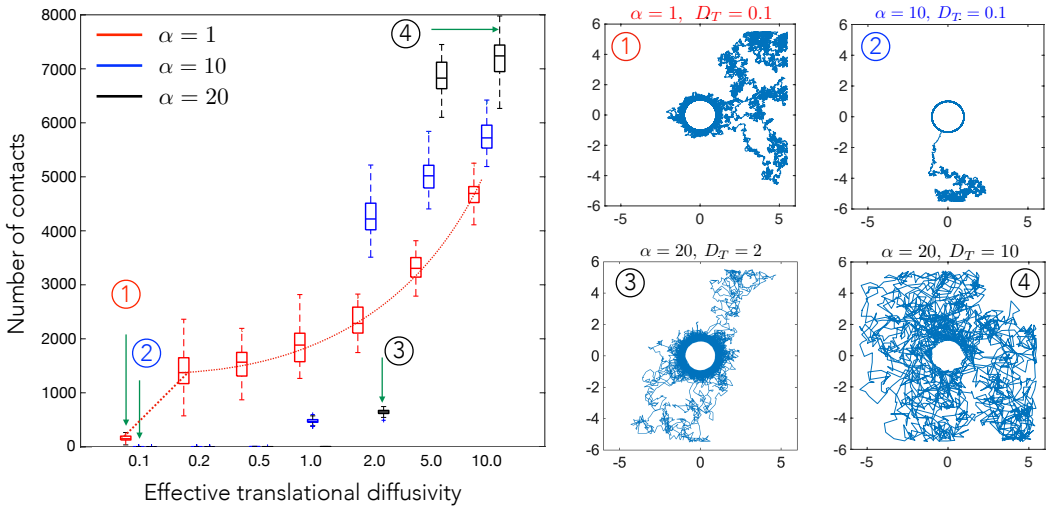

Figure 2.5: Number of cell–cell contact events in a fixed interval of time ($T = 1000$) plotted here as a function of the scaled effective diffusivity, D_T, which represents the random motility of cell B. Here we show how the number of cell–cell contact varies for three different elastic interaction strength values, α, corresponding to substrates with three different stiffness. The highlighted points numbered from (1)-(4), show representative cell trajectories over long times and highlight how varying α and D_T can yield states where the cells are in close proximity most of the time (low D_T, high α) or states where cells interact rarely (high D_T, low α). Interpretation of the box plots is the same as in Fig. 2.3. The simulation was run for a total time of $T = 1000$ and updates in cell position were made every $\delta t = 0.001$.

potential is strong enough to overcome the effect of diffusion. In this case, the motile cell is unable to move away from and makes stable contact with the stationary cell. For $\alpha = 5$ and $D_T = 1$ (trajectory 1), the test cell spends most of the time exploring space rather than near the stationary cell, which also reduces the number of contacts.

Upon increasing α to 10 (trajectory 2) the radius of influence increases, increasing the duration of contact and thereby increasing contacts. On further increasing α to 20 (trajectory 3), the test cell is tightly adhered to the stationary cell which allows only one single contact. Note that the statistics for the high D_T and low α regime are influenced by the confinement. Cells in this particular limit frequently escape the region of influence and wander away only to return again after encountering the wall and diffusing away. For instance, the number of contacts for $D_T = 5$ and $\alpha = 0.1$, combines the effect of repeated escapes from the region of influence and repeated returns due to confinement. Since the

size of the box is fixed, the increase in number of contacts with D_T for $\alpha = 0.1$ is still a signature of diffusive effects dominating the attractive potential.

We next investigated the effect of increasing diffusivity on the number of contacts for constant α (1, 10 and 20). Results from this set of simulations are shown in Fig. 2.5. The red dotted line serves as a guide to the eye highlighting the trend observed. We see a steady increase in cell-cell contacts with diffusivity. Without diffusion, the test cell shows unidirectional motion towards the central cell and remains in contact throughout the simulation. Increasing diffusion increases the chance of test cell to go out of the radius of influence and come back again (trajectories 3 and 4).

Overall combining the results shown in Fig. 2.4 and 2.5, we conclude that the number of contacts is maximized at an optimal value of the elastic interaction strength. If the elastic strength is too high or too low, the cell either makes stable contact or is too motile to make too many contacts. This optimal value scales with the diffusivity, which is a measure of the cell motility in our model. We note that these are precisely the behaviours seen in experiments on two-cell interactions and motility suggesting that purely long-ranged mechanical cell-cell interactions suffice to predict the contact frequency and the effective duration for which two cells can remain close to each other. This is important because for short-range interactions and specific biochemical recognition mechanisms to be initiated, cells have to first be drawn together. Our results suggest that mechanical interactions may play an important role in first getting cells close to one another in order for subsequent attractive or repulsive cell-cell direct interactions to then turn or and control subsequent dynamics. Taken together, our simulations suggest that elastic interactions can lead to stable contact between initially distant cells.

2.4.2 Cell motility characteristics depend on elastic interactions

To quantify the long-time statistics of the motility of cell A in the elastic potential field generated by cell B, we analyze the mean squared displacement (MSD) as given by equation (9) from simulation. The metric MSD measured in terms of a delay time τ contains information about the short time mobility of a cell, the long time mobility of the cell, and additionally provides signatures of capture and trapping effects. Specifically, the slope of the mean square displacement can be used to extract effective exponents that provides insight on the relative importance of diffusion and elastic attractive interactions. We plot the MSD in Fig. 2.6 for $D_T = 2$ and $\alpha = 0.1, 1, 5, 10, 20, 100$. For $\alpha = 0.1, 1, 5, 10$, we find

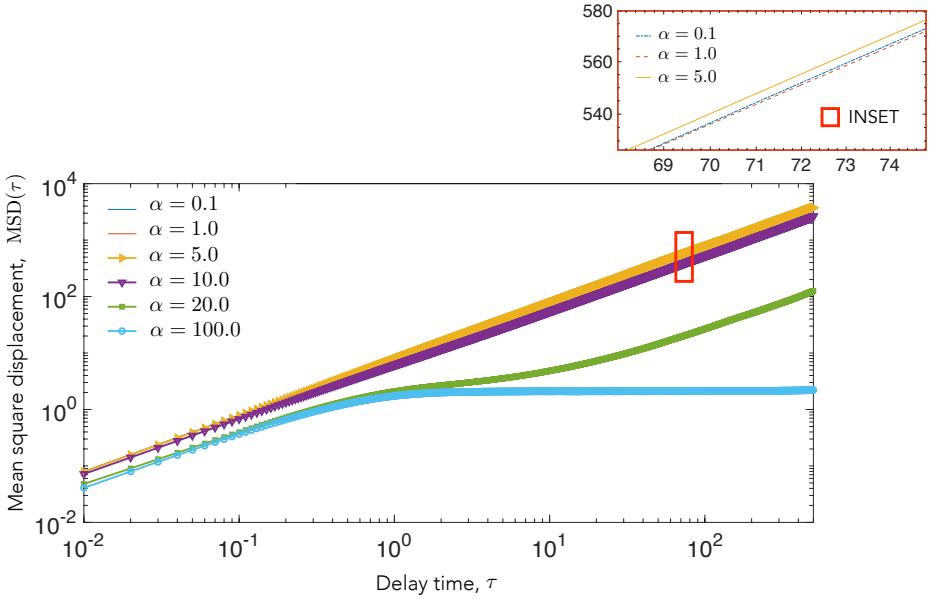

Figure 2.6: **Mean square displacement** (MSD) as a function of the delay time interval τ (calculated from Equation 9), for the motile cell A is shown. Here we explore the variation in the MSD for various values of substrate-mediated elastic interactions, α. The diffusivity D_T is held constant for these simulations with $D_T = 2$. Other diffusivities were explored (results not shown). At low elastic interaction strengths, α, corresponding to stiff substrates, the cell shows a purely diffusive trajectory, whereas at higher values of α, the motile cell is captured by the strong attractive interaction from the stationary cell, resulting in a flattening of the MSD (blue curve). At an intermediate interaction regime (green curve), the motile cell makes repeated contact with the fixed cell but is never fully captured.

that the slope is close to 1, which suggests diffusion drives the motion of the cell and the attractive potential is not strong enough to influence the movement of the cell. For higher α, we observe a transition towards sub-diffusive behavior at $\tau \sim 0.5$. At $\alpha = 20$ (green line), the curve shows a significant decrease in slope at $\tau = 2$, the time scale for which a test cell in average encounters the central cell for the first time and stays in contact for a while, as shown by trajectory 3, Fig. 2.5. The slope then increases again, but remains less than 1 suggesting a sub-diffusive behavior in the long run. At $\alpha = 100$ (blue line), the MSD saturates after initial diffusion to a zero slope which suggests that the motion is bounded, and it can only explore the circumference of the stationary cell.

2.4.3 Elastic interactions lead to effective capture of motile cell

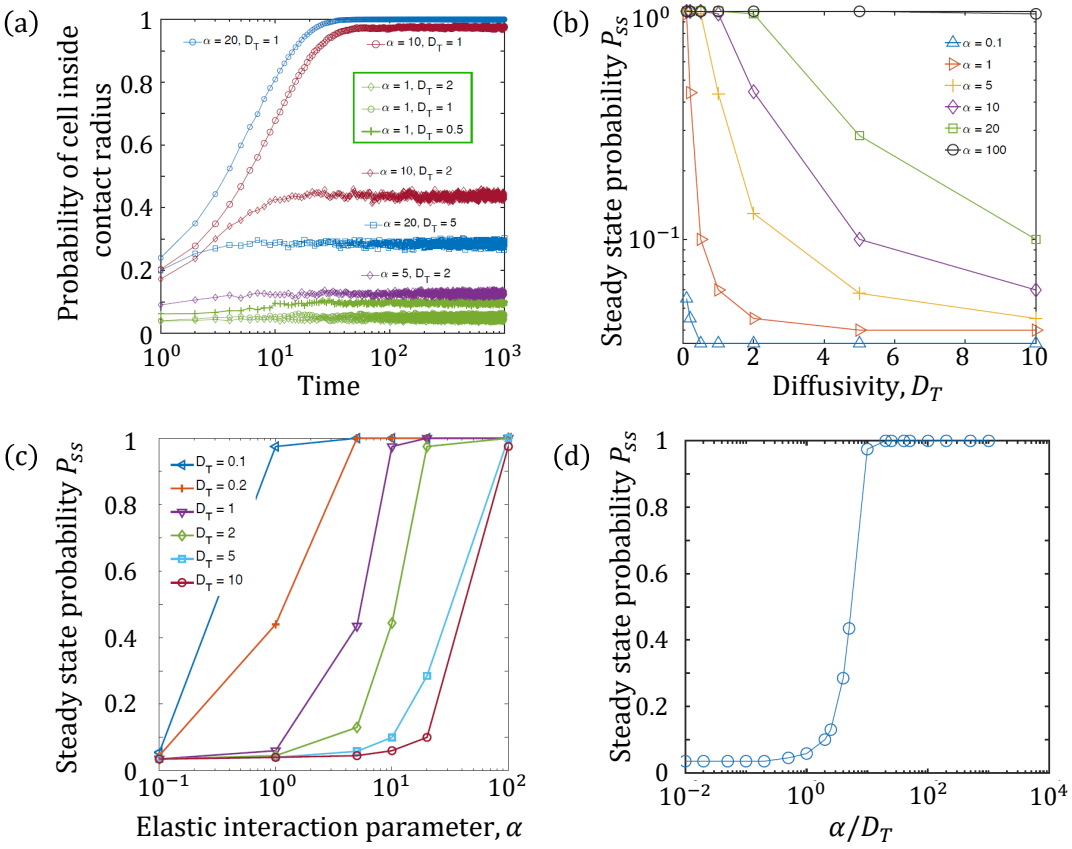

Figure 2.7: **Capture statistics of motile cell**. (A) Probability that cell B is inside contact radius as a function of time. (B and C) The dependence of steady state capture probability, P_{ss}, *i.e.* the fraction of cells captured within the contact radius after a long time interval, on simulation parameters. (B) shows the dependence on diffusivity,D_T at different values of the elastic interaction parameter, α, whereas (C) shows the dependence on α for different values of D_T. (D) The steady state capture probability, P_{ss}, data can be collapsed into a single master curve, when plotted vs. the key parameter, α/D_T, the strength of the elastic interactions relative to the diffusivity. This is expected since our model steady state is a thermal equilibrium with effective temperature set by the noisy cell motility, D_T, and the competition between attractive interactions and noise dictates the number of cells (cell trajectories) captured vs. the number that escape.

Fig. 2.4-2.6 suggest that the motile cell A (as it explores space and samples the potential field over its various trajectories) is attracted to the stationary cell with the attracting force increasing with decreasing distance r. Acting in tandem and superposed on

this aspect of the motion is diffusion that allows A to wander away from B multiple times. Therefore, we next explore the statistics of this capture process. Capture mechanisms underlying and influencing these statistics are potentially relevant for timescales of contact formation between initially well-separated motile cells that then form confluent monolayers, such as in mesenchymal–to–epithelial transitions during tissue morphogenesis [142]. In order to understand how parameters α and D_T affect this phenomenon, we tracked the number of cells inside the contact radius over the course of the simulation. The probability of cells inside the contact radius reached a steady state at time $t < 100$ for all parameters (Fig. 2.7A). Keeping α constant and increasing D_T the probability of cells being inside the contact radius decreases (Fig. 2.7B). The steady-state probability P_{ss} increases with increase in α for constant D_T (Fig. 2.7C). To understand the relationship between P_{ss} and both α and D_T, we investigated P_{ss} for the ratio α/D_T and showed that they remain constant for this ratio.

Plotting P_{ss} vs α/D_T, the strength of the elastic interactions relative to the diffusivity, we find that the data can be collapsed into a single master curve (Fig. 2.7D). The collapse of our data and the master curve plotted in Fig. 2.7D is expected; the competition between attractive interactions and noise meanwhile dictates the relative numbers of cells that are captured vs cells that escape.

Fig. 2.7 motivates thinking about the moving cell as exploring a special region where substrate mediated elastic cell-cell interactions dominate. This region has a characteristic of influence equal to the distance from the stationary cell at which its elastic attractive tendency approximately balances the random noisy movements of the motile cell. Here we use a simple balance to estimate this radius of influence. Working in dimensionless units, we note that the dipolar interaction potential fall off as α/r^3, while the effects of the randomizing diffusion – scale as $k_BT = \mu_T D_T$. Balancing these yields a length scale (for mechanical interaction) $\ell_{\mathrm{M}} \sim (\alpha/\mu_T D_T)^{1/3}$, which explicitly shows the importance of the α/D_T parameter. Thus, a stronger α from deformations exerted by the stationary cell (corresponding to softer substrate stiffness, or higher contractility) and lower random movements of the motile cell, D_T, leads to a larger radius of influence. This in turn implies that the probability of being captured within the contact radius increases because the stationary cell can influence motile cells over a larger area.

2.5 Discussion and future extensions to other forms of interactions

2.5.1 Anisotropic cell-cell elastic interactions

For polarized cells, that orient their cytoskeletal fibers and contractility along some principal axis, the cell-cell interaction potential is not isotropic. The individual cells on an elastic medium behave as force dipoles, with interaction potential energy having both attractive and repulsive regions that depend on mutual orientation of the two cells and their separation vector [130], as detailed in Appendix A. The force experienced by the motile cell has both radial and tangential components depending on its position and orientation relative to the central cell, and its direction is sensitive to the Poisson's ratio of the elastic medium [143]. Thus, trajectories of cell A interacting with stationary cell B when the fully anisotropic interaction potential (Equation A1 and A2, Appendix A) is included will differ from trajectories observed in isotropic potentials. The difference arises in part due to an additional torque that reorients cell A to preferentially align with cell B as it moves towards it. Nonetheless, qualitative nature of the capture process and the observation of an effective region of influence will still remain valid.

We would like to point out here that the term anisotropy of the interactions is coupled to the directionality of the dipole axis quantifying the contractile stresses exerted by the focal adhesions on the underlying substrate. The substrate by itself is still treated as a homogeneous linearly elastic isotropic material; the anisotropy specifically refers to the fact that cell-cell interactions are not not just dependent on the inter-cell distance but also on the relative angles between the their dipole axes. This is important for instance, in cells that vary their direction of motion slowly, or equivalently bleb and change their direction of motion very slowly. In this scenario the directions each cell is moving along is as important as the inter-cell distance (see Appendix A).

To illustrate this we simulated the equilibrium orientation of uniformly spaced (pinned) test dipolar cells on a square lattice which are kept fixed in a square box of length 10σ. The Poisson's ratio of the simulated substrate is 0.3 and α is 40. Results are shown in Fig. 2.8. None of the cells overlap with the central stationary cell; they may rotate to reorient their dipole axis but are restricted from translating. We re-iterate that the cells on the lattice do not mutually interact with each other, but are only meant to illustrate

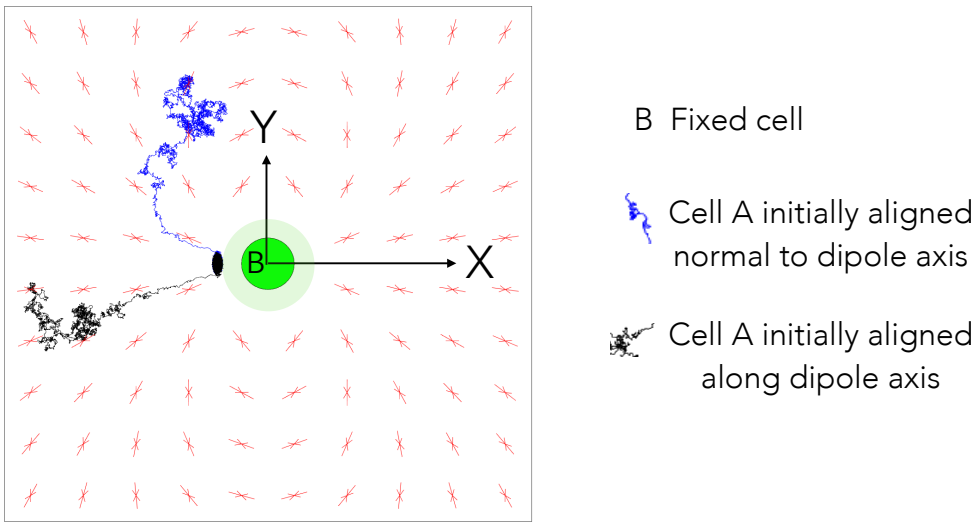

Figure 2.8: **Dipolar cell orientation and trajectory** The equilibrium orientation of contractile cells fixed in position, but free to reorient, and that are uniformly distributed in a square box of size 10σ, are depicted by two arrows (red) pointing towards each other. Each cell is influenced by the central stationary cell B (green) and not by each other. Two possible trajectories of cell A (blue and black) are recorded for $D_T = 0.1$, $\alpha = 40$ for total time $T = 500$ with time steps of $dt = 0.001$. The cells did not have any self propulsion or rotational diffusion. The Poisson's ratio ν of the substrate was considered 0.3 for this simulation

the interaction of a test dipolar cell A placed at different spatial locations with the central stationary cell B. We note that fixed cells adjust the axis of their contractile dipoles in accordance to the potential field due to cell B (the dipole axis of B is fixed). Superposed on this are two trajectories corresponding to two cells that are freed from constraints and allowed to rotate and translate in response to the two-cell potential and thermal noise. The two cells start from their equilibrium orientation - i.e, they are first held pinned and allowed to reorient until the dipole axis attains a static value and then the pinning constraint is removed. Cells in the close vicinity of the central cell's orientation axis exhibit a nearly linear motion to the pole of the fixed cell (trajectory in black). Cells away from the orientation axis take a longer route to come in contact with the central cell (trajectory in blue). The common attribute in both trajectories is that they prefer to adhere to the central cell's pole, that is cell A as it moves towards B also continuously reorients in a manner that brings it into alignment with the cell B's polar axis (the axis of the dipole).

2.5.2 Extensions to near-contact biochemical or bond interactions

In many realistic biological settings, cell-cell interactions are mediated by several different modalities, sometimes with parallel intercellular signaling events occurring together. The interplay between these different modalities is still unexplored. In addition to long range mechanical interactions, cells may sense other cells by short-range mechanosensation and adhesion mechanisms including ligand based bond interactions, by biochemical signalling and other molecular recognition mechanisms [113], by haptotaxis [114], as well as by responses to specific molecules or signals put forth by neighboring cells [118, 116]. A salient example is that of immune cells that can sense and respond to biophysical cues — from dynamic forces to spatial features — during their development, activation, differentiation and expansion as well as to biochemical cues. The biophysical signals modulate immune cell functions including leukocyte extravasation, macrophage polarization, T cell selection and T cell activation [144, 145]. Meanwhile cell-cell interaction between cells in close proximity may be impacted strongly by biochemical interactions. In lymphocytes, T cell receptors and B cell receptors recognize antigens and activate effector functions that combine chemical and mechanical features. In general, near-contact encounters between cells may be positive (attracting) as between T lymphocytes and B cells, or negative (repulsion) as occurs between IL-1-producing macrophages and endothelial or immune cells.

The agent based Langevin equation model here provides a foundation to analyze some forms of these biochemical or near-contact interaction mechanisms. As an first example, we consider integrin-ligand interactions that are hypothesized to mimic catch bonds [146, 147, 148, 149]. In previous work, one of the authors analyzed the kinetically driven capture of a cell (such as a leukocyte) by binders attached to a stationary surface [150]. In the context of the two interacting cells discussed here, similar near-contact binding interactions can be simulated by positing a distribution of bonds (with attachment and detachment probabilities/rates drawn from detailed mechanochemistry) on the surface of each cell. If mechanochemistry dictates that binders interact when the inter-cell distance is ℓ_B, then for soft to moderate substrates, we may expect $\ell_B \ll \ell_M$. That is, mechanical interactons are crucial in enabling close contact between cells first before the binder interactions kick in and either capture (attract) or deflect (repulse) the cell. A detailed model for this process is a part of current work.

As a second example, we consider motile cells that are elastically coupled, and

biochemically coupled through chemical agents and matching receptors. A specific example related to cultured microglia - the immune cells of the brain - where a number of chemical markers (e.g. $\alpha 5$-integrin) are left behind on the substrates as cells move with these surface bound degradable markers serving as signaling agents guiding two-cell interaction [114, 115, 116, 117, 118, 119]. This process by which microglia exhibit *haptotaxis* by following these chemical signal trails trails they generate may also be studied by coupling equations (1)-(7) or more generally equations (A1-A6) to a scalar equation for the time-dependent concentration field of these chemical markers. The limiting case where mechanical interactions are absent has been addressed earlier (see for instance, [114]).

Finally, the computational framework introduced and analyzed here can be extended to study *durotaxis* – that is, the modification of cell motility by variations in substrate elasticity at the single cell or tissue level and the motion of cells towards higher stiffness regions [151, 152].

2.6 Summary

Using our model for cell contractility and motility, we computed several metrics of experimental relevance such as number of cell–cell contacts, the mean square displacement of a motile cell in the presence of elastic deformations induced by a cell in its vicinity, and associated capture statistics resulting from attractive interactions between two such cells. In each case, we predict how the computed metric depends on the elastic properties of the substrate, captured in the interaction parameter, $\alpha \sim 1/E$, and on cell motility, captured by the effective diffusivity, D_T. Our results support the hypothesis that cell-cell interactions with purely mechanical origins can lead to mutual contact without requiring specific chemical factors to guide their motility. Our model also predicts that substrate stiffness is an important control parameter in guiding cell motility and forming multi-cellular structures.

Similar to the observations for pairs of endothelial cells mechanically interacting through the compliant substrates [5], we find that the motility and number of cell-cell contacts are lowered at large α, corresponding to softer substrates. This is because the elastic deformations of the substrate, and therefore, the cell–cell attractive interactions are stronger compared to the random motility. As observed in experiments, we also find that at intermediate interaction strength, the cells can make repeated contacts and withdrawals as

shown in the contact number measurements. For very stiff substrates, that is low interaction strength, we find the cell remains diffusive and can migrate away from the stationary cell and does not make frequent contacts. Our findings would therefore suggest an optimal substrate stiffness at which contact frequency is maximal. These trends are also reflected in the MSD measurements. Unlike the experiment, we don not find diffusive MSD for the strongly attractive case, but the MSD turns sub-diffusive, suggesting perhaps that such high interaction strengths were not probed in the experiment.

Biologically, altered motility and contact formation can be relevant for forming stable adhesive contacts between cells and tissue development, including that of blood vessels during vasculogenesis [153]. In our approach and in formulating the minimal model, we made several simplifying assumptions in the model (stated in section 2), including using a purely attractive and isotropic potential instead of the dipolar potential relevant for elongated and motile cells. Fig. 2.8 illustrates how the position and orientation of the motile cell with respect to the stationary cell leads to qualitatively different trajectories when the interaction potential is dipolar. Such an anisotropic potential is expected to lead to end–to–end alignment and contact formation of a pair of cells. With multiple cells, larger scale structures such as chains and networks of cells can result [130]. The influence of cellular motility on these structures will be the topic of a future study.

Cells are typically soft with values of estimated elastic moduli approximately equal to the range we have used here for the substrate stiffness. One may ask how the nominal cell stiffness or elasticity enters the model and the range of validity of the model. We note that, our model by itself holds for stiffer substrates as far as the response is that of a linear elastic material. With regard to the manner by which cell properties are implemented in the agent-based model, we point out that the underlying theoretical model that forms the basis of our agent based simulations treats the cell as a line dipole exerting contractile stresses on the substrate. In this minimal framework, properties of the cell such as its stiffness and the variation of the contractile stress with both cell properties (such as type and stiffness) are encapsulated in the dipole strength.

To improve on this further, we briefly consider recent advances that shed light on how cell (cortical) stiffness, the mechanical properties of the focal adhesion regions and alignment of intracellular structures affects the dipole strength. Recent work paints a complex and tightly coupled picture. (a) Cell elastic modulus is not a constant but dynamically and continuously altered dependent on substrate stiffness and topography (see [154] for

instance). (b) Thus the coupling between surface stresses, substrate stiffness, and focal adhesion dynamics is emergent and cannot be predicted *apriori*. It was recently shown in experiments using mouse embryonic fibroblasts [155] that vinculin regulates force transmission to the substrate and that vinculin and focal adhesion area did not correlate with traction force magnitudes at single focal adhesions, and this was consistent across different ECM stiffness and cytoskeletal tension states. Vinculin residence time varied linearly with applied force for stiff substrates; this was disrupted on soft substrates. (c) There is strong indication that local stiffness and alignment of intrafiber aggregates in the cell-substrate contact area are important. Vargas *et. al* [156] hypothesize that the point at which substrate stiffness becomes as high as that of the cell-cell interface corresponds to configurations where cell-substrate biophysics may dominate. (d) Atomic force microscopy (AFM) indentation measurements of cells cultured on deformable substrates suggest that cells adapt their stiffness to that of their surroundings. Recent work [108] probed the elasticity of microglial cells and fibroblasts cultured on soft matrices mimicking the mechanical properties of the physiological cell environment. Combining analytical estimates from Hertz contact theory with detailed finite element modeling, they found that cell stiffness was rather insensitive to substrate stiffness. These studies indicate that significant work still remains to be done to clarify the roles played by cell stiffness and substrate stiffness.

In this paper, we used a minimal model where microscopic details are coarse-grained. More detailed models and descriptions of cell and substrate deformation can be included if needed using finite element methods coupled with mechanochemical models that take into account detailed deformation history of the substrate and the cell-substrate region. The advantages of complementing experimental studies with modeling approaches as discussed in this paper is that hard to realize parameter regimes may be easily investigated. Furthermore, the role of different physical parameters may be clearly studied in isolation; a feature hard to achieve in an experimental setting. Understanding the mechanistic aspects of cell-cell interactions as done here has implications for regenerative medicine and tissue engineering and will guide and inform experiments exploring how cells communicate with each other in the process of organizing and moving collectively.

Chapter 3

Collective states of active particles with elastic dipolar interactions

This chapter is reproduced from our published article in *Frontiers in Physics*.

3.1 Introduction

Active matter typically comprises autonomous agents, biological or synthetic in origin, that harness internal energy sources to move [157, 57]. These agents often undergo complex interactions with each other and their surrounding media that influence their collective behavior [158]. Mammalian cells that move by crawling on elastic substrates such as tissue and constitute a canonical example of biological active matter in complex media, can cluster into persistently moving or rotating flocks [159]. These cells locomote by adhering to and exerting mechanical forces on their elastic extracellular substrate which they actively deform [94, 95]. The overall motility is guided by the cell's interactions with its substrate as well as with other cells [160]. Cell-cell interactions can include mechanical interactions mediated by their mutual deformations of the surrounding elastic substrate [5, 161]. This is particularly the case in dilute cell cultures where cells are not in direct contact. On the other hand, in dense active matter systems such as in confluent epithelial cell monolayers, direct cell-cell interactions including steric interactions can dominate [162]. Mechanical interactions through a material medium are by their nature long-range and are expected to govern the collective states of active particles[163], and enrich the large–scale phenomena such as phase separation that arise purely from motility [164, 165].

Mechanobiology experiments with adherent cells cultured on elastic hydrogel substrates [1, 134], suggest that substrate elasticity may provide a robust route to long lived and long ranged cell-cell interactions. Indeed, cell culture experiments indicate that cells exert measurable forces on their neighbors, either through direct cell-cell contacts, or indirectly through mutual deformations of a compliant, extracellular substrate [50, 166]. The substrate-mediated elastic interactions between such cells has important implications for biological processes such as self-organization during blood vessel morphogenesis [131] and synchronization of beating cardiac muscle cells [167, 125, 124, 168]. The overall motility of spatially separated cells is expected to depend on cell-cell mechanical interactions. This is revealed by experimental observations of substrate stiffness-dependent interactions of pairs of motile cells [169, 170].

In general, active particles endowed with a dipole moment are expected to interact at long range with each other while also propelling themselves. Passive dipolar particles such as ferromagnetic colloids at equilibrium will align end-to-end into linear structures such as chains or rings [171, 172]. At higher densities, the chains intersect to form gel-like network structures [173]. Topological defects in the networks such as junctions and rings are expected to affect the phases of passive dipolar fluids [174, 175]. When powered by chemical activity, dipolar colloidal systems exhibit self-assembly that depends on both the long-range, anisotropic interactions, as well as active motion, as revealed in recent experiments [176]. Such structures have also been studied in simulation in the context of active dipolar particles representing auto-phoretic colloids [177, 178], as well as swimming microorganisms [179] such as magnetotactic bacteria [180]. In related theoretical studies, constrained or bundled chains of self-propelling colloidal particles [181, 182, 183, 184] have also been shown to exhibit collective instabilities. Elasticity mediated interactions are seen to play critical roles, with the competition between mechanical interactions, steric interactions and activity determining the eventual dynamical behavior.

Here we build a minimal model of interacting elastic dipoles that is inspired by the mechanobiology of animal cells that actively deform their elastic substrate, while also exhibiting persistent motility. The starting point is the observation and deduction that contractile deformations of the underlying substrate originate from the elastic dipolar nature of stresses exerted by the cell on the substrate [185]. We show that incorporation of these substrate-mediated interactions offers a robust way to the formation of compact, and relatively stable collective states. Our model combining active self-propulsion of the

particles with their long-range dipolar interactions applies to a general class of experimentally realizable systems, including synthetic colloids endowed with permanent or induced magnetic or electric dipole moments [186]. By performing Brownian dynamics simulations on a collection of such dipolar active particles, we demonstrate the rich array of collective states that they can self-organize into. In particular, strong dipolar interactions promote end-to-end alignment of active particles, leading to self-assembled, motile chains. These chains can then further self-assemble into a hierarchy of larger-scale structures.

3.2 Model

Our model system consists of soft, repulsive, active Brownian particles (ABPs) [187, 188] in two dimensions (2D), that interact at long range through elastic dipolar interactions and strongly repel when they overlap. We have previously studied a simple isotropic interaction model valid in the limit where the propulsion direction was decoupled from the magnitude of cell-cell interactions [189]. Here, we analyze a more general model that accounts for the anisotropy of cell interactions, expected for the elongated shapes characteristic of migrating cells

The basis of elastic interactions between model cells is illustrated in Fig. 3.1. The schematic Fig. 3.1a shows the typical scenario of an adherent cell on top of an elastic substrate. The internal cytoskeletal machinery of the cell comprising actin stress fibers and myosin II molecular motors generates contractile mechanical forces, that are communicated to the external substrate through cell-substrate focal adhesions [190]. In a minimal, coarse-grained description, the traction force distribution of an elongated cell with a long axis $\mathbf{a}$ and exerting a typical force $\mathbf{F}$ at the adhesion sites, can be modeled as a force dipole with dipole moment $P_{ij} = F_i a_j$. The theory of continuous elastic media then determines that the distribution of forces from multiple cells will lead to a restoring stress σ in the medium, that satisfies a force balance [191], $\partial_j \sigma_{ij} = -\partial_j p_{ij}$, where the net dipole density, $p_{ij}(\mathbf{x}) = \Sigma_\alpha P_{ij}^\alpha \delta(\mathbf{x} - \mathbf{x}^\alpha)$ is the sum of traction forces exerted by each point-like cell dipole, here labeled by an index α. In modeling cells as point-like dipoles, we ignore their finite size, an assumption that is valid only at "far field", *i.e.* at distances large compared to cell length. While this is not strictly the case in our simulations, a more general model accounting for finite separation of the cell forces is expected to lead to qualitatively similar interactions [168].

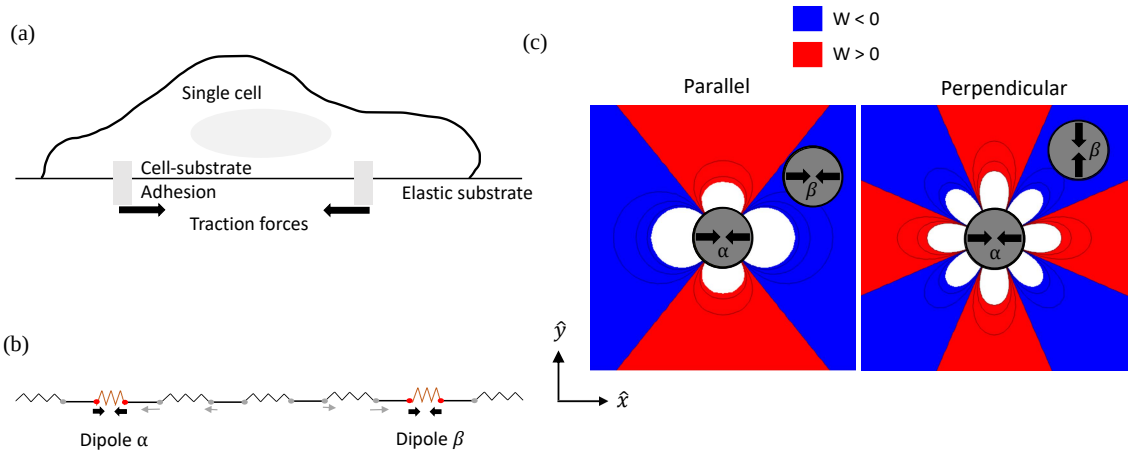

Figure 3.1: Elastic interactions between model cells on a substrate. (a) Schematic of adherent cell on an elastic substrate. (b) 1D spring model illustrating origin of elastic interaction potential between two contractile dipoles. The elastic energy stored in the medium corresponding to the deformation of springs depends on the relative placement of the dipoles. In particular, placing a contractile dipole in a region where the medium is already expanded by the other dipole can help to reduce the overall deformation of the medium. This leads to a strain-dependent interaction potential between the two dipoles. (c) Representative spatial maps of the interaction potential $W^{\alpha\beta}$ between two dipoles, from the solution of the strain field for the full linear elastic problem of forces exerted on the surface of a semin-infinite medium are showm. The interaction potential corresponds to the work done by a point-like dipole in deforming the substrate in the presence of the strain created by the other. The potential maps shown here are for a pair of contractile force dipoles of fixed orientation. The second dipole is free to translate but held parallel (left) or perpendicular (right) to the central dipole which is placed at the origin and aligned along the x-axis. The contour lines show how the potential decays in space, whereas blue and red regions correspond to attractive ($W^{\alpha\beta} < 0$) and repulsive ($W^{\alpha\beta} > 0$) interactions, respectively.

By considering two dipoles $\mathbf{P}^{\alpha}$ and $\mathbf{P}^{\beta}$, we can show that the work done by a dipole β in deforming the elastic medium in the presence of the strain created by the other dipole α, is given by [6]: $W^{\alpha\beta} = P^{\beta}_{ij} u^{\alpha}_{ij}(\mathbf{x}^{\beta})$. This minimal coupling between dipolar stress and medium strain represents the mechanical interaction energy between dipoles. The strain in the elastic medium created by dipole α at the position of the dipole β is given by the gradient of the displacement, $u_{ij}(x) = \frac{1}{2}(\frac{\partial u_i}{\partial x_j} + \frac{\partial u_j}{\partial x_i})$ and can be calculated using standard methods in linear elastic theory [191]. This is detailed in the Methods section, where we follow the treatment introduced in Ref. [6]. The mechanical interaction between a pair of

force dipoles is illustrated by the schematic in Fig. 3.1b in the form of a 1D series of springs representing the effect of the elastic substrate. While the springs underlying the contractile dipoles are compressed, the springs between them are stretched. By moving to different positions in the medium for a given position of dipole α, the dipole β can reduce the net substrate deformation energy by compressing regions stretched by dipole α. This leads to a substrate deformation-mediated elastic force on the dipole β,

$$f_{el}^{\beta} = -\frac{\partial W^{\alpha\beta}}{\partial \mathbf{x}^{\beta}} = -P_{ij}^{\beta}\frac{\partial u_{ij}^{\alpha}(\mathbf{x}_{\beta})}{\partial \mathbf{x}_{j}^{\beta}}, \tag{3.1}$$

given by the gradient of the strain induced by the other dipole, where the strain therefore acts as a potential. While the expressions vary in detail, this physical interaction between elastic dipoles considered here is analogous to the interaction of an electric dipole with the electric field induced by another dipole. A similar reciprocal force results on dipole α, since the interactions are based on an elastic free energy. The physical origin of this force is the tendency of the passive elastic medium to minimize its deformations in response to the active, contractile forces generated by the cells. This generic mechanical interaction between dipoles is not limited to cells [6], but also occurs for passive inclusions in an elastic medium [192]. Experimentally, hydrogen atoms in metals were shown to diffuse and distribute themselves according to configurations dictated by these elastic interactions [193].

Pairwise dipolar interactions are anisotropic and depend on both the distance between and relative orientations of the two particles with respect to their separation axis. Insights into the nature of the elastic interaction potential between a pair of force dipoles, may be obtained from Fig. 3.1c where we plot spatial maps of the interaction potential $W^{\alpha\beta}$ for two cells with fixed orientation. To plot these functions, we choose a reference contractile force dipole α that is fixed at the origin with its axis along the $-x$ direction, *i.e.* whose dipole moment has purely the P_{xx} component. A second test dipole β interacts with the reference dipole according to its position and orientation. The red (blue) regions in the potential maps in Fig. 3.1c represent repulsion (attraction) which arises from the substrate strain. Here, we use the convention that stretched (compressed) regions have positive (negative) strain, while compressive dipole moment is negative. While the map on the left corresponds to parallel alignment, that on the right maps the interaction potential for perpendicular alignment of the two dipoles. In this example, we fix the orientation of the second dipole to be either parallel or perpendicular, and therefore it couples to either the u_{xx} or the u_{yy} component of the strain according to Eq. 3.1. In general, the dipoles can

also rotate and change its relative orientations. In particular, while the favorable parallel configuration shown here leads to end-to-end alignment of the dipoles, the unfavorable perpendicular configuration will lead to mutual torques that tend to orient them in the favorable parallel configuration. The elastic material comprising the substrate is treated as homogeneous and isotropic with shear and compression modulii proportional to the Young's modulus E, and a Poisson ratio ν that provides a measure of its compressibility [130]. While the Poisson's ratio can in principle have the full range $-1 < \nu < 1/2$ in linear elasticity theory, the figures plotted here correspond to $\nu = 0.1$[1].

The interaction potential and model dynamics are detailed in the Methods Section 3.4 in Eq. 3.4-Eq. 3.7. As shown in Fig. 3.2a, the ABPs – here termed particles – are modeled as circular disks of diameter σ, each particle being endowed with a dipole moment and a self-propulsion direction $\hat{\mathbf{n}}$. The orientation of $\hat{\mathbf{n}}$ is aligned with the dipole axis (shown as the bold black line). This assumption is reasonable for motile cells with elongated shape, but is not necessarily satisfied for all cell types, where higher force multipoles may be relevant [170]. Particles are assumed to self-propel with a speed v_0. This phenomenologically models the movement of cells which require internal cell forces arising from actomyosin activity as well as the remodeling dynamics of the cell-substrate adhesions, not explicitly modeled here. Additionally, the motion of each particle is subject to forces and torques arising from dipolar interactions with other particles, as well as a random stochastic force. This latter mimics the effect of the thermal environment surrounding the particles, and leads to diffusive effects in both orientation and spatial position of the ABPs.

Since we are motivated by adherent cells on elastic substrates whose contractile traction forces act as elastic dipoles, a cutoff distance of $r_{\text{cut}} = 7\sigma$ (red dashed circle in Fig. 3.2a) is imposed on the long range dipolar interactions. The choice of a cut-off length for interactions is consistent with experimental observations that cells can interact with one another via mechanical signalling at distances that are up to a few cell lengths away [5, 167]. In addition to the long-range interactions mediated by the elastic substrate, cells may also interact via short-range interactions. Here we introduce short-range steric repulsion using a mechanical model using compressive springs that discourage overlap between neighbouring particles. Specifically, two particles in close-contact exert a repulsive elastic force on each

[1]This choice ensures end-to-end alignment of dipoles and provides interactions seen not just in cells but also in other types of active matter that feature particles with magnetic or electric dipole moments. The interactions at $\nu > 0.3$ have a different symmetry and can result in more complex structures such as short rings without any electric or magnetic analogs [194].

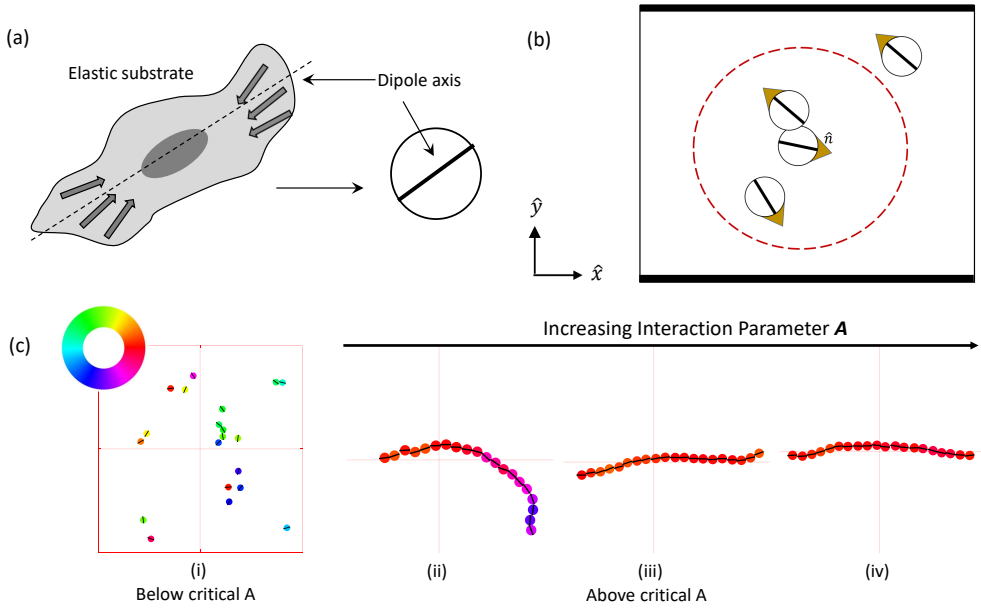

Figure 3.2: Overview of agent based simulations of active Brownian particles (ABPs) moving in the x-y plane and interacting mechanically via elastic deformations induced by contractile, active force dipoles. (a) An elongated cell with traction forces distributed around its long axis is modeled as a disk-like particle endowed with a dipole moment. (b) Each ABP has a dipole axis represented by the bold black line and an in-plane self-propulsion direction represented by the gold arrow. These particles move on a linearly elastic, thick, flat substrate, on which they exert contractile dipolar stresses. Substrate deformation due to one particle is sensed by neighbouring particles. These dipole-dipole elastic interactions are confined to particles within a cutoff distance $r_{\text{cut}} = 7\sigma$ (shown as the dashed red circle). Particle overlap is penalized by a short range steric repulsion. They are confined by steric repulsions along the top and bottom walls shown by the thick lines, while being free to move through periodic boundaries shown by the thin lines. (i) Simulation snapshot shows that weakly interacting particles do not stick to each other and move as independent entities. As the elastic dipolar interaction parameter A increases, the particles self-assemble into long chains ((ii)-(iv), zoomed view shown). The flexibility of the chains and fluctuations in the mean curvature both decrease with increasing values of the interaction parameter. The colors represent the self-propulsion direction of each particle, as indicated by the color wheel.

other when the center-to-center distance is less than the rest length σ of these springs.

The ensuing dipolar interactions, when strong enough relative to the stochastic noise, cause end-to-end chaining of the particles along their dipole axis. Examples of this chaining process are seen to occur in our simulations and representative snapshots are shown

in Fig. 3.2c. As expected intuitively, increasing interaction gives rise to stronger alignment resulting in chains that are progressively less flexible. The effective elastic bending modulus of these chains that determines the fluctuations of the backbone contour of the chained ABPs is thus higher with increasing interaction strength.

To illustrate the bulk behavior of interacting ABPs as well as the effect of confinement on emergent collective patterns, we simulate a few hundred of these particles in a box confined in the $y-$ direction, and periodic in the $x-$ direction. The confining boundary is lined by repulsive springs of the same type used to penalize particle overlap, and keeps the ABPs from escaping the simulation box. This setup mimics a channel geometry typically used in cell motility experiments [195] and is used in other works on simulations of ABPs under confinement [196, 197, 198]. We focus on the physical barriers to cell motility and not interfaces in the elastic medium. In principle, such elastic interfaces can lead to additional elastic torques and forces on dipoles by inducing "image forces" [6], but this is outside the scope of the present work. One way to realize this type of confining boundary that does not induce stresses in the elastic medium is to culture cells on a large and thick slab of hydrogel with uniform elastic properties, but micropattern a specific region of the substrate with ligands to which the cells can adhere – a common technique in mechanobiological cell culture studies. [1]

The important nondimensional control parameters in the model are the elastic dipole-dipole interaction strength A, the active self-propulsion velocity characterized by a Péclet number,. Pe, and the packing fraction, ϕ. The packing fraction used in simulations below is typically either $\phi = 0.08$ or 0.25 corresponding to relatively dilute regimes, except in a narrow channel geometry where we go up to $\phi = 0.75$. Definitions and physical interpretations of these parameters are provided in the Methods Section 3.4.

3.3 Results

3.3.1 Characteristic states of active dipolar particles: chains, polar bands, clusters and networks

We first explore the possible collective structures that result from the combination of active self-propulsion with dipolar attraction and alignment. We explore the parameter space of activity (given by the Péclet number, Pe) and strength of dipolar interactions (given by the effective elastic interaction parameter, A) for two representative systems: one

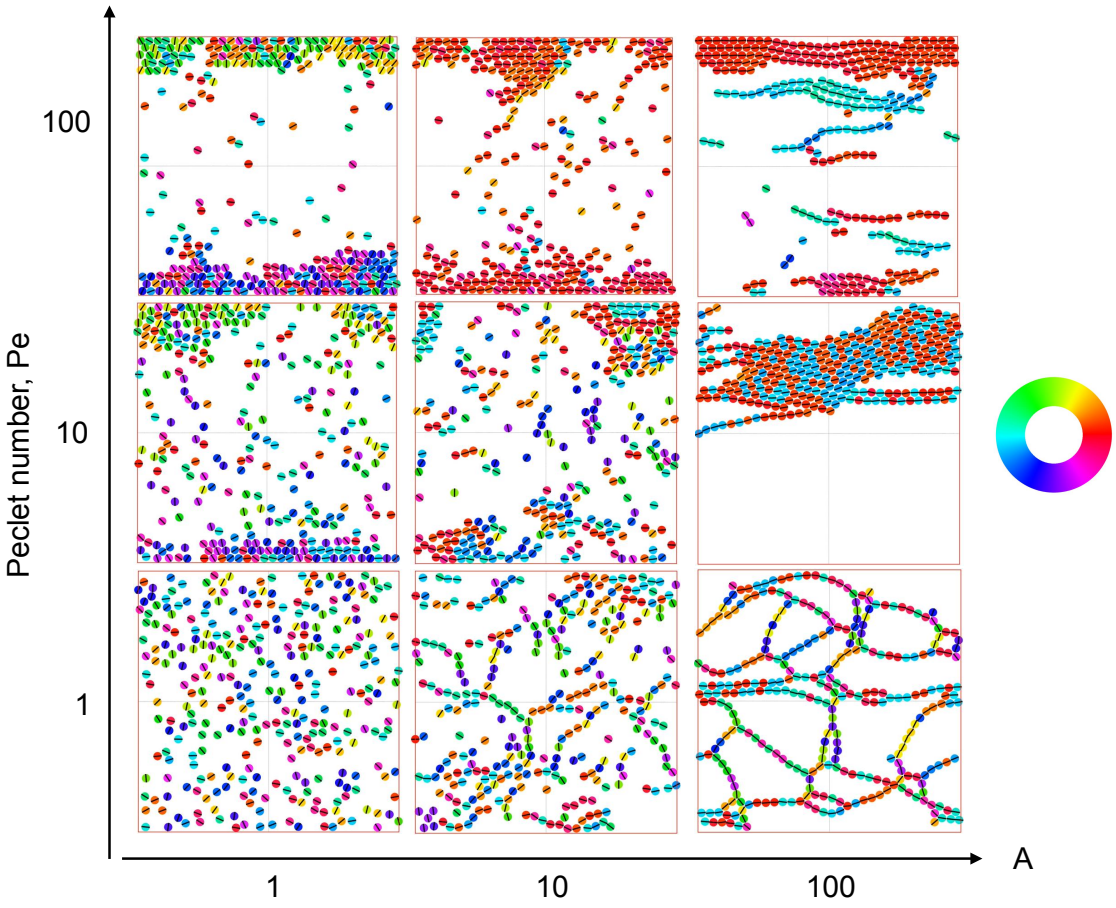

Figure 3.3: Simulation snapshots of active particles with short range steric repulsions and long-range elastic dipole-dipole interactions as a function of effective elastic interaction $A = P^2/E\sigma^3 k_{\mathrm{B}} T_{\mathrm{eff}}$ and Péclet number $Pe = \sigma v_0/D_{\mathrm{T}}$. Particles are confined in the y-direction, while they experience periodic boundary conditions in the x-direction. They are colored according to their self-propulsion direction $\hat{\mathbf{n}}$, and coded based on the color wheel. Motile particles at low effective elastic interaction collect into clusters at the boundaries. Strong elastic interactions promote network formation at low activity. Strong elastic interactions paired with high activity gives rise to active polymers and polar bands.

dilute and the other semi-dilute. We show representative snapshots of the steady states of the simulations by coloring the particles according their orientation. Collections of these snapshots as well as the color wheel corresponding to particle orientations are shown in Figs. 3.3, where the packing fraction $\phi \approx 0.25$, and Fig. 3.4, where the packing fraction $\phi \approx 0.08$.

We see from figure 3.3 that at both low motility and weak elastic interactions($A =$

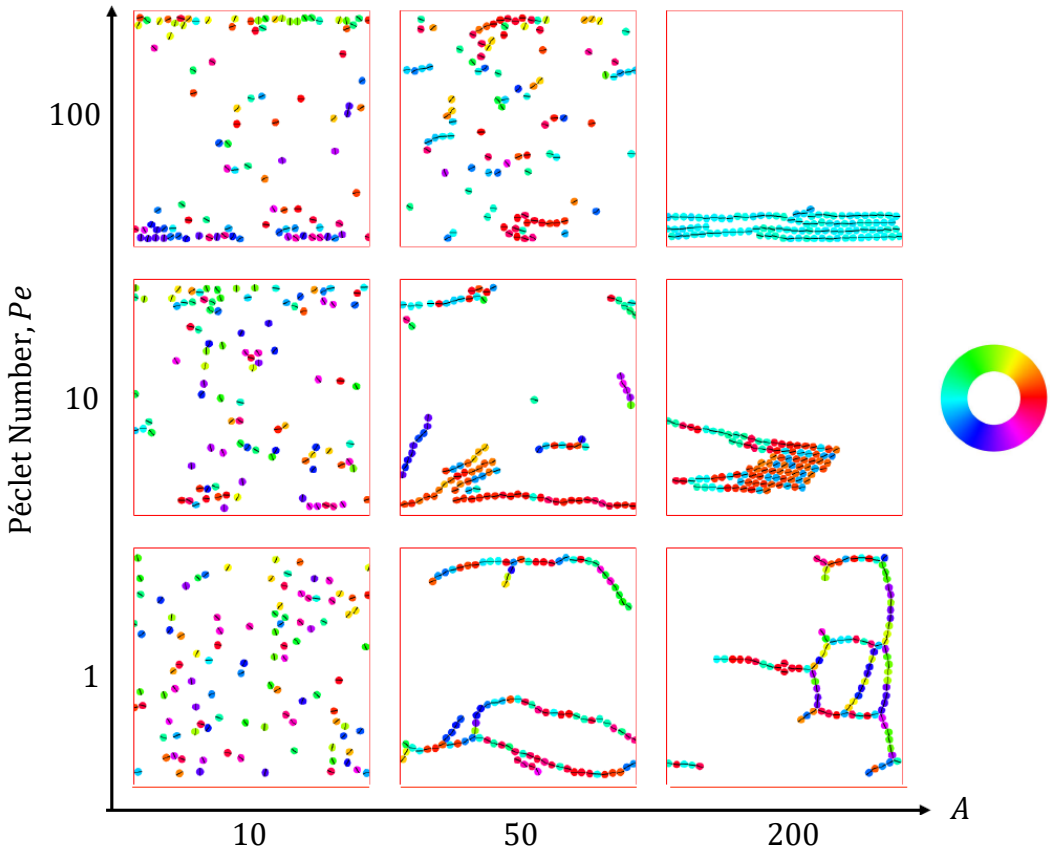

Figure 3.4: Simulation snapshots of active particles at low packing fraction - The interaction parameter $A \equiv P^2/E\sigma^3 k_{\mathrm{B}} T_{\mathrm{eff}}$ and Péclet number $Pe \equiv \sigma v_0/D_{\mathrm{T}}$ define the collective behavior of the particles. Particles are confined in the y-direction, while they experience periodic boundary conditions in the x-direction. They are colored based on the direction of $\hat{\mathbf{n}}$, as indicated by the color wheel. At low interaction parameter $A = 10$, the particles remain isolated and diffuse. At high Pe, more particles get collected at the confining boundary. At higher values of the interaction parameter, A, particles form chains. The typical length of the chains is seen to decrease with increasing Pe. At very high interaction parameter, $A = 200$, networks with multiple branches form at low Pe, while chains aggregate into polar clusters at $Pe = 10$. Although the particles in the cluster are oriented in opposite directions, the cluster is stable and moves in the direction given by its overall polarity. Again at very high Péclet, $Pe = 100$, the particles in the chains are oriented in the same direction.

1), particles do not form any ordered structures but are distributed uniformly in space, over the utilized simulation time. As motility is increased ($Pe \geq 10$), particles are seen to clump up at the boundary with their orientation vectors facing the wall at which they are localized. This is a familiar result of confined active Brownian particles (ABPs) wherein these tend

to point towards the wall until their orientation is sufficiently randomized by the rotational diffusion[199]. As elastic interactions are dialed up such that the motions resulting from the dipolar interactions are much stronger than the stochastic diffusion of the system, structures characteristic of dipolar interactions emerge. In the case of low particle motility ($Pe = 1$), and high elastic interactions, we see a branched network form. In the case of intermediate motility ($Pe = 10$), networks are broken down into a single traveling cluster. In the former case, the particles comprising any given chain can either be oriented parallel (0) or anti-parallel (π) with respect to one another as the dipolar interaction is head-tail symmetric. In the latter case, networks form at short timescales and are compressed into one motile cluster at long timescales. This motile cluster contains numerous defects (shown by their different color) - particles oriented anti-parallel to the direction of cluster motion - caused by the earlier stage of network formation. Lastly, in the case of high particle motility ($Pe = 100$), particles assemble into traveling flexible chains which predominantly move parallel to the confining boundary and undergo inter-chain collisions in the bulk. Much of our forthcoming analysis is focused on these highly ordered, yet highly dynamic, structures.

At low packing fraction (Fig. 3.4), for $A = 10$ the elastic interaction between the particles is low and they diffuse around in the simulation space which is in contrast to what we see for higher packing fraction (Fig. 3.3) where particles show alignment with weak attraction. Accumulation of the particles can be seen at the confining boundaries which is attributed to the activity of the particles. Upon increasing the elastic strength to $A = 50$, formation of chains has been observed. At $Pe = 1$, long and branched chains of particles are formed. Increasing motility leads to a decrease in length of the chains and an increased polarity. At even higher elastic strength of $A = 200$, long chains with multiple branches are seen for $Pe = 1$. At increased activity, the chains stick to each other and form an ordered cluster that moves coherently in the direction determined by the net polarity of the constituent particles.

3.3.2 Pair correlations reveal spatial organization of active chains

To quantify the spatial distribution of particles around their neighbors, we calculate the pair correlation function, $g(r, \theta)$, the probability of finding a neighboring particle at a distance r in a direction θ from the central agent's orientation axis. We calculate this quantity by averaging over the positions of all agents over time, and binning every other agent according to its separation vector (both distance and angle) from the current central

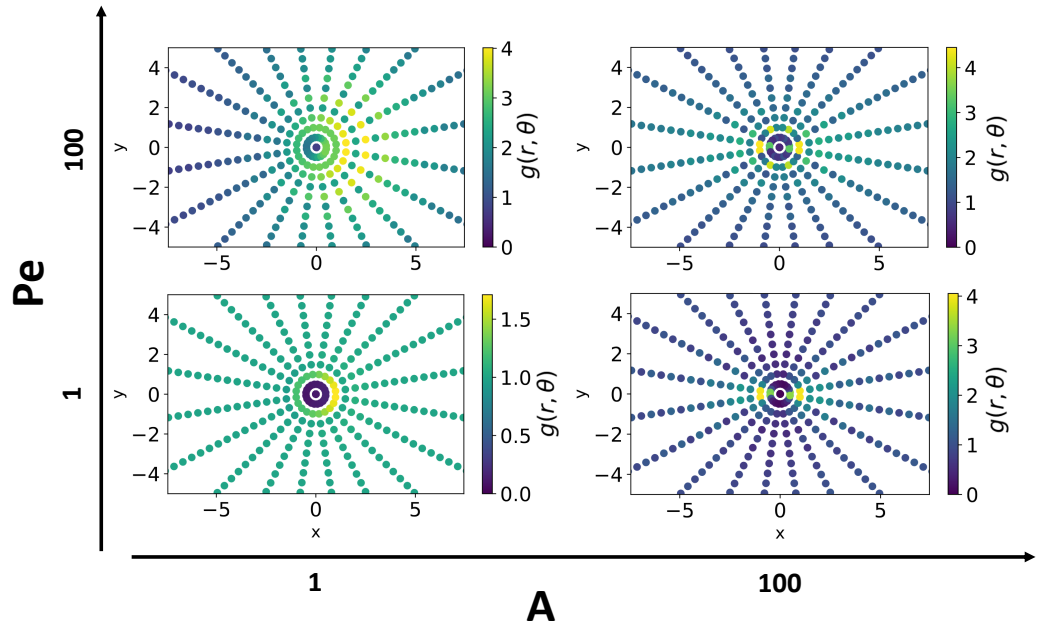

Figure 3.5: Angular dependent pair correlation function is affected by both motility and elastic interactions. Strong elastic interactions promote pair correlation peaks at $(r,\theta) =$ (σ,0) , (σ,π). At $Pe = 1$, these are the only prominent peaks in the pair correlation function. Motile activity gives rise to secondary peaks at roughly $(r,\theta) = (\sigma, \frac{\pi}{3} \bmod \pi)$, $(\sigma, \frac{2\pi}{3} \bmod \pi)$ as the preeminent structures are bundles of offset traveling chains. Weak elastic interactions broaden the pair correlation distribution. In this case, motility breaks head-tail symmetry and peaks can be seen at multiple integers of particle diameter at the head ($\theta = 0$ axis).

agent. Finally the distribution is normalized such that $g(r,\theta)$ approaches 1 for distance r going to infinity. We then analyze the peaks in (r,θ) space. Fig. 3.5 shows four such distance and angle dependent maps in the space of motility and elastic interaction. Elastic interactions localize the peaks of the pair correlation function. When motility is low, particles form branched networks and the primary configuration of particles is in straight chains. In this case, there exists two prominent peaks in the pair correlation function at (σ,0) and (σ,π). When both motility and elastic interactions are high, particles form into flexible traveling chains that have a tendency to join one another in a parallel fashion with an offset - a configuration that is energetically favorable to the elastic interaction and can be seen prominently in the simulation snapshot corresponding to $A = 100$ and $Pe = 100$ in Fig. 3.3. In this case, the primary peaks still occur at (σ,0) and (σ,π), but secondary peaks are present at $(\sigma, \frac{\pi}{3} \bmod \pi)$ and $(\sigma, \frac{2\pi}{3} \bmod \pi)$, indicating the offset parallel band structure.

Low elastic interactions constitute the more familiar case of collections of repulsive ABPs. In this regime, the head-tail symmetry characteristic of the elastic interactions is broken as particles are more likely to encounter other particles along their direction of propulsion [200]. There exists a single prominent peak at the head of the dipole that monotonically decreases on either side of the head axis. Increasing motility in the ABP system adds layers to the single peak function in integer multiples of particle size σ as collision frequency increases.

3.3.3 Activity and elastic interactions promote orientational order

At higher interaction strength, A, and higher motility, Pe, we see chains that move parallel to each other forming polar bands at high density (top right of Fig. 3.3). Since chains are elongated objects, a collection of them can give rise to orientational order, similar to active nematic and polar states that result from active, anisotropic particles [157]. This type of order commonly seen in active matter comprising suspensions of cytoskeletal filaments and motors [201]. To quantify the orientational order in these cases and to distinguish from the individual ABPs under confinement, we measure the nematic and polar order for these states. The magnitude of the nematic order parameter is defined as an average over the orientation of all particles, $S \equiv 2\langle \cos^2\theta \rangle - 1$, where θ is the angle between a particle's orientation and the average director. In this case, the global alignment direction is parallel to the confining boundaries given by the $x-$ axis. The nematic order tells us how well the dipoles are aligned, without distinguishing between the head and tail and contains no information about the motility direction. To quantify the oriented motion, we calculate the polar order, whose magnitude is given by, $|p| \equiv \sqrt{\langle n_x \rangle^2 + \langle n_y \rangle^2}$, where n_x and n_y are the x and y components of the orientation vector, $\hat{\mathbf{n}}$, respectively. This quantity is higher if the particles are oriented in the same direction, in addition to being aligned. While nematic alignment is encouraged by the passive dipolar interactions, active motility induces polar order.

Fig. 3.6(a,c) shows the global nematic order in time and Fig. 3.6(b,d) shows the time averaged spatial map of the polar order parameter, calculated by subdividing the simulation box into regions of dimension 3.75σ x 3.75σ, for both ABPs and traveling flexible chains. In the ABP system, the global nematic order is small due to the tendency of particles at the walls to be oriented orthogonal to the wall and those in the bulk to be oriented parallel to the wall, as well as the presence of orientational fluctuations from rotational diffusion.

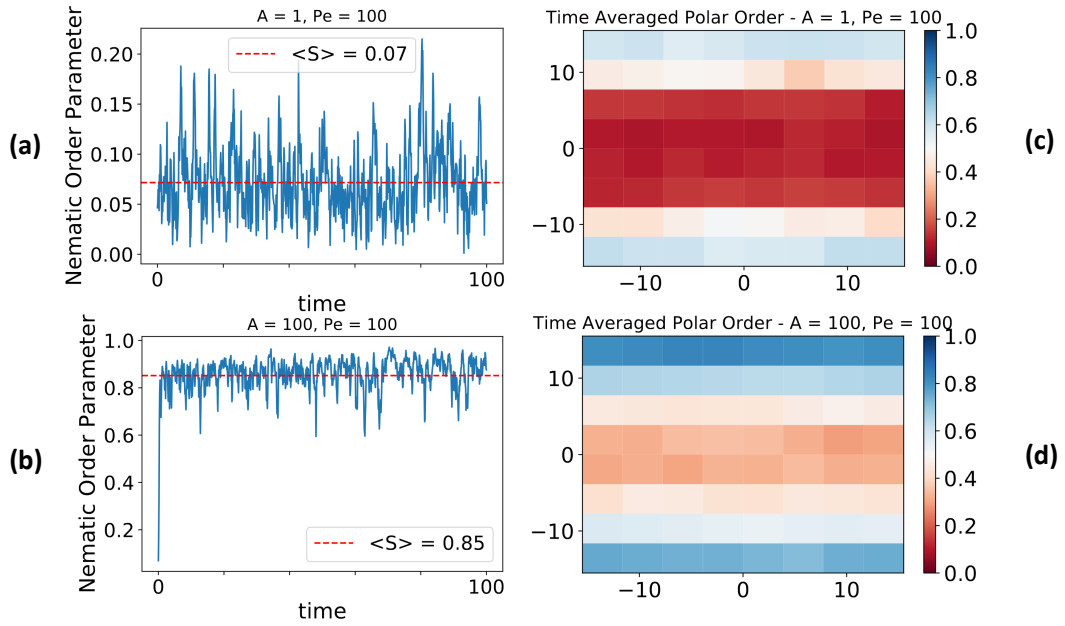

Figure 3.6: Elastic interactions promote global nematic order and local polar order. (a) Global nematic order, measuring the overall alignment of the particles' dipole axes, vs. time for low effective elastic interaction and high activity. Average global nematic order is negligible for these parameters. (b) Global nematic order vs. time for high effective elastic interaction and high activity. The system quickly gains a persistent global nematic order parameter near unity because the chains align parallel to each other. (c) Spatial distribution of time averaged polar order, where grid size is 3.75σ x 3.75σ, measuring the overall orientation of motility for the particles, for a characteristic run at low effective elastic interaction and high activity. Particles accumulate at the boundary and exhibit polar order along that boundary. This order rapidly decays away from the boundary and there is virtually no polar order observed in the bulk. (d) Spatial distribution of time averaged polar order, where grid size is 3.75σ x 3.75σ, for a characteristic run at high effective elastic interaction and high activity. A polar order near unity is observed at the boundary and persists into the bulk where near the middle of the channel $|p| \approx 0.3$.

Traveling flexible chains of dipolar particles exhibit a global nematic order close to unity as all particles in this system tend to point along a director parallel to the confined boundary. Spatially resolving the average of the magnitude of the polar order parameter gives us a picture of particle alignment at a smaller length scale. ABPs exhibit polar alignment at the boundary. This alignment quickly diminishes and no polar order is seen in the bulk. Traveling chains form bands at the boundary such that $p > 0.7$ up to 6σ away from the wall. The polar order of these flexible chains drops off far less drastically in the bulk than

the ABP system.

3.3.4 Transport properties of active chains are distinct from single particles

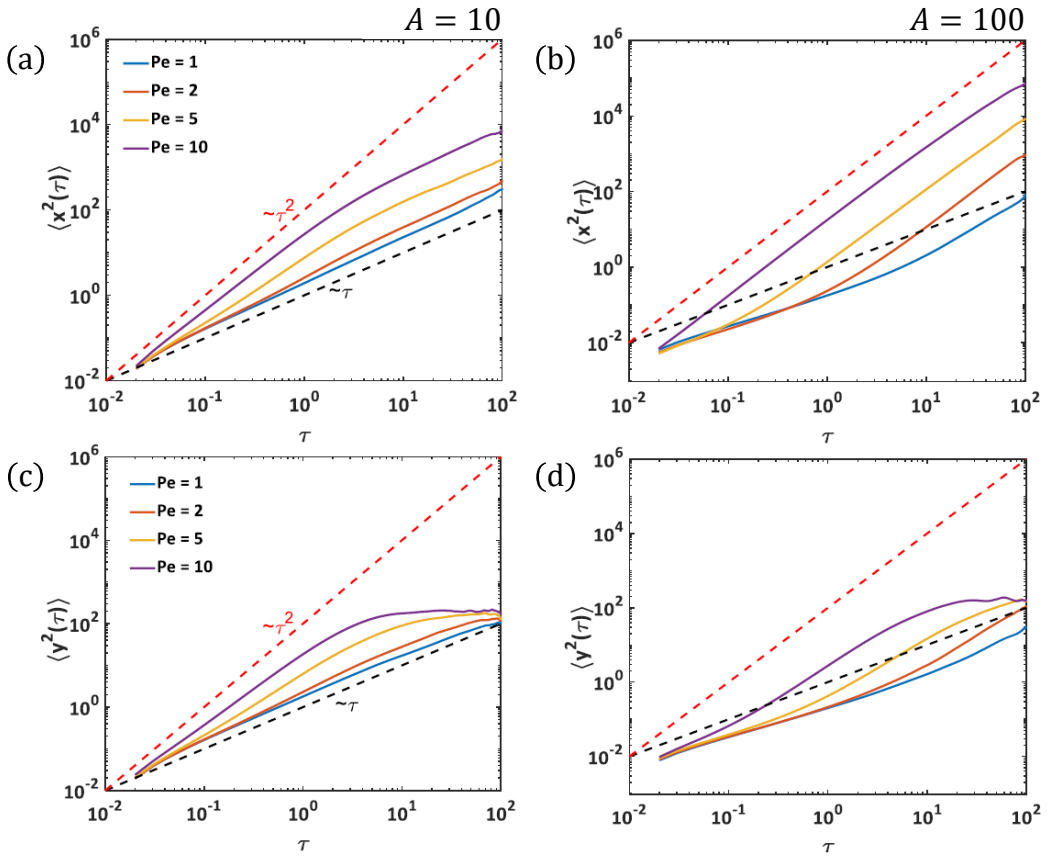

Figure 3.7: Mean-Squared Displacement or MSD vs. time interval, for 100 particles in a square simulation box of 30σ. Due to confinement of particles in y-direction, MSD is plotted separately for x and y components of displacement. (a), (b) MSD along unconfined direction: for $A = 10$, particles are super-diffusive at short time scale and diffusive at longer time scale, where the crossover time scale is determined by the Péclet number (Pe) of the particles. At $A = 100$, particles align themselves to form chains or clusters. At low Pe, the particles show sub-diffusive behavior at shorter times and ballistic behavior at longer times. At higher Pe, the ballistic behavior of particles is observed at all time scales. (c), (d) MSD along confined direction: particles reach the confining boundary at shorter times for high Pe number, and also at low elastic interactions A. At higher A, particles chain up and move predominantly parallel to the confining boundary.

The mean-squared displacement or MSD is a typical metric that quantifies how

motile entities cover space in time. In Fig. 3.7, we report the MSD for simulations with a packing fraction $\phi \approx 0.08$ in a square box of size 30σ, corresponding to the structures shown in Fig. 3.4. Given the confinement along one direction, we calculate the MSD separately for the confined (y-) and unconfined (x-) directions. The unconfined MSD, $\langle x^2 \rangle$, for particles with low elastic interaction *e.g.*, at $A = 10$, shows similar trends to individual active Brownian particles [202]. At short time intervals, individual ABPs propel persistently in the direction of their orientation, leading to ballistic behavior. In Fig. 3.7a, we see such behavior at very short time scales which gave way to super-diffusive behavior at intermediate time scales, where particles are slowed down by collisions with other particles. At sufficiently long time scales, the particles are diffusive as the rotational diffusion randomizes their orientation. Increasing Péclet number increases the timescale for super-diffusive behavior as the persistence time is longer.

We see qualitatively different regimes in the MSD for particles with stronger interaction in Fig. 3.7b. At interaction strength $A \geq 100$, which leads to formation of long, stable chains, we observe larger-scale structures such as branches, clusters and networks in the simulation snapshots shown in Fig. 3.4. In this case, the particles show sub-diffusive behavior at shorter time scales when they are still moving individually in an uncorrelated manner and beginning to form these structures. On the other hand, at longer time scales, they cluster into larger scale structures that move coherently in a specific direction like polar flocks, giving rise to a ballistic behavior. The crossover from subdiffusive to nearly ballistic behavior occurs earlier for higher Péclet numbers. At higher particle motility, we obtain ballistic behavior for all time scales. The resulting behavior is thus qualitatively different from single ABP behavior, which show a crossover from persistent to diffusive motion at timescales longer than the persistence time ($\sim Pe$). Here, on the other hand, the long time behavior is dictated by large-scale, polar structures that self-assemble irreversibly and move persistently at long times.

The MSD in the confined direction, $\langle y^2 \rangle$, plateaus off at long times, both for the individual ABPs (Fig. 3.7c) and the larger scale structures (Fig. 3.7d). The time scale to reach a plateau in the MSD corresponds to the time it takes an entity to reach the confining walls from the bulk of the simulation box. Thus, $\langle y^2 \rangle$ reaches a plateau at a shorter time scale for highly motile particles, as compared to the less motile ones. Due to the confining wall in the y-direction and strong alignment with neighboring particles at $A = 100$, the particles line up into chains that orient and move parallel to the confining walls, and not

as much in the y-direction. Thus, $\langle y^2 \rangle$ for $A = 100$ reaches the plateau later than for the $A = 10$ case, for corresponding values of Pe.

3.3.5 Collisions of active chains reveal stable, mobile structures

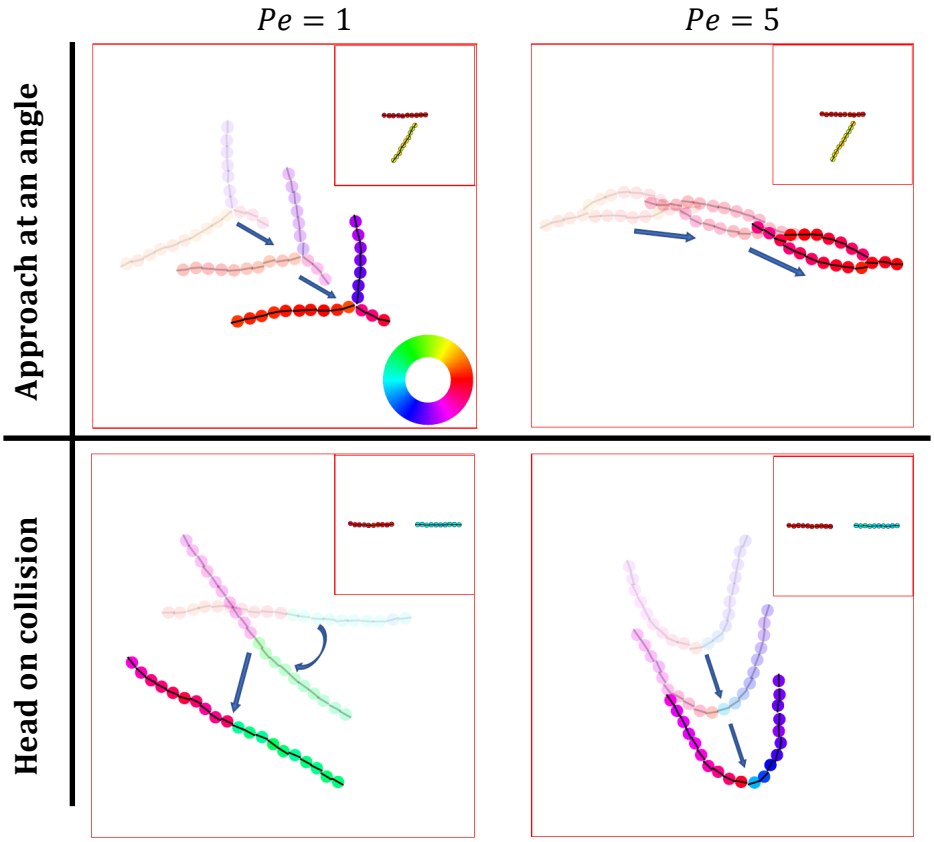

Figure 3.8: Interaction of two motile chains (Supplementary Movie (Supplementary Movie 8). Two straight chains of 10 particles each are initialized to approach each other at an angle of $\frac{\pi}{3}$ and also π ("head-on") at $Pe = 1$ and 5. At $Pe = 1$, a 'Y' junction forms for an approach angle of $\frac{\pi}{3}$ whereas at $Pe = 5$, an 'eye' (two junctions) occurs. Upon head-on collision, a longer fluctuating chain with negligible net motility results at $Pe = 1$, and a propelling, buckled shape is observed at $Pe = 5$. Insets at the top corners represent the approach of the chains. Color represents angle of orientation of particles. The arrows indicate progression in time and suggest that the configurations are both stable and motile.

We observe from simulations at low packing fraction (Fig. 3.4) that once particles self-assemble into chains, these can intersect to form junctions and get organized into larger-

scale polar structures. We now explore in more detail the inter-chain interactions responsible for this self-organization. To do this, particles were initialized in an ordered chain and oriented in the same direction. Two such chains were oriented initially at different angles to control their approach direction, as shown in the insets in Fig. 3.8.

At $A = 200$ the junctions formed by chains depended on the Péclet number and the angle and position of approach. The 'Y' junction was the most observed for all Péclet number, which is formed from when the second chain attaches itself at the middle of the first chain (Figure 3.8, top left). An 'eye' (Figure 3.8, top right) is formed from two closely spaced 'Y's, which is observed for higher Péclet number, $Pe = 5$ and 10 and when the chains are oriented in the same direction. Again, at low particle motility $Pe = 1$, the chains upon colliding head on form a longer and more rigid chain (Figure 3.8, bottom left). On the other hand, at $Pe = 5$ chains show buckling upon undergoing head on collision which leads to a propelling 'necklace' (Figure 3.8, bottom right). At even higher Péclet number, the force between the particles is overpowered causing particles to detach from a chain and thereby creating defects. All these cases have been observed for $A = 200$. These junctions are also observed at lower elastic strength $A = 50$ and 100, but were unstable giving rise to many defects. Chains may interact with each other in a head-tail fashion which results in a stable longer chain. Chains with multiple defects have also been observed to form these 'Y' and 'eye' structures at $A = 200$ and $Pe = 1$ (Figure 3.4).

3.3.6 Stronger confinement in narrow channels reveals polar clustering dynamics

In our system of traveling flexible chains comprised of strongly interacting and highly motile dipolar particles ($A = 100, Pe = 100$), bands that form along the confining boundary are relatively stable compared to those that form in the bulk. The latter are subject to more frequent collisions with other traveling chains. In order to gain understanding of these chain collision dynamics, we confine the same number of particles into a channel of width $L_y = \frac{L}{3}$, where L is the box size of our original simulation space, in order to induce more frequent and global chain-chain collisions. In this system we find a cyclic tripartite state dynamic. As shown in figure 3.9a, at some point, the particles with orientations $+x$ become well mixed with particles with orientations $-x$. The particles will then separate into lanes according to their polarity so that they can move unimpeded. These lanes will then collide which initializes another well mixed system and the cycle repeats.

This effect of colliding lanes can be seen quantitatively by tracking the magnitude of the polar order parameter averaged over boxes of width 3σ and height 2.5σ in time shown in figure 3.9b. The well mixed system has an average polar order parameter of $p \approx 0.2$. The system then phase separates into lanes with average polar order parameter ≈ 0.6. The $+x$ and $-x$ lanes collide and the resultant combination has an average polar order parameter ≈ 0.4. When the channel is sufficiently wide, collisions between opposite lanes is less common, and the average polar order is bolstered by persistent polar chains at the confining boundary as seen in Fig. 3.9c.This time dependent formation and disbanding of polar structures is consistent with bead spring simulations of semiflexible filaments in the high activity regime [203].

3.4 Methods

Here, we present the equations governing the motion of the active motile particles discussed earlier and their interaction via the elastic substrate on which they move. In our model, we treat the particles as circular active Brownian particles (ABPs) that interact with other particles via long-range substrate modulated interactions and direct short-range particle-particle steric contact interactions. Long range interactions arise as each ABP exerts a contractile stress dipole $\mathbf{P}$ on the flat, semi-infinite, linearly elastic, isotropic substrate, thereby inducing strain fields which induces an effective force on nearby particles. For simplicity, we assume that the dipole axis is coincident with the direction of motion of the particle. For instance in an elongated cell, the force dipole axis coincides with the orientational axis of the cell, that is also the direction of self-propulsion.

In the derivation that follows we use Einstein summation convention over the Latin indices, while Greek indices are used to label the particles. Consider a particle α that deforms the substrate. The work done by the associated dipole, $\mathbf{P}^{\alpha}$ in deforming the substrate in the presence of the strain created by a second dipole $\mathbf{P}^{\beta}$ (generated by a second particle β) is given by [6],

$$W_{\alpha\beta} = P_{ij}^{\beta}\partial_j\partial_l G_{ik}^{\alpha\beta}(\mathbf{r}_{\alpha\beta})P_{kl}^{\alpha}, \tag{3.2}$$

where $\mathbf{r}_{\alpha\beta} = \mathbf{r}_{\beta} - \mathbf{r}_{\alpha}$ is the separation vector connecting the centers of particles α and β (Fig. 3.10) (c.f [185, 130]). The elastic half space or Boussinesq Green's functionm that gives the displacement field in the linearly elastic medium at the location of one particle

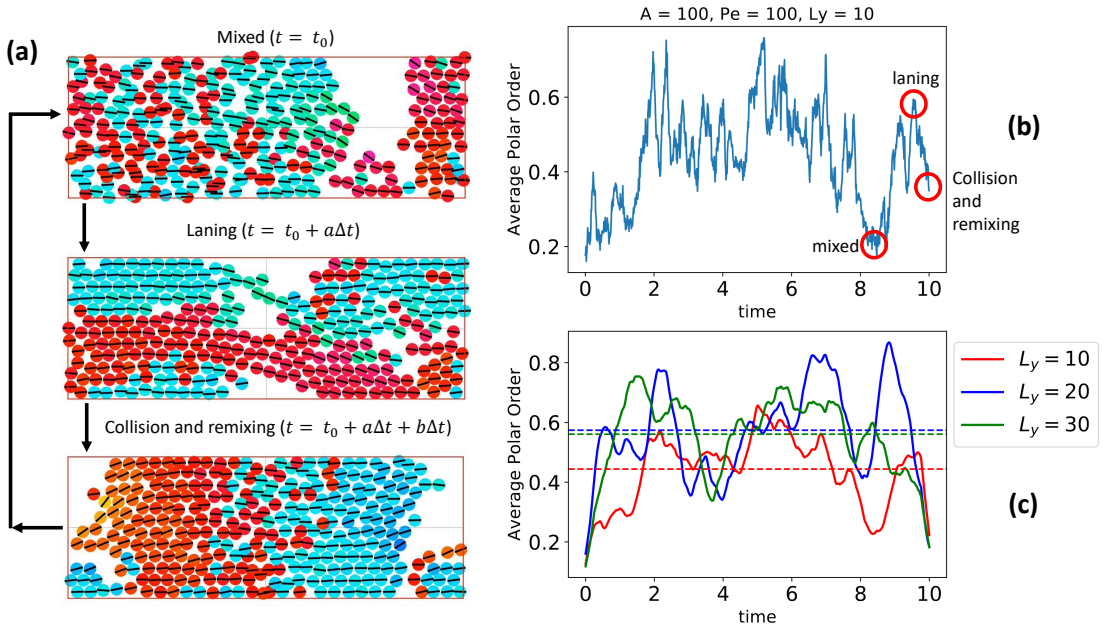

Figure 3.9: Traveling chains in a narrow channel exhibit cycles of mixing, laning, and collision and remixing. (a) Snapshots of a simulation where channel width has been decreased by a factor of 3. Dynamics of the system are encompassed by three cyclic states: A mixed state shown at an arbitrary initial time t_0, a phase separated laning state shown a short time after t_0, and a collision and remixing state shown a short time after the laning state. (b) Polar order averaged over boxes of width 3σ and height 2.5σ versus time is shown to elucidate the three states described in (a). The polar order for a mixed - laning - collision and remixing cycle are shown in the red circles. When the system is well mixed, the average polar order is small ($p \approx 0.2$). When the particles separate into lanes, the polar order increases rapidly ($p \approx 0.6$). When the lanes then collide and begin remixing, the remnants of the bulk of the lanes provide polar order while mixed particles and the interface between lanes decreases polar order ($p \approx 0.4$). (c) Polar order averaged over boxes of width 3σ and height 2.5σ versus time for three channel widths. Time averaged polar order, shown in dashed horizontal lines, is similar for the $L_y = 20$ and $L_y = 30$ cases when collision dynamics occur in the bulk, but non-interacting traveling chains line the boundaries. Time averaged polar order is smaller for the $L_y = 10$ case as collision dynamics are global phenomena.

caused by the application of a point force at the location of the other is given by [191],

$$G_{ik}^{\alpha\beta}(\mathbf{r}_{\alpha\beta}) = \frac{1+\nu}{\pi E}\left[(1-\nu)\frac{\delta_{ik}}{r_{\alpha\beta}} + \nu\frac{r_{\alpha\beta,i}r_{\alpha\beta,k}}{r_{\alpha\beta}^3}\right], \tag{3.3}$$

where E is the stiffness (Young's modulus) and ν is Poisson's ratio of the substrate. Given the linearity of the problem, superposition of strain fields each of which is obtained by using

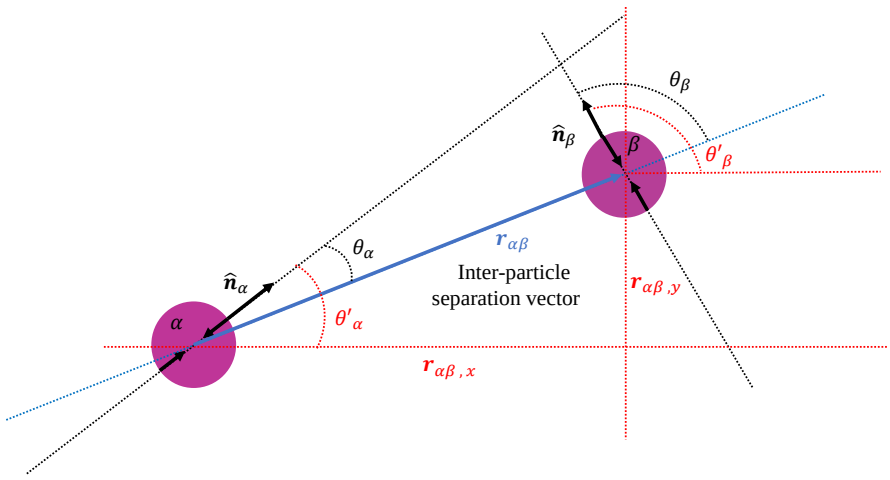

Figure 3.10: Schematic of two interacting particles with all relevant angles and vectors labeled. $\hat{\mathbf{n}}_i$ are unit vectors of force dipoles. θ'_i are angles of force dipoles with respect to the lab frame x-axis. θ_α and θ_β are angles of force dipoles with respect to their separation vector $\mathbf{r}_{\alpha\beta}$ which has components $\mathbf{r}_{\alpha\beta,x}$ and $\mathbf{r}_{\alpha\beta,y}$.

the Green's function (1) appropriately provides the net displacement at a test position due to particles around it.

Two particles in our model interact via a combination of pairwise long-range and short-range interactions. The long range interaction forces originate from the substrate-mediated, elastic dipole-dipole interaction potential, $W^{\alpha\beta}$. The short-range interactions are steric in nature and prevent ABPs from overlapping. This functionality is achieved in the framework of our model by linear springs that only resist compression. Taken together, the total interaction potential between particles α and β can be written as,

$$\begin{aligned} W^{\alpha\beta} &= \frac{1}{2}k(\sigma - r_{\alpha\beta})^2, \quad \text{when} \quad 0 \leq r_{\alpha\beta} < \sigma \\ &= \frac{P^2}{E}\frac{f(\nu,\theta_\alpha,\theta_\beta)}{r^3_{\alpha\beta}}, \quad \text{when} \quad \sigma \leq r_{\alpha\beta} < r_{\text{cut}} \\ &= 0, \quad \text{when} \quad r_{\alpha\beta} \geq r_{\text{cut}}. \end{aligned} \tag{3.4}$$

where k is the spring constant of the linear (repulsive) spring preventing overlap, σ is the particle diameter (kept constant in our simulations), and r_{cut} is a cutoff distance beyond

which the dipolar interactions are neglected. The magnitude of each force dipole is taken to be the same value denoted by P. The dependence of the pairwise dipolar interactions on the orientations of the two dipoles with respect to their separation vectors, and on the Poisson ratio of the medium, ν, is expressed compactly in the expression [130],

$$f(\nu,\theta_\alpha,\theta_\beta) = \frac{\nu(\nu+1)}{2\pi}\Big(3(\cos^2\theta_\alpha+\cos^2\theta_\beta-5\cos^2\theta_\alpha\cos^2\theta_\beta-\tfrac{1}{3})- \\ (2-\nu^{-1})\cos^2(\theta_\alpha-\theta_\beta)-3(\nu^{-1}-4)\cos\theta_\alpha\cos\theta_\beta\cos(\theta_\alpha-\theta_\beta)\Big). \tag{3.5}$$

where $\cos\theta_\alpha = \hat{\boldsymbol{n}}_\alpha\cdot\vec{\boldsymbol{r}}_{\alpha\beta}$ and $\cos\theta_\beta = \hat{\boldsymbol{n}}_\beta\cdot\vec{\boldsymbol{r}}_{\alpha\beta}$ are the orientations of particles, α and β, with respect to their separation vector, respectively (Fig. 3.10).

Motivated by natural and synthetic systems to which our model is applicable, we assume that the particles are in an over-damped viscous environment, and the inertia of the ABPs can be ignored. We can then write the equations of motion governing the translation and rotation, respectively, of particle α as,

$$\frac{d\mathbf{r}_\alpha}{dt} = v_0\hat{\mathbf{n}}_\alpha - \mu_T\sum_\beta\frac{\partial W^{\alpha\beta}}{\partial\mathbf{r}_\alpha} + \sqrt{2D_\mathrm{T}}\ \boldsymbol{\eta}_{\mathrm{T},\alpha}(t) \tag{3.6}$$

and

$$\frac{d\hat{\mathbf{n}}_\alpha}{dt} = -\mu_R\sum_\beta\hat{\mathbf{n}}_\alpha\times\frac{\partial W^{\alpha\beta}}{\partial\hat{\mathbf{n}}_\alpha} + \sqrt{2D_\mathrm{R}}\ \boldsymbol{\eta}_{\mathrm{R},\alpha}(t), \tag{3.7}$$

where $\mathbf{r}_\alpha$ and $\hat{\mathbf{n}}_\alpha$ are the position and orientation of particle α, respectively. In the equations above D_T and D_R are the translational and rotational diffusivity quantifying the random motion of a single particle, respectively. The viscous environment results in the translational and rotational mobilities, μ_T and μ_R respectively. Random white noise terms $\boldsymbol{\eta}_\mathbf{T}$ and $\boldsymbol{\eta}_\mathbf{R}$ have components that satisfy $\langle\eta_{i,\mathrm{T}}(t)\eta_{j,\mathrm{T}}(t')\rangle = \delta(t-t')\delta_{ij}$ and $\langle\eta_{i,\mathrm{R}}(t)\eta_{j,\mathrm{R}}(t')\rangle = \delta(t-t')\delta_{ij}$. Since the fluctuation dissipation theorem is not necessarily satisfied for a nonequilibrium system, the translational and rotational diffusivity are independent of each other. However, to reduce the number of free parameters and in the interest of simplicity, we assume that $D_\mathrm{T} = \sigma^2 D_\mathrm{R}$ and $\mu_\mathrm{T} = \sigma^2\mu_\mathrm{R}$. This allows the definition of an effective temperature, $k_B T_\mathrm{eff} = D_\mathrm{T}/\mu_T$. Finally we emphasize that each particle is endowed with the same dipole strength, P, and self-propulsion velocity, v_0, both of which are constant.

We now choose the cell diameter σ, the diffusion time, σ^2/D_T, and the effective thermal energy that quantifies the strength of stochastic fluctuations, D_T/μ_T, as physically relevant length, time, and energy scales in our model. Solutions to the scaled dynamical

model are then dependent on three non-dimensional numbers,

$$Pe = \frac{v_0\sigma}{D_{\mathrm{T}}},\ A = \frac{\mu_T P^2}{E\sigma^3 D_{\mathrm{T}}},\ k^* = \frac{\mu_{\mathrm{T}} k\sigma^2}{D_{\mathrm{T}}} \tag{3.8}$$

where Pe is the Péclet number that is a measure of the self-propulsion in terms of the diffusion of motile particles, A is an effective elastic dipole-dipole interaction parameter, and k^* is the nondimensional steric spring constant.

Nondimensional forms of the dynamical equations Eq. 3.6-3.7 are discretized and numerically solved using the explicit half-order Euler-Maruyama method [204]. We use a time step of $\Delta t = 10^{-4}$ for a total of $10^5 - 10^6$ timesteps corresponding to a total simulation time of $10 - 100$. Each particle was initialized with a random position and orientation in our simulation box of size $L_x = 30\sigma$ and $10\sigma \leq L_y \leq 30\sigma$ with periodic boundary conditions in x and confinement modeled by repulsive springs identical to those used for particle-particle steric repulsions, with a fixed spring constant, $k^* = 10^4$, placed along the top and bottom walls. In our simulations, we want particles near each other to interact via the elastic potential at every time step, and to ensure that the overlap of particles is minimized. Furthermore, to ensure that the particles are not subject to unphysical repulsive forces, we choose k^* such that $k^*\Delta t = 1$. We show in the Supplementary Figure that the higher order structures formed by the particles at different k^* are qualitatively similar when the timestep is appropriately rescaled. A and Pe are varied and analyzed in the Results section of the text.

3.5 Discussion

We have shown the typical collective behavior that emerges when active particles interact with each other as dipoles, using Brownian dynamics simulations. This minimal model is inspired by collective cell motility on elastic substrates where the cell-cell interaction is mediated by their mutual deformations of the passive substrate. While some of the emergent collective structures have analogs in cell culture experiments, such as the network organization of endothelial cells [153], our model is not intended to capture any specific biological behavior. We expect the first tests of our model to happen in dilute cell culture experiments that measure both pairwise cell interactions and substrate traction forces as in Ref. [169, 170].

The passive dipolar interactions lead to the end-to-end alignment of the particles

into motile chains, which can be mutually aligned into polar bands and clusters because of their active motion. Polar chains that travel in opposite directions would be sorted into bands that get out of each others' way. These basic implications of our model, while specifically demonstrated here for elastic dipoles, belong to a broader class of active particles with dipolar interactions [177, 178, 205], and may therefore also be experimentally realized in active colloids endowed with permanent or induced dipole moments [176, 206]. We note that the symmetry of the elastic dipolar interactions is modified at higher Poisson's ratio [130], which is expected to result in structures such as active rings with rotational motion. This richer behavior with elastic interactions is a direct consequence of the tensorial, as opposed to vectorial nature of the elastic dipoles, in contrast with magnetic or electric dipoles, and will be the subject of future study.

We further note that the mechanical interactions between cells in elastic media is in reality expected to include effects not considered here including from the nonlinear elastic properties of the substrate and nonlinear effects arising from the cells actively maintaining mechanical homeostasis at their boundaries, such as by regulating their shape [137]. We also ignore the elastic response of the cells themselves, which can give rise to additional interactions similar to that between rigid inclusions in soft media [207].

We focused on the strong elastic interaction cases in the dilute regime, where the self-assembly and dynamics of single chains can be studied. Since the chains are stable in this regime, they resemble other active polymer systems [201], that typically arise in gliding assays of biological filaments [208] or with synthetic colloids [172]. Polar bands are also seen at a higher density of active polymers [203]. However, in our system where these chains are self-assembled by dipolar interactions, multiple chains can stick to each other at higher interaction strength, while they can also fall apart, when colliding at high motility. By showing how a pair of chains interact with each other, we show the stable higher order structures that form and contribute to the polar clusters seen at higher density. Although not investigated in detail here, it will also be interesting to explore the bending dynamics of a single active polymer [209, 210] and characterize how the bending rigidity increases with dipolar interaction strength or decreases with particle motility.

To conclude, we note that our cell mechanobiology-inspired model also realizes a new class of active matter with long-range dipolar interactions. The emergent self-organization behavior distinct from the two typically studied pathways to the clustering of active particles: motility-induced phase separation [164], and Vicsek-style models [211].

In the latter, particle alignment is imposed in an agent-based manner, whereas here alignment emerges as a natural consequence of physical interactions.

Chapter 4

Elastic interactions compete with persistent cell motility to drive durotaxis

This chapter is reproduced from our published article in *Biophysical Journal*.

4.1 Introduction

Animal cells migrate by crawling on elastic substrates during many crucial biological processes such as wound healing, tumor progression and tissue development [29]. Cell migration is responsive to physical cues of their extracellular environment, such as extent and degree of confinement and stiffness of the ambient material or the substrate [212]. Migrating cells consume energy in the form of ATP to generate directed motion interspersed with stochastic reorientations. Cell trajectories may thus be represented by active particle models [187], where "active" implies autonomous energy-consuming units that generate their own motion. Collections of such active particles constitute out-of-equilibrium complex systems and exhibit unusual statistical properties such as motility-induced phase separation and accumulation at confining boundaries [213, 164]. The extracellular matrix of migrating cells are typically heterogeneous in stiffness and geometry, which implies that cell migration is influenced by mechanical boundaries. Motile cells may therefore be considered as living active matter that interact with their complex environments [158].

At the cellular scale, the actomyosin cytoskeletal machinery leads to coordinated, directed migration, which manifests as persistent motion interspersed with speed and orientation fluctuations on uniform two-dimensional substrates. The complex polarity processes and protrusion formation can be effectively captured by the self-propulsion speed with a characteristic persistent time scale, and the translational noise in phenomenological models for cell motility [214]. As cells migrate, they exert traction forces on the underlying substrate. These forces are generated within the cell by its actomyosin cytoskeletal machinery and are communicated to the extracellular substrate through localized focal adhesions [49]. These traction forces can be significant and generate measurable deformation in the elastic extracellular substrate [50, 51].

By actively deforming the substrate, cells sense geometric and mechanical cues in their micro-environment, including material properties such as the substrate stiffness [215] and viscoelasticity [216]. This gives rise to the possibility of long range cell-cell mechanical communication mediated by mutual deformations of the elastic substrate [194], for which there is mounting experimental evidence. For example, endothelial cells modulate their pairwise inter-cellular contact frequency according to substrate stiffness [5], while forming multicellular networks on substrates of appropriate stiffness [217, 153]. Recent theoretical works show that both these trends can be quantitatively understood through substrate-mediated cell-cell mechanical interactions [189, 218].

The cells may use these mechanical cues, in addition to chemical signaling that is ubiquitous in biology, to direct their persistent migration [160, 219].

The observed preferential migration of cells along gradients in substrate stiffness, usually towards stiffer regions, has been termed "durotaxis" [3, 220, 221]. Durotaxis has been observed both in single cells in culture [222, 223, 224, 4], as well as in collections of confluent migrating cells [225], including *in vivo* [226]. Small cell clusters have also been observed to exhibit negative durotaxis and migrate towards softer substrate regions [227]. Durotaxis is influenced by matrix composition, as observed in the case of vascular smooth muscle cells on fibronectin substrates but not on cells on laminin-coated substrates [228]. Suggested biophysical mechanisms for durotaxis include enhanced persistent cell motility due to enhanced cell polarization on stiffer substrates [229], larger local deformation of the softer substrate when the cell or collective is spread across a gradient resulting in overall translation of the center of mass towards the stiffer side [225, 227], and more stable focal adhesions on the stiffer side. While the higher persistence of cell motion on stiffer substrates

may be rationalized based on the strongly polarized cell shapes in stiffer environments [230, 231], this does not address the important roles of cell traction forces exerted on the substrate, and of cell-substrate adhesion, in driving durotaxis. Recent work using molecular clutch models at the level of single cells or confluent tissue have explained durotaxis as arising from stiffness-dependent cell-substrate adhesive interaction [225, 227, 232, 91]. However, these mechanistic models do not lend easily to the evaluation of the statistical distributions of numerous cell trajectories at long times.

Experimental measurements of time-averaged traction forces mapped to cell shapes [134] suggest that stresses can be effectively resolved into a contractile force dipole acting along a preferred axis [233]. Thus, traction force patterns exerted by a cell on underlying elastic substrates may be modeled as a force dipole. This force distribution also satisfies internal force balance [215] as required. Such a minimal theoretical description of traction forces exerted by an adherent cell leads to a natural organization principle for cells in compliant media [130]. By orienting along directions of maximal stretch, as well as moving towards stretched regions of the substrate, a contractile cellular force dipole can lower the elastic deformation energy of the substrate. This naturally leads to configuration-dependent torques and forces that may drive directed motion or durotaxis of the cellular force dipole near an elastic interface between a softer and stiffer region [6]. While this static theoretical model predicts the alignment and attraction of the cell towards the stiffer region, it does not address how a self-propelling cell with intrinsically noisy dynamics moves to this favored configuration.

A complete description of durotaxis thus requires combining the elastic model for cell traction-induced matrix deformations by adherent cells, with an appropriate model for stochastic cell movement [170, 189, 234]. We consider here persistently motile cells that move in a directed manner for a characteristic time before reorienting. Since migrating cells generate protrusions that may be randomly driven by noisy internal signalling [235], the motion of our model cells feature stochastic reorientations and velocity fluctuations [214]. Cells are assumed to move persistently and exert traction along their long axis, such that the the polarization coincides with their principal traction axis [236, 237]. We here propose and study a general, phenomenological model that incorporates these key elements to provide a statistical physics description of durotaxis.

Figs. 4.1(a) and (b), reproduced from Ref. [3], illustrate the scenario we wish to analyze theoretically. The authors here examined the behavior of a fibroblast cell cultured

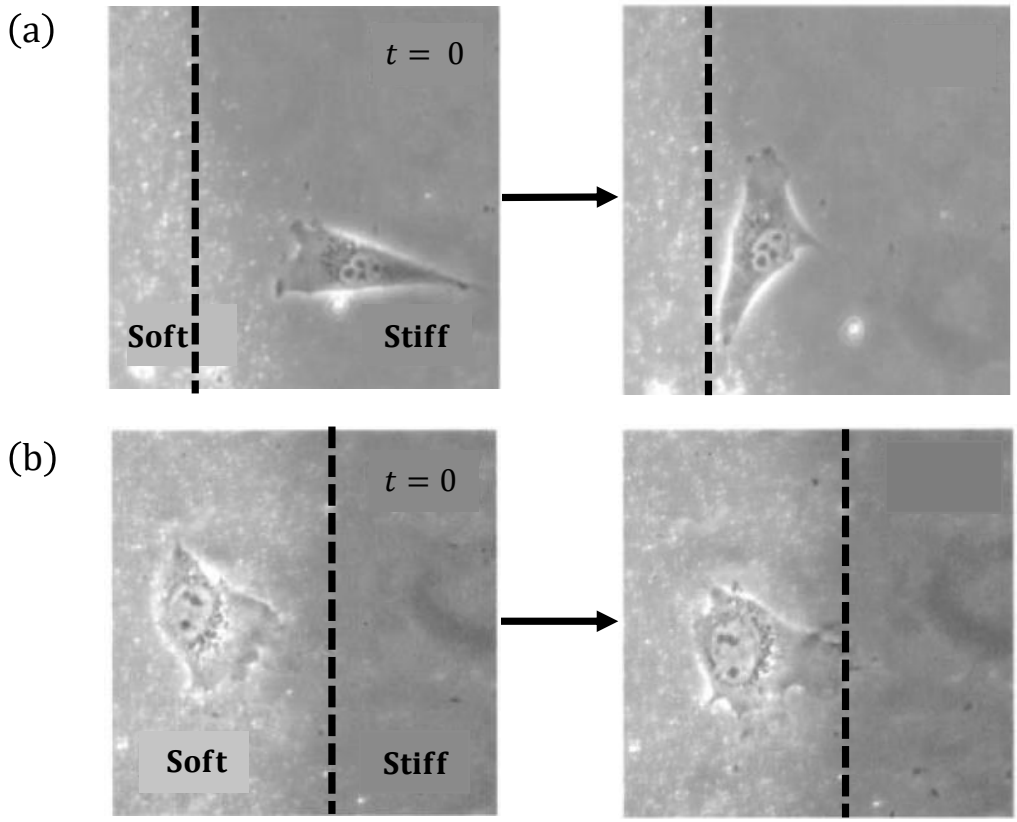

Figure 4.1: **Experimental motivation and model setup.** (a, b) Isolated fibroblasts near interfaces between soft and stiffer regions of a polyacrylamide gel substrate (reproduced with permission from Ref. [3]). (a) A cell approaching the interface from the stiffer side (left) aligns parallel to the interface and remains in the stiffer region. (b) A cell on the softer side aligns normal to the interface and eventually crosses over to the stiffer side.

on a deformable polyacrylamyde hydrogel substrate, and located near an interface separating a soft region from a stiffer region. When the cell is on the stiff side, it aligns parallel to the interface and remains on the stiffer side. On the other hand, when the cell starts off on the soft side, it aligns perpendicular to the interface and eventually moves and crosses over to the stiffer side (not shown). This behavior may be understood by considering the polarized cell as a force dipole acting along its axis of elongation [6]. When on the stiffer side (Fig. 4.1(a)), the cell deforms the interface and the softer elastic medium on the other side of the interface can easily displace, resulting in an effectively stress-free boundary condition. Conversely, when the cell is on the soft side (Fig. 4.1 (b)), the rigid medium on

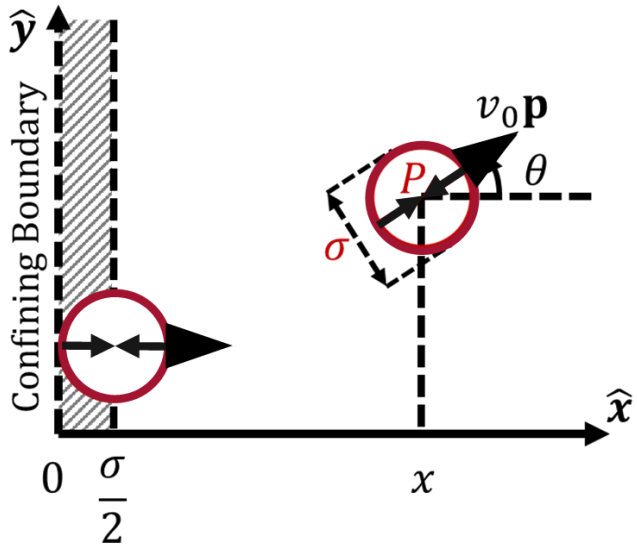

Figure 4.2: **Model setup.** Schematic of a cell moving on a flat linear elastic substrate with uniform stiffness (given by Young's modulus E, and Poisson's ratio ν) near a confining boundary. Clamped or free elastic boundary conditions are employed to distinguish between the cell being on the softer or stiffer region of the substrate, respectively. Unlike the experiment, the simulated cell is not allowed to cross the boundary. Traction forces generated by the cell are reduced to a contractile force dipole of strength $\mathbf{P}$ (red, inward pointing arrows) acting on the substrate. Cells are modeled as circular discs (shown here as red circles) of diameter σ. The direction of propulsion $\mathbf{p}$ is assumed to be along the cell dipole axis and makes an angle θ with the horizontal axis. The cell lies a horizontal distance x from the boundary (the y axis). An excluded region of extent $\sigma/2$ (a lower limit) at the boundary models confinement.

the other side undergoes minimal displacement at the interface, resulting in an effectively clamped boundary. In fact, it was shown in Ref. [6] that when the interface acts as a clamped (free) boundary, the effective elastic interaction potential between a cell dipole and the interface computed by a full consideration of the virtual image stress distribution required to satisfy the relevant boundary condition, yields an attractive (repulsive) force on the dipole. Additionally, elastic interactions also result in a torque that orients the dipole perpendicular (parallel) to the interface. This model based on cell response to substrate strain is inherently long-ranged. It thus allows a cell to detect a sharp interface in substrate stiffness from afar, without requiring it to sense both soft and stiff regions at the same time. These local interactions may predominate when the cell is on a substrate with a continuous stiffness gradient [221], or close to a step-like interface in stiffness, but are not included in

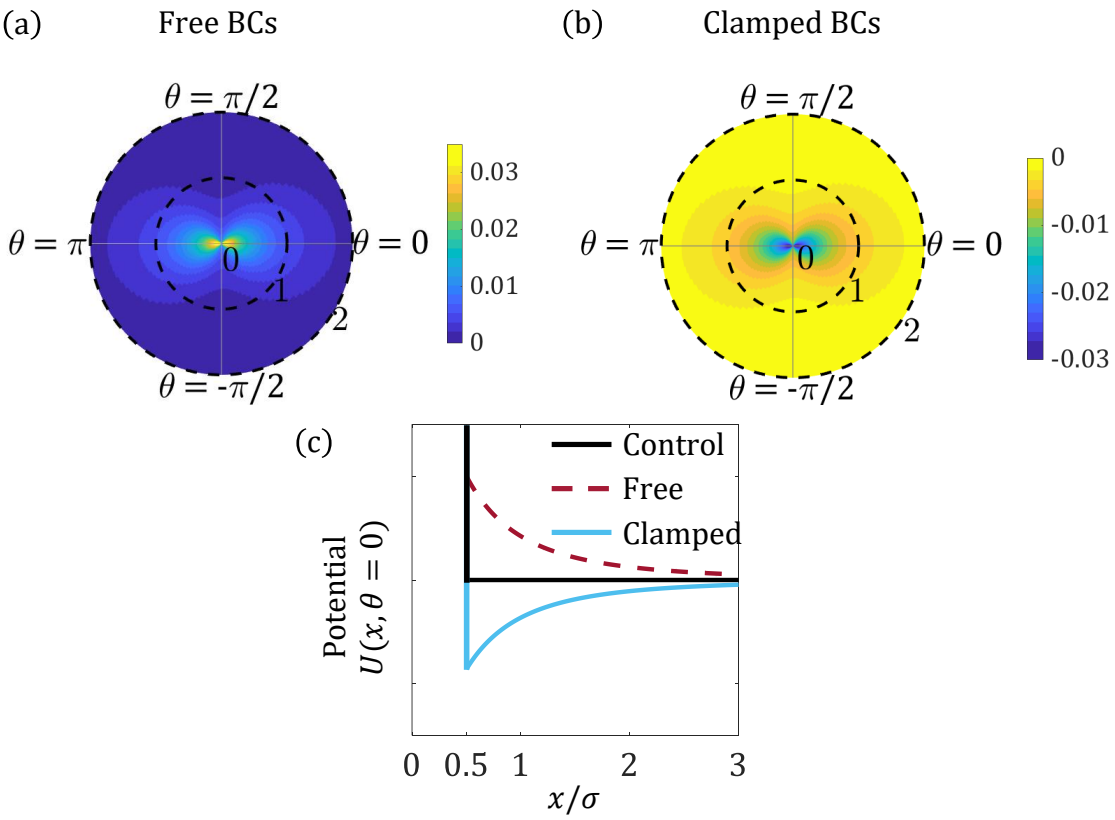

Figure 4.3: **Experimental motivation and model setup.** (a,b) The spatial map of the elastic interaction potential experienced by the cell as a function of distance from the boundary and the orientation is shown for free and clamped boundaries, respectively. (c) The potential is plotted as a function of distance for the control case representing pure confinement without elastic interactions (solid black), the repulsive free boundary (dashed, brown) and the attractive clamped boundary (solid, cyan).

the present work.

While this static model for an adherent cell provides a heuristic explanation for single-cell durotaxis [6], we consider here the role of cell motility, in the presence of such an elastic boundary interaction arising from cell traction. Unlike the original durotactic experiment [3], we also choose to confine the model cell to either the softer or stiffer region. This mimics complex or micro-patterned environments and allows us to study the interplay of motility,confinement and elastic interactions. The model setup of a cell moving on an elastic substrate near a confining boundary is illustrated in Fig. 4.2. The substrate

deformation-mediated elastic interaction potential experienced by a stationary cell is depicted in Figs. 4.3. The elastic potential as a function of the cell orientation is shown for free and clamped boundaries in Figs. 4.3(a) and (b), respectively. These highlight the repulsive and attractive nature of the interactions, as well as the favored parallel and perpendicular orientations. Fig. 4.3(c) shows the long-range spatial decay of the potential away from the interface in the clamped, free and "control" regions, the latter corresponding to only steric interactions with the confining boundary. Using this model setup, described in more detail in the next section, we seek to predict how statistical distributions of cells depend on the persistent and stochastic aspects of motility, as well as the strength and nature of the elastic interactions with the boundary.

4.2 Model for cell motility and elastic cell-boundary interactions

The motion of each cell is modeled using Langevin dynamics in the overdamped limit since inertial effects are negligible at the microscale. Each cell is treated as a disk of diameter of diameter σ moving on a 2D xy-plane corresponding to the surface of an idealized, infinitely thick elastic substrate. The state of each cell is defined by its position vector $\mathbf{r}$ corresponding to the cell center, and unit orientation vector $\mathbf{p}$ associated with its self-propulsion direction (Fig. 1(c)). Cells move with speed v_0 in the direction $\mathbf{p}$ (with Cartesian components $(\cos\theta, \sin\theta)$), and interact with boundaries through a potential $U(x, \theta)$ that depends on the normal distance from the boundary x (see Fig. 4.3 -(c)), and on the angle θ [6]. The equations that govern the dynamics of a cell modeled as an active Brownian particle in an elastic potential are,

$$\frac{\partial \mathbf{r}}{\partial t} = v_0 \mathbf{p} - \mu_T \nabla U + \sqrt{2D_T}\boldsymbol{\eta}_{\mathrm{T}}(t), \tag{4.1}$$

$$\frac{\partial \theta}{\partial t} = -\mu_R \frac{\partial U}{\partial \theta} + \sqrt{2D_R}\eta_{\mathrm{R}}(t), \tag{4.2}$$

where D_R and D_T are diffusion coefficients associated with orientational and translational fluctuations of the cell's principal axis and center of mass, respectively, while μ_R and μ_T represent the corresponding rotational and translational mobility.

For passive bodies in an ambient viscous medium, mobility coefficients depend on the medium's viscosity and thermodynamic temperature, and are coupled via the body's geometry, through the Stokes-Einstein relationship [238, 239]. Living cells, however, being

active and not at equilibrium, do not have to adhere to this constraint. Their self-propulsion velocity can be resolved into a persistent as well as a stochastic part, the latter arising from random protrusions created by cytoskeletal processes. Thus, in principle, the cell is free to set effective translational and rotational diffusivities, D_T and D_R, independently. For migratory cells, mobility coefficients arise from dissipative frictional mechanisms at the cell-substrate interface. The friction can contribute additional terms due to memory and inertial effects in the cell dynamics [240], while the statistics of the cell trajectory may deviate from a persistent random walk [241] in 3D [242], effects which we ignore here for simplicity. We include the effects of stochastic noise via the last terms on the right hand side of Eqs. (4.1) and (4.2), $\boldsymbol{\eta}_{\mathrm{T}}(t)$ and $\eta_{\mathrm{R}}(t)$ respectively, and correspond to white noise.

The boundary interaction potential includes contributions from cell-boundary interactions mediated by the underlying elastic substrate, and an additional short-range steric interaction term that prevents cells from penetrating the boundaries. Exact implementations of this steric interaction are discussed in Supp Note 1. The elastic potential arising from the interaction of the cell force dipole with the substrate deformation (strain) it generates in the vicinity of the free or clamped boundary is of the form [130],

$$U(x,\theta) = -\left(\frac{P^2}{256\pi E}\right)\frac{f_\nu(\theta)}{x^3}, \tag{4.3}$$

where P is the strength of the cellular force dipole that is aligned with the cell major axis, parallel to the direction of motility $\mathbf{p}$, and $f_\nu(\theta) = (a_\nu + b_\nu \cos^2\theta + c_\nu \cos^4\theta)$ encodes the angular dependence of the potential U that is separable in x and θ coordinates. Substrate elastic properties affect the potential U through its dependence on the Young's modulus E, and the Poisson's ratio ν. Specifically, the angular factor $f_\nu(\theta)$ depends on the substrate Poisson ratio via constants a_ν, b_ν and c_ν (see Supp. Note 1). Importantly, the constants vary depending on the type of boundary condition - i.e., whether the boundary is free or clamped. Exact forms of these from Ref. [130] are provided in Supp. Note 1. Subsequently, we use a scaled form of the angular factor defined as $\tilde{f}_\nu(\theta) \equiv \frac{50}{256\pi} f_\nu(\theta)$, such that $\tilde{f}_\nu(\theta) \sim 1$.

The spatial dependence of the potential may be rationalized as follows. The force dipole exerted by the cell interacts with local deformation arising due to the presence of the boundary. This strain field is generated by the associated "image" dipole configuration required to satisfy the free or clamped condition on the boundary [243]. The strain created by a dipole in an elastic half-space decays with distance as $1/x^3$, while it is linear in the magnitude of the dipole moment, P. The dipole-dipole interaction potential therefore scales

as P^2/x^3. In writing down equations Eqs. (4.1), (4.2) and (4.3), we made a simplifying assumption, valid for highly polarized cells such as fibroblasts, by identifying the dipole axis with the direction of motion [229, 189]. The coarse-grained model of cell traction force distribution as a force dipole is a far-field approximation, valid when the cell-boundary distance is greater than the cell diameter.

Our model features four dimensionless parameters controlling cell trajectories:

$$Pe \equiv \frac{v_0}{D_R\sigma},\ A \equiv \frac{1}{50}\left(\frac{\mu_T P^2}{E D_R \sigma^5}\right),\ B \equiv \frac{1}{50}\left(\frac{\mu_R P^2}{E D_R \sigma^3}\right),\ D \equiv \frac{D_T}{D_R\sigma^2}. \tag{4.4}$$

The Péclet number Pe quantifies the relative importance of directed self-propulsion and random motion, and is a measure of persistent motion of the particles in the absence of boundary potential U. Parameter A quantifies the strength of the force, while B quantifies the strength of re-orienting torque, both acting on the cell due to cell-boundary elastic interactions. Both parameters depend on the elastic properties of the substrate but are notably independent of active self-propulsion. The factor of 50 in the definition of A and B results from the angular average $\langle f_\nu(\theta)\rangle \equiv (1/2\pi)\int_0^{2\pi} f_\nu(\theta)d\theta = 1/50$. In this work, we set the substrate Poisson's ratio to a representative value of $\nu = 0.3$ [3, 244].

In general, A and B can differ in value depending on the specific mode of cell migration. The ratio A/B is equivalent to $(\mu_T/\mu_R\sigma^2)$. For a passive spherical particle at equilibrium in a viscous medium, the ratio $A/B = 1/3$. For elongated rod-like objects, the ratio depends on the aspect ratio and tends to $1/9$ in the limit of infinitesimally thin rods [245, 246, 247]. The case of cells on an elastic substrate is more complex. The values of A and B can strongly depend on the internal mechanisms driving cell motility, an example being internal changes in cell biochemistry that determine the direction of protrusions in the cells.

To estimate A in cell culture experiments, we use the typical value for the traction force of a contractile cell adhered to an elastic substrate $F \sim 10 - 100$ nN, with a distance of $\sigma \sim 10 - 50$ μm separating the adhesion sites. This results in a force dipole moment for a single cell, $P = F\cdot\sigma \sim 10^{-12} - 10^{-11}$ J [130]. Using typical values of substrate stiffness in durotaxis experiments, $E \sim 10$ kPa [4], rotational diffusion, $D_R \sim 10^{-2}$ min^{-1} [231], cell size $\sigma \sim 20$ μm, and previously estimated translational mobility [218], $\mu_T \sim 0.1\,\mu\text{m/min}\cdot\text{pN}^{-1}$, we estimate $A \sim 1$. By changing substrate stiffness and allowing for variation in cell types, we estimate a typical range of $A \sim 0.1 - 10$, where A can be small on very stiff substrates. Further using $\mu_R \sim 10^{-4}$ $\mu\text{m}^{-1}\text{min}^{-1}\text{pN}^{-1}$, we estimate $B \sim 1$. We again estimate a typical

range of $B \sim 0.1-10$ by changing the substrate stiffness, where B is small on high substrate stiffness.

We estimate $Pe \sim 0-10$ based on typical cell migration velocities [231], $v_0 \sim 0-100$ μm/hr. We choose to keep the parameter $D = (D_T/D_R\sigma^2)$ fixed at 0 or 1 in our simulations. The former simplifying choice corresponds to the regime of highly persistent cell migration characterized by high Pe values, where the effective translational diffusion results from cell reorientations, and is given by v_0^2/D_R. We also fix the size of the simulation box to $L = 40\sigma$.

4.3 Results

4.3.1 Elastic interactions determine steady state distributions near free and clamped elastic boundaries

Cells migrating through their complex extracellular matrix sense and respond to physical cues [212]. They are expected to respond to both gradients in substrate stiffness and confining boundaries. Theoretical models describing the statistical behavior of active particles under confinement have been studied extensively in earlier works. These works compute the density, surface density, polarization, and orientation distributions of active particles between two parallel confining boundaries or at straight or curved boundaries [196, 198, 197, 248, 249]. These studies show that statistical steady state distributions depend strongly on particle activity, the shape of the particles, and the curvature of the boundaries. Passive particles moving in a constant temperature, non-deforming medium without persistent self-propulsion ($Pe = 0$), are expected to reach thermodynamic equilibrium and have uniform distribution between the boundaries that maximizes entropy. In contrast, as $Pe \to \infty$, particles populate the boundaries at all times with the probability of finding particles at the boundary tending to unity resulting in a diverging surface density. The surface density also depends on the curvature of the surface [250].

Cell-boundary interactions mediated by an ambient material medium have also been investigated in detail for a related class of microswimmer problems, including the interaction of low Reynolds number microswimmers such as bacteria, algae and sperm with boundaries [251, 252, 253, 254, 255, 256, 257, 258, 259, 260, 261]. Unlike the animal cells studied here that act as contractile dipoles, free swimming organisms can act as pushers (bacteria, and sperm) or pullers (algal cells). Far from interfaces, pushers generate extensile

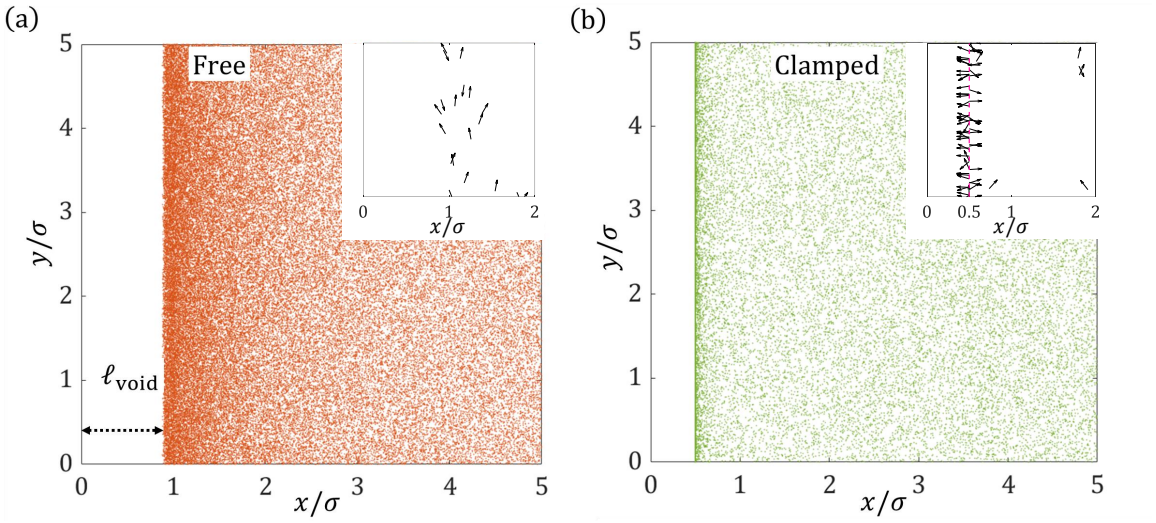

Figure 4.4: **Spatial distribution profiles of single motile cell near free and clamped elastic boundaries.** Spatial distribution map of model cells for (a) free ($A = B = 16$, $Pe = 8$), and (b) clamped boundaries ($A = B = 8$, $Pe = 8$), where the data points represent the occurrence of cells at corresponding positions, sampled at regular intervals from multiple simulation trajectories. Insets show a magnified view close to the boundary, at $x_b = \sigma/2$, with arrows indicating the orientation of the self-propulsion of the cell at each sampled position in its trajectory. In (a), the repulsive potential from the free boundary results in a void region of extent ℓ_{void}, which cells are unable to access. Cells close to the boundary are oriented parallel to it due to elastic torques (see inset). In (b), the attractive potential from the clamped boundary causes accumulation of cells while the elastic torque orients the cells perpendicular to the boundary (inset in (b)). In the inset in (b), the pink dashed line shows the center of all the cells at $x = 0.5\sigma$.

force dipoles on the ambient fluid, while pullers exert contractile force dipoles. Additional stresses on the fluid are generated in pushers due to "rotlet" dipoles arising from counter-rotation of the cell body and the flagellar bundle. The presence of interfaces near swimming cells results in wall induced forces and torques on these swimmers; these effects arise due to the requirement that the overall fluid fields generated by the moving cells, and mediated by the interface(s), satisfy appropriate boundary conditions – that is no-slip for solid walls, or stress-free for free surfaces. Experimental studies on swimmers near surfactant-free, solid, no-slip surfaces indicate that, irrespective of the type of dipolar swimmer, microorganisms tend to accumulate near the interface albeit with varying orientations. Pushers tend to align parallel to no-slip solid interfaces due to hydrodynamic torques, and swim along the surface

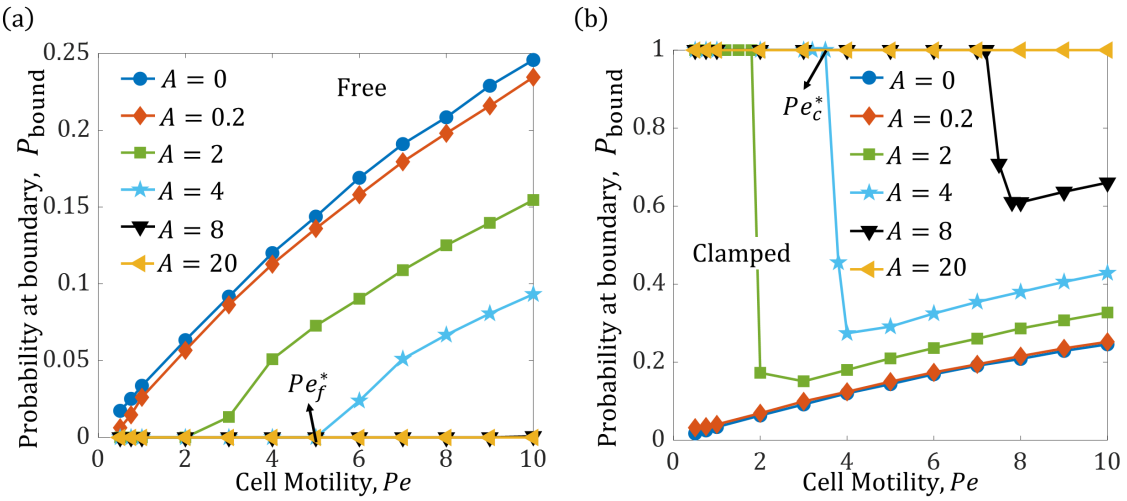

Figure 4.5: **Probability of finding motile cell dipoles near free and clamped elastic boundaries.** (a,b) We quantify the localization of particles at the free (a) and clamped (b) boundaries as a function of Pe for various values of $A(= B)$. (a) For the free boundary, the localization at the boundary decreases with A. The value of P_{bound} increases with Pe due to motility induced accumulation at the boundary. At very high A, the particles cannot get close to the boundary leading to $P_{\text{bound}} = 0$. Pe_f^* corresponds to the critical value of Pe at which the cell's motility can overcome the repulsive boundary force and reach the boundary at any specific value of A. Pe_f^* increases with A (only shown for $A = 4$). (b) The localization at a clamped boundary increased with A. At low A, the boundary probability P_{bound} increases with Pe, since faster cells reach the boundaries easily. At higher values of A, cells stay at the boundary until reorientation events occurs. The high speed (high Pe) leads to rapid escape, resulting in a sharp drop in P_{bound}. There is further increase in P_{bound} due to persistence-driven accumulation. At very high A the particles don't leave the boundary leading to $P_{\text{bound}} = 1$. Here, Pe_c^* corresponds to the critical value of Pe at which the cell's motility can overcome the attractive boundary force at any specific value of A. We note that Pe_c^* increases with A, the trend being shown here at $A = 4$).

exhibiting long residence times [251, 259]. Analyzing the competition between cell-wall hydrodynamic attraction and rotational diffusion, Drescher *et al.* estimated characteristic cell-wall interaction time scales and deduced that hydrodynamic wall-induced attraction dominates provided the distance from the wall $x < P(a/v_0 D_R)$ where σ is the cell (body) size, P is the hydrodynamic dipole strength, and v_0 is the self propulsion speed. Contractile pullers meanwhile have been observed to align perpendicular to the interface and remain trapped until they can reorient and escape due to thermal noise or rotational diffusion

arising from variations in the swimming mechanism [251, 262]. Interestingly, pushers are theorized to be attracted to surfactant-free (clean) interfaces with the Stokes dipole oriented and aligned parallel to the interface, for both free surfaces as well as for solid walls [259, 257].

In this work, we investigate the effects of cell-interface elastic and steric interactions on the boundary and bulk distributions of active particles representing motile cells on elastic substrates. Motivated by the process of single cell durotaxis across sharp gradients of substrate stiffness as shown in Figs. 4.1a , we study the effect of elastic forces and torques on the density and orientational distributions of motile cells at the confining boundary. We carry out simulations of cell trajectories using the model Eqs. 4.1-4.2 for a range of values of self-propulsion, $Pe = 0.5 - 10$, and elastic interaction strength, $A(= B) = 0$ to 20, that were estimated in the model section for cell culture experiments. From these simulations, we compute the probability of finding a particle at the boundary using $P_{\text{bound}} = N_{\text{bound}}/N_{\text{total}}$, where N_{bound} is the number of occurrences of the particle at the boundary – that is, its center is located at $x = x_b \equiv \sigma/2$ *after* the instantaneous displacement/reassignment step (Appendix C). N_{total} meanwhile is the total number of times the particle is observed.

To aid in the analysis and interpretation of results, we set $D = 0$, that is we switch off translational diffusivity $D_T = 0$, in our simulations. In the short time limit relative to the persistence time D_R^{-1}, this allows cells to localize and stay at the boundary except when the directed self-propulsion drives them away. Over longer times however, an effective diffusivity that is v_0^2/D_R arises due to the combination of self-propulsion and re-orientations represented by rotational diffusion.

As a point of departure, we first describe the results in the absence of elastic interactions with the boundary, $A = B = 0$. Geometric confinement prevents cells from leaving the system in the direction normal to the boundaries. Consistent with previous studies on non-interacting Active Brownian Particles (ABPs) [196], we observe localization of cells at the boundaries, with the associated number densities at the boundaries (N_{bound}) increasing with the Péclet number (Pe). To rationalize this, we note that increasing Pe is equivalent to faster cell migration speed and more persistent motion (Fig. 4.5). Cells are able to translate over longer distances due to decreased effects of diffusion. Once the cells reach the boundaries however, they tend to remain there since they are oriented towards the wall, until reorientation is caused by rotational diffusion over the characteristic timescale $\sim D_R^{-1}$. Upon reorientation, the cell's orientation given by the polarization vector's angle is pointed away from the boundary, $\theta < \pi/2$. If the cell's self-propulsive force is strong

enough to overcome the elastic attractive force, the cell escapes from boundary trapping and moves back into the bulk. Increasing cell Pe decreases the time spent between the confining boundaries which in turn increases their probability to be at the boundary.

Such localization at the boundary, while well-known for microswimmers (as previously described), and also for synthetic active particles, is yet to be demonstrated for crawling animal cells. We propose that this effect may be detected by tracking spatial probability of cells in a dilute cell culture experiment where confinement is created by micro-patterning the underlying elastic substrate into two discrete regions, only one of which favors adhesion. The interface between these two regions will act as a confining boundary that restricts cell migration into the unfavorable region where cells cannot adhere. Henceforth in this work, we term this increased localization of cells at the confining boundary by purely kinetic means, motility-induced accumulation (MIA).

The probability of a cell being at the boundary is strongly modulated by the nature of elastic interactions in our model. Specifically, the sign of elastic interaction depends on the type of boundary condition, clamped (i.e. "no displacement") or free (i.e., "no stress"). For stress-free boundary conditions representing an interface with a softer substrate, increasing repulsive forces act on the cells as they approach the boundary. Therefore in this case, cells are unable to reach the boundary and remain a distance away from it, see Fig. 4.4(a). Furthermore, the torque from the elastic interaction induces cells close to the boundary to align parallel to it, see inset to Fig. 4.4. Increasing the interaction parameter A (here we set $B = A$) increases the length of the region over which the repulsive force acts and reduces the probability of a cell being at the boundary. For $A > 0$ and low Pe, there is no localization at the boundary, Fig. 4.5(a). Quantifying this localization by a probability density of observing particles at the boundary we find from our simulations that for each value of A, there exists a critical Péclet number Pe_{f}^{*} at which the localization probability, P_{bound} at the boundary becomes non-zero. For $A > 0$, increasing the Péclet number to values larger than Pe_{f}^{*}, increases the probability of the cells to localize at the boundary. When $Pe < Pe_{\mathrm{f}}^{*}$, cells cannot reach the boundary resulting in a void region evident in Fig. 4.5 (a). We find that Pe_{f}^{*} increases with the interaction parameter A. This increase is expected to be linear from force balance.

The situation is quite different for cells interacting with clamped boundaries. In this case, cell-boundary elastic interactions are attractive and increasing A localizes more cells at the boundary, Fig. 4.4(b). In addition, the elastic torque from the boundary orients

cells orthogonal to the boundary, seen in Fig. 4.4(b) (inset). At low values of A (for $A < 2$), we find that P_{bound} increases monotonically with Pe. This is a consequence of the enhanced flux towards the boundary due to the higher speed (Pe), and the attractive potential that traps the cells. For higher A ($A > 2$), and at low Pe, cells are strongly localized at the boundary with $P_{\text{bound}} = 1$ due to the strongly attractive elastic force from the clamped boundary. For $Pe \geq 1$, we see a reduction in P_{bound} as escape from the boundary is increasingly facilitated by the greater speed. The critical Péclet number Pe_{c}^{*} at which the cells overcome the attractive interaction with the clamped boundary and escape into the bulk increases with A and is expected to be linear from force balance. Eventually however as $Pe \gg 1$, the role of the elastic potential becomes subdominant to the effects of increased motility, and particles are more likely to be observed at the boundary than in the bulk. In contrast, for a clamped elastic boundary, when the strength of the elastic attraction A is sufficiently larger than the persistent cell motility Pe, $P_{\text{bound}} = 1$ implying cells are strongly localized at the boundary. These cells have a higher chance of crossing over to the stiffer side. On the other hand, an elastic free boundary decreases P_{bound} thereby reducing the cells' tendency to go towards the softer substrate. Both these types of interactions from clamped and free boundaries, while distinct, promote durotaxis. On the other hand, higher cell migration speeds promote their motility-induced accumulation at a confining boundary without discriminating between stiffer and softer substrates.

4.3.2 Free elastic (repulsive) boundary induces depletion and prevents anti-durotaxis

We have demonstrated that our simulated cells are repelled by the free boundary due to the nature of the elastic potential. We track the positions of all cells over time and establish the closest distance from the boundary accessed by each. We showed in Sec. 4.2 that the repulsive force from the free boundary induces a effective void region where cell do not penetrate, see Fig. 4.4(a).

To characterize this void region systematically, we plot the statistically attained (time averaged and ensemble averaged for all cells) probability distribution function $\rho(x)$ as a function of x (the distance from the boundary) for various values of A and Pe. To obtain $\rho(x)$, we simply record the positions of the cells after sufficient time required to reach steady state has elapsed. The length of the void region ℓ_{void} is evaluated through these distributions, and is measured as the minimum distance at which the spatial density

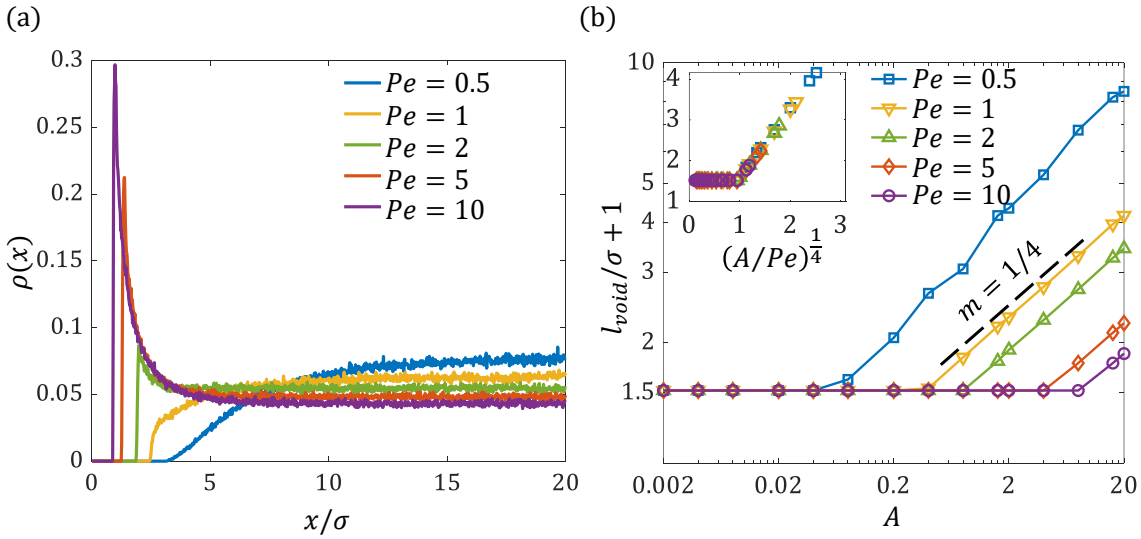

Figure 4.6: **Depletion region near a free boundary, and its dependence on motility and elastic strength interaction parameters.** (a) The probability distribution $\rho(x)$ of a particle is plotted as a function of closest distance x from the boundary for $A = 20$ with $Pe = 0.5, 1, 2, 5, 10$. Increasing Pe leads to a reduction in the length of the void region. (b) The void length scales as $A^{1/4}$, and $Pe^{-1/4}$ (for constant A) as predicted from force balance,see Eq. (4.5). Inset shows the collapse of the $\ell_{\text{void}} + 1$ vs $(A/Pe)^{1/4}$ for $Pe = 0.5, 1, 2, 5, 10$.

attains a non-zero value. For fixed values of A (for instance, A=20 in Fig. 4.6 - (a)), we find that increasing Pe decreases the length of the void region. In general, increasing A increases ℓ_{void} while increasing Pe decreases it.

We estimate ℓ_{void} for Pe from 0.1 to 10 and for $A = B$ from 0.002 to 20 to discern trends from physical scaling. Consider the balance of forces acting on a cell located at $x = \ell_{\text{void}}$. Balancing the self-propulsion ($\sim Pe$) and elastic interaction forces ($\sim A/(x/\sigma + 1)^4$) that move the cell, we obtain

$$(\ell_{\text{void}}/\sigma) + 1 \sim (A/Pe)^{\frac{1}{4}} . \tag{4.5}$$

Indeed, void lengths extracted from simulated probability distributions confirm this theoretically predicted scaling in Fig. 4.6(b). Experimentally, the presence of a void region may be detected by culturing and tracking cells on a stiff adhesive region of an elastic substrate, adjoining a very soft, non-adhesive region that acts as a free boundary. Our model predicts low probability of finding cells in a void region.

4.3.3 Clamped (attractive) boundary induces durotactic trapping

In our model, the clamped boundary condition represents the cell being on the softer substrate. It facilitates durotaxis by inducing an attractive force and aligning torque on the cellular force dipole. Such cells therefore tend to be trapped at the confining boundary. Since cell migration is stochastic and not deterministic, they can sometimes go opposite to the durotactic direction. This is possible in our model through reorientation via rotational diffusion, which represents random internal fluctuations in cell polarity. Once the cell reorients and points away from the confining boundary, it can escape from the trapped state if the self-propulsion is strong enough to overcome the elastic attraction, $Pe \gtrsim A$.

When $A \geq 1$ and $Pe \sim 1$, cells tend to localize at the clamped boundary, as seen in Figs. 4.4(b) and 4.5(b). At the same time, a large elastic torque, $B \geq 1$, orients the direction of propulsion directly towards or away from the boundary, as shown in the schematic Fig. 4.7(a). We now quantitatively investigate the rate at which the cells trapped at the boundary flip their orientation from pointing towards the boundary to pointing away from the boundary, or *vice versa*. This provides as estimate of the time scale over which escape of trapped cells can occur. Since reorientation dynamics is dominated by the boundary-induced elastic torque, we focus on B as our parameter of interest in this subsection. Since escape after rotation diffusion-enabled reorientation is possible through persistent motility alone when $Pe > A$, we continue to keep the translational diffusion parameter $D = 0$ in this section.

In the limit of large elastic torque parameter $B \gg 1$, cells at the boundary are always oriented perpendicular to the boundary, pointing towards or away from it. As depicted in Fig. 4.7(a), a cell can thus reside in one of two possible orientation states: either pointing towards the boundary ($\theta = 0$), or away from ($\theta = \pi$) the boundary. These two states are the minima of the potential double well in orientation, $U(x = x_b, \theta)$. Flips are defined as the large, stochastic, reorientation events caused by rotational diffusion when θ changes from π to 0 or *vice versa*. To measure the average frequency of flips, we track the change in orientation of cells localized at the boundary, given by the angle θ, see Fig. 4.2. Thus, flips result in change in sign of $\cos\theta$, seen in Fig. 4.7(a). A typical simulation trajectory in Fig. 4.7(b) shows that flipping occurs multiple times during a given simulation run, even at high values of B. We define and measure a time taken by a cell to flip, τ_{flip} , as the residence time of the cell in either state. Following the orientation of a single cell

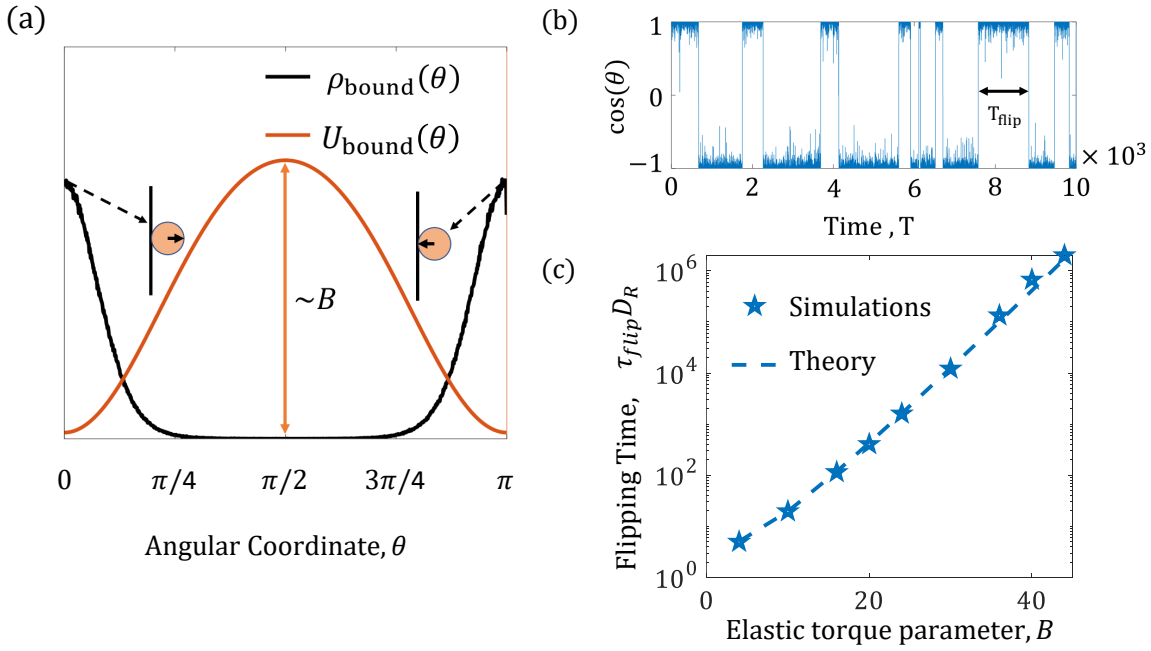

Figure 4.7: **Cell reorientation (flip) kinetics at clamped (attractive) boundary quantified by barrier crossing theory.** (a) For a clamped boundary, and at very high values of A and B, cells localize at the boundary even at high values of Pe, and are oriented perpendicular to the boundary. (b) Rotational diffusion enables the cell to transition from the parallel to the anti-parallel configuration. These random flips are recorded for a cell stuck at the boundary for $A = B = 20$. (c) The average frequency of these flips is observed as a function of B. The flipping time follows Kramer's theory of barrier crossing and is given by Eq. (4.6).

over the time it is trapped at the boundary provides a distribution of flipping times. In Fig. 4.7(c), we show the mean flipping time τ_{flip}, averaged over many cell trajectories, for a range of large B values ($B = 4 - 45$) with A set to equal B. The dependence of τ_{flip} on B follows the predicted form of Kramer's theory of barrier crossing [263],

$$\tau_{\text{flip}} = \frac{2\pi}{\mu_R \sqrt{U''(0)|U''(\pi/2)|}} \exp\left(\mu_R \frac{U(\pi/2) - U(0)}{D_R}\right) \sim \frac{1}{B} \exp\left(B \frac{(b_\nu^c + c_\nu^c)}{864\pi}\right). \quad (4.6)$$

where we used the form of the elastic potential $U(x, \theta)$ given in Eq. 4.3. Note that since our simulation is for cells trapped at the boundary that are free to change orientation, the potential $U(x, \theta)$ is evaluated at a fixed value of $x = \sigma/2$. The theoretically predicted flipping times from Eq. 4.6 (dashed line) closely agree with the simulation data in Fig. 4.7(c).

For low or moderate values of B however, cells at the boundary may adopt orienta-

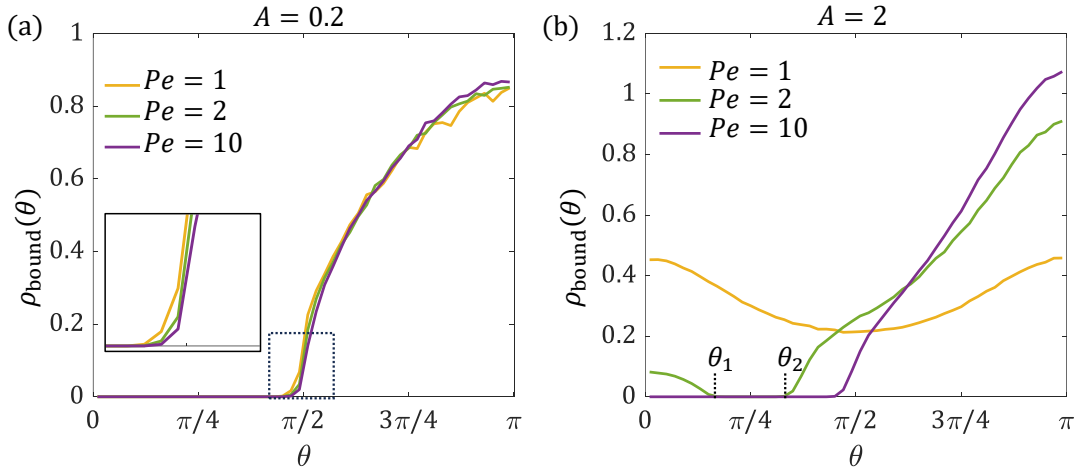

Figure 4.8: **Orientational probability profiles of cells at clamped boundary provides bounds for escape.** The angular probability distribution at the boundary $\rho_{\text{bound}}(\theta)$ is plotted for $A = 0.2$ and $A = 2$. Here we set $B = A$ in both cases. (a) For $A = 0.2$, cells are weakly attracted by the boundary and since $B = 0.2$, the torque due to elastic interaction is low. Under these conditions $\rho_{\text{bound}}(\theta) > 0$ when cells are oriented towards the boundary. Increasing the Pe increases the angle through which the cell can escape from the boundary (inset (a)). θ_{esc} is observed to be 77.4^0, 81^0 and 84.6^0 for $Pe = 1$, 2 and 10 respectively. (b) When $A = B = 2$, we identify 3 distinct regimes that are Pe dependent. For $Pe = 1$, the cells are stuck to the boundary but free to reorient due to rotational diffusion, preferentially orthogonal to the boundary. At $Pe = 10$ the cells can escape the boundary forces when the cell is oriented away from the boundary. At $Pe = 2$, the cells are only able to escape when their orientation lies in the angular pocket between $\theta = 0$ and $\pi/2$, denoted by dotted lines at $\theta_1 = 30.7^0$ and $\theta_2 = 55.8^0$.

tions other than just p and π. This is captured by the steady state orientational probability distribution $\rho_{\text{bound}}(\theta)$ of the cells at the boundary, shown in Fig. 4.8 for two representative values of B. At $A = B = 0.2$, Fig. 4.8(a), both force and torque from the elastic interactions with the boundary are low. Cells pointing away from the boundary with $\cos\theta > 0$ are not strongly attracted by the boundary and may escape by self-propulsion. The angle at which these cells lose contact with the boundary, defined here as θ_{esc}, is then the minimum angle at which $\rho_{\text{bound}}(\theta)$ just becomes non-zero. There is no probability of finding cells at the boundary with orientation, $\theta < \theta_{\text{esc}}$ at steady state, because these cells have escaped back into the bulk. In this small B regime, the escape angle is close to, but smaller than $\pi/2$. Increasing Pe increases the θ_{esc} slightly towards $\pi/2$, as shown in the inset to Fig. 4.8(a).

For moderate values of B, such as when $B = A = 2$, we observe three distinct regimes separated by two transition Péclet numbers, Pe_1 and Pe_2, as seen in Fig. 4.8(b). All results in Fig. 4.8, including the three possible behaviors in Fig. 4.8(b), may be quantitatively understood from a simple force balance argument. In these simulations without translational diffusion ($D = 0$), a cell can escape from the boundary only if the attractive force from the boundary is overcome by the normal component of its self-propulsive force. Evaluated at the boundary position, $x = x_b = \sigma/2$, this force balance has the form

$$Pe\cos\theta = \frac{3A}{(x_b/\sigma + 1)^4}\tilde{f}_\nu(\theta) \tag{4.7}$$

where $\tilde{f}_\nu(\theta)$ is the rescaled form of $f_\nu(\theta)$ in Eq. 4.3, such that $\tilde{f}_\nu(\theta) \sim 1$. The conditions for the existence of solutions of this force balance equation (detailed in see Appendix D) determine three possible regimes of escape behavior. For low values of $Pe \leq Pe_1$, the elastic attractive force from the boundary, given by A, is strong enough to prevent cell escape, even when the cell is oriented away from the boundary. At high Péclet number, $Pe > Pe_2$, cells are able to escape the boundary interactions provided the orientation angle $\theta < \theta_{\text{esc}}$, where $0 < \theta_{\text{esc}} < \pi/2$. At intermediate Péclet numbers, $Pe_1 < Pe < Pe_2$,there exists a range of orientation angles, $0 < \theta_1$ to $\theta_2 < \pi/2$,between which cells can escape. If $\theta < \theta_1$, the attractive force from the boundary is too strong and if $\theta > \theta_2$, the cell leans towards the boundary and cannot propel away. Thus, there is an angular cone of escape between θ_1 and θ_2.

When $A = 2$, we estimate $Pe_1 = 1.82$ and $Pe_2 = 2.14$, respectively. This corresponds to the results in Fig. 4.8b, for $B = A = 2$, where all the three regimes discussed above occur. The cells with $Pe = 1 < Pe_1$ cannot escape at any angle. Those with the intermediate $Pe_1 < Pe = 2 < Pe_2$ exhibit a range of escape angle, where the probability density vanishes. Cells with high $Pe = 10 > Pe_2$ can escape at all angles higher than a θ_{esc} near $\pi/2$. This last case is observed at all Pe values shown for $A = 0.2$ in Fig. 4.8a, since the theoretically estimated values of Pe_1 and Pe_2 from the analysis in Appendix D are 0.182 and 0.214 respectively. Thus, the force balance in Eq. 4.7 and resulting self-propulsion-dependent escape criteria quantitatively explain our simulated orientational distributions for cells trapped at the boundary in Figs. 4.8.

If the elastic force from the boundary is very strong, i.e., $A \gg Pe$ the cells cannot escape the influence of the boundary and will all participate in durotaxis. Escape is likelier when the gradient in substrate stiffness is small, such that the boundary attractive force

and the cell's active propulsive force are comparable. The rotational diffusion in our model corresponds to random protrusions and internal chemical signaling that can reverse the polarization of the cells, while the propulsion drives them away from the boundary.

Three mechanisms influence the motion of cells - elastic interaction forces, self-propulsion, and random motion. For zero to very small Pe numbers, we expect random motion to dominate over the deterministic self-propulsion force. Balancing elastic interaction energy in the vicinity of the clamped boundary with effective thermal energy gives us $P^2/(E\ell_{\rm E}^3) \sim D_R\sigma^2/\mu_R$, or $\ell_{\rm E} \sim \sigma A^{1/3}$, the length-scale quantifying the distance from the boundary for which elastic interactions dominate. For A in the range $1-10$, we find that $\ell_{\rm E}/\sigma$ varies from 1 to ≈ 2.15. For moderate to large Péclet numbers, the relevant balance now comes from the competition between the attractive elastic force, and the self-propulsion force. In this case, we find $\ell_{\rm E} \sim \sigma(A/Pe)^{1/4}$. We note that the propulsion force may not always act in parallel to the elastic force. Nonetheless, when $x < \ell_{\rm E}$ elastic forces win and the net force moves cells towards the boundary. When the typical cell spacing is larger than these elastic interaction length scales, as expected for dilute cell cultures, our single cell model will apply.

Our predictions for the orientational distribution and dependence of reorientation (flipping) timescales may be checked in experiment by tracking the orientation and polarization (*i.e.* the direction of migration) of cells cultured on elastic substrates. How these quantities depend on on A and Pe may be checked by performing experiments on substrates of varying stiffness and quantifying cell traction (related to A) and migration speed (related to Pe).

4.3.4 Comparison with experiment and predicted durotactic phase diagram

So far, we have shown that elastic interactions promote accumulation and trapping at the clamped boundary, thus facilitating durotaxis. On the other hand, cell motility enables escape from the boundary, thus counteracting durotaxis. We now quantify the extent of durotaxis in terms of some possible definitions of tactic index used in prior work. Based on our theory and simulations, we predict how the extent of durotaxis varies with the two main parameters in our model: the elastic cell-boundary interactions, $A = B$, and persistent cell motility, Pe. We focus on the case of a clamped boundary relevant for the cell located on the softer part of the substrate.

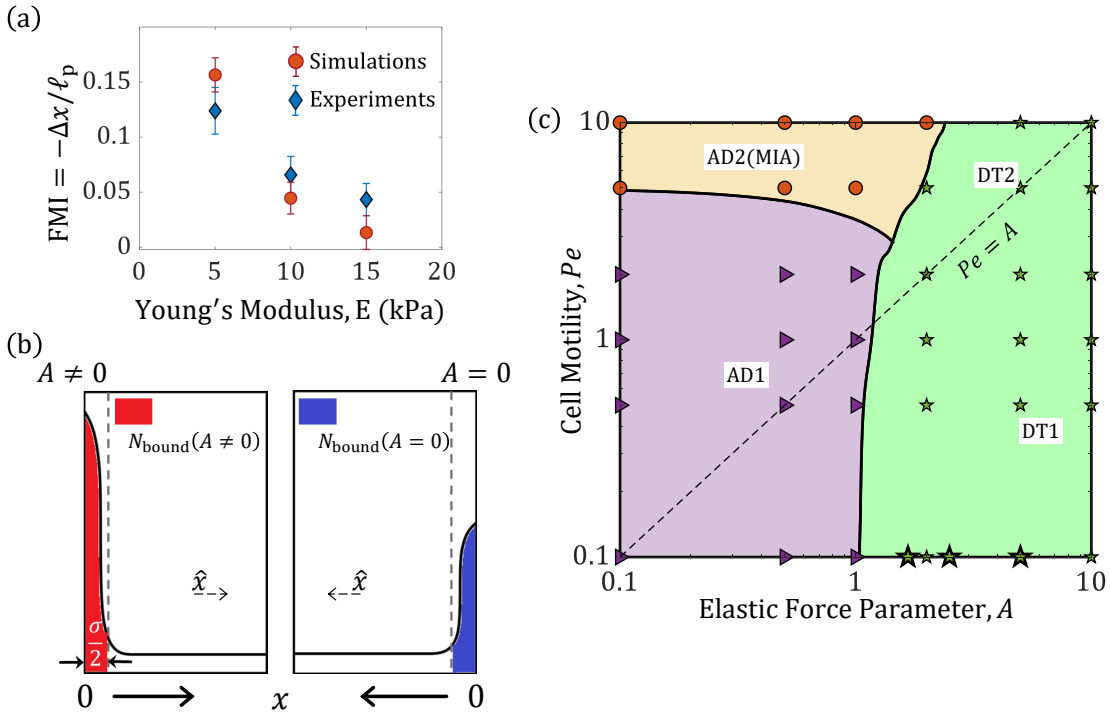

Figure 4.9: **Comparison of cell migration index with experiment and a predicted durotactic phase diagram.** (a) The forward migration index defined as the ratio of cell displacement towards the boundary and its total path length, FMI $= -\Delta x/\ell_p$, is calculated from simulations at $Pe = 0.1$ and $D = 1$. Simulation results (blue diamonds) compare well with experimental data (orange circles) obtained by DuChez et al. for U-87 gliblastoma cells on an elastic substrate with gradient in stiffness from $2 - 18$ kPa [4]. The substrate had three different stiffness regions with effective Young's modulus of 5 kPa (soft), 10 kPa (medium) and 15 kPa (stiff). (b) To calculate the value of durotactic index (DI, defined in Eq. (4.8)), we simulate and compare the number of cells trapped at a confining boundary for $A \neq 0$ with the corresponding $A = 0$ case at the same Pe value. (c) Simulated phase diagram in $A - Pe$ space classified according to durotactic index and boundary accumulation. The durotactic region (green) corresponds to simulated cells (green pentagrams) with a DI greater than a threshold value (DI$>$ 0.27), which corresponds to the DI value of cells at $A = 1$, escaping through random diffusive motion. The $Pe = A$ line separates the durotactic region into the diffusion-dominated regime (DT1) and motility-dominated regime (DT2). The cells with DI smaller than the $A = 1, Pe = 0$ case (DI$<$ 0.27) are classified as adurotactic, AD1 (purple), or adurotactic with motility-induced accumulation, AD2(MIA) (orange), depending on the boundary localization given by P_{bound}. Experimental data points observed by DuChez et al. [4] are estimated to lie on the $Pe = 0.1$ line in the durotactic region (DT1), marked by the large stars.

The elastic interaction parameter in our model, $A \sim P^2/E$, can be tuned by varying substrate stiffness, E. For a cell with fixed contractility P, the elastic interaction scales inversely with E, thus predicting a reduction in durotaxis with increasing substrate stiffness. We first compare our predictions with DuChez *et al.* [4], where the authors observed durotaxis of migrating U-87 glioblastoma cells up a stiffness gradient on polyacrylamide substrates. They quantified the extent of durotaxis as a forward migration index (FMI), defined as the ratio of the displacement of a cell up the stiffness gradient to its total path length. For simulations, we consider the situation where random protrusions enable translational motion of the cell away from the attractive clamped boundary. Such protrusions, when large and frequent, lead to random movements of the cell center of mass, that has to be taken into account through non-zero values of the translational diffusion co-efficient, which we now set $D = D_T/D_R = 1$. In our simulation setup, this corresponds to $-\Delta x/\ell_p$, that is, the ratio of displacement of the cell towards the clamped boundary to the total path length traversed along its trajectory. The substrate in the experiment comprised of three, connected, 250 μm-wide regions, labeled "soft", "medium", and "stiff", with average Young's moduli (E) of 5 kPa, 10 kPa and 15 kPa, respectively. This allows us to map the dependence of a tactic index on A and Pe and enables quantitative comparison of experimental observations with our model predictions.

Using typical values for cell diameter, $\sigma \sim 20$ μm, and traction forces ~ 2.5 nN [264], we estimate the elastic interaction parameter $A = B$ to be 5, 2.5, and 1.7, corresponding to the three average substrate stiffness values in the experiment. We estimate $Pe \sim 0.1$ for cells in all these regions, based on their measured migration speed, $v_0 \approx 0.4\mu$ m/hr, and persistence time, $D_R^{-1} \approx 0.1$ hr. The results from the simulation are plotted along with experimental data in Fig. 4.9(a). We find that the three data points for FMI from the experiment agree closely with those obtained from simulations for corresponding estimated $A = B$ values. Overall, this demonstrates that durotaxis increases when the cell is initially on softer substrates.

To classify our simulated results into qualitatively different regimes, we define tactic indices that predict the dependence of durotaxis on two key model parameters. These are: A (here we have chosen $B = A$), which represents the elastic cell-boundary interactions that drive durotaxis, and the persistent cell motility represented by Pe. Higher values of Pe induce accumulation of cells at a confining boundary but also facilitate escape from "durotactic trapping" induced by the elastic potential. Thus, in our model setup, accumu-

lation does not imply durotaxis. To distinguish accumulation from durotaxis, we define and calculate a durotactic index (DI), that is distinct from the propensity to accumulate at a confining boundary given by p_{bound}. To define DI, we need to consider the accumulation driven by elastic interactions alone. We thus compare N_{bound}, the number of occurrences of a cell at the boundary at steady state, at some motility Pe, for $A \neq 0$ and $A = 0$:

$$\text{DI} = \frac{N_{\text{bound}}(A, Pe) - N_{\text{bound}}(A = 0, Pe)}{N_{\text{bound}}(A, Pe) + N_{\text{bound}}(A = 0, Pe)}. \tag{4.8}$$

This definition allows us to subtract out the effect of motility-induced accumulation from the net accumulation. This may be visualized in the simulation setup shown in Fig. 4.9(b). In one case, we consider a confining boundary with clamped elastic boundary condition corresponding to $A \neq 0$, while in the other, the confining boundary has no elastic interactions, $A = 0$. The difference in the number of accumulated cells between the two boundaries at steady state is then our chosen measure of durotaxis. This is analogous to the definition of DI used in previous works [231, 229]: $\text{DI} = (N_f - N_r)/(N_f + N_r)$, the normalized difference in the number of steps N_f in a cell trajectory in the "forward" direction - that is, the direction up a stiffness gradient, and the number of steps N_r in the "reverse" (down the stiffness gradient) direction,.

Next, we synthesize all simulation results for the clamped boundary case and organize them into a phase diagram in the space spanned by A and Pe. In this simulated phase diagram shown in Fig. 4.9c, we classify the region corresponding to DI above a critical value ($\text{DI} \geq 0.27$) to be "durotactic". This choice corresponds to the calculated value of DI at $Pe = 0$, $A = 1$, since we expect elastic attraction to dominate over diffusive (random) cell motion for $A \geq 1$. The phase boundaries are constructed by interpolating through 200 simulation data points ($A = 0$ to 10 and $Pe = 0$ to 10). The durotactic region can be further separated into two regimes by the line $Pe = A$. The $Pe < A$ region corresponds to a diffusion-dominated regime (DT1), where escape from the attractive boundary is facilitated by cell protrusion-facilitated random motion. The motility-dominated regime (DT2) occurs when $Pe > A$, and in this case escape from the attractive boundary is driven by persistent motility, without requiring any separate diffusive motion. Thus, in each case, it is the random or persistent motility, given by D and Pe respectively, which primarily competes with elastic interactions to reduce durotaxis.

For $A < 1$ or at high motility relative to elastic interactions $Pe \geq 5A$, the cells do not show sufficient durotaxis. These cells yield $\text{DI} < 0.27$, and are not considered to

be in the DT regime. They can still accumulate at the boundary if the motility is high enough. We denote this latter regime "motility induced accumulation" (AD2-MIA), and distinguish it from the adurotactic (AD1) region without accumulation, using a threshold value of P_{bound}. At $A = 0$, we consider the value of P_{bound} at $Pe = 5$ to be the cut-off value ($P_{\text{bound}} = 0.18$) to separate regions AD1 and AD2(MIA). $P_{\text{bound}} > 0.18$ corresponds to MIA while $P_{\text{bound}} < 0.18$ corresponds to AD1. All three datapoints from the DuChez et al. experiment [4] shown in Fig. 4.9a lie in the DI region of the phase diagram and are indicated by large stars in the phase diagram in Fig. 4.9c.

The main prediction of our simulated phase diagram is that durotaxis occurs when the strength of cell-boundary elastic interactions is large enough compared to random or persistent cell motility. This is realized when $A > A_c$, where the threshold value $A_c = 1$ at $Pe = 0$, and decreases with Pe. Higher values of A can result from increased cell contractility, reduced substrate stiffness and/or less random cell movement. Higher persistent motility (larger Pe) helps the cell overcome the elastic boundary attraction and reduces durotaxis. While the predicted dependence on substrate stiffness is borne out by the data from Ref. [4], the dependence on migration speed (Pe) is yet to be systematically tested in experiments because of the low value $Pe < 1$ for cell migration in many cases.

4.3.5 Clamped (attractive) elastic boundary: escape facilitated by random translational protrusions ($Pe < A$)

In the previous sections, we derived conditions for the motility-enabled escape after re-orientation of a cell away from the clamped boundary at which it was trapped. Our analysis of flipping dynamics and analytical prediction of the relevant time scale allows us to predict the first part of the overall escape process - i.e., the cell switching to a configuration favourable for escape, and concomitant conditions on Pe for cells to leave the boundary. We also saw that the migration index in experiments does not have a high value, i.e. the migration index is not close to 1. Hence we explore the possible cause for such behavior.

We extend our analysis and derive analytical expressions for the time required for cells to escape from the boundary to a dimensionless length-scale $L_{\text{esc}} \gg 1$. This corresponds to a distance far enough from the potential well at $x = 0$, where the torque and force arising from boundary interactions are negligible relative to random noise.

To aid the analytical derivation of the escape time from barrier crossing theory and enable comparison with our simulation results, we initialize our cells at a position

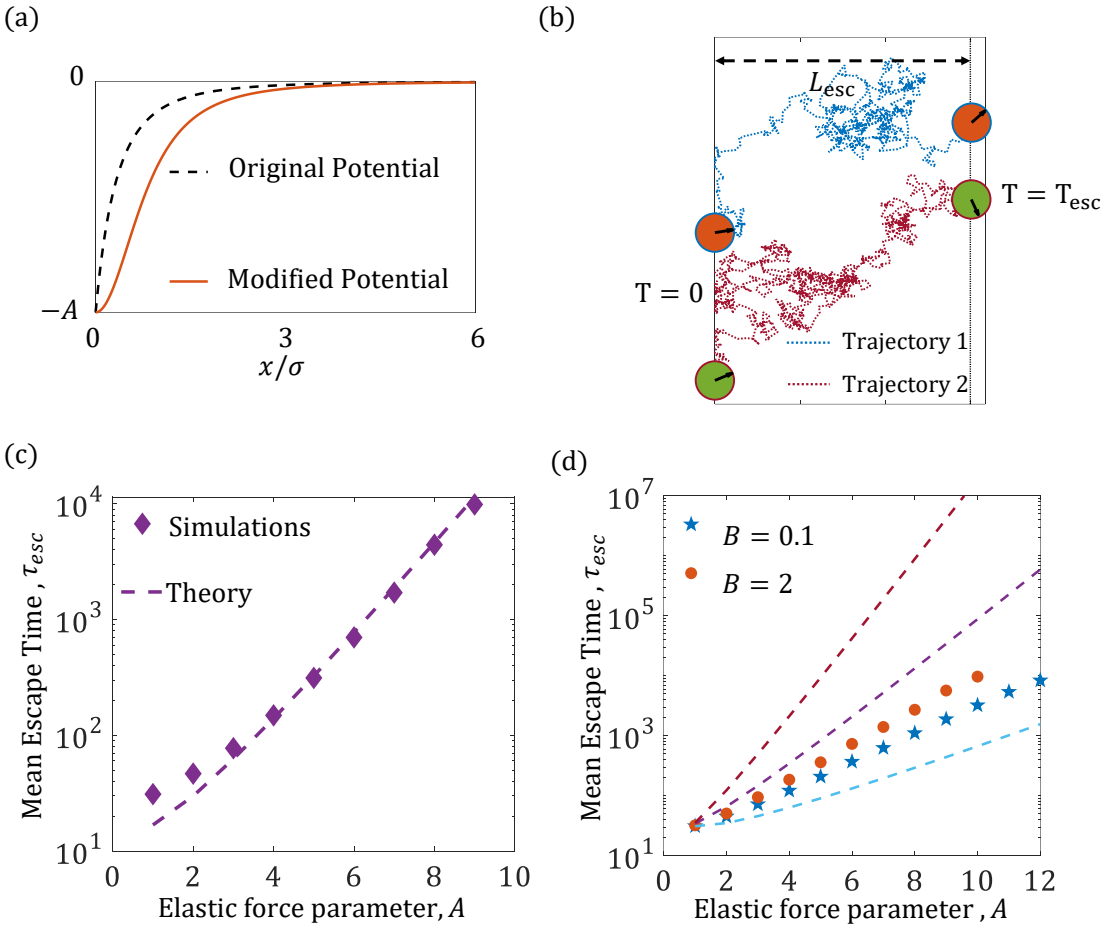

Figure 4.10: **Diffusive escape from clamped boundary is governed by modified Kramers' theory.** (a) The angle-averaged original potential (black, dashed),given by Eq. (4.3), is modified to a form (orange, solid), given by Eq. (4.9), that introduces an analytical minimum at the boundary ($x = 0$), thus making the potential amenable to analysis in terms of barrier crossing theory. (b) Two trajectories of cells starting of at the boundary ($x = 0$) with random orientation at time $t = 0$ are shown with blue and maroon dashed lines. L_{esc} is the distance beyond which the interaction potential is very low, here $L_{\text{esc}} = 6\sigma$ (c) Average (mean) escape time is plotted for a simplified 1D potential which is orientation angle independent. We observe that the results follow a modified version of Kramer's theory given by Eq. (4.10) for $\tilde{f}_\nu(\theta) = 1$. (d) τ_{esc} for the 2D potential with both spatial and orientation dependence is plotted vs A at $B = 0.1$ and 2, at $Pe = 0$. The dashed lines represent the analytical escape times (purple, for $\tilde{f}_\nu(\theta) = 1$), escape along the direction of least resistance (light blue, escape along $\theta = \pi/2$) and escape along the direction of maximum resistance (brown, escape along $\theta = 0$ or π).

corresponding to the local minimum in a potential V satisfying the constraints $\partial V/\partial x = 0$ and $\partial^2 V/\partial x^2 > 0$ at $x = 0$. This is done by modifying the functional form of the elastic potential while taking care to not change the long range behavior at $x \gg 1$ (see Fig. 4.10-a). This modified potential has a local minimum at the boundary as required for fidelity and consistency:

$$V(x,\theta) = -\frac{A}{((x/\sigma)^2+1)^{3/2}}\tilde{f}_\nu(\theta). \tag{4.9}$$

When $x/\sigma \sim L_{\text{esc}}$, the magnitude of the potential is significantly lower than at the boundary. This furnishes the constraint that needs to be satisfied for escape, $A/L_{\text{esc}}^3 \ll 1$ (Fig. 4.10-a, b). Thus complete escape from the boundary is achieved if a cell starting at the boundary is able to leave the region $x/\sigma < L_{\text{esc}}$ (Fig. 4.10-b).

The potential in Eq. (4.9) is used to obtain asymptotic estimates of the escape time, and also to investigate escape dynamics in our simulations. To allow for accurate statistics, we tracked $N = 10^4$ cells in this potential for various values of Pe, A, and B. The position and orientation were tracked for cells initialized at the boundary ($x = \sigma/2$) until they crossed $x/\sigma = L_{\text{esc}}$ for the first time. This data was used to relate the probability of escape and the average time of escape τ_{esc}, to interaction parameters A and B, and to the motility parameter Pe.

As a prelude to developing a theoretical expression for active barrier crossing in a 2D potential, we first evaluate the mean escape time τ_{esc} for cells without persistent motility ($Pe = 0$), that is when cell dynamics correspond to thermally diffusive particles. We further reduce the dimensionality of the problem by considering a potential that is independent of the orientation of cells, thus fixing the angular factor $\tilde{f}_\nu(\theta)$ to be a constant. This corresponds to a particle either maintaining a constant orientation θ, or exploring all angles equally such that the angular factor averages out to unity. This reformulated problem is equivalent to a 1D escape problem of a diffusing particle in an external potential, here arising from cell-boundary elastic interaction. Adapting previous work on Kramer's theory applied to a particle in a generalized Lennard-Jones potential [265] to our modified potential, we find that the average escape time increases exponentially with the interaction parameter A, as seen in Fig. 4.10-(c). Here, the theoretical curve is calculated from the expression for escape time given by,

$$\tau_{\text{esc}}^{\text{1D}} \simeq \frac{1}{D_R}\left(\frac{L_{\text{esc}} - A^{\frac{1}{3}}}{\sqrt{A}}\right) e^{A\tilde{f}_\nu(\theta)} \qquad \text{for} \quad \frac{A}{L_{\text{esc}}^3} \ll 1, \tag{4.10}$$

where the calculation is detailed in Appendix E. As shown in Eq. (B.24), the pre-factor of the rate of barrier crossing in this long-range power law potential differs from the classical Kramer's theory. In our simulations, we choose $L_{\text{esc}} = 6$ such that A/L_{esc}^3 ranges from 0.005 to 0.055, thus ensuring the validity of the approximation, $A \ll L_{\text{esc}}^3$, required to obtain the asymptotic expression for mean escape time. The simulation results are consistent with theoretical predictions for all values of $A \geq 3$ reported in Fig. 4.10(c). The average escape time, τ_{esc} is seen to increase exponentially with interaction parameter A.

Starting from the orientation-independent asymptotic calculation for τ_{esc}, we next proceed to incorporate the orientation dependence of the potential U, while still keeping $Pe = 0$. The escape problem is now two-dimensional, being in x-θ space, and the dynamics of cell reorientation affects the trajectories and probability of escape. In Fig. 4.10(d), we compare the simulation results of mean escape time τ_{esc} with the theoretical bounds corresponding to escape along the direction of least resistance (light blue, Eq. (4.10) corresponding to $\tilde{f}_\nu(\theta = \pi/2) = 0.53$), escape along direction of maximum resistance (brown, Eq. (4.10)) corresponding to $\tilde{f}_\nu(\theta = 0) = \tilde{f}_\nu(\theta = \pi) = 1.8$ and the effectively 1D result (purple, Eq. (4.10) corresponding to averaging out the angular degree of freedom, $\tilde{f}_\nu(\theta) = 1$). Note that the force resisting escape corresponds to the attractive elastic force generated by the clamped boundary, which scales with the angular factor, $\tilde{f}_\nu(\theta)$. The elastic force and torque parameters, A and B, are chosen from representative values in the range $A = 1 - 12$, and $B = 0.1, 2$ respectively.

The two representative values of B are chosen to highlight different regimes of orientation fluctuations during escape. In the low torque regime represented by $B = 0.1$, cells can freely reorient due to rotational diffusion and tend to escape first along the angle that results in least resistive force from the boundary. However, constant fluctuations in their orientation cause them to deviate from this path. This leads to a higher τ_{esc} than the theoretical prediction for the minimum resistance direction ($\theta = \pi/2$, light blue curve) in Fig. 4.10(d). However, the τ_{esc} values remain below that given by the average of all orientations (brown). In the high torque regime, $B = 2$, cells get aligned orthogonal to the boundary ($\theta = 0$ or $\pi/2$) when they are close to it. They thus experience a stronger attractive force from the boundary, and have higher τ_{esc} values, than in the low B case. We do not report the cases when both A and B are high, because the mean escape times become too long to observe in our simulation time scale.

Motivated by the theoretical analysis for the 1D or angle-independent case, we

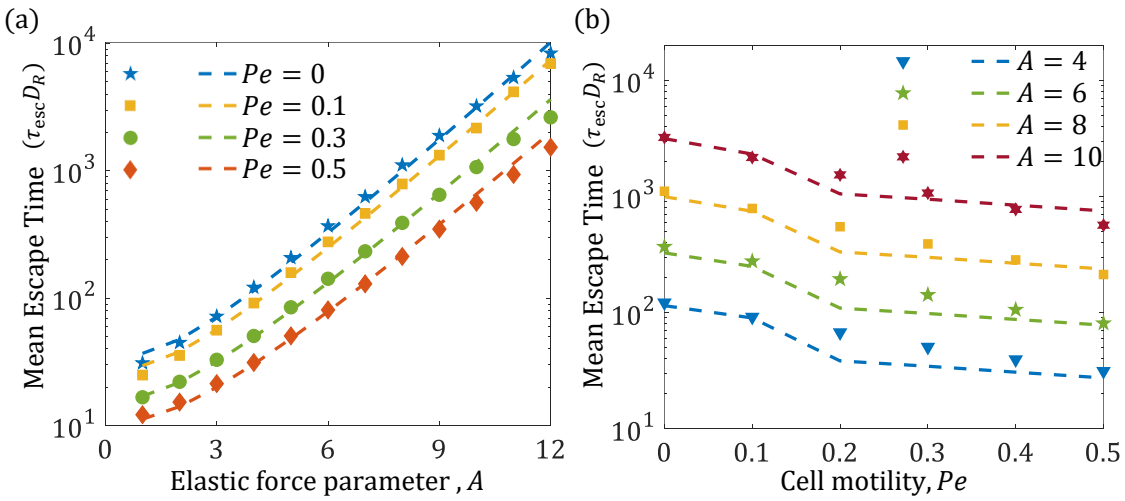

Figure 4.11: **Self propulsion-assisted escape from the attractive clamped boundary (at fixed $B = 0.1$).** (a) The normalized mean escape time $\tau_{\rm esc}D_R$ in simulation for varying Pe (shown by markers) follows the modified exponential relations in Eq. (4.14) with increasing A (shown by dashed lines) by only fitting pre-factor $m(\mathrm{Pe})$ at the given range of values of $\mathrm{Pe} = 0.1 - 0.5$. Here, we assume the coupling between position and orientation results in an effective value of $f^* = 0.651$, which is determined from fitting values for 2D passive particles at the given value of $B = 0.1$. The function m is linear in the Péclet number and is found to be $m(Pe) = 4.13 - 3.17Pe$. (b) Simulation results of the mean escape time (shown by markers) $\tau_{\rm esc}D_R$ for $A = 4, 6, 8, 10$ also follows the theoretical Ansatz, Eq. (4.14) (dashed lines) with Pe based on the fitting pre-factor $m(Pe)$.

now account for this effect of orientation fluctuations by assuming the Ansatz,

$$\tau_{\rm esc}^{\rm 2D} \simeq \frac{1}{D_R} m(B) \left(\frac{L_{\rm esc} - A^{\frac{1}{3}}}{\sqrt{A}} \right) \mathrm{e}^{Af^*(B)}, \tag{4.11}$$

and estimating the functions $m(B)$ and $f^*(B)$ by fitting to simulation data. Here, we interpret $f^*(B)$ as a function of an effective weighted mean of the angle of escape of the cells, which corrects the deviation from the ideal 1D escape result. Thus, the function $f^*(B)$ quantifies the effect of coupling between the positional and orientational degrees of freedom on the effective energy landscape. The parameter $m(B)$ explicitly corrects for orientational effects on the frequency of possible escape trajectories, and thus on the escape time. By definition, for passive particles in 1D, $f^* = 1$. The function $m(B)$ satisfies $m = 1$ for the passive 1D case, and deviates from this value when $B > 0$. Qualitatively, introducing the pre-factor $m(B)$ allows us to treat the full 2D escape problem as an appropriately averaged

1D escape problem.

Intuitively, we expect that self-propulsion helps particles escape from a confining potential. Thus our expectation is that τ_{esc} is reduced for $Pe > 0$ in comparison to $Pe = 0$, as confirmed by the simulation results in Fig. 4.11. The effective potential barrier that the cell has to escape, modified now by its self propulsion velocity, can be written as [266]

$$\phi = \frac{Af^*}{({C_1}^2 + 1)^{3/2}} - \frac{Af^*}{({C_2}^2 + 1)^{3/2}} - Pe\,(C_2 - C_1)\,. \tag{4.12}$$

Here C_1 and C_2 are the positions where the active self-propulsive force of the cell is equal to the attractive force from the boundary elastic potential (derivation and details in Appendix E). For the case at hand, this force balance provides a relationship between the constants (C_1 and C_2) and parameters Pe, A, and B,

$$\frac{\left(\tilde{x}^2 + 1\right)^{\frac{5}{2}}}{\tilde{x}}|_{C_2,C_1} = 3\frac{Af^*}{Pe} \tag{4.13}$$

which we solve for $\tilde{x}$ to determine C_1 and C_2 (see Appendix E-3). The final expression for the mean escape time of a self-propelling cell for the full potential is

$$\tau_{\text{esc}} \simeq \frac{1}{D_R}\left(\frac{L_{\text{esc}} - A^{\frac{1}{3}}}{\sqrt{A}}\right) m(B, Pe) \exp\left(Af^*\left(\frac{1}{(C_1^2 + 1)^{3/2}} - \frac{1}{(C_2^2 + 1)^{3/2}}\right) - Pe\,(C_2 - C_1)\right). \tag{4.14}$$

We observe that the function $m(B, Pe)$ changes with activity (via Pe), and the elastic potential (via B), see Eq. (4.11). An estimate for $m(B)$ obtained by comparing the theoretical prediction with the simulation results is provided in the Appendix E. We simulate and observe the effect of Pe on τ_{esc}, for $B = 0.1$ and A ranging from $1 - 12$. We show that the escape time τ_{esc} increases exponentially with A (Fig. 4.11-a), and decreases exponentially with Pe (Fig. 4.11-b). Thus, in this $A \gg Pe$ regime, where escape from the large elastic attractive potential is facilitated by translational random movements, increasing persistent motility is expected to reduce the extent of durotaxis.

We observe that the DI metric clearly corresponds to the escape time trends as shown in (Fig. 4.11). We expect cells to be more durotactic when escape time is longer, which corresponds to higher A and lower Pe. This is indeed borne out by the correlation between the values of DI and mean escape time (τ_{esc}) measured in simulation, and shown in Fig. 4.12. Each data point corresponds to the same values of A, Pe and $B = 0.1$.

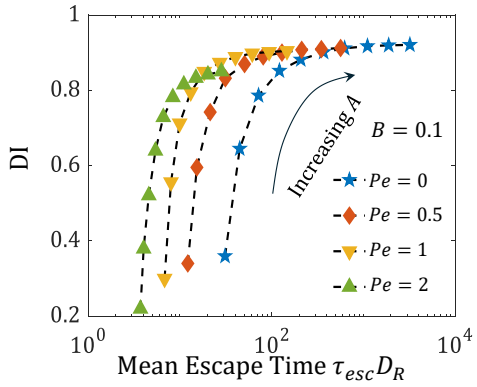

Figure 4.12: Cells are more likely to show durotaxis if they have higher escape time. For given Pe and B, increasing A increases mean escape time, corresponding to Fig. (4.11), as well as DI. On the other hand, increasing Pe reduces both mean escape time and DI.

4.4 Discussion

In this work, we combine a static elastic dipole model for cell-substrate mechanical interactions with a phenomenological model for persistent cell motility. We use this model to simulate cell dynamics and durotaxis at an elastic interface. The elastic dipole model for cell traction was invoked by Bischofs et al. [130, 6] to rationalize experimental observations of Lo et al. [3] that a fibroblast that is initially on the stiffer (softer) region, changes its orientation and aligns parallel (perpendicular) to the interface. The model as proposed was static without any cell dynamics, whereas we incorporate here both persistent and random contributions to cell motion. In this model setup, the accumulation of cells at the clamped (attractive) boundary facilitates durotaxis, since these cells can then cross over to the stiffer side. On the other hand, the motility-assisted escape from this boundary reduces durotaxis, since the cell can reorient and make its way back to the softer side. Our predictions for the reorientation (flipping) time given in Eq. (4.6) and cell migration index values (Fig. 4.9) may be used to infer how durotaxis depends on cell traction force (via A, and B), substrate stiffness values (also via A and B), and motility (via Pe).

Based on our simulations, we predict a phase diagram of cell durotactic behavior. We show that durotaxis is enhanced when the cell-substrate elastic interactions are large enough (high $A = B$), and the cell is not very persistently motile (low Pe). Our results quantitatively explain the finding by DuChez et al. [4] that the tactic index decreases with

increasing local substrate stiffness. Our results are also qualitatively supported by the recent observation of Yeoman *et al.* that weakly adherent breast cancer cells show comparatively less durotaxis than their strongly adherent counterparts [223]. Weakly adherent cells are expected to undergo rapid assembly/disassembly of focal adhesions leading to faster motility as was indeed observed in the study. Faster cells are expected to have higher Pe value according to an established universal exponential correlation between cell migration speed and persistence [267] based on experimental data. The observation that breast cancer cells are less durotactic is thus consistent with our predicted inverse relationship of durotaxis and persistent motility, seen in the phase diagram in Fig. 4.9c.

Yeoman *et al.* performed traction force measurements and drug-treatment assays that inhibit the actomyosin cytoskeletal activity, but did not separately measure the effects of drug treatment on cell motility and contractility. Further experimental exploration using substrates of varying stiffness and adhesivity (e.g. by micropatterning) is needed for quantitative and conclusive comparisons with our theoretical predictions for the dependence of durotactic index on cell traction and migration velocity. We also predict a motility-induced accumulation regime where cells are expected to be preferentially located near a confining boundary. While this has been demonstrated for active synthetic particles and swimming bacteria, elucidating this hitherto unexplored effect for crawling cells requires experiments on micropatterned substrates. Future experiments can also test our model prediction that a cell can detect and respond to a sharp interface in substrate stiffness from a long range (a distance of a few cell lengths away), without needing to be in direct contact with both softer and stiffer regions of the substrate.

To directly demonstrate durotaxis in our model, we consider the movement of cells across a sharp interface between two regions with contrasting substrate stiffness. In this simulation setup shown in Fig. 4.13, the left side has a lower stiffness than the right side of the interface. The left and right boundaries at $x/\sigma = \pm 15$ provide only confinement and not elastic interaction. We use the simplifying assumption of large stiffness contrast, such that a cell in the $x < 0$ ($x > 0$) region is considered to be interacting with a clamped (free) boundary, respectively. In Figs. 4.13 a and b, we show representative trajectories of single cells initialized on the softer side and close to the interface. Most cells are seen to cross over to the stiffer side, but for higher Pe values, a few are able to make their way back to the stiffer side. This illustrates our central point: that persistent motility can compete with elastic interactions. The steady state probability distributions in Figs. 4.13c and d further

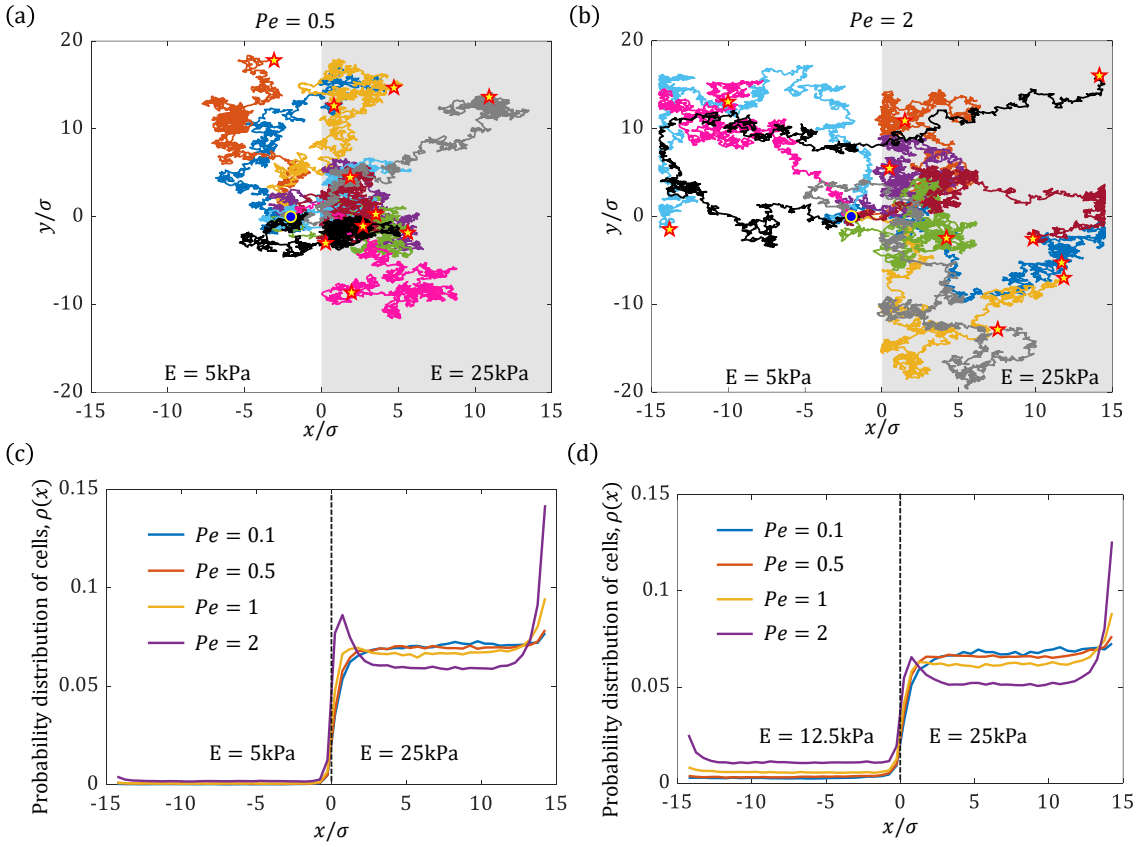

Figure 4.13: **Durotaxis across sharp gradient of substrate stiffness** modeled by clamped and free boundary conditions - (a, b) Representative cell trajectories allowed to move across an interface between two regions (distinguished by white and gray) of contrasting substrate stiffness. In this example, they are chosen to have representative values of the Young's modulus of 5 kPa and 25 kPa, corresponding to $A = B = 5$ and 1, respectively. Each plot shows 10 single cell trajectories starting at $x/\sigma = -2$ with $D = 1$ (marked by a yellow disk) and terminating at different end points (marked by filled yellow pentagrams) after a total simulated time of $T = 20$. (a) All cells with lower $Pe = 0.5$ cross over to and spend more time on the stiffer side. (b) A few of the cell trajectories with $Pe = 2$ spend more time on the softer side as compared to the ones at lower values of Pe. (c, d) The steady state probability distribution demonstrates higher probability of finding cells on the stiffer side. The small probability of finding cells on the softer side is less for higher stiffness contrast in (c). It increases with decreased stiffness contrast in (d). The trend is more apparent at higher Pe, which allows cells to escape the attractive boundary force and spend more time on the softer side. Higher Pe also lets the cells overcome the repulsion on the stiffer side, and form the small peak near the interface.

illustrate that a lower stiffness contrast leads to lower durotactic index. This is especially apparent at higher Pe, when the difference in number of cells between the two regions is reduced for lower stiffness contrast. Further, the higher $Pe = 2$ cells show some motility-induced accumulation on the repulsive side of the interface, whereas at lower $Pe < 2$, a depleted layer is seen as the self-propulsion is unable to overcome the repulsion.

We use the approximately clamped or free boundary condition limits because the general elastic interaction potential between two substrate regions with arbitrary stiffness values lacks a simple analytically tractable form [243]. Further, when a cell moves across the stiffness interface, other shorter-range effects beyond the scope of this study are expected to dominate its dynamics. For example, a cell that can extend across the interface will deform the soft side more than the stiff side, leading to an effective translation towards the latter, which may drive durotaxis across gradual gradients in stiffness [221]. Analogously, short-range effects are thought to drive "viscotaxis" of microswimmers [268, 269], in addition to longer range hydrodynamic interactions with an interface [270]. In this latter context, scattering or change in direction of microswimmers, analogous to refraction of light, has been seen to occur across a viscosity interface [271]. In the SI Fig. S4, we consider such effects in the zero noise ($D = 0$), limit of our model, and show that a scattering close to the interface also results from the elastic potential.

Recent observations of "negative durotaxis" or "anti-durotaxis", *i.e.,* directed migration from softer to stiffer substrates suggest that cells do not always move *up* stiffness gradients, but rather move towards an optimal substrate stiffness where their contractility is maximal [227]. We note that the elastic dipole model can give rise to such an optimal stiffness when the mechanosensitivity of the cell to substrate properties is incorporated by including explicit feedback between cell traction force (the contractile dipole strength) and substrate deformation [230]. This is motivated by experiments that suggest that cells sense and adapt their traction and effective force dipole moment to substrate strain [272]. The inclusion of cell polarizability in the elastic dipole model creates additional interaction terms of the cell dipole with its image dipoles induced by the confining boundary. These additional pairwise interaction terms can be stronger and have the opposite sign from the direct interactions [273]. This may result in the clamped (free) boundary switching roles and being repulsive (attractive), which would drive negative durotaxis in our model. Alternatively, some adherent cells are known to be capable of regulating their traction forces to maintain different types of mechanical homeostasis depending on substrate stiffness [274, 275]. In the

derivation of the (attractive) cell-boundary interaction energy used in this work in Eq. (4.3), cellular forces (or dipole moment) have been assumed to be constant, indicating stress or force homeostasis. If, instead, cells maintain constant displacement (known as displacement homeostasis) [274], then the attraction to the rigid boundary could turn repulsive [275], resulting in negative durotaxis. These effects will be explored in future work. In general, our work paves the way for exploring active cell migration under confinement and various tactic stimuli [276] that may be expressed as effective potentials.

Chapter 5

Analysis of elastic strains reveals shape selection pathways in active gels

5.1 Introduction

Thin elastic sheets can buckle in response to nonuniform in-plane strains [277], because their bending energy is much lower than stretching. This phenomenon is utilized to engineer self-actuating materials that generate complex 3D shape transformation with oscillatory capabilities [278, 279]. Unlike uniformly stimulated elastic gel sheets[280, 281, 282], actomyosin gel sheets contract and wrinkle spontaneously without pre-imposed gradients in material properties[81, 60]. This phenomenon remains insufficiently explored, especially concerning the dynamics of shape transformation and the rules governing shape selection. Therefore, we lack a comprehensive understanding of how myosin motor-induced contractile stresses in actomyosin gels result in various 3D shapes and the rules that govern their dynamics and final configurations. The similarity between the wrinkled shapes of actomyosin sheets and thin actin-filled lamellipodia protrusions in migrating cells further motivates a thorough study of shape deformation in these systems[68].

To address this gap, we study the displacement of local regions of the actomyosin gel through particle image velocimetry (PIV) and analyze it with our model of axially symmetric elastic deformations of a contracting active gel. Gels synthesized with the same

initial components in the same material composition, *i.e.* identical material composition, can show different morphologies depending on their initial geometry. These differences in contraction phenomena can be observed in their radial displacement profiles, as extracted from PIV. By systematically analyzing the radial profiles of displacement and strains, we aim to infer the distribution of active stresses in the disk using suitable continuum mechanics models. Additionally, we make predictions about the final morphology of the active gel from the contraction dynamics. By understanding these principles, we gain insights into biological processes and potential applications in material science, motivating further exploration into the dynamic behaviors of these active biological materials.

5.1.1 Preparation of intrinsically contractile elastic actomyosin gel discs

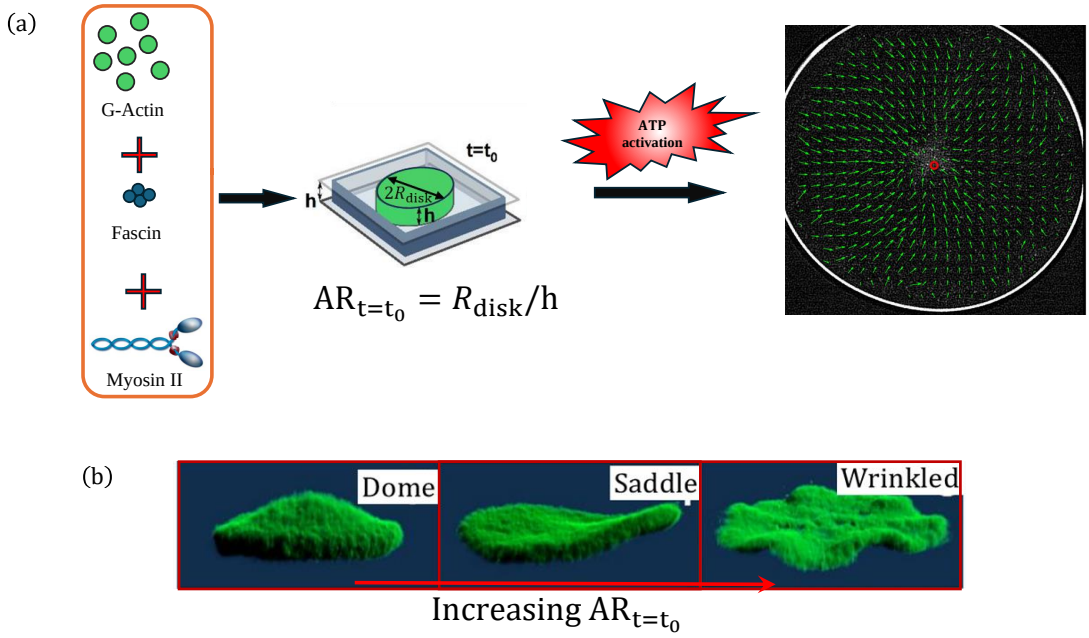

Figure 5.1: **ATP activated contraction of actomyosin gel**(a)Schematic shows the formation of actomyosin gel upon mixing g-actin, fascin and myosin motors and contraction upon ATP activation. (b) Formation of different morphologies of gel depends on the intial aspect ratio of the gel, which is controlled by the thickness of the chamber and volume of the solution used.

Actomyosin gel discs were prepared by polymerizing 5μM G-actin with 16.7nM myosin II (in large aggregates of $\sim$ 150 myosin dimers), 280nM fascin, and 2mM ATP [283],[81],[60] . ATP-regenerating system and an anti-bleaching solution were used. The

percentage of labeled G-actin and myosin II is 5mol%. A drop of that solution is squeezed between two PEG passivated cover-slips, placed in a homemade sample holder [283, 60]. Discs of variable height h and radii R are generated by varying the drop volume and spacing between the two coverslips . G-actin starts to polymerize to form F-actin which gets further cross-linked by fascin to form thicker actin bundles. Myosin complexes are activated by ATP and exert forces on the actin bundles by walking on them. The system starts to contract with time as shown in Fig. 5.1(a). The gels contract and reach a final steady state 3D shape over a timescale of minutes, that they retain. These shapes could be dome-like (with single bump in the inner region) or wrinkled (multiple undulations along the circumference), or various kinds of intermediate shapes, an example being the 2-peak "saddle" shown here. These shapes are characteristic of elastic buckling and suggest that the gel remains a solid at long times, although its dynamics follows poroelastic behavior with outflow of the solvent as the gel shrinks in time [81]. The time scale of contraction can be as high as 400s for a dome gel and as low as 20s for a wrinkled one.

5.2 Analysis Methods

5.2.1 Particle Image Velocimetry

Particle Image Velocimetry (PIV) is a non-invasive optical method to visualize flows in a plane. A high speed camera fixed in position captures the time evolution of a flow process and PIV correlates between the images to determine average instantaneous velocity associated with each local region. This reveals a global flow pattern in the system. PIV also proved to be a great tool to analyze the contraction phenomena of active gels. Here, PIV tracks the fluorescently labeled cross-linked actin fibers to determine the instantaneous velocity in different parts of the gel. The actomyosin gel is a poroelastic material but the speed of contraction is slow enough to consider it to be a linearly elastic at short time scales of 0.1s, much shorter than the characteristic poroelastic stress relaxation time scale, which was estimated to be around 20s in earlier work [81] Hence, these local velocities can be considered as short time displacements (Fig. 5.2; Gels 1-8). Gels 2, 3, 4, and 6 have been reported to show dome like 3D structure during its contraction period. On the other hand, gels 5, 7 and 8 form wrinkles. Gel 1 forms a 2-peak saddle.

The local displacements thus obtained for the gels reveal a center of contraction inside the gel. This is the point where all (or most) of the displacement vectors apparently

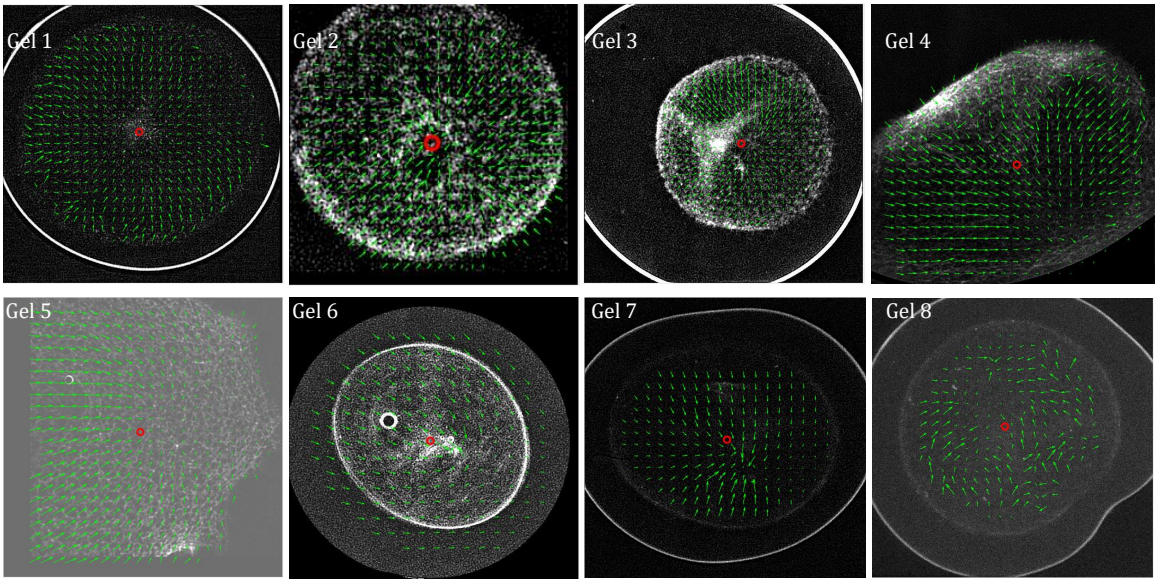

Figure 5.2: **Particle Image Velocimetry (PIV) of active gels obtained from phase contrast images reveals displacements of local regions at short time scales.** The PIV of 8 different analyzed gels is shown here. The green arrows oriented inwards represent displacement vectors and show the direction of contraction. The red circle in the center is the geometric centroid of the gel.

intersect. In most ideal cases, the center of contraction overlaps with the centroid or geometric center of the gel. Gels 1, 2 and 8 (as mentioned in Fig. 5.2) are very good examples of that. In certain cases, the centroid of the gel changes with time (In Fig. 5.2, gel 4 is stuck at a point at the edge of the gel). In those scenarios, the rigid body motion of the gel is subtracted to obtain the displacement vectors with respect to the centroid of the gel which in turn gives a new center of contraction. The rigid body motion is obtained by computing the mean of all displacement vectors associated with the gel. The displacement vectors thus obtained are used to obtain the Cartesian components of the strain tensor, as well as the mean radial and azimuthal displacements and strains.

5.2.2 Strain tensor obtained from the spatial arrangement of displacement vectors

The displacement vectors obtained from PIV are in cartesian coordinates given by (u_x) and (u_y) for x and y directions respectively. The PIV data is obtained at regularly spaced square lattice points, size of which is defined by the diameter of the gel. The different components of the strain matrix given by ε_{xx}, ε_{xy}, ε_{yx} and ε_{yy} are calculated as

follows ([191]):

$$\varepsilon_{xx} = \frac{\partial u_x}{\partial x} \qquad \varepsilon_{yy} = \frac{\partial u_y}{\partial y} \qquad \varepsilon_{xy} = \varepsilon_{yx} = \frac{1}{2}\left(\frac{\partial u_x}{\partial y} + \frac{\partial u_x}{\partial y}\right)$$

where the strains are assumed small with possible geometric non-linearities ignored. The strain matrices for each lattice point of the gel are obtained by implementing the central difference scheme of finite difference method on the displacement vectors (see Appendix C).

Most of the gels are circular disks contracting in an apparent axially symmetric manner. Hence, we consider radial and azimuthal components of the strain to better address this geometric feature of the gels. The strain tensor components obtained in Cartesian coordinates can be converted to 2D polar coordinates. The distance between the center of contraction and each lattice point is given by the radial coordinate, r. The angle ϕ is made by the position vector of each lattice point from the center of contraction with respect to the horizontal :

$$\varepsilon_{rr} = \varepsilon_{xx}\cos^2\phi + \varepsilon_{yy}\sin^2\phi + \varepsilon_{xy}\sin(2\phi) \tag{5.1}$$

$$\varepsilon_{\phi\phi} = \varepsilon_{xx}\sin^2\phi + \varepsilon_{yy}\cos^2\phi - \varepsilon_{xy}\sin(2\phi) \tag{5.2}$$

$$\varepsilon_{r\phi} = \varepsilon_{\phi r} = -(\varepsilon_{xx} - \varepsilon_{yy})\sin(2\phi) + 2\varepsilon_{xy}\cos(2\phi) \tag{5.3}$$

5.3 Results

5.3.1 Area strain reveals regions of contraction and stretching

The 2D heatmaps of bulk area strain are obtained by tracing filled contour plots of the trace of the strain tensor ($\varepsilon_{xx} + \varepsilon_{yy}$) at each lattice point. This measures the net area deformation (contraction or expansion) in each region. We show area strain plots for Gels 1, 3 and 5 (Fig. 5.3). Here, the trace of the strain is normalized by the maximum positive and negative values of trace for the whole gel. All three gels show high intensity blue regions (negative strain) close to the center which correspond to high contraction. Close to the periphery of the gel, there are regions of bright yellow spots corresponding to positive strain. This suggests that the gels are getting stretched close to the boundary.

Even though the PIV of the gel corresponds to global contraction, the strain analysis gives us more information about the local regions. It is important to study the radial dependence of the displacement and the strain because of its apparent axisymmetric

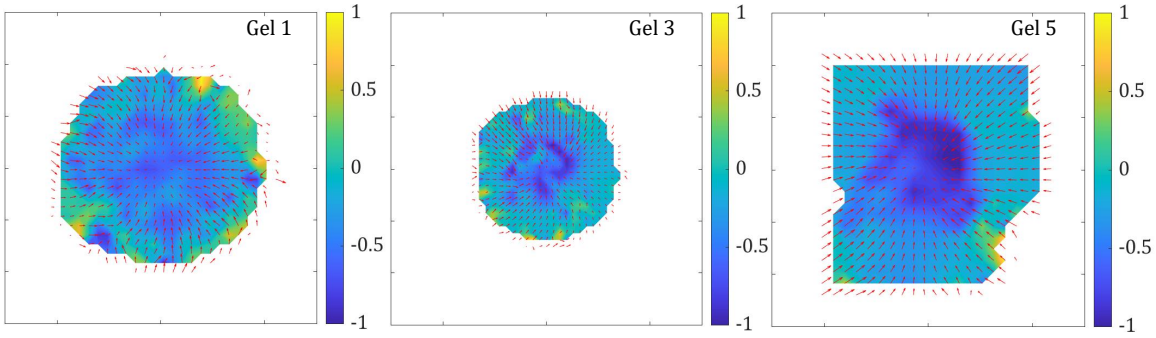

Figure 5.3: **Area strain reveals regions of contraction and stretching.** Area strain (trace of the strain tensor) is shown as heatmaps for Gels 1, 3 and 5 for corresponding frames in Fig. 5.2. The red arrows show the PIV displacements after subtracting the rigid body motion of the gel. The inner region of the gels is highly contracted shown by dark blue regions. Close to the boundary there are patches of stretched regions shown by bright yellow spots. (All strains are normalized by their maximum positive and negative values)

contraction and varying length of displacement vectors from the center of contraction to the periphery.

5.3.2 Radial and azimuthal displacement obtained from axisymmetric assumption of gel contraction

We consider circular annuli of equal thickness from the gel boundary to the center (a total of 25 annular bins) (Fig. 5.4-a). If the gel is not circular around the center of contraction, we consider a smaller region which makes a circular arc at the boundary (for example, Gel 5 is formed from part of a circular gel). In each of these annular bins, there are multiple PIV lattice points. We calculate the mean and standard deviation of the radial and azimuthal displacements in each of these annular bins. To validate our assumption of axisymmetric contraction, we consider azimuthal displacement as a function of the normalized distance from the center of the gel (Fig. 5.4-b) as observed for Gel – 1 (Fig. 5.2). It fluctuates close to 0, suggesting no apparent azimuthal displacement, which supports our assumption of axisymmetric contraction. From the angle-averaged radial displacements in annular bins, we obtain an inner region which shows linear dependence with distance from the center. Closer to the boundary, the radial displacement profile curves up to form a "hockey stick"-like shape suggesting radial stretching. This stretching close to

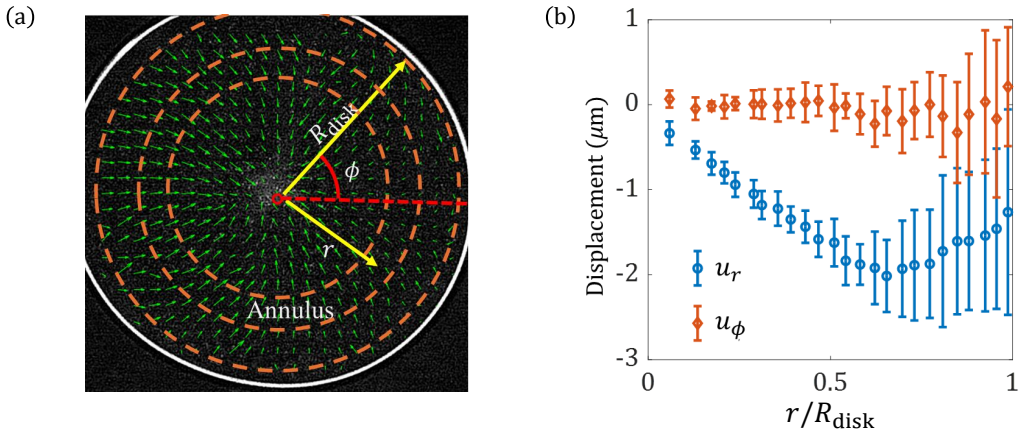

Figure 5.4: **Azimuthal averaging over annular bins gives radial and azimuthal displacement** (a) Circular annular bins are constructed around the center of contraction. The radial and azimuthal components of the displacements are averaged over all angles from center to the boundary. (b) The angle averaged azimuthal displacement (u_ϕ) does not change with distance from the center of the gel and fluctuates close to 0. The angle averaged radial displacement (u_r) increases linearly in magnitude from the center in the inner region and decreases closer to the boundary in the outer region.

the boundary correlates with the observed positive patches of area strain in the plots in Fig. 5.3 (a).

5.3.3 Radial dependence of displacement reveals a boundary layer

This hockey stick behavior is seen in most analyzed gels. The comparison of displacement profile of gels 1 and 3 are shown in *Fig.* 5.5. The time evolution of the radial displacement profile is shown for these 2 gels in Fig. 5.5-a and b. Since each gel is contracting with time, the displacements at different regions of the gel becomes smaller at higher times. The position at which the radial displacement profile curves up relative to disk size does not change much with time. The normalized length between this turning point at the boundary, denoted by δ/R_{disk}, remains constant for individual gels.

We estimate R_{disk} and δ at every frame from the radial displacement profile, plotted together in Fig. 5.5-c and d respectively for gels 1 and 3 . Here, we note that the radius of the gel decreases with an exponential of time constant 26.32s for gel 1 and 55 s for gel 3 (Fig. 5.5-c and d). Interestingly, we note that in majority of the time during its

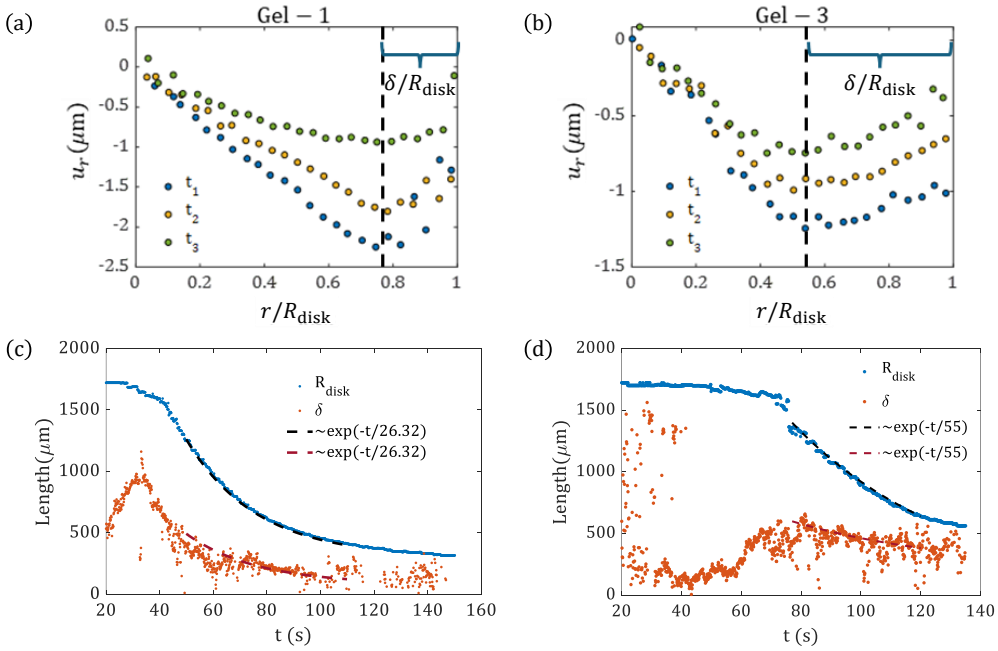

Figure 5.5: **Time dependent comparison of radial displacements (u_r) for different gels** (a,b) Radial displacement profiles of gels 1 and 3 respectively at times $t_1 < t_2 < t_3$ are plotted with respect to the normalized distance (r/R_{disk}) from center to the boundary. The magnitude of u_r decreases from that at t_1 to t_3 but the normalized boundary length δ/R_{disk} remains constant for both gels. (c,d) Both the radius of the gel and the boundary length δ decrease exponentially with the same time scale.

signature hockey stick contraction profile, the boundary region δ also decreases with the same time constant as the gel radius itself, indicating a single contraction time scale in each experiment, which is likely related to the poroelastic time scale for stress diffusion and solvent outflow .

5.3.4 Analysis of radial strain profile reveals active stress distribution

Here we study the time evolution of angle averaged radial and azimuthal strains (Fig. 5.6). At any given time, the radial and azimuthal strains are equal and constant close to the center of the gel. This suggests that the gel is contracting isotropically close to the center. There is no apparent alignment of actin fibers close to the center (Fig. 5.7-b) which upon contracting gives isotropic contraction. As we go close to the boundary, the radial strain gradually becomes positive suggesting radial stretching. But the azimuthal strain, while close to 0, is still negative. This suggests that there is some azimuthal contraction

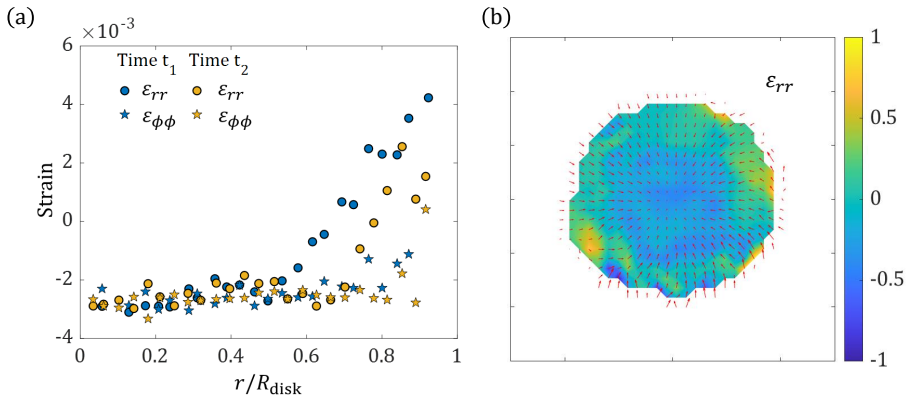

Figure 5.6: **Strain plots reveal a contracting inner region and a stretched outer region** (a) Angle averaged radial and azimuthal strain plots are shown for Gel 1 at times $t_1 < t_2$. Close to the center, the radial and azimuthal strains are constant and equal in both gels, suggesting isotropic contraction. In the transition region, there is a gentle increase in radial strain which becomes positive close to the boundary, suggesting possible stretching. The azimuthal strain increases and approaches 0 close to the boundary. (b) 2D plot of radial strain for gel 1 shows the local strains as estimated from the center of contraction.

close to the boundary. Even at longer times, the magnitude of the strain close to the center remained the same. This suggests that the contraction rate close to the center does not change with time. This contraction behavior is also observed from the radial strain heatmap of the gel (Fig. 5.6). The inner region shows constant negative strain while close to the boundary, the strain is positive.

5.3.5 Predicted contraction phenomenon from analysis of strain

It has been observed in experiments that the actin fibers align azimuthally closer to the boundary (Fig. 5.7-a). This alignment is expected from the onset of contraction at the boundary, and from the relative freedom of polymers to fluctuate when parallel to the boundary . The alignment of the actin fibers dictates the orientation of myosin attachment and therefore, that of contractile active stresses. We explore the eigenvalues and eigenvectors of the strain tensor to determine the principal directions of stretching and contraction. We show the maximum magnitude eigenvalue of gel 5 plotted as heatmap in Fig. 5.7-b. The eigenvectors corresponding to these eigenvalues are shown by the arrows on top of the heatmap and give the direction of contraction. We find that, the alignment is

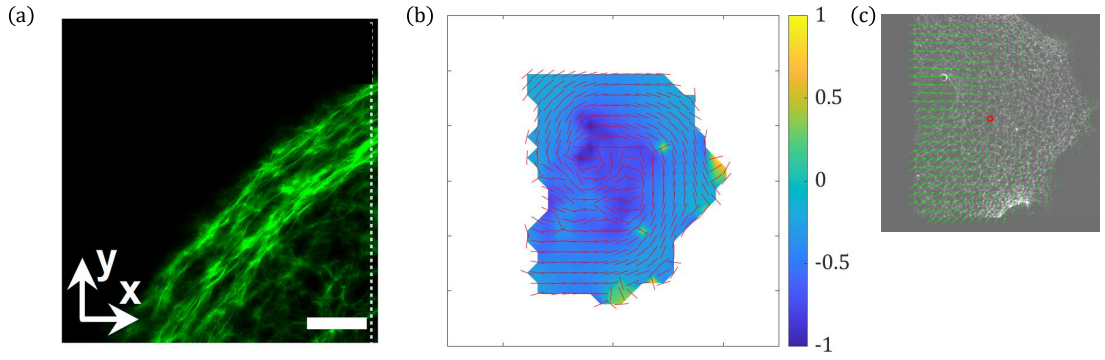

Figure 5.7: **Gel contracts azimuthally close to the boundary** (a) Confocal image of gel reveals an azimuthally aligned region of actin fibers suggesting azimuthal contraction (b) Eigenvalue and eigenvector analysis of area strain gives the principal directions of contraction and stretching. Azimuthally aligned eigenvectors close to the boundary suggests azimuthal contraction while eigenvectors pointing in random directions close to the center suggest an isotropic contraction core.

azimuthal close to the boundary, suggesting azimuthal contraction (associated eigenvalues are negative). Close to the center of contraction of the gel, there is no apparent direction of alignment. The corresponding PIV for this frame is shown in Fig. 5.7-c . Although this is shown for a gel -5, this is a general behavior that is observed in other gels as well.

After exploring and analyzing the contraction directions and behaviors of the gel we propose a theoretical model for the contraction process. The contraction of the gels arises from myosin motors pulling on the cross linked actin fibers and generating forces. As discussed in earlier chapters, the contractile units of actomyosin can be modeled as force dipoles embedded in an elastic medium, which here corresponds to the elastic network of crosslinked actin fibers. In case of axisymmetry, there is only radial displacement, and the radial and azimuthal strain components are given by

$$\varepsilon_{rr} = \frac{\partial u_r}{\partial r}, \tag{5.4}$$

$$\varepsilon_{\phi\phi} = \frac{u_r}{r}. \tag{5.5}$$

In the case of isotropic contraction, *i.e.* when there is no apparent alignment of actin fibers, there is equal contraction in all directions. The radial and azimuthal strains

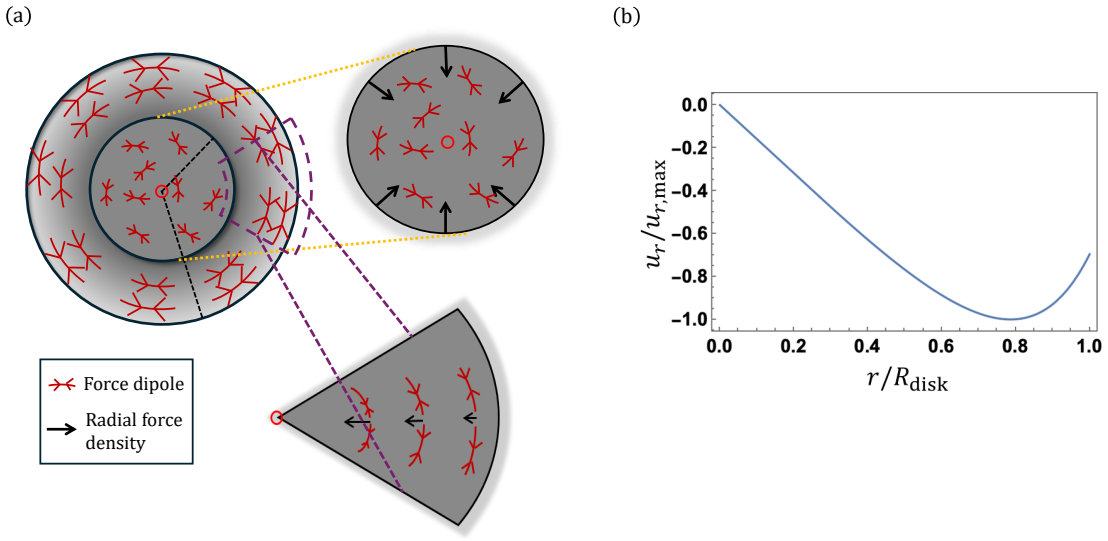

Figure 5.8: **Proposed contraction model as interpreted from analysis of PIV of gels** (a) This is the proposed schematic for gel contraction with axisymmetry. Each contractile actomyosin unit produces an active stress in the gel, which maybe considered as a force dipole. Close to the boundary, the alignment of stress generated by actin fibers, is represented by contractile force dipoles. These are aligned azimuthally, *i.e.* parallel to the the boundary of the gel. In the inner region there is no specific alignment of force dipoles leading to isotropic contraction. The resulting active forces from the force dipoles at different local regions of the gel are shown by black arrows in the insets. In an overdamped elastic contraction model, these forces direct the local displacement of the gel. (Top inset) Due to isotropic distribution of the force dipoles, the net force at any location in the inner region is 0. But at the edge of the isotropic region, there is an unbalanced force pointing radially inwards (Bottom inset) Due to the azimuthal alignment of the force dipoles, there is an inward pointing unbalanced radial force. The force decreases as $1/r$ from the center, due to the curvature in the direction of alignment of the force dipoles. (b) Analytically calculated radial displacement profile for the model reproduces characteristic "hockey-stick" shape found from the PIV analysis of experimental data. The inner isotropic region shows linear increase in magnitude of displacement. Closer to the boundary, the magnitude of displacement reduces, since the force gets smaller.

are expected to be equal and constant:

$$\frac{\partial u_r}{\partial r} = \frac{u_r}{r} = C. \tag{5.6}$$

This corresponds to linear dependence of radial displacement with distance from the center. This is indeed the behavior seen from the PIV analysis (refer to Fig.5.6 - a) in the inner region of the contracting gel.

In the isotropic region, the force dipoles do not have any specific alignment. The net contractile force generated in the whole isotropic region vanishes, since equal force dipoles cancel each other in the bulk. At the boundary of the isotropic region, there is some unbalanced radial force, oriented towards the center (Fig. 5.8). This is different from the radial alignment of force dipoles, since in that case, there is an unbalanced stretching force throughout, including at the center .

Considering only azimuthal alignment of force dipoles in the outer region of the gel, the curvature of the azimuthal alignment of force dipoles leads to unbalanced radial forces (refer to Fig. 5.9(a)). This radial force is proportional to the curvature of the circular contour lines, and therefore is inversely related to radial distance from the center ($Force \propto 1/r$). The force at the boundary of a large disk is thus very small compared to the center. Hence, the displacement vector becomes small close to the boundary. The center of the gel is fixed so there is no displacement. So we expect that the magnitude of the displacement to increase with r and then decrease close to the boundary, as seen in Fig. 5.9(a). With this model of isotropic inner region and azimuthal alignment at the boundary, we can explain the hockey stick behavior of the radial displacement of the gel. This phenomenon can be analytically understood through an active elastic model that integrates the orientational order of filaments in an active gel with elastic deformations and motor-induced active stresses. The model illustrates how strain-induced alignment, represented as a nematic order parameter, directs active stresses to form deformation patterns. Consequently, there is a feedback loop between active stresses, elastic deformation, and nematic order, leading to self-organized deformation and alignment above the nematic-isotropic transition point. The results for elastic displacement and alignment profiles are similar to those obtained from experimental actomyosin gel disks using PIV analysis and microscopy imaging of fiber alignment.

Nematic order can be quantified by a order parameter tensor $\mathbf{Q}$ which comprises of average direction of order (director field $\overleftrightarrow{n}$) and magnitude S:

$$Q_{ij} = S(n_i nj - \frac{1}{2}) \tag{5.7}$$

where $\mathbf{Q}$ is a symmetric traceless tensor and can be represented in cartesian coordinate as: $\mathbf{Q} = \begin{pmatrix} q_1 & q_2 \\ q_2 & -q_1 \end{pmatrix}$ where two components are two scalars q_1 and q_2. The magnitude of Q gives quantitative scalar value of nematic order and it can be calculated simply as

$S = \sqrt{q_1^2 + q_2^2}$.

Strain tensor due to pulling of myosin motors in the actin filament network is denoted by $\varepsilon_{ij} = \frac{1}{2}(\partial_i u_j + \partial_j u_i)$, where u_i is displacement of the network. The elastic stress due to the strain in the network is given by

$$\sigma_{ij}^{el} = F_{el}\varepsilon_{ij} = 2\mu(\varepsilon_{ij} - \frac{1}{2}\delta_{ij}\varepsilon_{kk}) + K_b\varepsilon_{kk}\delta_{ij} \tag{5.8}$$

where K_b is bulk modulus and and μ is shear modulus. Active stress due to the nematic alignment Q is given by $\sigma_{ij}^{active} = A(\delta_{ij} + Q_{ij})$. Here, A is the strength of the active forces generated in the disc. We consider that the active forces have a radial dependence and are not constant throughout the gel. We obtain the total stress by combining the elastic and the active components of the stress

$$\sigma_{ij}^{total} = \sigma_{ij}^{el} + \sigma_{ij}^{active} \tag{5.9}$$

We obtain the different components of the total stress tensor in polar form as

$$\sigma_{rr}^{total} = (K_b + \mu)\,\varepsilon_{rr} + (K_b - \mu)\,\varepsilon_{\phi\phi} + A\,(1 + Q_{rr}) \tag{5.10}$$

$$\sigma_{\phi\phi}^{total} = (K_b - \mu)\,\varepsilon_{rr} + (K_b + \mu)\,\varepsilon_{\phi\phi} + A\,(1 + Q_{\phi\phi})\,, \tag{5.11}$$

where K_b and μ are the bulk and shear moduli of an isotropic, homogeneous and linear elastic medium in 2D.The other components of the strain tensor are 0 in the axisymmetric situation and thus the corresponding stress components vanish as well. Thereafter, we calculate the displacement from the divergence of stresses using,

$$\gamma\partial_t u_i = \partial_j\sigma_{ij}^{total} = \partial_j(\sigma_{ij}^{el} + \sigma_{ij}^{active}) = K_b(\partial_i\partial_j u_j) + \mu\partial_j^2 u_i + A\partial_j Q_{ij}, \tag{5.12}$$

which is a statement of force balance in the system. The left hand side of the equation corresponds to frictional forces generated on the gel by surrounding solvent (γ is a friction constant), and the right hand side contains elastic and active forces, respectively. The solvent flow is assumed to be very small, which is the elastic limit of a poroelastic model. This is justified over short time scales compared to the poroelastic time scale (*i.e.*, the fluid does not have enough time to flow out). The solvent flow is also small when the gel fraction is very small compared to the fluid fraction, which is indeed the case in the actomyosin gels, at least in the early stages of contractions. With proper boundary conditions for displacement and elastic stress, and nematic alignment parameter, and also modulating the activity parameter (A) we obtain the radial profiles of displacement and strains, which resemble the characteristic profiles obtained from the PIV analysis of experimental data.

5.3.6 Differentiating domes from wrinkled gels

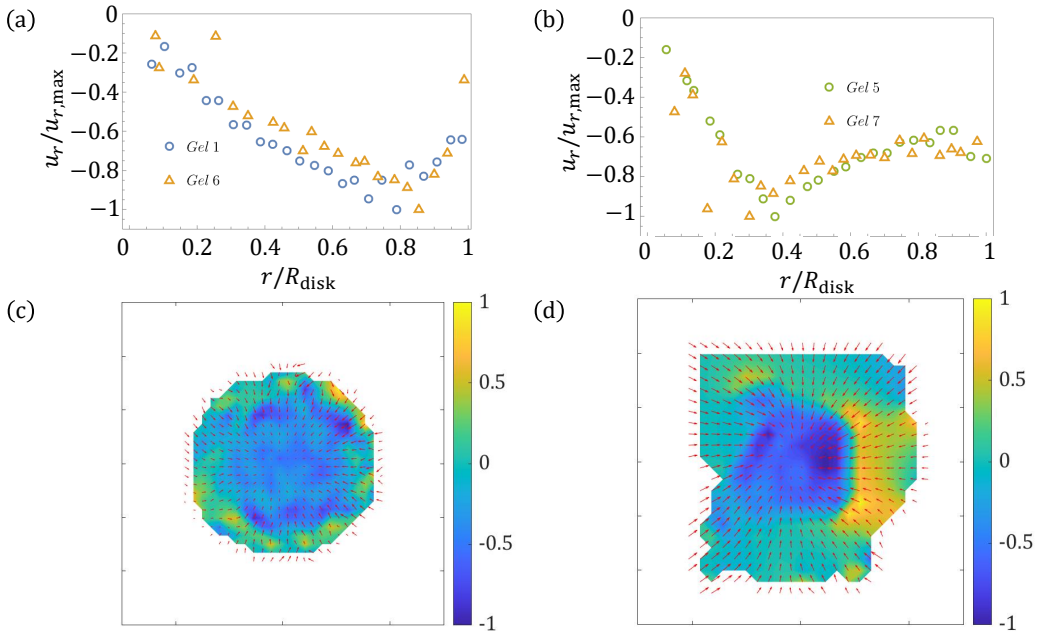

Figure 5.9: **Differences in radial displacement and strain profiles dictate formation of different gel morphologies**(a,b)The radial displacement profiles obtained from PIV analysis of different gels shows the contrast in curvature between "domes" and "gels" as predicted by the model. (c) The radial strain heatmap of Gel - 1 shows inner radial contraction region and gentle in increase in radial strain close to the boundary in case of "dome". (d) The radial strain heatmap for wrinkles (Gel - 5) shows a sharp increase in radial strain from inner to outer region and then a gentle decrease close to boundary. (All strains are normalized by their maximum positive and negative values)

We address the reason for the distinct final morphologies, namely domes or wrinkles obtained for the different gels. To do so, we compare the radial profiles of displacements and strains. In case of gels 1 and 6 that give dome structure (as observed by confocal microscopy), the radial profile of the radial displacements show a gentle decrease of magnitude and positive curvature from the turning point (Fig. 5.9-a). This is noticeably distinct from the cases of Gels 5 and 7 which give final wrinkled structures (Fig. 5.9-b). The radial profile of radial displacement shows an initial sharp increase at the turning point, and the magnitude of displacement decreases slowly.

The radial strain analysis of the gels allows a concrete distinction between the two morphologies. In case of a dome, the radial strain shows a gentle increase from a negative value at the isotropic core to a positive value close to the boundary (Fig. 5.9-c). The radial

strain in case of wrinkles, shows a sharp increase from the isotropic core to a positive value and then gently decreases to zero close to the boundary (Fig. 5.9-d).

The contraction of gels have distinct dynamics which can be classified as dome-like contraction (which comprise of domes and 2 peak saddle gels) and wrinkle-like contraction (which show 1 or more wrinkles). Experimentally, it has been observed that the gels with dome-like contraction begin to contract radially inwards from the boundary, squeezing the fluid out of lateral surfaces of the gel, before showing vertical contraction [81]. The wrinkled gel initially contracts in the vertical direction, squeezing out fluid predominantly through the upper and lower surfaces before contracting in the radial direction. We observe that the dynamics of the radial displacement profile also show a distinct behavior for these dome-like (Gel 1 and 6) and wrinkle-like gels (Gel 5 and 7).

We are currently extending our model to include poroelastic effects, that is the coupling of elastic gel deformation and solvent flow [284], to potentially explain the radial displacement profiles corresponding to the wrinkle-like cases (gels 5 and 7). These gels clearly contract much faster in the inner isotropic region, resulting in excess circumference and a wrinkled shape. However, we are yet to theoretically explain the extent of the inner isotropic region and its rate of contraction. We hypothesize that this is due to predominant fluid outflow through the top and bottom surfaces in the thinner gels. So, we require a dynamic model, going beyond the present quasi-static model used in Eqns. 5.12, to capture this effect.

5.3.7 Locating wrinkles in gel

Once we identify the expected final morphology of the gel, we expect to locate the position of wrinkles, if any. At the onset of wrinkle formation, the azimuthal components of the PIV displacement vectors show azimuthal dependence as shown in (Fig. 5.10-a). The green region in the schematic shows high azimuthal strain. This phenomenon is temporary and will die down after a wrinkle is formed. Gel-5 shows wrinkle formation at the boundary and can be associated with high concentration of accumulation of actin fibers than its neighboring regions as pointed by the big white arrows (Fig. 5.10-b). The angle dependence of azimuthal strain is shown between angles $-\pi/3$ and $\pi/3$ (Fig. 5.10-c). It clearly shows high magnitude of azimuthal strain at the locations where wrinkles are forming. The azimuthal strain is calculated by averaging over 10 frames so that any fluctuations in azimuithal strain dies down.

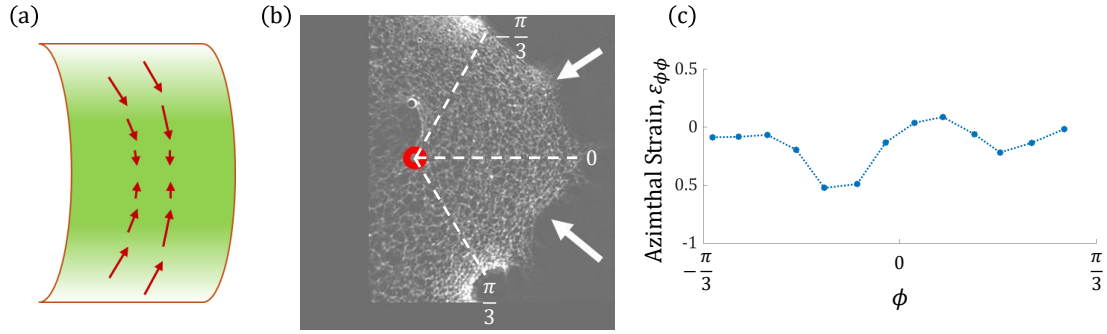

Figure 5.10: **Azimuthal strain reveals formation of wrinkles** (a) Temporal and spatial variations in PIV vectors can lead to high azimuthal strain demarking the onset of formation of wrinkles. (b) Thickening of actin bundles is observed in the phase contrast image of the gel at the locations indicated by the big white arrows. (c) Azimuthal strain at the boundary increases in magnitude at the locations where a wrinkle is forming which is observed at two angular regions between $-\frac{\pi}{3}$ and $\frac{\pi}{3}$

5.4 Discussion

In this chapter, we show analysis of the displacement and strain profiles of different gels and address the different possible pathways an active gel contracts to attain different morphologies. We consider the radial profile of radial displacement under the limit of axially symmetric contraction and observe the hockey stick shape behavior. The inner region with linearly decreasing displacement suggests a core of isotropic contraction of the gel. This behavior is also observed from radial dependence of radial and azimuthal strains which are negative, constant and equal. The radial displacement profile changes slope close to the boundary and becomes positive. This suggests a radially stretched boundary region that is clearly shown by the radial strain profile becoming positive close to the boundary. On the other hand, the azimuthal strain is still negative, suggesting azimuthal contraction which corresponds to high azimuthal alignment of actin filaments close to the boundary. This was confirmed by the experimental image of the actin alignment and principal direction of contraction (eigenvector analysis) close to the boundary.

Thereafter, we propose a schematic to show the axisymmetric contraction phenomenon of gel. This shows an inner isotropic core, *i.e.* no apparent alignment of stresses which gently transitions to an azimuthally aligned region close to the boundary. We see

that the alignment of the stresses is not enough to determine the final morphology of the gel. It has been observed in experimental images in Ref. [60] that thicker poroelastic active gels contract laterally before contracting vertically. On the other hand, the thinner gels contract longitudinally before it contracts laterally. This leads to differential alignment of actin fibers in the contraction process of different morphologies of gels. Hence, we hypothesize that there is difference in activity between the different types of gels. In the case of dome, the difference in contraction between the inner region and the boundary region is very small, while in case of wrinkles, there is a very big difference between the activity of the inner and the outer regions. This hypothesis can be validated with analytical modeling of contraction of gels. In the end, in this work we were also able to locate the position at which new wrinkles are formed from the analysis of its azimuthal strain.

The theory of linear elasticity helps us to understand the phenomenon of gel contraction and validates some of our hypothesis. The elastic model is well suited for very slowly contracting gels, such as domes. But we need to model dynamics for the rapidly contracting gels like the wrinkled ones. We cannot understand everything from elasticity theory, which is quasi-static, for example, the location of the turning point and the inverse curvature of the boundary region in wrinkled gels as compared to domes. To address these questions, we need a more dynamic model (poroelastic model), *i.e.*, including the elastic outflow of the solvent as the gel contracts. We will explore the effect of poroelasticity in our future work.

Chapter 6

Conclusions

In this work, I have explored the importance of actomyosin cytoskeletal network in cell migration and generating elastic stresses on substrates mediating cell–cell interactions and defining shapes in active gels.

In Chapter 2, using our model for cell contractility and motility, we computed several metrics related to cell interactions. These metrics include the number of cell-cell contacts, the mean square displacement of motile cells influenced by elastic deformations from neighboring cells, and capture statistics resulting from attractive interactions between two cells. The computed metrics depend on the elastic properties of the substrate. Specifically, the interaction parameter ($\alpha \sim 1/E$) captures the strength of the mechanical forces. The effective diffusivity (D_{T}) represents cell motility. Interestingly, our results support the hypothesis that purely mechanical cell-cell interactions can lead to mutual contact without relying on specific chemical factors to guide cell movement. Our model predicts that substrate stiffness plays a crucial role in guiding cell motility and shaping multi-cellular structures. We then explore the anisotropic interaction between cells interacting by means of elastic substrate deformation and study the collective behavior captured by it.

In Chapter 3, we explore how passive interactions between dipolar cells cause them to align end-to-end, forming motile chains. These chains can further organize into polar bands and clusters due to their active motion. When polar chains move in opposite directions, they naturally segregate into separate bands to avoid interference. Although our model specifically demonstrates this behavior for elastic dipoles, it applies to a broader category of active particles with dipolar interactions [177, 178, 205]. Experimental realiza-

tion of these phenomena is possible in active colloids equipped with permanent or induced dipole moments[176, 206]. In particular, at higher Poisson ratios, the symmetry of elastic dipolar interactions changes [130], potentially leading to structures such as actively rotating rings. We further note that the mechanical interactions between cells in elastic media is in reality expected to include effects not considered here including from the nonlinear elastic properties of the substrate and nonlinear effects arising from the cells actively maintaining mechanical homeostasis at their boundaries, such as by regulating their shape [137]. We also ignore the elastic response of the cells themselves, which can cause additional interactions similar to those between rigid inclusions in soft media [207].

In Chapter 4, we studied the effect of elastic interactions with mechanical boundaries, namely free and clamped boundaries to address durotaxis, a process by which cells preferentially migrate towards the stiffer side of the substrate. Our model is motivated by and explains the key observation in one of the first demonstrations of durotaxis [3]. The elastic forces and torques resulting from the elastic potential drive the cells to orient perpendicular (parallel) to the boundary and accumulate (deplete) at the clamped (free) boundary. The clamped boundary that induces an attractive potential drives durotaxis, while a free boundary that induces a repulsive potential prevents anti-durotaxis. By quantifying the steady-state positional and orientational probability densities, we show how the extent of accumulation (depletion) depends on the strength of the elastic potential and motility. While the elastic interaction drives durotaxis, cell migratory movements such as random reorientation and self-propulsion enable escape of the cell from the attractive elastic potential thereby reducing durotaxis. We distinguish between and calculate the mean escape time for weak and strong regimes of the elastic potential: escape through self-propulsion following reorientation away from the confining boundary and through random translational protrusions, a scenario captured by a modified Kramer's theory of barrier crossing.

To study the escape phenomenon of cells from clamped boundaries we propose experiments with micropatterned substrates with sharp gradient of substrate stiffness that correspond to clamped or free boundary conditions in simulations[285, 286]. The micropatterning is done so that there are no adhesion sites on the stiff side of the substrate to ensure only a clamped boundary interaction. Cell migratory behavior and escape time can be analyzed from trajectories close to the stiffness gradient. We further define metrics quantifying boundary accumulation and durotaxis, and present a phase diagram that identifies three possible regimes: durotaxis, adurotaxis without accumulation, and adurotaxis

with motility-induced accumulation at a confining boundary. Cells moving on elastic media are not very persistent, hence, the motility induced accumulation phase is physiologically unattainable for motile cells. We suggest micro patterning the substrate such that cells can only move along the track (like a race track experiment)[287, 288], which will increase the persistence of the cells.

Overall, our model predicts how durotaxis depends on cell contractility and motility, and successfully explains some of its aspects seen in previous experiments while providing testable predictions to guide future experiments.

In Chapter 5, we study how myosin motor-induced forces in the actin cytoskeleton are responsible for changes in cell and tissue shape in living systems. We consider in vitro experiments where a set of actomyosin gel disks spontaneously contract and buckle into a family of initial-geometry dependent, 3D shapes ranging from domes to wrinkled. We observe azimuthal alignment of actin fibers at the boundary of the gel as a response to contraction and densification. This alignment is crucial to setting up the in-plane strain profile and ensuing contraction dynamics of the gel.

A main contribution of this thesis has been to the analysis of particle imaging velocimetry (PIV) data on gels of different initial shapes to obtain the in-plane distribution of elastic strains. Resolving the radial and azimuthal components of the strain reveals the robust occurrence of an inner isotropic contracting region, surrounded by an outer region with radial stretching. Comparison with a model for active stresses in elastic disks allows us to infer an outer region with azimuthal-aligned force dipoles representing myosin activity. Our findings support the hypothesis that this differential distribution of active stresses arises from the local alignment of actin bundles induced by contraction along the gel boundary. Future work will reveal how the in-plane strain distribution determines the final 3D buckled shapes. We will aim to predict the dynamic pathways for the formation of domes, wrinkles, or intermediate shapes, based on the strain profiles. According to our current hypothesis, this may be done by modeling the poroelastic dynamics of actively contracting gels.

Appendix A

A.1 Model for a moving cell interacting with a stationary cell via substrate elasticity

The flat substrate is treated as being semi-infinite (Figure 1) and comprised of a linearly elastic, isotropic gel-like material with Young's modulus E and Poisson's ratio ν, that capture its stiffness and compressibility respectively. The minimal model that describes the deformations created by cells exerting contractile forces on the substrate is a point-like force dipole [6]. Two identical dipolar cells denoted by A and B move in the upper plane (chosen to be the x-y plane, see Figure 1). Cell A is allowed to move and its dynamics is specified completely by its location on the substrate $\mathbf{r}^A(t)$ and by its self-propulsion direction $\mathbf{e}^A(t)$. Cell B is held fixed at point $\mathbf{r}^B$. As a result of the contractile dipoles exerted on the substrate the cells communicate elastically. The potential W^{AB} characterizing this elastic interaction between the two cells is given by

$$W^{AB}(\mathbf{r}) = P^2 e_j^B e_i^B \partial_j \partial_l G_{ik}^{AB}(\mathbf{r}) e_k^A e_l^A, \quad \text{with} \quad \mathbf{r} = \mathbf{r}^A - \mathbf{r}^B, \tag{A.1}$$

where P is the strength of the force dipole capturing the contractile stresses exerted by a cell on the medium. In writing (A1), we have made the plausible assumption that cells orient their cytoskeletal structures such as stress fibers and exert their traction primarily along their motility axis, such that the force dipole tensor, which captures the moment of their force distribution, is assumed to be, $P_{ij} = P e_i e_j$. The tensor

$$G_{ij}^{AB}(\mathbf{r}) = \frac{1+\nu}{\pi E}\left[(1-\nu)\frac{\delta_{ij}}{r} + \nu\frac{r_i r_j}{r^3}\right], \tag{A.2}$$

is the Green's function that captures the displacement in the elastic medium at the location of one cell (dipole) caused by the application of a point force at the location of the other

[191]. The partial derivatives in (A1) on the right hand side are taken with respect to relative position vector $\mathbf{r}$. Standard Einstein notation has been chosen in writing the form of W^{AB} and the derivatives in equations (A1) and (A2).

To obtain the force and torque balance equations that govern the dynamics of cell A, we make the simplifying assumption that the cells move in an overdamped fashion. This implies that hydrodynamic interactions between cells are ignored, and that each cell feels a resisting viscous frictional drag/torque that is proportional to its velocity/rotation rate. Conversely, when acted on by a force $\mathbf{F}$ or a torque $\mathbf{T}$, a cell in this overdamped environment will move with velocity $\mu_T\mathbf{F}$ or rotate at a rate $\mu_R\mathbf{T}$ respectively. Here, μ_T and μ_R are appropriate mobility terms that depend on the cell size.

The micro-dynamics of cell A moving on the substrate is governed by the Langevin equations for the translation and rotary motion of cell. Recognizing that the elastic interaction generates (extra) forces and torques that act on each cell, and including the effects of fluctuating time dependent forces $\boldsymbol{\xi}^T(t)$ and torques $\boldsymbol{\xi}^R(t)$ originating from thermal noise, we can write the equations for the position and orientation of cell A in the presence of cell B as

$$\frac{\partial \mathbf{r}^A}{\partial t} = v_0\mathbf{e}^A - \mu_T\frac{\partial W^{AB}}{\partial \mathbf{r}^A} + \mu_T\boldsymbol{\xi}^T(t), \quad \text{and} \tag{A.3}$$

$$\frac{\partial \mathbf{e}^A}{\partial t} = -\mu_R\left(\mathbf{e}^A \times \frac{\partial W^{AB}}{\partial \mathbf{e}^A}\right) + \mu_R\boldsymbol{\xi}^R(t). \tag{A.4}$$

In an equilibrium situation, the random forces and torques are white noise terms and are related to one another by the equipartition and fluctuation-dissipation theorems: $\langle\boldsymbol{\xi}^T(t)\boldsymbol{\xi}^T(t')\rangle = (2k_BT/\mu_T)\boldsymbol{\delta}\delta(t-t')$ where $\boldsymbol{\delta}$ is the Kronecker delta function. For active cells however, these restrictions do not hold; these terms are set by active internal cell responses to the substrate properties. Equations (A1-A4) are used in the results illustrated in Figure 5.

In the bulk of the paper and for results presented in Figures 1-4, we use an isotropic version of the potential in equation (A1) that ignores orientational dynamics that are in general present for highly elongated cells. This assumes a separation of scales between the time over which cells reorient and the dipole axis changes and the time for the center of the cell to move significantly such as when the rotation noise in (A4) is significant. In this limit, one can average over the rapid reorientations of the cells and replace $e_j^B e_i^B$ by δ_{ij} and $e_k^A e_l^A$ by δ_{kl}. Equation (A1) then reduces to the simpler form that we employ in the main

discussion of the paper and implement as a numerical simulation,

$$W^{AB}(\mathbf{r}) = P^2 \partial_i \partial_k G^{AB}_{ik}(\mathbf{r}) = \frac{P^2}{E} \frac{\phi(\nu)}{r^3} \tag{A.5}$$

with the function $\phi(\nu) = (1 - \nu^2)/\pi$ dependent solely on the Poisson ratio, and hence fixed in the simulation. Furthermore, since the dipole axis of cell A reorients in time scales much faster than its slower rate of translation, the $v_o \mathbf{e}^A$ term in (A3) simplifies to a time fluctuating variable with a mean that is roughly zero but with a non-zero variance. Thus its net effect may be incorporated by appropriately modifying the translational diffusivity. For an isotropic symmetric potential as here, the equation that needs to be solved is then

$$\frac{\partial \mathbf{r}}{\partial t} = -\mu_T \frac{\partial W^{AB}}{\partial \mathbf{r}} + \mu_T \boldsymbol{\xi}^T_*(t), \tag{A.6}$$

with the modified random force $\boldsymbol{\xi}^T_*$ reflecting an effective translational diffusivity D_{eff} different from the thermal diffusivity D_0, through a relation, $\langle \boldsymbol{\xi}^T_*(t) \boldsymbol{\xi}^T_*(t') \rangle = (D_{\text{eff}}/\mu_T^2) \boldsymbol{\delta} \delta(t - t')$. We define the dimensionless number $D_T \equiv D_{\text{eff}}/D_0$. Consistent with this, we choose $\mu_T = D_{\text{eff}}/k_B T$.

Appendix B

B.1 Model for substrate mediated cell-interface interactions

Adherent cells exert dipolar contractile stresses on the underlying elastic substrate; these are generated by actomyosin fibers (actin and myosin II complexes), usually referred to as stress fibers, that generally connect the opposite sides of the cell and terminate at focal adhesions (FAs) [289, 215, 290]. On a larger scale, the entire contractile cell can be represented as a force dipole that deforms its extracellular environment typically modeled as a linear elastic continuum [215, 51]. The concept of force dipoles has found wide-ranging applications in various biological phenomena. [130, 6, 291, 79, 215, 292, 215, 230, 215, 293, 215].

Here, we use the force dipole concept and extend current theory to the interactions of active, motile cells with an underlying elastic substrate and constrained to remain within a domain (with boundaries) using a combination of simulations and analytical theory. In this minimal model, the entire, polarized cell, is coarse-grained and approximated as a single, evolving force dipole that moves on an elastic substrate, and is further subject to forces generated due to its interaction with the substrate and its boundaries. For the purposes of the analysis however, we use the word active to specifically mean self-propelling cells. Given the assumption of isotropic linear elasticity of the extracellular material, and the strength and orientation of the cell generated dipole, we can calculate stress and strain fields by solving the elastic equations with appropriate boundary conditions. These stress/strain fields then affect the motion of the cell by allowing cells to re-orient towards preferred alignments in order to optimize the deformation energy generated by the dipole in the substrate. Two canonical reference cases, namely 1) free boundaries, where the normal traction vanishes at the stiff-soft boundary (useful to analyze cells located on stiffer side), and 2) clamped bound-

aries, where the displacements vanish at the stiff-soft boundary (relevant to cells initially located on softer side) are analyzed. Such reduced descriptions are particularly appropriate when the stiffness contrast is high. The corresponding elastic boundary value problems with these limiting boundary conditions can be solved using the method of images [6].

In general, the interaction energy of the adherent cell (force dipole) with the surface [6] scales as $U \sim P^2 f_\nu(\theta)/(Ex^3)$, where f_ν is a function of substrate Poisson's ratio ν, and the orientation of the cell relative to boundaries. Here, the spatial and angular coordinates x and θ are as defined in Fig. 4.2. The substrate mediated elastic cell-boundary interaction can be modeled as an effective potential $U(x,\theta)$ acting on the adherent cells (generating a force dipole) thus,

$$U(x,\theta) = -\left(\frac{P^2}{256\pi E}\right)\frac{f_\nu(\theta)}{(x+\sigma)^3},$$
$$f_\nu(\theta) = a_\nu + b_\nu \cos^2\theta + c_\nu \cos^4\theta,$$

with P being the force dipole, E and ν being the Young's modulus and Poisson's ratio of the substrate, respectively. The parameters a_ν, b_ν, c_ν are different for free and for clamped boundary conditions. These are, respectively (with superscript f denoting free, and superscript c denoting clamped)

$$\begin{aligned}
a_\nu^f &= -\frac{(1+v)[5+2v(6v-1)]}{(1-v)},\\
a_\nu^c &= \frac{(1+v)[15+32v(v-1)]}{(1-v)(3-4v)}\\
b_\nu^f &= -\frac{(1+v)[22+4v(2v-9)]}{(1-v)},\\
b_\nu^c &= \frac{(1+v)\left(34+32v^2-72v\right)]}{(1-v)(3-4v)}\\
c_\nu^f &= -\frac{(1+v)\left[13(1-2v)+12v^2\right]}{(1-v)},\\
c_\nu^c &= \frac{(1+v)(7-8v)}{(1-v)(3-4v)}
\end{aligned} \tag{B.1}$$

Preferred cell orientations, as predicted by calculating configurations that minimize deformation energy, are parallel/perpendicular to the boundary line for free/clamped boundaries. Hypothesizing that this holds even for motile cells, and accounting for the effects of self-propulsion, we deduce that motile cells preferentially move toward a clamped boundary, but tend to migrate away from a free boundary.

In addition to elastic effects, boundaries may physically constrain cells from cross-

ing. This constraint is implemented by explicit displacements of the cells, as explained in the next section.

Table B.1: List of biophysical parameters.

Parameter	**Meaning**	**Value(s)**
σ	Cell diameter	$10 - 100$ μm
v_0	Cell velocity	$0 - 80$ μm hr^{-1}
μ_T	Translational Mobility	0.1 m^2 min^{-1} pN^{-1}
μ_R	Rotational Mobility	25 μm^2 min^{-1}
D_{eff}	Rotational Diffusivity	$0.01 - 0.1$ min^{-1}
E	Young's modulus	$0.5 - 100$ kPa
ν	Poisson's ratio	0.3
P	Contractility	$10^{-12} - 10^{-11}$ N $\cdot$ m

Table B.2: List of simulation parameters.

Parameter	**Meaning**	**Definition**	**Value(s)**
A	Cell-boundary force parameter	$\frac{\mu_T P^2}{(E D_T \sigma^3)}$	$0.1 - 100$
B	Cell-boundary torque parameter	$\frac{\mu_R P^2}{(E D_R \sigma^3)}$	$0.1 - 100$
Pe	Péclet Number	$\frac{v_0}{(\sigma D_{\text{R}})}$	$0 - 10$

B.2 Simulation model details

The position and orientation of the cells is governed by over-damped Langevin equations. The simulation box has a square geometry with lateral dimension L with x representing the scaled distance measured normal to the boundary (see Fig. 4.2). We perform the simulations in dimensionless units. To do this, we choose $1/D_R$ as the characteristic time scale, and introduce dimensionless time t^* related to dimensional time t' by $t^* \equiv t' D_R$. The diameter of the cell σ is used to scale lengths, so that the dimensionless positions (x^*, y^*) are related to the dimensional ones (x', y') via $x^* \equiv x'/\sigma$, $y^* \equiv y'/\sigma$ and $\mathbf{r}^* \equiv \mathbf{r}'/\sigma$.

The equations when scaled assume the form

$$\frac{d\mathbf{r}^*}{dt^*} = Pe\,\mathbf{p} - \frac{3A}{(x^*+1)^4}\tilde{f}_\nu(\theta)\hat{\mathbf{x}} + \sqrt{2D}\boldsymbol{\eta}_T^* \tag{B.2}$$

$$\frac{d\theta}{dt^*} = -\frac{B}{(x^*+1)^3}\frac{\partial \tilde{f}_\nu(\theta)}{\partial\theta} + \sqrt{2}\eta_R^* \tag{B.3}$$

where A and B are the dimensionless interaction parameters for force and torque respectively and Pe is the Péclet number which determines the persistent motion of the cells(Eq. 4.4)). D is the scaled coefficient of diffusion (Eq. (4.4)) while $\boldsymbol{\eta}_T^*$ and η_R^* are the scaled Gaussian white noise for translation and rotation respectively. In our simulations ν is fixed at 0.3 [3] and $f_\nu(\theta)$ is scaled such that $\tilde{f}_\nu(\theta) = (50/256\pi)f_\nu(\theta)$. Superscripts * in Eqs. (B.2) and (B.3) denote non-dimensional quantities. Henceforth, we will drop this superscript for ease of use and thus in the final equations simulated (x, y, t) are all dimensionless.

B.3 Simulation methodology

Simulations are conducted, unless mentioned otherwise, with $N = 200$ active Brownian particles (cells) of diameter σ. In scaled units, the cells have diameter of 1, and move within a square box of size $L = 40$. Cells do not interact with each other. We choose the origin and coordinate axes x and y so that the domain is $-L/2 \leq x \leq L/2$ and $-L/2 \leq y \leq L/2$. Periodic boundary conditions are imposed at the lower and upper boundaries.

Lateral boundaries correspond to flat interfaces that interact elastically with cells and also impose confinement. We ignore deformations of the boundary so that these interfaces are always parallel to the y-axis at $x = -L/2$ and $x = L/2$. Confinement is directly imposed by maintaining an exclusion region of $\sigma/2$ exists around each interface; cells are thus prevented from partially or fully penetrating the wall. We implement this condition as follows. We make sure that if a particle makes a virtual displacement where the center of the particle is $x + \Delta x > L/2 - \sigma/2$, it is brought back to a distance $L/2 - \sigma/2$ and similarly to $-L/2 + \sigma/2$ on the other confining boundary. The free and clamped boundary conditions are associated with the confining boundaries to ensure that the particles cannot cross the threshold potential. The coordinate system shown in Fig. 4.2, demonstrates symmetry (in both the type of boundary conditions, and potential field from the boundary) about the origin $x = 0$, and reflection symmetry about the y axis. Since x denotes the variable quantifying the normal distance measured from the edge of the boundary, our simulation

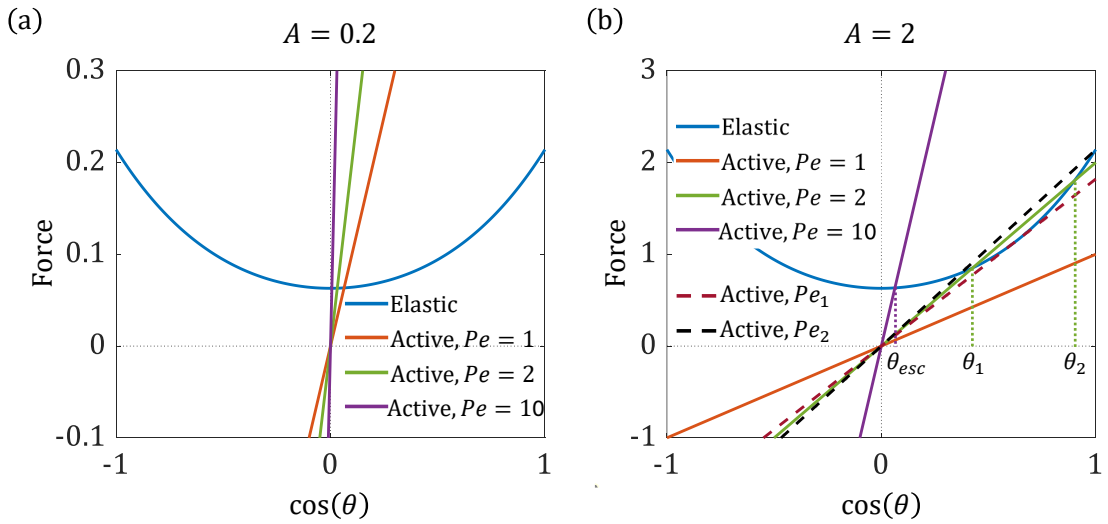

Figure B.1: The force from the boundary and active force orthogonal to the boundary both depend on the angle of orientation with the boundary. We compare the forces at the boundary to graphically estimate the angle of escape of the particles. We compare the force from the boundary (solid blue) at (a) $A = 0.2$ and (b) $A = 2$ with active forces perpendicular to the boundary (dashed) at $Pe = 1, 2, 10$. The particle can escape at angles where the orthogonal component of the active force is greater than the boundary interaction. (a) At $A = 0.2$, for all values of Pe, the particles can escape the boundary through any angle θ such that $cos\theta > 0$. Increasing Pe increases the angle of escape. (b) At $A = 2$ we observe 3 different behaviors. For $Pe = 1$ orthogonal component of active force is always less than the boundary force. At $Pe = 10$, the active force is higher than the boundary force and intersect each other at 1 point. The active force is higher than the boundary force only inside angular pockets for $Pe = 2$.

methodology implies that particles are excluded from occupying a region of width $1/2$ (corresponding to the radius of the cell $\sigma/2$ in dimensional units) at the boundary (see Fig. 4.2 and Fig. 4.3-c).

Dimensionless forms of the dynamical equations Eq. B.2-B.3 are discretized and numerically solved using the explicit half-order Euler-Maruyama method [204]. We initialize 200 non-interacting particles uniformly distributed inside the simulation box and study its probability distribution as function of distance from the boundary. These particles interact with the elastic boundaries depending on the proximity and orientation with respect to the boundary. Simulating a large number of non-interacting cells at the same time allows us to obtain detailed statistics for single particle interaction with the elastic boundary in

a speedy and efficient manner. The dimensionless time step is $dt = 10^{-3}$ such that the displacement in each time step is small ($\sim 10^{-2}\sigma$ or smaller). We sample the data every 10^3 steps. When the probability distribution does not change with time (subject to a pre-specified precision), we consider that statistical steady state has been reached. Steady state is achieved at different times which depend on the parameters A, B and Pe. Steady state time under no force or torque from the boundary can be estimated to be $\sim L^2/D_{\text{eff}}$ where $D_{\text{eff}} = v_0^2/D_R$. In our initial simulations, we set the scaled translational diffusion $D = 0$. Thereafter, we study the distribution of particles as a function of distance from the boundary by averaging over all particles and time after steady state is achieved. We count the number of particles at $x = \sigma/2$ to determine the localization of particles at the boundary.

At steady state we look at the distribution of particles throughout the domain from the left wall to the midpoint of the domain, and also analyze the localization of particles near the boundary (over a region ranging from a cell diameter to a few cell diameters). This is done by studying the time evolution of the effective number of particles/cells a certain distance from the wall. If the interface was a penetrable surface, higher localization at the boundary would imply a higher probability of cells and a larger current/flux crossing the interface. For a free boundary, we study the effect of simulation parameters on the void length and orientation dynamics of particles at the clamped boundary. Our simulations complemented by a simple model for barrier crossing based on Kramer's theories allow us to identify conditions particles can escape the influence of the boundary interactions.

B.4 Determining escape conditions

Here we graphically explore the escape of particles from the boundary at different different interaction parameters, A, and Péclet number, Pe. We further determine the critical values $Pe_1(A)$ and $Pe_2(A)$ which dictate the different regimes of particle localization at the boundary. Particles remain trapped at the boundary when $Pe < Pe_1$. For $Pe > Pe_2$, there exists a characteristic angle θ, above which trapped particles can attain a configuration favorable for escape from the boundary. This critical angle, θ_{esc} depends on Pe (Fig. 4.8(a), Fig. B.1(a)). For $Pe_1 < Pe < Pe_2$ particles can only escape the boundary when their orientation θ lie in the angular region between θ_1 and θ_2 (Fig. 4.8(b)).

The particles can potential attain a configuration favorable for escape escape when

the self-propulsion active force of the particle has an orthogonal component sufficient large to overcome the elastic attraction from the boundary. For a particle/cell trapped at the boundary $x = x_b = \sigma/2$, a balance yields

$$Pe = \frac{1}{\cos\theta}\,\frac{3A}{(x+1)^4}\tilde{f}_\nu(\theta), \quad \tilde{f}_\nu(\theta) = \frac{50}{256\pi} f_\nu(\theta). \tag{B.4}$$

At $Pe = Pe_1$, the tangent construction evaluating the elastic force originating due to cell-boundary interactions (see figure B.1) provides Pe_1,

$$Pe_1 = \frac{3A}{(x+1)^4}\frac{50}{256\pi}\left(2|b^c_\nu|\cos\theta + 4|c^c_\nu|\cos^3\theta\right) \tag{B.5}$$

Eqs. (B.4) and (B.5) provide the ratio $Pe_1/A = 0.91$ at $x = x_b = \frac{\sigma}{2}$. At $A = 2$, $Pe_1 = 1.819$ and at $A = 0.2$, Pe_1 is expected to be 0.182.

To determine Pe_2, we consider $\theta_1 = 0$, since beyond Pe_2, θ_1 would cease to exist as particles can escape at angles less than θ_2. Balancing forces at $\theta = 0$, we get

$$Pe_2 = \frac{3A}{(x+1)^4}\frac{50}{256\pi}(|a^c_\nu| + |b^c_\nu| + |c^c_\nu|) \tag{B.6}$$

This gives the ratio $Pe_2/A = 1.07$. For $A = 2$, Pe_2 is determined to be 2.14 and for $A = 0.2$, it is 0.214.

B.5 Escape of cells from the attractive clamped boundary

B.5.1 Adaptation of Kramer's theory to the frequency of orientation flips for spatially localized cells

We analyze the flips in cell orientation, that is in the angle θ, when the cell is at a fixed location near the boundary. This is done via an adaptation of the classical theory due to Kramer [263]. Consider a collection of independent Brownian cells/particles in an external 1D potential $U(z)$ that depends on a generalized coordinate z. Let the potential exhibit a meta-stable minimum at location A, with the maximum in the value occurring at the crest of a potential barrier at B, as shown in Fig. (B.2). The well is sufficiently deep so particles inside the well cannot escape in short time intervals. Assuming that particles in the well minima are close to equilibrium and cross the barrier diffusively, we aim to obtain the rate at which this escape takes place. The dynamics of a test particle can be described by the over-damped Langevin equation in 1D,

$$\frac{dz_p}{dt} = -\mu U'(z_p) + \eta(t) \tag{B.7}$$

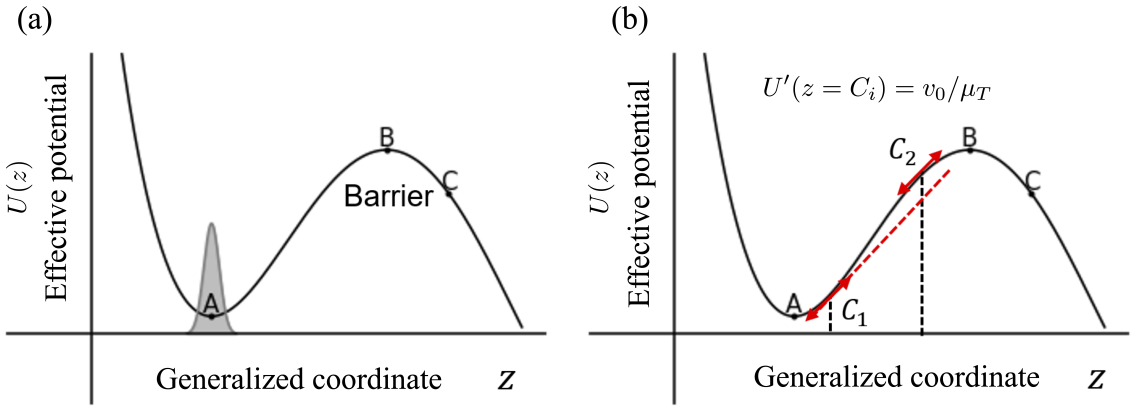

Figure B.2: (a) Schematic of the classical Kramers' Problem for escape from a potential well and across a potential barrier. Particles move in a spatially varying potential $U(z)$, shown as the black curve, that is a function of a general coordinate z. The potential $U(z)$ exhibits two minima: the first at location $z = A$, and a second minimum beyond point $z = C$. Additionally, to get from A to C, particles subject to $U(z)$ have to surmount and pass through a barrier with a local maximum at $z = B$ where $A < B < C$. We analyze an ensemble of particles initially in an equilibrium distribution at the bottom of the cell $z \sim A$, and study the rate at which they escape the barrier at B, and reach C. (b) Schematic of the barrier crossing problem for active self-propelled particle escaping from a potential well.

with μ being the mobility and $-U'(z_p)$ the linear drag force acting on the particle located at z_p. The particle is also subject to a white noise $\eta(t)$, with zero mean $\langle \eta(t) \rangle = 0$ and variance $\langle \eta(t)\eta(t') \rangle = 2D\delta(t - t')$. Here D and μ are generalized diffusivity and mobility coefficients that characterize the random diffusion and frictional effects as the particle/cell moves along z. Barrier crossing is achieved after many attempts - that is, the crossing is driven by diffusive processes.

These approximations allow us to move from the Langevin equation to the Fokker-Planck equivalent. We recast the problem in terms of a probability distribution function $P(z,t)$ that may be mapped to either the probability of a single particle or the density of a collection of particles (as in simulations). We assume that the system is close to equilibrium so that crossing flux $J(z,t)$ may be related to gradients in $P(z,t)$,

$$\frac{\partial P(z,t)}{\partial t} = \frac{\partial}{\partial z}\left[\mu \frac{\partial U}{\partial z} P + D\frac{\partial P}{\partial z}\right] = -\frac{\partial J}{\partial z} \tag{B.8}$$

$$J = -\mu P(z,t)\partial_z U - D\partial_z P(z,t) \tag{B.9}$$

$$J = -De^{-\frac{U(z)}{k_B T}} \frac{\partial}{\partial z}\left(e^{\frac{U(z)}{k_B T}} P(z)\right). \tag{B.10}$$

We have invoked the Stokes-Einstein relationship so that $D = \mu k_B T$. For a system that is approximately in equilibrium and in quasi-steady conditions with a large barrier height satisfying $[U(B) - U(A)]/(k_B T) \ll 1$, the current J across the barrier is small and the rate of depletion at the well is small. Since the system is close to quasi-steady sate, the probability distribution $P(z,t)$ doesn't change quickly with time, and so $\partial_t P(z,t) \approx 0$. Moreover, based on Eq. B.8, the current is then to leading order constant and independent of z and t.

$$\frac{J}{D} e^{\frac{U(z)}{k_B T}} = -\frac{\partial}{\partial z}\left[e^{\frac{U(z)}{k_B T}} P(z,t)\right]. \tag{B.11}$$

Due to the barrier crossing event being a rare event, we next invoke the approximation $P(A) \gg P(C) \sim 0$.

To calculate the escape flux, we assume that re-crossings into the well are not permitted once the particle reaches location C. That is, we let C correspond to an absorbing boundary so that the probability density there is zero. Integrating Eq. B.11 between locations A and C, and using $P(C) = 0$, we obtain

$$\frac{J}{D}\int_A^C e^{\frac{U(z)}{k_B T}} dz = e^{\frac{U(A)}{k_B T}} P(A). \tag{B.12}$$

The left side integral can be asymptotically estimated to leading order by using the saddle point method by expanding $U(z)$ in a Taylor series approximation and noting that the first derivative at B is zero,

$$\begin{aligned} \int_A^C e^{\frac{U(z)}{k_B T}} dz &\approx \int_A^C e^{\frac{U(B)+\frac{1}{2}U''(B)(z-B)^2}{k_B T}} dz \\ &\approx e^{\frac{U(B)}{k_B T}} \int_{-\infty}^{\infty} e^{\frac{-|U''(B)|(z-B)^2}{2k_B T}} dz = e^{\frac{U(B)}{k_B T}} \sqrt{\frac{2\pi k_B T}{|U''(B)|}}. \end{aligned} \tag{B.13}$$

To evaluate the escape rate r_{esc}, we recognize that this rate is the same as the current going out of the metastable well at A, given that the particles are initially situated inside it, $J = p_A r_{\text{esc}}$. Assuming an initial close equilibrium state with

$$P(z) = P(A) \exp\left[-[U(z) - U(A)]/k_B T\right]$$

and using the expansion

$$U(z) \approx U(A) + \frac{1}{2}U''(A)(z - A)^2,$$

the probability to be inside the well is approximately

$$\begin{aligned} p_A = \int_{A-\Delta}^{A+\Delta} P(z)\, dz &\approx P(A) \int_{-\infty}^{\infty} e^{-\frac{U''(A)(z-A)^2}{2k_BT}} dz \\ &= P(A)\sqrt{\frac{2\pi k_B T}{U''(A)}}. \end{aligned} \tag{B.14}$$

Here Δ denotes a suitably small range in the neighborhood of point A. The saddle point approximation allows us to eventually extend the domain of integration from $-\infty$ to ∞. Thus, the escape time satisfies,

$$\tau_{\text{esc}} = \frac{1}{r_{\text{esc}}} = \frac{p_A}{J} = \frac{2\pi k_B T \exp\left(\frac{U(B)-U(A)}{k_BT}\right)}{D\sqrt{U''(A)\,|U''(B)|}} \tag{B.15}$$

To use Eq. B.15 to study flipping dynamics, we consider a particle located at a *fixed position* x and study the time it takes to reorient from $\theta = 0$ (bottom of the potential well), to $\theta = \pi/2$ (top of the barrier). The escape time can be mapping into the $1D$ circle motion with periodic boundary condition $P(\theta = 0) = P(\theta = 2\pi)$ (cite Sommerfeld's book). Identifying the coordinate z as θ and reintroducing the location dependence x (here considered constant), we obtain the escape time at fixed x

$$\begin{aligned} \tau_{\text{esc}} D_R &= \frac{2\pi k_B T \exp\left(\frac{U(x,\pi/2)-U(x,0)}{k_BT}\right)}{\sqrt{[U''(x,0)\,|U''(x,\pi/2)|]}} \\ &\sim \frac{1}{B}\exp\left(\frac{B}{B^*}\right). \end{aligned} \tag{B.16}$$

B.5.2 1D and 2D passive case: Escape time without self-propulsion in attractive power-law potentials

Here we focus on a motile test cell $Pe > 0$ that is in the attractive domain. As discussed earlier, the wall induced elastic potential $U(x, \theta)$ depends on both cell distance normal to the boundary x, and cell orientation θ. To understand the escape for motile cells, we first investigate escape dynamics for non-motile cells and set $Pe = 0$. This result will form the foundation for our analysis of activity assisted escape that is valid for small values of Pe.

Let us first consider possibly the simplest case - the dynamics of a non-motile cell/particle in one dimension. Specifically, we assume there is no orientation coupling $f_\nu(\theta) = 1$ and so the potential U is a function of x alone. The physical motivation for

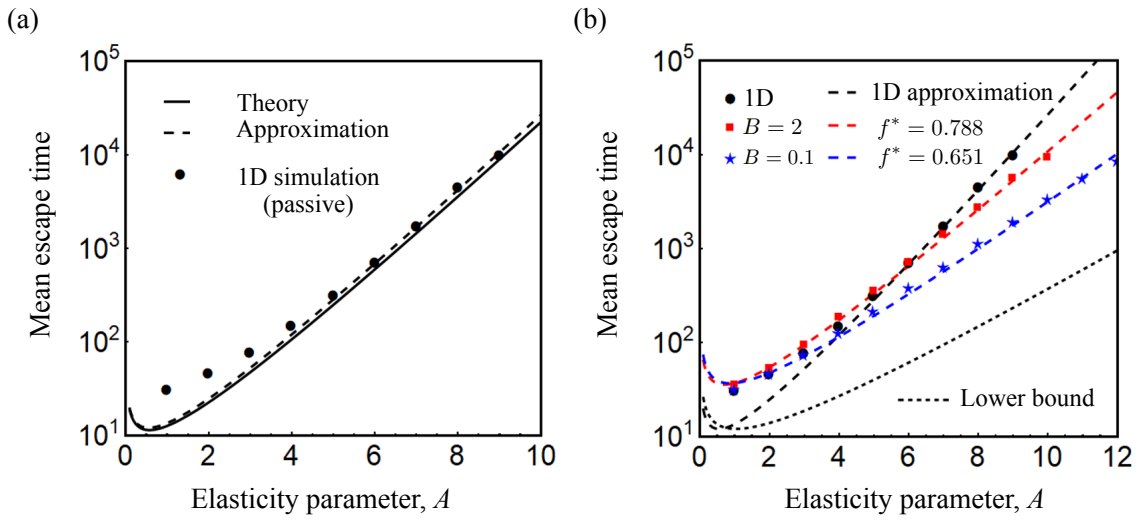

Figure B.3: (a) The mean escape time evaluated from simulation (solid black circles) follows the modified Kramer's theory of barrier crossing for passive particles with $Pe = 0$ moving in the 1D modified potential without the coupling between position and orientation ($\tilde{f} = 1$). In the limiting cases resulting in Eq. B.24, the solid line and dashed line represent the analytical results and the approximation, respectively. (b) Results for the mean escape time from simulations (black circle, red square and blue star symbols) for passive particles in 1D, and with $B = 2, 0.1$ in 2D, respectively. Values of effective f^* averaged over orientational degrees of freedom is by fitting and estimated to be 0.788 and 0.651 for $B = 2, 0.1$, respectively. For larger B, the particles always flip between orientations $\theta = 0$ and $\theta = \pi$, and thus confirm to the 1D situation. Thus, the upper bound of f^* is given by 1 corresponding to 1D case. The lower bound could be estimated by the $f^* \approx \tilde{f}(\theta = \pi/2)$.

this comes from the recognition that $U(x, \theta)$ is the product of two functions one of which depends only on x, and the second (via $f_\nu(\theta)$) depends on θ alone. When cell reorientations occur on time-scales that are much shorter than the time for cells to escape, it is possible to average over accessible orientations and replace the function f with a suitably averaged constant (which for our simulations with fixed D and D_R is a pure number). Biologically, such a process is applicable to cells with rapid and highly stochastic blebbing.

Since there is no saddle point in the original potential derived from elastic interactions (a power-law potential), we consider a modified potential $U(z)$ (in k_BT units) with z being a (scaled) coordinate obtained by replacing the term $(z+1)^{-3}$ with $(z^2+1)^{-3/2}$ so that

$$U(z) = -\frac{A}{(z^2+1)^{3/2}}, \quad \text{with} \quad A \equiv \left(\frac{P^2\langle f_\nu\rangle}{256\pi E k_B T}\right). \tag{B.17}$$

The Fokker-Planck equation for the probability Ψ in terms of z and (scaled) time τ may

then be written

$$\frac{\partial \Psi}{\partial \tau} = \frac{\partial}{\partial z}\left(\frac{\partial \Psi}{\partial z} + \Psi \frac{\mathrm{d}U}{\mathrm{d}z}\right) \tag{B.18}$$

We use the method of separation of variables to convert Eq. B.18 into an eigenvalue problem. Setting $\Psi(z,\tau) = \mathrm{e}^{-U(z)} g(z) \mathrm{e}^{-\mu\tau}$ where $g(z)$ then quantifies a small deviation from the equilibrium solution as $\tau \to \infty$, we find

$$\frac{\mathrm{d}^2 g}{\mathrm{d}z^2} - \frac{\mathrm{d}U}{\mathrm{d}z}\frac{\mathrm{d}g}{\mathrm{d}z} + \mu g = 0. \tag{B.19}$$

The appropriate boundary conditions may be deduced from the simulations. At the local minimum $z^* = z = 0$, we assume an impenetrable boundary that prevents particles from escaping, and so $g'(0) = 0$. Meanwhile, we can define the annihilation point being $z = L_{\mathrm{esc}}$ where the potential is indeed nearly flat at this point.

Now, if the potential well is sufficiently deep, the method of dominant balance can be used to show that the behavior of $g(z)$ is largely determined by the asymptotic behavior of $U(z)$ for $z \gg 1$. We denote this long-range attraction by $U(z) = -Az^3$, and exploit the fact that μ is exponentially small. Thus we may write

$$\frac{\mathrm{d}^2 g}{\mathrm{d}z^2} - \frac{\mathrm{d}U}{\mathrm{d}z}\frac{\mathrm{d}g}{\mathrm{d}z} = 0 \tag{B.20}$$

and therefore,

$$g(z) = \int_z^{L_{\mathrm{esc}}} e^{U(z')} dz'. \tag{B.21}$$

Since $g(z)$ was computed under the assumption that $\mu \simeq 0$, it represents a pseudo-steady solution. Applying this to the corresponding Kramers formulation for the escape flux, which gives the rate constant as the ratio of the steady-state flux to the number of reactant particles, and using $g(L_{\mathrm{esc}}) = 0$, we get

$$\begin{aligned} \mu &= \frac{g\left(z^*\right) - g(L_{\mathrm{esc}})}{\int_{z^*}^{L_{\mathrm{esc}}} \mathrm{e}^{U(z')}\mathrm{d}z' \int_0^{L_{\mathrm{esc}}} \mathrm{e}^{-U(z')} g(z')\mathrm{d}z'} \\ &= \left[\int_0^{L_{\mathrm{esc}}} \mathrm{e}^{U(z)}\mathrm{d}z \int_0^{L_{\mathrm{esc}}} \mathrm{e}^{-U(z)}\mathrm{d}z\right]^{-1}. \end{aligned} \tag{B.22}$$

We estimate the integrals as follows:

$$\begin{aligned} \int_0^{L_{\mathrm{esc}}} \mathrm{e}^{U(z)}\mathrm{d}z &= \frac{L_{\mathrm{esc}}}{3}\left(\frac{A}{L_{\mathrm{esc}}^3}\right)^{\frac{1}{3}} \Gamma\left[-\frac{1}{3}, \frac{A}{L_{\mathrm{esc}}^3}\right] \\ &\xrightarrow{\frac{A}{L_{\mathrm{esc}}^3} \ll 1} L_{\mathrm{esc}} + \frac{1}{3}\Gamma[-\frac{1}{3}]A^{\frac{1}{3}} \\ \int_0^{L_{\mathrm{esc}}} \mathrm{e}^{-U(z)}\mathrm{d}z &\sim \frac{1}{\sqrt{A}}\mathrm{e}^{A} \end{aligned} \tag{B.23}$$

where we retained only the leading order asymptotic terms in the expansion leading to Eq. B.23. Note that our simulation parameters are $L_{\rm esc} = 6$, with $1 < A < 12$, and hence $L_{\rm esc} > A^{1/3}$ as required for this approximation to hold. The specific parameter evaluates to $\Gamma[-1/3]/3 = -1.35$, which we approximate to obtain an asymptotic estimate for the escape time,

$$\tau_{\rm esc} \approx (L_{\rm esc} + \frac{1}{3}\Gamma[-\frac{1}{3}]A^{\frac{1}{3}})\frac{1}{\sqrt{A}}{\rm e}^{A} \approx \frac{(L_{\rm esc} - A^{\frac{1}{3}})}{\sqrt{A}}{\rm e}^{A} \tag{B.24}$$

In the 1D passive case considered here, there is no rotational diffusion D_R, and the characteristic relaxation time σ^2/D_T is used to convert dimensional times to dimensionless ones.

The form of Eq. B.24 motivates an extension of the results to the escape of a particle subject to a more complex orientation and space dependent 2D potential $U(z, \theta)$. We still assume a passive particle so that Pe = 0. The physical boundary is such that the test cell particle is on the soft side. Since orientational effects are to be considered here, we expect that the escape time will now depend on both A and B rather than on A alone. Based on these observations, propose the ansatz

$$\tau_{\rm esc} = \left(\frac{1}{D_R}\right)\, m(B) \left(\frac{L_{\rm esc} - A^{\frac{1}{3}}}{\sqrt{A}}\right) \exp\left[Af^*(B)\right]. \tag{B.25}$$

Here $f^*(B)$ is an effective parameter which comes from the coupling between the positional and orientational coupling. Parameter $m(B)$ takes into account the two dimensional nature of the potential and explicitly corrects for orientational effects on possible escape trajectories, and thus escape time.

It is useful to briefly consider the $(L_{\rm esc} - A^{\frac{1}{3}})$ term in Eq. B.25. Escape from the potential well is dominated by two effects depending on the distance from the well minimum. Close to the minimum, the potential dominates and the particle moves with an effective speed that depends on the force due to the potential. At distances $\sim A^{\frac{1}{3}}$, the strength of the potential is unity, and thus for distances larger than this value, diffusion dominates and aides the escape over the barrier. One may treat $(L_{\rm esc} - A^{\frac{1}{3}})$ as an effective distance over which particles diffuse in order to leave the well.

B.5.3 Activity-assisted escape from the attractive clamped boundary for small and $O(1)$ Pe: Reduced durotaxis

We conclude by analyzing the escape dynamics of migratory, motile cells from clamped boundaries. In our simplified model, they correspond to active motile particles

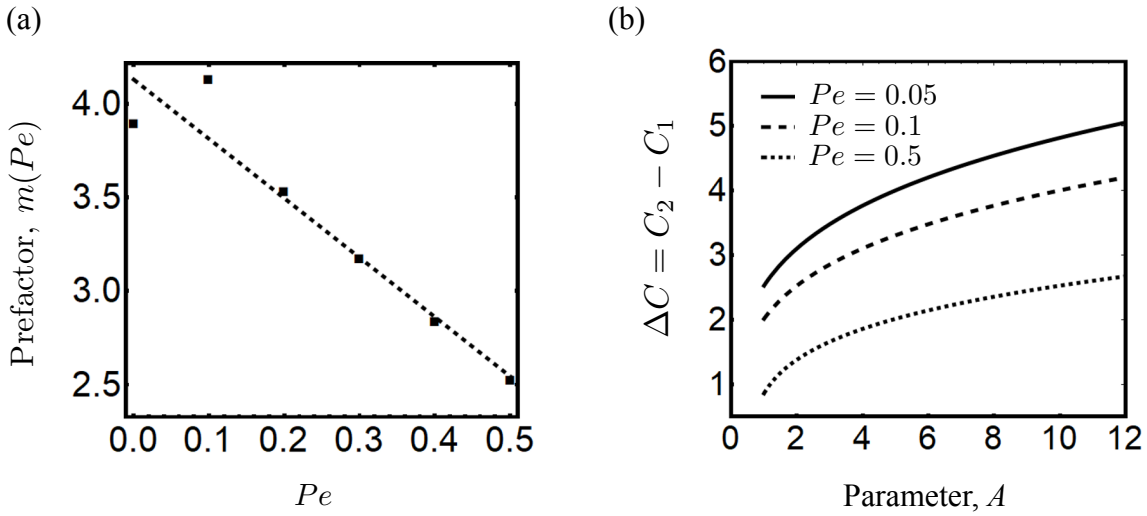

Figure B.4: (a) The fitting pre-factor $m(Pe)$ (black squares) follows a linear form $m(Pe) = 4.24 - 1.74Pe$ (dashed line) for $B = 0.1$. (b) For $f^* = 1$, the magnitude (extent) of the ΔC region increases as A increase, but decreases as Pe increases.

with $Pe > 0$ moving in a suitable 2D potential with orientational coupling.

Even for the 2D passive case, the substrate-mediated cell-boundary potential $U(x, \theta)$ with full coupling between position r and orientation θ it is difficult to exactly calculate the escape time. To make the theory tractable while still remaining faithful to the physics of the problem, we introduced a parameters f^* to quantify the effective coupling effects as in Eq. B.25. Since the orientation dynamics are highly dependent on parameter B, we further assumed f^* is determined by B. Using this approximate treatment, the escape time problem can be reduced to barrier crossing of run and tumble particles (or diffusing particles) in a 1D trap.

Recently, it was shown for a run-and-tumble active particles that the escape time from a trap depends on the detailed structure of the potential [266]. Importantly, it is not a simply exponential function of the potential depth as shown in the classical Kramer's theory. Woillez et al [266] recently investigated the activated escape of run-and-tumble particles from metastable wells, an example of which is illustrated in Fig. B.2 (b). In the figure, C_1, C_2 are locations satisfying $\partial_z U(C_i) = v_0/\mu_T$ where the potential force arising from the elastic interaction equals the self-propulsion force. The minimal action for the particle to escape from the potential well is to move right away from the base of the well

(with orientation angle, $\theta = 0$). The most probable path is then given by

$$\mathcal{A}[z] = \frac{1}{4}\int_{\infty}^{\infty}(\dot{z} + \mu_T \partial_z U(z) - v_0)^2 dt' \tag{B.26}$$

Following the arguments in Woillez et al [266], we find the instanton solution obeys $\dot{z} = \partial_z\{\mu_T[U(z)-U(C_1)]-v_0(z-C_1)\} \equiv \partial_z\varphi(z)$. The problem with self-propulsion may then be analyzed in an equilibrium setting with an effective tilted potential $\varphi(z)/\mu_T$ that is modified by the activity. Thus the escape time from the trap depends exponentially on the modified potential barrier as $\langle\tau_{\rm esc}\rangle \propto \exp(\phi/D_T)$ in the limit of $D_T \to 0$. The quasi-potential barrier is $\phi = \mu_T[U(z) - U(C_1)] - v_0(z - C_1)$, after modification by the self-propulsion speed v_0.

In our case, the escape dynamics for the 2D passive particles from the barrier (the annihilation point L) in the 1D power-law like potential $U(x)/k_BT = -Af^*/(x^2+1)^{3/2}$, can be reduced to barrier crossing of diffusing particles in a 1D trap by introducing an effective parameter f^*. Then, the escape dynamics in the 2D active particles simplify to the escape problem of run-and-tumble particles in the power-law-like potential as in Woillez et al [266]. We assume the pre-factor depending on the dimensionless parameters A in the active case is the same as the passive case. The mean escape time of particles crossing the barrier can be written as

$$\tau_{\rm esc} = \left(\frac{L_{\rm esc} - A^{\frac{1}{3}}}{\sqrt{A}}\right) m(B, Pe) \exp\left(\frac{\phi\,(v_0)}{D_T}\right) \tag{B.27}$$

$$\phi(v_0) = \mu_T\left[U\left(C_2\right) - U\left(C_1\right)\right] - v_0\left(C_2 - C_1\right). \tag{B.28}$$

where the effective dimensional potential $\phi(v_0)$ involves the effects of active work due to the self-propulsion speed $v_0 > 0$ ($Pe > 0$). Note that for the passive case, $v_0 = 0$ and therefore $Pe = 0$. Coordinate values (points) C_2, C_1 that are spatial locations are functions of Pe and A where the active self-propulsion force balances the elastically derived interaction force. In dimensional form, these locations satisfy the conditions

$$\frac{v_0}{\mu_T} = |\partial_x U(x,\theta)|, \quad \text{at} \quad x = C_1,\ x = C_2. \tag{B.29}$$

For the passive case $v_0 = 0$ and so $Pe = 0$, and we find $C_1 = 0$ and $C_2 \sim L$ (that is $L_{\rm esc}$ in simulation terminology). For the active motile case where $Pe > 0$, the dimensional balance when scaled yields,

$$\frac{\left(\tilde{x}^2+1\right)^{\frac{5}{2}}}{\tilde{x}}\Big|_{\tilde{C}_2,\tilde{C}_1} = \frac{3Af^*}{Pe}, \tag{B.30}$$

Note that the two points $\tilde{C}_i = C_i/\sigma$ depend on dimensionless parameters A, B and Pe. The form of the quasi-potential barrier is as follows,

$$\frac{\phi}{D_T} = \frac{Af^*}{(\tilde{C_1}^2 + 1)^{\frac{3}{2}}} - \frac{Af^*}{(\tilde{C_2}^2 + 1)^{\frac{3}{2}}} - Pe\left(\tilde{C}_2 - \tilde{C}_1\right). \tag{B.31}$$

Further imposing that f^* depend only the parameter B (in the limit of small Pe), we replace f^* by the corresponding values for the 2D $Pe = 0$ passive case at the same B. The pre-factor function $m(B, Pe)$ however remains dependent on both B and on Pe. In order for the $Pe \to 0$ limit of this theory to yield the 2D escape time estimate calculated earlier, we require $m(B, Pe)$ to be a linear function of Pe. Combining these ideas, we propose that

$$\tau_{\text{esc}} = \left(\frac{L_{\text{esc}} - A^{\frac{1}{3}}}{\sqrt{A}}\right) m(B, \text{Pe}) \exp(\frac{\phi}{D_T}) \tag{B.32}$$

At $B = 0.1$, $f^* = 0.651$. The fitting pre-factor m is found to be $m(Pe) = 4.24 - 1.74\,Pe$ as shown in Fig. B.4-(a). Furthermore, $\Delta C(Af^*, Pe) \equiv \tilde{C}_2 - \tilde{C}_1$ depends strongly on A and Pe as shown in Fig. B.4 (b).

B.6 Measurement of tactic indices from simulation

Here we summarize the methodology used to compute the various tactic indices used in the main text, from our simulations. One of these metrics, the FMI is used to compare our results with the analysis of experiments in Ref. [4]. In these experiments, cells were tracked every 15 minutes and the FMI was calculated at 1 hour intervals, for a total period of 24 hours. The authors also quantified the persistence of trajectories by estimating the ratio of displacement and the distance covered by the cell in these 1 hour intervals. This quantity was measured to be approximately 0.35 for cells moving in all three regions. The persistence time – that is, the time over which the cells travel more-or-less in the same direction – is around 0.1 hour. To calculate the FMI defined in Ref. [4] from our simulations, the following procedure was used. The position of a test cell is tracked every $\Delta T = 2.5$ dimensionless times (15 minutes in experiments). From these positions, the FMI is evaluated every $\Delta T = 10$ times (1 hour in experiments). Cells move in the domain and sometimes upon reaching the boundary move along it. We do not consider the contribution of particles trapped at the boundary or traveling along the boundary in the FMI calculation, since the biological experiments are in unconfined geometries (corresponding to cells at the boundary just crossing over). We also evaluated the FMI for only up to a dimensionless

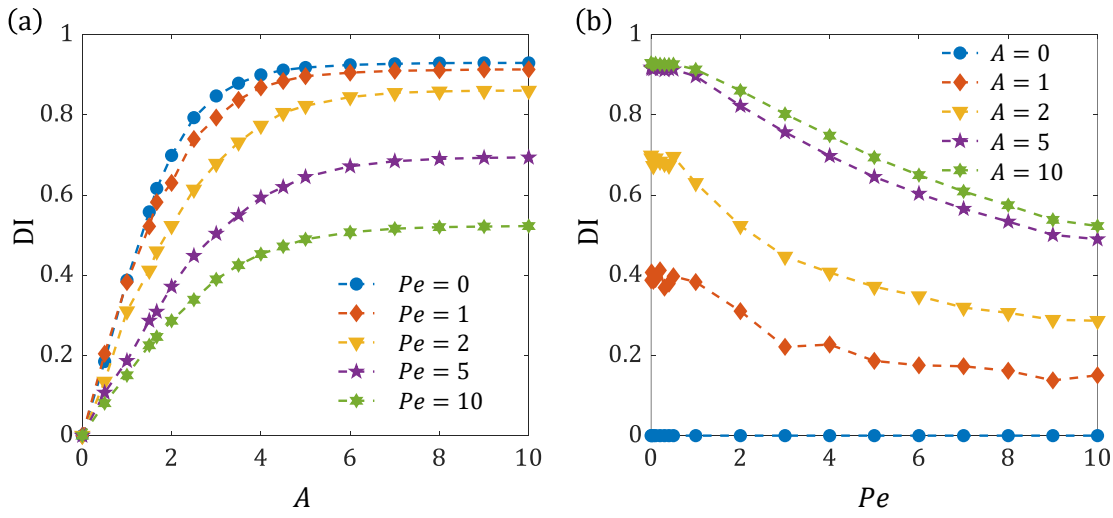

Figure B.5: The durotactic index DI as defined in Eq. 8 is plotted here in two ways. In (a), we observe that DI increases with elastic force parameter, A when Pe is held constant and reaches limiting values. (b) For A held fixed, we find that DI decreases with cell motility, Pe. The index is 0 by definition for $A = 0$.

observation time $T = 10$, since most particles reach the boundary within that time. We calculate the FMI inside a region 6σ from the boundary, since we already established that beyond this region the influence of the elastic potential of the boundary is very low.

To calculate the durotactic index (DI), we combine the results of two different simulations, $A \neq 0$ and $A = 0$, corresponding to the same value of Pe. Here, A ranges from $0 - 10$. In these simulations, we consider the same elastic force and torque interaction parameters for cells with the boundary such that $A = B$. Then, we consider the difference in the steady state numbers of cells localized at the boundary between $A \neq 0$ and $A = 0$, to calculate the DI. We observe that DI increases with A and reaches a limiting value, for all values of Pe (Fig. B.6(a)), while for given A, the DI decreases with Pe (Fig. B.6(b)).

B.7 Scattering of motile cells across elastic interface

Here we analyze the deterministic trajectories (without noise) of cells across a sharp gradient of substrate stiffness. The interface is located at $x = 0$, where the $x < 0$ is soft, with Young's modulus 5kPa (and correspond to $A = B = 5$) and $x > 0$ being stiff with Young's modulus 25kPa (and correspond to $A = B = 1$). We consider clamped and free

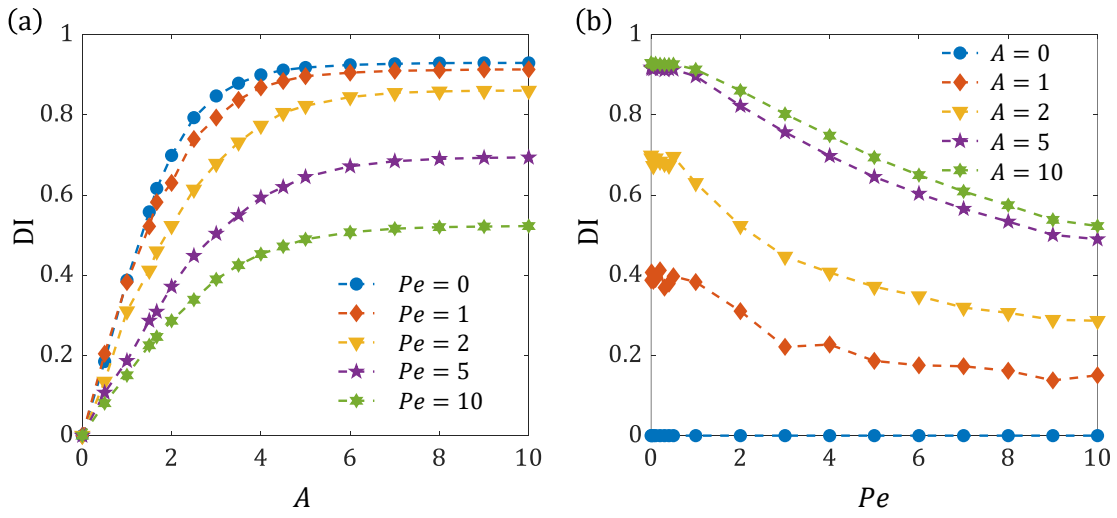

Figure B.6: The durotactic index DI as defined in Eq. 4.8 is plotted here in two ways. In (a), we observe that DI increases with elastic force parameter, A when Pe is held constant and reaches limiting values. (b) For A held fixed, we find that DI decreases with cell motility, Pe. The index is 0 by definition for $A = 0$.

boundary conditions on the interface if the cells are on the soft and stiff surfaces respectively. The interaction potential obtained for substrate mediated elastic cell-boundary interaction is mentioned in Supp. Note 1. We do not consider any rotational or translational diffusion for these trajectories. After initializing cells on either side of the interface, i.e. at $x = -5$ and $x = 5$, at different angles (20 angles linearly distributed between -1 to 1 radian when on soft side of the substrate and $\pi - 1$ to $\pi + 1$ when initialized on stiff side of the substrate), we observe how the orientation of the cells change as they approach the interface.

First, we focus on a simple condition where force from the interface is 0, but cells are still acted on by the elastic torque from the substrate interface, i.e. $A = 0$ (but $B \neq 0$). We obtain trajectories of cells approaching the substrate interface and have a motility of $Pe = 2$ (Fig. B.7). The cells initialized on the soft side of the substrate prefer to align perpendicular to the interface when they approach it (Fig. B.7a). This behavior resembles light refraction when it moves from a rarer to a denser medium. The gentle transition of incident angle suggests a gentle increase in the refractive index of the medium. On the other hand, cells initialized on the stiffer side of the substrate prefer to bend parallel to the interface while approaching (Fig. B.7b). This behavior resembles light refraction from

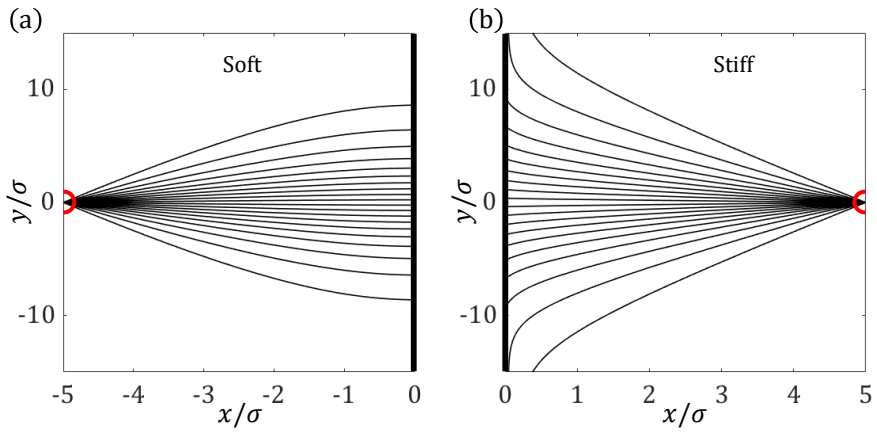

Figure B.7: The elastic torque from interface between the soft and stiff substrate tries to align the cells perpendicular or parallel to the boundary depending on the direction of approach to the interface. In these trajectories we do not consider any translational or rotational diffusion and also neglect the force from the interface. We observe the effect of elastic torque on the trajectory of cell approaching from the same distance on either side of the interface. (a) When cells are approaching from the softer side of the interface ($x = -5$, $y = 0$, shown by red semicircle) where the interface is at $x = 0$, with $Pe = 2$, the particle trajectories (shown by black lines) get aligned perpendicular to the interface. This kind of behavior is observed in case of refraction when light is traveling from a rarer to a denser medium. Here the refractive index can be realized to be increasing as it approaches the interface. The torque parameter $B = 5$ in the softer substrate region. (b) Cells approaching the interface from the stiffer side of the interface ($x = 5$, $y = 0$, shown by red semicircle) aligns parallel to the interface. This kind of of behavior is observed when light is traveling from a optically denser to a rarer medium. The torque parameter $B = 1$ in the softer substrate region.

a denser to a rarer medium. Decreasing Péclet number implies slower moving cells that get more time to reorient. This is analogous to higher contrast of refractive index as light approaches closer to the interface, while for higher Péclet number, the contrast in refractive index is smaller.

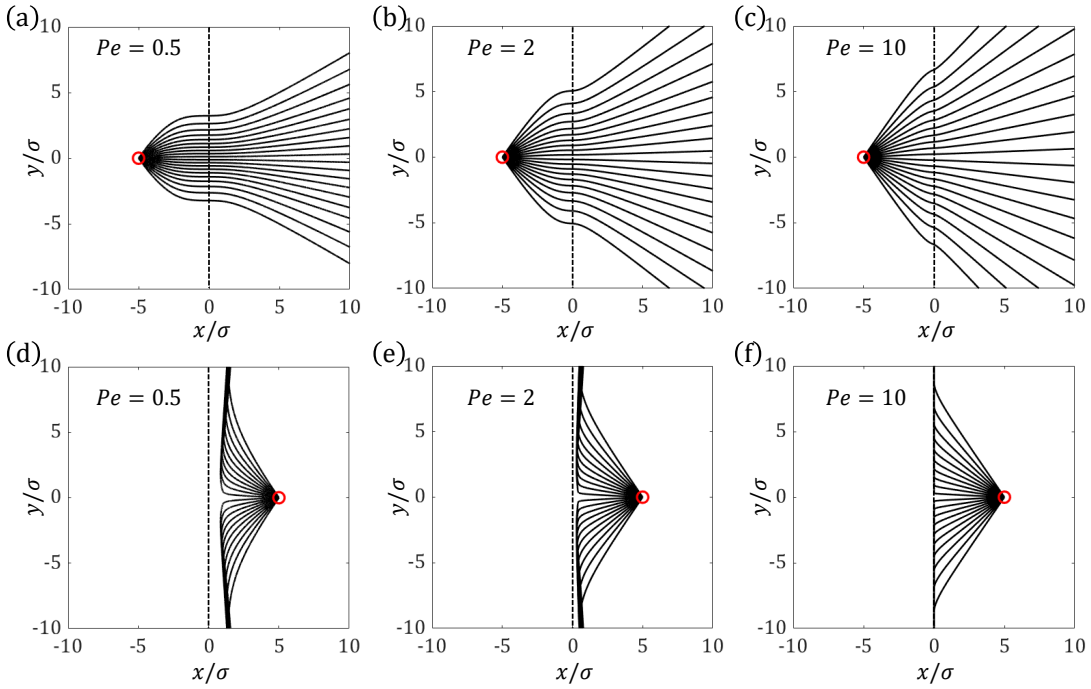

Figure B.8: The trajectories that are allowed to cross the interface are shown by black lines. The cells approaching the interface (shown by dashed line at $x = 0$) from either side of the interface have motility (a,d) $Pe = 0.5$, (b,e)$Pe = 2$ and (c,f)$Pe = 10$. The soft side of the substrate ($x < 0$) has a Young's modulus of 5kPa ($A = B = 5$), while the stiff side ($x > 0$) of the substrate has a Young's modulus of 25 kPa ($A = B = 1$).

If we consider the non-zero force from the boundary, that is, $A = B$, cells moving from the soft side to the stiffer side cross over (Fig. B.8a,b,c) even with low motility ($Pe = 0.5, 2$, shown in Fig. B.8a,b), because of the attractive nature of the clamped boundary condition and they reorient perpendicular to the interface when they cross over. After they have crossed, the elastic torque scatters their trajectories. At high motility, $Pe = 10$ (Fig. B.8c), cells do not have enough to sense torque and do not scatter much from the initial angle of incidence. On the other hand, cells approaching from the stiff side of the substrate (Fig. B.8d,e,f) do not cross the interface at low motility ($Pe = 0.5$ and 2, as shown in Fig. B.8d,e respectively) as they are pushed away by the repulsive free boundary.

At high motility ($Pe = 10$, as shown in Fig. B.8f) although the cells manage to reach the interface, the strong clamped boundary condition with interaction strength $A = 5$ on the soft side of the substrate does not allow the cells to move any further and crawl along the interface.

Appendix C

C.1 Displacement and strain analysis between frames

The actomyosin gel is a poroelastic material and the speed of contraction is slow enough to consider it to be linearly elastic at short time scales of 0.1s, which is shorter than the poroelastic stress relaxation time scale. The displacement vectors obtained from the PIV are located at regularly spaced lattice points. Spacing between lattice points depends on the radius of the gel at any point of time and may vary between frames. We can obtain strain generated in the gel from these evenly spaced displacement vectors.

C.1.1 Central differing scheme to obtain strain from displacements

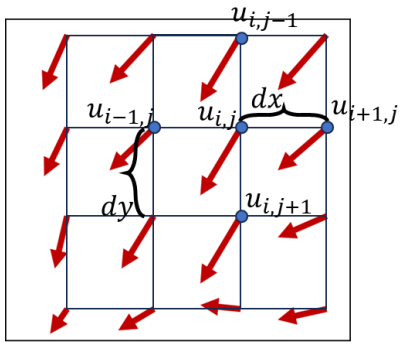

Figure C.1: Different components of the strains are obtained from the central difference method.

The displacement vectors obtained from the PIV are located at regularly spaced

lattice points. Spacing between lattice points depend on the radius of the gel at any point of time and may vary between frames. We can obtain strain generated in the gel from these evenly spaced displacement vectors. To obtain the different components of the strain tensor, i.e ε_{xx}, ε_{xy}, ε_{yx} and ε_{yy} at location (i, j), we consider the displacements $u_{i-1,j}$, $u_{i,j-1}$, $u_{i+1,j}$ and $u_{i,j+1}$ i.e. displacements at locations $(i-1, j)$, $(i, j-1)$, $(i+1, j)$ and $(i, j+1)$ respectively as shown in Fig. C.1. Thereafter, we use the three point central difference method to obtain the strain tensor components.

$$\varepsilon_{xx} = \frac{1}{2}\frac{u_{xi+1,j} - u_{xi-1,j}}{dx} \tag{C.1}$$

$$\varepsilon_{yy} = \frac{1}{2}\frac{u_{yi,j+1} - u_{yi,j-1}}{dy} \tag{C.2}$$

$$\varepsilon_{xy} = \varepsilon_{yx} = \frac{1}{4}\left(\frac{u_{yi+1,j} - u_{yi-1,j}}{dx} + \frac{u_{xi,j+1} - u_{xi,j-1}}{dy}\right) \tag{C.3}$$

C.1.2 Estimation of local displacements and strains in polar form

Most of the gels are circular disks contracting in an apparent axially symmetric manner. Hence, we consider radial and azimuthal components of the displacement and strain to better address this geometric feature of the gels. The strain tensor components obtained in Cartesian coordinates are converted to 2D polar coordinates.

- Locating the centroid of the gel - The mean of all unmasked lattice points gives us the location of the centroid of the gel.
- The center of the gel is set as the origin, i.e. (0,0) and polar coordinates of the lattice points are calculated with respect to the centroid. The distance between the centroid and each lattice point is given by separation length (r). The angle ϕ is made by the position vector of each lattice point from the center of contraction with respect to the horizontal.
- Displacements in polar form are calculated as follows

$$u_r = u_x\cos(\phi) + u_y\sin(\phi) \tag{C.4}$$

$$u_\phi = u_x\cos(\phi) + u_y\sin(\phi) \tag{C.5}$$

- Strain is calculated in polar coordinates in the following way

$$\varepsilon_{rr} = \varepsilon_{xx}\cos^2\phi + \varepsilon_{yy}\sin^2\phi + 2\varepsilon_{xy}\cos\phi\sin\phi \quad \text{(C.6)}$$

$$\varepsilon_{\phi\phi} = \varepsilon_{xx}\sin^2\phi + \varepsilon_{yy}\cos^2\phi - 2\varepsilon_{xy}\cos\phi\sin\phi \quad \text{(C.7)}$$

$$\varepsilon_{r\phi} = \varepsilon_{\phi r} = -\left(\varepsilon_{xx} - \varepsilon_{yy}\right)\sin\phi\cos\phi + \varepsilon_{xy}\left(\cos^2\phi - \sin^2\phi\right) \quad \text{(C.8)}$$

C.1.3 2D plots of area strain

The 2D heatmaps of bulk area strain are obtained by tracing filled contour plots of the trace of the strain tensor $(\varepsilon_{xx} + \varepsilon_{yy})$ at each lattice point. This measures the net area deformation (contraction or expansion) in each region. The area strain gives the net contraction or stretch in the gel. Here, the area strain is normalized by the maximum positive and negative values for the whole gel.

Here the centroid of the gel is demarcated by the red circle, the PIV arrows are shown in red and the area strain is shown as heatmap. The contracting regions, i.e. regions with negative strain are shown in blue, while the stretched regions with positive strain are in yellow.

We can also analyze 2D heatmaps of other components of the strain. We can achieve this by simply changing the definition of U in the code. The radial strain ε_{rr}, and azimuthal strain $\varepsilon_{\phi\phi}$, reveals the stretch or compression in radial and azimuthal directions respectively and are important quantities to analyze.

C.1.4 2D plots of Eigenvalues

We can obtain the principal directions of stretch and contraction from the analysis of eigenvalues and eigenvectors of the strain tensor at the lattice points. We distinguish the eigenvalues depending on their magnitude and analyze the direction of eigenvectors corresponding to maximum and minimum magnitude of eigenvalues. We expect that the eigenvector associated with maximum magnitude eigenvalue gives the direction of alignment of actin bundles, since contraction or stretch is expected to occur in the direction or orthogonal to the alignment of the actin bundles.

C.1.5 Radial and azimuthal displacement and strain obtained from axisymmetric assumption of gel contraction

We consider circular annuli of equal thickness from the gel boundary to the center (a total of 25 annular bins). In each of these annular bins, there are multiple PIV

lattice points. We calculate the mean and standard deviation of the radial and azimuthal displacements in each of these annular bins. To validate our assumption of axisymmetric contraction, we consider azimuthal displacement as a function of the normalized distance from the center of the gel as observed for Gel – 1. It fluctuates close to 0, suggesting no apparent azimuthal displacement, which verifies axisymmetric contraction . For angle-averaged radial displacements in annular bins, we obtain an inner region which shows linear negative dependence with distance from the center. Closer to the boundary, the radial displacement profile curves up to form a "hockey stick"-like shape suggesting radial stretching. This stretching close to the boundary correlates with the observed positive patches of area strain.

C.1.6 Calculation of center of contraction

Some gels often contract to a point which is not the centroid. We locate the center of contraction for such gels from the displacement vectors and estimate the radial profiles of displacements and strains with respect to the center of contraction.

- To determine the location of the center of contraction, we first estimate the mean direction of displacement of the gel.

- When the center of contraction of the gel is different from the centroid of the gel, there is a rigid body motion associated with the gel. The mean displacement of the gel is also its rigid body motion. Subtracting the rigid body motion of the gel, the PIV vectors are changed although the strain components remain the same. A comparison of PIV with strain heatmap is shown for gel before and after subtracting the rigid body motion of the gel in Fig.

- Like all lattice points in the gel, the centroid (CoM) is also moving towards the center of contraction (CoC), i.e. $r_{CoC} = r_{CoM} + \alpha\langle u\rangle$. To determine α, we consider the intersection of the mean displacement vector and all displacement vectors in the gel, i.e. $r_{CoC} = r_{CoM} + r + \beta u$. Here, u is the displacement vector at any lattice point whose position is given by vector r.

- We get $\alpha = \frac{xu_y - yu_x}{\langle u\rangle_x u_y - \langle u\rangle_y u_x}$ where x and y are the cartesian coordinates for a lattice point whose position is given by r. The displacement components u_x and u_y are associated with the lattice point, while $\langle u\rangle_x$ and $\langle u\rangle_y$ are the components of the mean

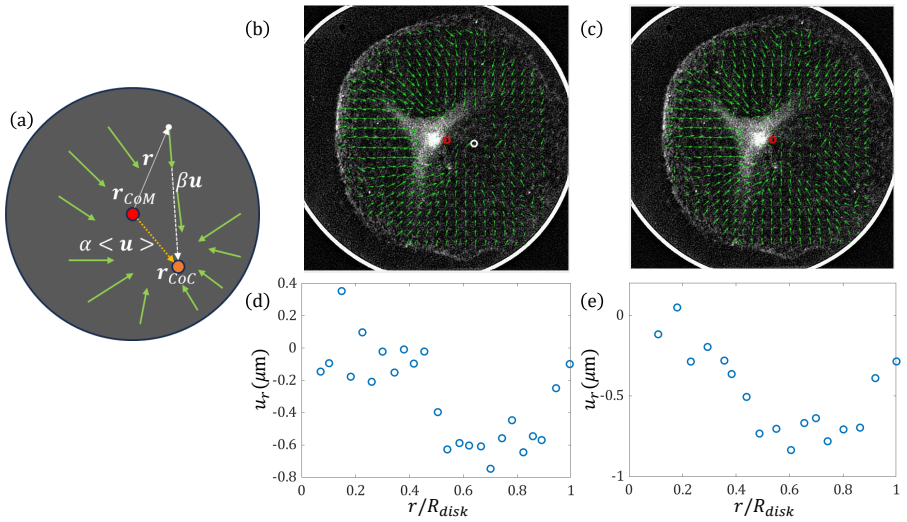

Figure C.2: **Center of contraction to estimate radial profile:** (a) When the gel gets stuck at any point which is not the centroid (r_{CoM}), the center of contraction (r_{CoC}) is shifted to that point. (b) A sample PIV with centroid of the gel shown by a red circle while the center of contraction is shown by a white circle. (c) The PIV changes after subtracting the rigid body motion of the gel. The center of contraction coincides with the centroid shown by the red circle. (d) A very noisy radial profile of the radial displacement is obtained with respect to the centroid of the gel. (e) Noise is reduced when radial profile is obtained from the center of contraction.

displacement along x and y-directions. Due to spatial fluctuations in the PIV data, we obtain a range of values for α, from which we consider a median value to finally estimate the center of contraction. Fig. C.2(a) shows how the centroid (CoM) of the gel is different from the center of contraction (CoC). The comparison of PIV before and after subtracting the rigid body motion of the gel is shown in Fig. C.2(b, c)

- With this new center, we calculate the new radial and azimuthal displacements, where radial direction is estimated from the lattice points on the gel to the CoC. From the new set of radial and azimuthal displacements, we estimate the new radial displacement profile which is less noisy as shown in Fig. C.2 (d,e).

Appendix D

Code Availability

The codes for simulations and analysis are provided in the following repositories -

Chapter 2 repository

Chapter 3 repository

Chapter 4 repository

Chapter 5 repository

Bibliography

[1] N. Q. Balaban, U. S. Schwarz, D. Riveline, P. Goichberg, G. Tzur, I. Sabanay, D. Mahalu, S. Safran, A. Bershadsky, L. Addadi, and B. Geiger, "Force and focal adhesion assembly: a close relationship studied using elastic micropatterned substrates," *Nature Cell Biology*, vol. 3, p. 466, Apr 2001. Article.

[2] K. Dasbiswas, S. Hu, F. Schnorrer, S. A. Safran, and A. D. Bershadsky, "Ordering of myosin ii filaments driven by mechanical forces: experiments and theory," *Philosophical Transactions of the Royal Society B: Biological Sciences*, vol. 373, no. 1747, p. 20170114, 2018.

[3] C.-M. Lo, H.-B. Wang, M. Dembo, and Y.-l. Wang, "Cell movement is guided by the rigidity of the substrate," *Biophysical journal*, vol. 79, no. 1, pp. 144–152, 2000.

[4] B. J. DuChez, A. D. Doyle, E. K. Dimitriadis, and K. M. Yamada, "Durotaxis by human cancer cells," *Biophysical journal*, vol. 116, no. 4, pp. 670–683, 2019.

[5] C. A. Reinhart-King, M. Dembo, and D. A. Hammer, "Cell-cell mechanical communication through compliant substrates," *Biophysical Journal*, vol. 95, no. 12, pp. 6044 – 6051, 2008.

[6] I. B. Bischofs, S. A. Safran, and U. S. Schwarz, "Elastic interactions of active cells with soft materials," *Phys. Rev. E*, vol. 69, p. 021911, Feb 2004.

[7] R. Phillips, J. Kondev, and J. Theriot, *Physical Biology of the Cell*. New York: Garland Science, Taylor & Francis Group, November 2008.

[8] E. National Academies of Sciences, Medicine, *et al.*, "Physics of life," 2022.

[9] D. A. Fletcher and J. A. Theriot, "An introduction to cell motility for the physical scientist," *Physical biology*, vol. 1, no. 1, p. T1, 2004.

[10] S. F. Gilbert, J. M. Opitz, and R. A. Raff, "Resynthesizing evolutionary and developmental biology," *Developmental biology*, vol. 173, no. 2, pp. 357–372, 1996.

[11] A. Nagy, "Manipulating the mouse embryo. a laboratory manual," *(No Title)*, 2003.

[12] M. R. Hutson and M. L. Kirby, "Model systems for the study of heart development and disease: cardiac neural crest and conotruncal malformations," in *Seminars in cell & developmental biology*, vol. 18, pp. 101–110, Elsevier, 2007.

[13] K. Molyneaux and C. Wylie, "Primordial germ cell migration," *International Journal of Developmental Biology*, vol. 48, no. 5-6, pp. 537–543, 2004.

[14] E. T. Stoeckli, "Understanding axon guidance: are we nearly there yet?," *Development*, vol. 145, no. 10, p. dev151415, 2018.

[15] G. L. Burn, A. Foti, G. Marsman, D. F. Patel, and A. Zychlinsky, "The neutrophil," *Immunity*, vol. 54, no. 7, pp. 1377–1391, 2021.

[16] A. D. Luster, R. Alon, and U. H. von Andrian, "Immune cell migration in inflammation: present and future therapeutic targets," *Nature immunology*, vol. 6, no. 12, pp. 1182–1190, 2005.

[17] A. J. Ridley, M. A. Schwartz, K. Burridge, R. A. Firtel, M. H. Ginsberg, G. Borisy, J. T. Parsons, and A. R. Horwitz, "Cell migration: integrating signals from front to back," *Science*, vol. 302, no. 5651, pp. 1704–1709, 2003.

[18] A. M. Smits, "Cell migration in the cardiovascular system: a force to be reckoned with?," *Cardiovascular Research*, vol. 114, no. 11, pp. e78–e80, 2018.

[19] J. Begum, S. R. Weaver, A. J. Iqbal, G. E. Rainger, and H. M. McGettrick, "Cell migration in cardiovascular diseases," in *Cell Movement in Health and Disease*, pp. 159–175, Elsevier, 2022.

[20] P. Friedl and K. Wolf, "Tumour-cell invasion and migration: diversity and escape mechanisms," *Nature reviews cancer*, vol. 3, no. 5, pp. 362–374, 2003.

[21] N. A. Kurniawan, P. K. Chaudhuri, and C. T. Lim, "Mechanobiology of cell migration in the context of dynamic two-way cell–matrix interactions," *Journal of biomechanics*, vol. 49, no. 8, pp. 1355–1368, 2016.

[22] C. D. Allen, T. Okada, and J. G. Cyster, "Germinal-center organization and cellular dynamics," *Immunity*, vol. 27, no. 2, pp. 190–202, 2007.

[23] A. Müller, B. Homey, H. Soto, N. Ge, D. Catron, M. E. Buchanan, T. McClanahan, E. Murphy, W. Yuan, S. N. Wagner, *et al.*, "Involvement of chemokine receptors in breast cancer metastasis," *nature*, vol. 410, no. 6824, pp. 50–56, 2001.

[24] D. Rossi and A. Zlotnik, "The biology of chemokines and their receptors," *Annual review of immunology*, vol. 18, no. 1, pp. 217–242, 2000.

[25] P. N. Devreotes and S. H. Zigmond, "Chemotaxis in eukaryotic cells: a focus on leukocytes and dictyostelium," *Annual review of cell biology*, vol. 4, no. 1, pp. 649–686, 1988.

[26] U. Mrowietz, U. Schwenk, S. Maune, J. Bartels, M. Küpper, I. Fichtner, J. Schröder, and D. Schadendorf, "The chemokine rantes is secreted by human melanoma cells and is associated with enhanced tumour formation in nude mice," *British journal of cancer*, vol. 79, no. 7, pp. 1025–1031, 1999.

[27] T. H. Weiss, A. L. Mills, G. M. Hornberger, and J. S. Herman, "Effect of bacterial cell shape on transport of bacteria in porous media," *Environmental science & technology*, vol. 29, no. 7, pp. 1737–1740, 1995.

[28] D. L. Bodor, W. Pönisch, R. G. Endres, and E. K. Paluch, "Of cell shapes and motion: the physical basis of animal cell migration," *Developmental cell*, vol. 52, no. 5, pp. 550–562, 2020.

[29] K. M. Yamada and M. Sixt, "Mechanisms of 3d cell migration," *Nature Reviews molecular cell biology*, vol. 20, no. 12, pp. 738–752, 2019.

[30] A. D. Doyle, R. J. Petrie, M. L. Kutys, and K. M. Yamada, "Dimensions in cell migration," *Current opinion in cell biology*, vol. 25, no. 5, pp. 642–649, 2013.

[31] T. Watanabe, H. Kuramochi, A. Takahashi, K. Imai, N. Katsuta, T. Nakayama, H. Fujiki, and M. Suganuma, "Higher cell stiffness indicating lower metastatic potential in b16 melanoma cell variants and in (-)-epigallocatechin gallate-treated cells," *Journal of cancer research and clinical oncology*, vol. 138, pp. 859–866, 2012.

[32] V. Swaminathan, K. Mythreye, E. T. O'Brien, A. Berchuck, G. C. Blobe, and R. Superfine, "Mechanical stiffness grades metastatic potential in patient tumor cells and in cancer cell lines," *Cancer research*, vol. 71, no. 15, pp. 5075–5080, 2011.

[33] R. Penta, L. Miller, A. Grillo, A. Ramírez-Torres, P. Mascheroni, and R. Rodríguez-Ramos, "Porosity and diffusion in biological tissues. recent advances and further perspectives," *Constitutive modelling of solid continua*, pp. 311–356, 2020.

[34] F. J. Maksoud, M. F. V. de la Paz, A. J. Hann, J. Thanarak, G. C. Reilly, F. Claeyssens, N. H. Green, and Y. S. Zhang, "Porous biomaterials for tissue engineering: a review," *Journal of Materials Chemistry B*, vol. 10, no. 40, pp. 8111–8165, 2022.

[35] J. S. Joseph, S. T. Malindisa, and M. Ntwasa, "Two-dimensional (2d) and three-dimensional (3d) cell culturing in drug discovery," *Cell Culture*, vol. 2, pp. 1–22, 2018.

[36] K. Duval, H. Grover, L.-H. Han, Y. Mou, A. F. Pegoraro, J. Fredberg, and Z. Chen, "Modeling physiological events in 2d vs. 3d cell culture," *Physiology*, vol. 32, no. 4, pp. 266–277, 2017.

[37] M. Krause and A. Gautreau, "Steering cell migration: lamellipodium dynamics and the regulation of directional persistence," *Nature reviews Molecular cell biology*, vol. 15, no. 9, pp. 577–590, 2014.

[38] D. J. Tschumperlin, "Fibroblasts and the ground they walk on," *Physiology*, vol. 28, no. 6, pp. 380–390, 2013.

[39] R. M. Garner and J. A. Theriot, "Leading edge maintenance in migrating cells is an emergent property of branched actin network growth," *Elife*, vol. 11, p. e74389, 2022.

[40] E. Vercruysse, D. B. Brückner, M. Gómez-González, A. Remson, M. Luciano, Y. Kalukula, L. Rossetti, X. Trepat, E. Hannezo, and S. Gabriele, "Geometry-driven migration efficiency of autonomous epithelial cell clusters," *Nature Physics*, pp. 1–9, 2024.

[41] B. S. Wong, P. Mistriotis, and K. Konstantopoulos, "Exposing cell-itary confinement: Understanding the mechanisms of confined single cell migration," *Biomechanics in Oncology*, pp. 139–157, 2018.

[42] D. E. Discher, P. Janmey, and Y.-l. Wang, "Tissue cells feel and respond to the stiffness of their substrate," *Science*, vol. 310, no. 5751, pp. 1139–1143, 2005.

[43] A. M. Handorf, Y. Zhou, M. A. Halanski, and W.-J. Li, "Tissue stiffness dictates development, homeostasis, and disease progression," *Organogenesis*, vol. 11, no. 1, pp. 1–15, 2015.

[44] J. Fenner, A. C. Stacer, F. Winterroth, T. D. Johnson, K. E. Luker, and G. D. Luker, "Macroscopic stiffness of breast tumors predicts metastasis," *Scientific reports*, vol. 4, no. 1, p. 5512, 2014.

[45] L. G. Vincent, Y. S. Choi, B. Alonso-Latorre, J. C. Del Álamo, and A. J. Engler, "Mesenchymal stem cell durotaxis depends on substrate stiffness gradient strength," *Biotechnology journal*, vol. 8, no. 4, pp. 472–484, 2013.

[46] B. Alberts, *Molecular biology of the cell*. Garland science, 2017.

[47] K. Burridge and C. Guilluy, "Focal adhesions, stress fibers and mechanical tension," *Experimental cell research*, vol. 343, no. 1, pp. 14–20, 2016.

[48] S. Tojkander, G. Gateva, and P. Lappalainen, "Actin stress fibers–assembly, dynamics and biological roles," *Journal of cell science*, vol. 125, no. 8, pp. 1855–1864, 2012.

[49] M. L. Gardel, I. C. Schneider, Y. Aratyn-Schaus, and C. M. Waterman, "Mechanical integration of actin and adhesion dynamics in cell migration," *Annual Review of Cell and Developmental Biology*, vol. 26, no. 1, pp. 315–333, 2010. PMID: 19575647.

[50] R. J. Pelham and Y.-l. Wang, "Cell locomotion and focal adhesions are regulated by substrate flexibility," *Proceedings of the National Academy of Sciences*, vol. 94, no. 25, pp. 13661–13665, 1997.

[51] N. Q. Balaban, U. S. Schwarz, D. Riveline, P. Goichberg, G. Tzur, I. Sabanay, D. Mahalu, S. Safran, A. Bershadsky, L. Addadi, *et al.*, "Force and focal adhesion assembly: a close relationship studied using elastic micropatterned substrates," *Nature cell biology*, vol. 3, no. 5, pp. 466–472, 2001.

[52] A. K. Harris, P. Wild, and D. Stopak, "Silicone rubber substrata: a new wrinkle in the study of cell locomotion," *Science*, vol. 208, no. 4440, pp. 177–179, 1980.

[53] C. N. Holenstein, U. Silvan, and J. G. Snedeker, "High-resolution traction force microscopy on small focal adhesions-improved accuracy through optimal marker distribution and optical flow tracking," *Scientific reports*, vol. 7, no. 1, p. 41633, 2017.

[54] E. Schrödinger, "What is life? the physical aspect of the living cell.," 1944.

[55] S. Ramaswamy, "The mechanics and statistics of active matter," *Annu. Rev. Condens. Matter Phys.*, vol. 1, no. 1, pp. 323–345, 2010.

[56] M. C. Marchetti, J.-F. Joanny, S. Ramaswamy, T. B. Liverpool, J. Prost, M. Rao, and R. A. Simha, "Hydrodynamics of soft active matter," *Reviews of modern physics*, vol. 85, no. 3, pp. 1143–1189, 2013.

[57] G. Gompper, R. G. Winkler, T. Speck, A. Solon, C. Nardini, F. Peruani, H. Löwen, R. Golestanian, U. B. Kaupp, L. Alvarez, T. Kiørboe, E. Lauga, W. C. K. Poon, A. DeSimone, S. Muiños-Landin, A. Fischer, N. A. Söker, F. Cichos, R. Kapral, P. Gaspard, M. Ripoll, F. Sagues, A. Doostmohammadi, J. M. Yeomans, I. S. Aranson, C. Bechinger, H. Stark, C. K. Hemelrijk, F. J. Nedelec, T. Sarkar, T. Aryaksama, M. Lacroix, G. Duclos, V. Yashunsky, P. Silberzan, M. Arroyo, and S. Kale, "The 2020 motile active matter roadmap," *Journal of Physics: Condensed Matter*, vol. 32, p. 193001, feb 2020.

[58] F. Jülicher, S. W. Grill, and G. Salbreux, "Hydrodynamic theory of active matter," *Reports on Progress in Physics*, vol. 81, no. 7, p. 076601, 2018.

[59] J. R. Howse, R. A. Jones, A. J. Ryan, T. Gough, R. Vafabakhsh, and R. Golestanian, "Self-motile colloidal particles: from directed propulsion to random walk," *Physical review letters*, vol. 99, no. 4, p. 048102, 2007.

[60] G. Livne, S. Gat, S. Armon, and A. Bernheim-Groswasser, "Self-assembled active actomyosin gels spontaneously curve and wrinkle similar to biological cells and tissues," *Proceedings of the National Academy of Sciences*, vol. 121, no. 2, p. e2309125121, 2024.

[61] M. F. Staddon, E. M. Munro, and S. Banerjee, "Pulsatile contractions and pattern formation in excitable actomyosin cortex," *PLOS Computational Biology*, vol. 18, no. 3, p. e1009981, 2022.

[62] H. Koyama, H. Okumura, A. M. Ito, K. Nakamura, T. Otani, K. Kato, and T. Fujimori, "Effective mechanical potential of cell–cell interaction explains three-dimensional morphologies during early embryogenesis," *PLoS Computational Biology*, vol. 19, no. 8, p. e1011306, 2023.

[63] D. T. Kysela, A. M. Randich, P. D. Caccamo, and Y. V. Brun, "Diversity takes shape: understanding the mechanistic and adaptive basis of bacterial morphology," *PLoS Biology*, vol. 14, no. 10, p. e1002565, 2016.

[64] A. Livshits, L. Shani-Zerbib, Y. Maroudas-Sacks, E. Braun, and K. Keren, "Structural inheritance of the actin cytoskeletal organization determines the body axis in regenerating hydra," *Cell reports*, vol. 18, no. 6, pp. 1410–1421, 2017.

[65] Y. Maroudas-Sacks, L. Garion, L. Shani-Zerbib, A. Livshits, E. Braun, and K. Keren, "Topological defects in the nematic order of actin fibres as organization centres of hydra morphogenesis," *Nature Physics*, vol. 17, no. 2, pp. 251–259, 2021.

[66] T. Lecuit and P.-F. Lenne, "Cell surface mechanics and the control of cell shape, tissue patterns and morphogenesis," *Nature reviews Molecular cell biology*, vol. 8, no. 8, pp. 633–644, 2007.

[67] M. Tozluoglu and Y. Mao, "On folding morphogenesis, a mechanical problem," *Philosophical Transactions of the Royal Society B*, vol. 375, no. 1809, p. 20190564, 2020.

[68] S. S. Lou, A. S. Kennard, E. F. Koslover, E. Gutierrez, A. Groisman, and J. A. Theriot, "Elastic wrinkling of keratocyte lamellipodia driven by myosin-induced contractile stress," *Biophysical Journal*, vol. 120, no. 9, pp. 1578–1591, 2021.

[69] J. Prost, F. Jülicher, and J.-F. Joanny, "Active gel physics," *Nature physics*, vol. 11, no. 2, pp. 111–117, 2015.

[70] A. Bernheim-Groswasser, N. S. Gov, S. A. Safran, and S. Tzlil, "Living matter: mesoscopic active materials," *Advanced Materials*, vol. 30, no. 41, p. 1707028, 2018.

[71] S. Banerjee, M. L. Gardel, and U. S. Schwarz, "The actin cytoskeleton as an active adaptive material," *Annual Review of Condensed Matter Physics*, vol. 11, no. 1, pp. 421–439, 2020.

[72] E. Moeendarbary, L. Valon, M. Fritzsche, A. R. Harris, D. A. Moulding, A. J. Thrasher, E. Stride, L. Mahadevan, and G. T. Charras, "The cytoplasm of living cells behaves as a poroelastic material," *Nature Materials*, vol. 12, p. 253, Jan 2013. Article.

[73] Z. Wang, M. C. Marchetti, and F. Brauns, "Patterning of morphogenetic anisotropy fields," *Proceedings of the National Academy of Sciences*, vol. 120, no. 13, p. e2220167120, 2023.

[74] D. Pearce, S. Gat, G. Livne, A. Bernheim-Groswasser, and K. Kruse, "Defect-driven shape transitions in elastic active nematic shells," *arXiv preprint arXiv:2010.13141*, 2020.

[75] F. Backouche, L. Haviv, D. Groswasser, and A. Bernheim-Groswasser, "Active gels: dynamics of patterning and self-organization," *Physical biology*, vol. 3, no. 4, p. 264, 2006.

[76] J. Alvarado, M. Sheinman, A. Sharma, F. C. MacKintosh, and G. H. Koenderink, "Molecular motors robustly drive active gels to a critically connected state," *Nature physics*, vol. 9, no. 9, pp. 591–597, 2013.

[77] H. Ennomani, G. Letort, C. Guérin, J.-L. Martiel, W. Cao, F. Nédélec, M. Enrique, M. Théry, and L. Blanchoin, "Architecture and connectivity govern actin network contractility," *Current Biology*, vol. 26, no. 5, pp. 616–626, 2016.

[78] Y. Ideses, A. Sonn-Segev, Y. Roichman, and A. Bernheim-Groswasser, "Myosin ii does it all: assembly, remodeling, and disassembly of actin networks are governed by myosin ii activity," *Soft Matter*, vol. 9, no. 29, pp. 7127–7137, 2013.

[79] M. Soares e Silva, M. Depken, B. Stuhrmann, M. Korsten, F. C. MacKintosh, and G. H. Koenderink, "Active multistage coarsening of actin networks driven by myosin motors," *Proceedings of the National Academy of Sciences*, vol. 108, no. 23, pp. 9408–9413, 2011.

[80] I. Linsmeier, S. Banerjee, P. W. Oakes, W. Jung, T. Kim, and M. P. Murrell, "Disordered actomyosin networks are sufficient to produce cooperative and telescopic contractility," *Nature communications*, vol. 7, no. 1, p. 12615, 2016.

[81] Y. Ideses, V. Erukhimovitch, R. Brand, D. Jourdain, J. S. Hernandez, U. R. Gabinet, S. A. Safran, K. Kruse, and A. Bernheim-Groswasser, "Spontaneous buckling of contractile poroelastic actomyosin sheets," *Nature Communications*, vol. 9, no. 1, p. 2461, 2018.

[82] D. Ambrosi, G. A. Ateshian, E. M. Arruda, S. Cowin, J. Dumais, A. Goriely, G. A. Holzapfel, J. D. Humphrey, R. Kemkemer, E. Kuhl, *et al.*, "Perspectives on biological growth and remodeling," *Journal of the Mechanics and Physics of Solids*, vol. 59, no. 4, pp. 863–883, 2011.

[83] P. Kollmannsberger, C. Bidan, J. Dunlop, and P. Fratzl, "The physics of tissue patterning and extracellular matrix organisation: how cells join forces," *Soft matter*, vol. 7, no. 20, pp. 9549–9560, 2011.

[84] V. S. Deshpande, R. M. McMeeking, and A. G. Evans, "A bio-chemo-mechanical model for cell contractility," *Proceedings of the National Academy of Sciences*, vol. 103, no. 38, pp. 14015–14020, 2006.

[85] V. S. Deshpande, R. M. McMeeking, and A. G. Evans, "A model for the contractility of the cytoskeleton including the effects of stress-fibre formation and dissociation," *Proceedings of the Royal Society A: Mathematical, Physical and Engineering Sciences*, vol. 463, no. 2079, pp. 787–815, 2007.

[86] E. G. Rens and R. M. Merks, "Cell shape and durotaxis explained from cell-extracellular matrix forces and focal adhesion dynamics," *Iscience*, vol. 23, no. 9, p. 101488, 2020.

[87] T. Mitchison and M. Kirschner, "Cytoskeletal dynamics and nerve growth," *Neuron*, vol. 1, no. 9, pp. 761–772, 1988.

[88] C. E. Chan and D. J. Odde, "Traction dynamics of filopodia on compliant substrates," *Science*, vol. 322, no. 5908, pp. 1687–1691, 2008.

[89] W. Shu and C. N. Kaplan, "A multiscale whole-cell theory for mechano-sensitive migration on viscoelastic substrates," *bioRxiv*, 2022.

[90] Z. Gong, S. E. Szczesny, S. R. Caliari, E. E. Charrier, O. Chaudhuri, X. Cao, Y. Lin, R. L. Mauck, P. A. Janmey, J. A. Burdick, *et al.*, "Matching material and cellular timescales maximizes cell spreading on viscoelastic substrates," *Proceedings of the National Academy of Sciences*, vol. 115, no. 12, pp. E2686–E2695, 2018.

[91] W. Shu and C. N. Kaplan, "Effects of matrix viscoelasticity and geometrical constraint on cell migrations: A multiscale bio-chemo-mechanical model," *Biophysical Journal*, vol. 122, no. 3, p. 535a, 2023.

[92] K. Schakenraad, L. Ravazzano, N. Sarkar, J. A. Wondergem, R. M. Merks, and L. Giomi, "Topotaxis of active brownian particles," *Physical Review E*, vol. 101, no. 3, p. 032602, 2020.

[93] S. Hermann, P. Krinninger, D. de Las Heras, and M. Schmidt, "Phase coexistence of active brownian particles," *Physical Review E*, vol. 100, no. 5, p. 052604, 2019.

[94] B. Ladoux and R.-M. Mège, "Mechanobiology of collective cell behaviours," *Nature Reviews Molecular Cell Biology*, vol. 18, pp. 743–757, Dec 2017.

[95] R. Alert and X. Trepat, "Physical models of collective cell migration," *Annual Review of Condensed Matter Physics*, vol. 11, no. 1, pp. 77–101, 2020.

[96] J. P. . Winer JP, Oake S, "Non-linear elasticity of extracellular matrices enables contractile cells to communicate local position and orientation.," *PLoS ONE*, vol. 4, no. 7, p. e6382, 2009.

[97] D. E. Discher, P. Janmey, and Y.-l. Wang, "Tissue cells feel and respond to the stiffness of their substrate," *Science*, vol. 310, no. 5751, pp. 1139–1143, 2005.

[98] A. Vaziri and A. Gopinath, "Cell and biomolecular mechanics in silico," *Nature materials*, vol. 7, pp. 15–23, 2008.

[99] A. J. Engler, S. Sen, H. L. Sweeney, and D. E. Discher, "Matrix elasticity directs stem cell lineage specification," *Cell*, vol. 126, no. 4, pp. 677–689, 2006.

[100] J. Eyckmans, T. Boudou, X. Yu, and C. Chen, "A hitchhiker's guide to mechanobiology," *Developmental Cell*, vol. 21, no. 1, pp. 35–47, 2011.

[101] E. H. Barriga, K. Franze, G. Charras, and R. Mayor, "Tissue stiffening coordinates morphogenesis by triggering collective cell migration in vivo," *Nature*, vol. 554, pp. 523–527, 2018.

[102] S.-Y. Tee, J. Fu, C. S. Chen, and P. A. Janmey, "Cell shape and substrate rigidity both regulate cell stiffness," *Biophysical Journal*, vol. 100, pp. L25–27, 2011.

[103] A. Chopra, E. Tabdanov, H. Patel, P. A. Janmey, and J. Y. Kresh, "Cardiac myocyte remodeling mediated by n-cadherin-dependent mechanosensing," *American journal of physiology*, vol. 300, pp. H1252–1266, 2011.

[104] S. Vichare, S. Sen, and M. M. Inamdar, "Cellular mechanoadaptation to substrate mechanical properties: contributions of substrate stiffness and thickness to cell stiffness measurements using afm," *Soft Matter*, vol. 10, pp. 1174–1181, 2014.

[105] J. R. Staunton, B. L. Doss, S. Lindsay, and R. Ros, "Correlating confocal microscopy and atomic force indentation reveals metastatic cancer cells stiffen during invasion into collagen i matrices," *Sci. Rep.*, vol. 6, p. 19686, 2016.

[106] S. E. Cross, Y. S. Jin, J. Rao, and J. K. Gimzewski, "Nanomechanical analysis of cells from cancer patients," *Nature nanotechnology*, vol. 2, pp. 780–783, 2007.

[107] S. J. Han, K. S. Bielawski, L. H. Ting, M. L. Rodriguez, and N. J. Sniadecki, "Decoupling substrate stiffness, spread area, and micropost density: a close spatial relationship between traction forces and focal adhesions," *Biophysical Journal*, vol. 103, pp. 640–648, 2012.

[108] J. Rheinlaender, A. Dimitracopoulos, B. Wallmeyer, N. M. Kronenberg, K. J. Chalut, M. C. Gather, T. Betz, G. Charras, and K. Franze, "Cortical cell stiffness is independent of substrate mechanics," *Nature Materials*, vol. 19, p. 1019–1025, 2020.

[109] C.-L. Guo, M. Ouyang, J.-Y. Yu, J. Maslov, A. Price, and C.-Y. Shen, "Long-range mechanical force enables self-assembly of epithelial tubular patterns," *Proceedings of the National Academy of Sciences*, vol. 109, no. 15, pp. 5576–5582, 2012.

[110] H. Wang, A. Abhilash, C. S. Chen, R. G. Wells, and V. B. Shenoy, "Long-range force transmission in fibrous matrices enabled by tension-driven alignment of fibers," *Biophysical Journal*, vol. 107, no. 11, pp. 2592 – 2603, 2014.

[111] S. Natan, Y. Koren, O. Shelah, S. Goren, and A. Lesman, "Long-range mechanical coupling of cells in 3d fibrin gels," *Molecular Biology of the Cell*, vol. 31, no. 14, pp. 1474–1485, 2020. PMID: 32374653.

[112] P. Pakshir, M. Alizadehgiashi, B. Wong, N. M. Coelho, X. Chen, Z. Gong, V. B. Shenoy, C. A. McCulloch, and B. Hinz, "Dynamic fibroblast contractions attract remote macrophages in fibrillar collagen matrix," *Nature Communications*, vol. 10, p. 1850, Apr 2019.

[113] X. Zhang, T.-H. Kim, T. J. Thauland, H. Li, F. S. Majedi, C. Ly, Z. Gu, M. J. Butte, C. Rowat, A, and S. Li, "Unraveling the mechanobiology of immune cells," *Current Opinion in Biotechnology*, vol. 66, pp. 236–245, 2020.

[114] T.-G. Kwon, T. D. Yang, and K. J. Lee, "Enhancement of chemotactic cell aggregation by haptotactic cell-to-cell interaction," *PLoS ONE*, vol. 11, p. e0154717, 2016.

[115] T. D. Yang, T. G. Kwon, J.-S. Park, and K. J. Lee, "Trail networks formed by populations of immune cells," *New J Physics*, vol. 16, p. 023017, 2014.

[116] K. Nasu-Tada, S. Koizumi, and K. Inoue, "Involvement of 1 integrin in microglial chemotaxis and proliferation on fibronectin: Different regulations by adp through pka," *Glia*, vol. 52, pp. 98–107, 2005.

[117] L. Fetler and S. Amigorena, "Brain under surveillance: the microglia patrol," *Neuroscience*, vol. 309, pp. 329–393, 2005.

[118] C. Vincent, T. A. Siddiqui, and L. C. Schlichter, "Podosomes in migrating microglia: components and matrix degradation," *J Neuroinflammation*, vol. 9, p. 190, 2012.

[119] C. Théry, M. Ostrowski, and E. Segura, "Membrane vesicles as conveyors of immune responses," *Nat Rev Immunol.*, vol. 9, p. 581–593, 2009.

[120] T. C. Theoharides, I. Tsilioni, and M. Bawazeer, "Mast cells, neuroinflammation and pain in fibromyalgia syndrome," *Frontiers in cellular neuroscience*, vol. 13, p. 353, 2019.

[121] C. Demopoulos, S. Antonopoulou, and T. C. Theoharides, "Covid-19, microthromboses, and platelet activating factor," *Biofactors*, vol. 46, pp. 927–933, 2020.

[122] J. Yuval and S. A. Safran, "Dynamics of elastic interactions in soft and biological matter," *Phys. Rev. E*, vol. 87, p. 042703, Apr 2013.

[123] X. Tang, P. Bajaj, R. Bashir, and T. A. Saif, "How far cardiac cells can see each other mechanically," *Soft Matter*, vol. 7, pp. 6151–6158, 2011.

[124] I. Nitsan, S. Drori, Y. E. Lewis, S. Cohen, and S. Tzlil, "Mechanical communication in cardiac cell synchronized beating," *Nature Physics*, vol. 12, pp. 472–477, May 2016.

[125] K. Dasbiswas, S. Majkut, D. E. Discher, and S. A. Safran, "Substrate stiffness-modulated registry phase correlations in cardiomyocytes map structural order to coherent beating," *Nature Communications*, vol. 6, p. 6085, 2015.

[126] J. J. Tomasek, G. Gabbiani, B. Hinz, C. Chaponnier, and R. A. Brown, "Myofibroblasts and mechano-regulation of connective tissue remodelling," *Nature Reviews Molecular Cell Biology*, vol. 3, pp. 349–363, May 2002.

[127] T. Korff and H. Augustin, "Tensional forces in fibrillar extracellular matrices control directional capillary sprouting," *Journal of Cell Science*, vol. 112, no. 19, pp. 3249–3258, 1999.

[128] Z. Liu, S. Woo, and O. D. Weiner, "Nodal signaling has dual roles in fate specification and directed migration during germ layer segregation in zebrafish," *Development*, vol. 145, no. 17, 2018.

[129] R. J. Pelham and Y.-l. Wang, "Cell locomotion and focal adhesions are regulated by substrate flexibility," *Proceedings of the National Academy of Sciences*, vol. 94, no. 25, pp. 13661–13665, 1997.

[130] I. B. Bischofs and U. S. Schwarz, "Cell organization in soft media due to active mechanosensing," *Proceedings of the National Academy of Sciences*, vol. 100, no. 16, pp. 9274–9279, 2003.

[131] R. van Oers, E. Rens, D. LaValley, C. Reinhart-King, and R. Merks, "Mechanical cell-matrix feedback explains pairwise and collective endothelial cell behavior in vitro.," *PLoS Comput Biol*, vol. 10, no. 8, p. e1003774, 2014.

[132] U. S. Schwarz and S. A. Safran, "Physics of adherent cells," *Rev. Mod. Phys.*, vol. 85, pp. 1327–1381, Aug 2013.

[133] J. Yang, P. E. Arratia, A. E. Patteson, and A. Gopinath, "Quenching active swarms: effects of light exposure on collective motility in swarming serratia marcescens," *J. Roy. Soc. Interface*, vol. 16, p. 1620180960, 2019.

[134] K. Mandal, I. Wang, E. Vitiello, L. A. C. Orellana, and M. Balland, "Cell dipole behaviour revealed by ecm sub-cellular geometry," *Nature Communications*, vol. 5, p. 5749, Dec 2014.

[135] T. Mura, *Micromechanics of Defects in Solids*. TheHague: Martnius Nijhoff, 1991.

[136] D. Ben-Yaakov, R. Golkov, Y. Shokef, and S. A. Safran, "Response of adherent cells to mechanical perturbations of the surrounding matrix," *Soft Matter*, vol. 11, pp. 1412–1424, 2015.

[137] R. Golkov and Y. Shokef, "Shape regulation generates elastic interaction between living cells," *New Journal of Physics*, vol. 19, p. 063011, jun 2017.

[138] Y. Fily, P. Subramanian, T. M. Schneider, R. Chelakkot, and A. Gopinath, "Buckling instabilities and spatio-temporal dynamics of active elastic filaments," *J. Roy. Soc. Interface*, vol. 17, p. 20190794, 2019.

[139] J. Notbohm, A. Lesman, P. Rosakis, D. A. Tirrell, and G. Ravichandran, "Microbuckling of fibrin provides a mechanism for cell mechanosensing," *Journal of The Royal Society Interface*, vol. 12, no. 108, p. 20150320, 2015.

[140] X. Xu and S. A. Safran, "Nonlinearities of biopolymer gels increase the range of force transmission," *Phys. Rev. E*, vol. 92, p. 032728, Sep 2015.

[141] R. Golkov and Y. Shokef, "Elastic interactions between anisotropically contracting circular cells," *Phys. Rev. E*, vol. 99, p. 032418, Mar 2019.

[142] D. Pei, X. Shu, A. Gassama-Diagne, and J. P. Thiery, "Mesenchymal–epithelial transition in development and reprogramming," *Nature Cell Biology*, vol. 21, pp. 44–53, Jan. 2019.

[143] I. B. Bischofs and U. S. Schwarz, "Effect of poisson ratio on cellular structure formation," *Phys. Rev. Lett.*, vol. 95, p. 068102, Aug 2005.

[144] J. Hong, C. Ge, P. Jothikumar, Z. Yuan, B. Liu, K. Bai, K. Li, W. Rittase, M. Shinzawa, and Y. e. a. Zhang, "A tcr mechanotransduction signaling loop induces negative selection in the thymus," *Nat Immunol*, vol. 19, pp. 1379–1390, 2018.

[145] S. Kumari, M. Mak, Y.-C. Poh, M. Tohme, N. Watson, M. Melo, E. Janssen, M. Dustin, R. Geha, and D. J. Irvine, "Cytoskeletal tension actively sustains the migratory t-cell synaptic contact," *EMBO J*, vol. 39, p. e102783, 2020.

[146] T. Iskratsch, H. Wolfenson, and M. P. Sheetz, "Appreciating force and shape — the rise of mechanotransduction in cell biology," *Nat Rev Mol Cell Biol*, vol. 15, pp. 825–833, 2014.

[147] M. Huse, "Mechanical forces in the immune system," *Nat Rev Immunol*, vol. 17, pp. 679–690, 2017.

[148] C. Zhu, W. Chen, J. Lou, W. Rittase, and K. Li, "Mechanosensing through immunoreceptors," *Nature Immunology*, vol. 20, pp. 1269–1278, 2019.

[149] M. Huse, "Integrins and their role in immune cell adhesion," *Cell*, vol. 177, pp. 499–501, 2019.

[150] M. Mani, A. Gopinath, and L. Mahadevan, "How things get stuck: kinetics, elasto-hydrodynamics, and soft adhesion," *Phys. Rev. Lett.*, vol. 108, p. 226104, 2012.

[151] R. Sunyer, V. Conte, J. Escribano, A. Elosegui-Artola, A. Labernadie, L. Valon, D. Navajas, J. M. García-Aznar, J. J. Muñoz, P. Roca-Cusachs, and X. Trepat, "Collective cell durotaxis emerges from long-range intercellular force transmission," *Science*, vol. 353, no. 6304, pp. 1157–1161, 2016.

[152] E. A. Novikova, M. Raab, D. E. Discher, and C. Storm, "Persistence-driven durotaxis: Generic, directed motility in rigidity gradients," *Phys. Rev. Lett.*, vol. 118, p. 078103, Feb 2017.

[153] J. P. Califano and C. A. Reinhart-King, "A balance of substrate mechanics and matrix chemistry regulates endothelial cell network assembly," *Cellular and Molecular Bioengineering*, vol. 1, p. 122, Oct 2008.

[154] C. T. McKee, V. K. Raghunathan, P. F. Nealey, P. Russell, and C. J. Murphy, "Topographic modulation of the orientation and shape of cell nuclei and their influence on the measured elastic modulus of epithelial cells," *Biophysical J*, vol. 101, no. 9, pp. P2139–2146, 2011.

[155] D. W. Zhou, T. T. Lee, S. Weng, J. Fuc, and A. J. García, "Effects of substrate stiffness and actomyosin contractility on coupling between force transmission and vinculin–paxillin recruitment at single focal adhesions," *MBoC*, vol. 28, pp. 1901–1911, 2017.

[156] D. A. Vargas, T. Heck, B. Smeets, H. Ramon, H. Parameswaran, and H. Van Oosterwyck, "Intercellular adhesion stiffness moderates cell decoupling on stiff substrates," *bioRxiv 802520*, 2019.

[157] M. C. Marchetti, J. F. Joanny, S. Ramaswamy, T. B. Liverpool, J. Prost, M. Rao, and R. A. Simha, "Hydrodynamics of soft active matter," *Rev. Mod. Phys.*, vol. 85, pp. 1143–1189, Jul 2013.

[158] C. Bechinger, R. Di Leonardo, H. Löwen, C. Reichhardt, G. Volpe, and G. Volpe, "Active particles in complex and crowded environments," *Reviews of Modern Physics*, vol. 88, no. 4, p. 045006, 2016.

[159] K. Copenhagen, G. Malet-Engra, W. Yu, G. Scita, N. Gov, and A. Gopinathan, "Frustration-induced phases in migrating cell clusters," *Science Advances*, vol. 4, no. 9, 2018.

[160] T. E. Angelini, E. Hannezo, X. Trepat, J. J. Fredberg, and D. A. Weitz, "Cell migration driven by cooperative substrate deformation patterns," *Phys. Rev. Lett.*, vol. 104, p. 168104, Apr 2010.

[161] U. S. Schwarz and S. A. Safran, "Physics of adherent cells," *Rev. Mod. Phys.*, vol. 85, pp. 1327–1381, Aug 2013.

[162] S. Henkes, K. Kostanjevec, J. M. Collinson, R. Sknepnek, and E. Bertin, "Dense active matter model of motion patterns in confluent cell monolayers," *Nature communications*, vol. 11, no. 1, pp. 1–9, 2020.

[163] H. Chaté, F. Ginelli, G. Grégoire, F. Peruani, and F. Raynaud, "Modeling collective motion: variations on the vicsek model," *The European Physical Journal B*, vol. 64, pp. 451–456, Aug 2008.

[164] M. E. Cates and J. Tailleur, "Motility-induced phase separation," *Annual Review of Condensed Matter Physics*, vol. 6, no. 1, pp. 219–244, 2015.

[165] P. Digregorio, D. Levis, A. Suma, L. F. Cugliandolo, G. Gonnella, and I. Pagonabarraga, "Full phase diagram of active brownian disks: From melting to motility-induced phase separation," *Physical review letters*, vol. 121, no. 9, p. 098003, 2018.

[166] M. Dembo and Y.-L. Wang, "Stresses at the cell-to-substrate interface during locomotion of fibroblasts," *Biophysical Journal*, vol. 76, no. 4, pp. 2307 – 2316, 1999.

[167] X. Tang, P. Bajaj, R. Bashir, and T. A. Saif, "How far cardiac cells can see each other mechanically," *Soft Matter*, vol. 7, pp. 6151–6158, 2011.

[168] O. Cohen and S. A. Safran, "Elastic interactions synchronize beating in cardiomyocytes," *Soft matter*, vol. 12, no. 28, pp. 6088–6095, 2016.

[169] C. A. Reinhart-King, M. Dembo, and D. A. Hammer, "Endothelial cell traction forces on rgd-derivatized polyacrylamide substrata," *Langmuir*, vol. 19, pp. 1573–1579, Mar 2003.

[170] B. Palmieri, C. Scanlon, D. Worroll III, M. Grant, and J. Lee, "Substrate mediated interaction between pairs of keratocytes: Multipole traction force models describe their migratory behavior," *Plos one*, vol. 14, no. 3, p. e0212162, 2019.

[171] P. G. de Gennes and P. A. Pincus, "Pair correlations in a ferromagnetic colloid," *Physik der Kondensierten Materie*, vol. 11, pp. 189–198, Aug. 1970.

[172] D. Nishiguchi, J. Iwasawa, H.-R. Jiang, and M. Sano, "Flagellar dynamics of chains of active janus particles fueled by an AC electric field," *New Journal of Physics*, vol. 20, p. 015002, jan 2018.

[173] P. Ilg and E. Del Gado, "Non-linear response of dipolar colloidal gels to external fields," *Soft Matter*, vol. 7, pp. 163–171, 2011.

[174] T. Tlusty and S. A. Safran, "Defect-induced phase separation in dipolar fluids," *Science*, vol. 290, no. 5495, pp. 1328–1331, 2000.

[175] L. Rovigatti, J. Russo, and F. Sciortino, "No evidence of gas-liquid coexistence in dipolar hard spheres," *Physical review letters*, vol. 107, no. 23, p. 237801, 2011.

[176] N. Sakaï and C. P. Royall, "Active dipolar colloids in three dimensions: strings, sheets, labyrinthine textures and crystals," *arXiv preprint arXiv:2010.03925*, 2020.

[177] A. Kaiser, K. Popowa, and H. Löwen, "Active dipole clusters: From helical motion to fission," *Phys. Rev. E*, vol. 92, p. 012301, Jul 2015.

[178] G.-J. Liao, C. K. Hall, and S. H. L. Klapp, "Dynamical self-assembly of dipolar active brownian particles in two dimensions," *Soft Matter*, vol. 16, no. 9, pp. 2208–2223, 2020.

[179] F. Guzmán-Lastra, A. Kaiser, and H. Löwen, "Fission and fusion scenarios for magnetic microswimmer clusters," *Nature Communications*, vol. 7, p. 13519, Nov 2016.

[180] V. Telezki and S. Klumpp, "Simulations of structure formation by confined dipolar active particles," *Soft Matter*, vol. 16, pp. 10537–10547, 2020.

[181] S. Fatehiboroujeni, A. Gopinath, and S. Goyal, "Nonlinear oscillations induced by follower forces in prestressed clamped rods subjected to drag," *Journal of Computational and Nonlinear Dynamics*, vol. 13, no. 12, p. 121005, 2018.

[182] A. S. Sangani and A. Gopinath, "Elastohydrodynamical instabilities of active filaments, arrays, and carpets analyzed using slender-body theory," *Physical Review Fluids*, vol. 5, no. 8, p. 083101, 2020.

[183] Y. Fily, P. Subramanian, T. M. Schneider, R. Chelakkot, and A. Gopinath, "Buckling instabilities and spatio-temporal dynamics of active elastic filaments," *Journal of the Royal Society Interface*, vol. 17, no. 165, p. 20190794, 2020.

[184] R. Chelakkot, M. F. Hagan, and A. Gopinath, "Synchronized oscillations, traveling waves, and jammed clusters induced by steric interactions in active filament arrays," *Soft Matter*, vol. 17, no. 4, pp. 1091–1104, 2021.

[185] U. S. Schwarz and S. A. Safran, "Elastic interactions of cells," *Phys. Rev. Lett.*, vol. 88, p. 048102, Jan 2002.

[186] J. Yan, M. Han, J. Zhang, C. Xu, E. Luijten, and S. Granick, "Reconfiguring active particles by electrostatic imbalance," *Nature materials*, vol. 15, no. 10, pp. 1095–1099, 2016.

[187] P. Romanczuk, M. Bär, W. Ebeling, B. Lindner, and L. Schimansky-Geier, "Active brownian particles," *The European Physical Journal Special Topics*, vol. 202, no. 1, pp. 1–162, 2012.

[188] M. C. Marchetti, Y. Fily, S. Henkes, A. Patch, and D. Yllanes, "Minimal model of active colloids highlights the role of mechanical interactions in controlling the emergent behavior of active matter," *Current Opinion in Colloid & Interface Science*, vol. 21, pp. 34–43, 2016.

[189] S. Bose, K. Dasbiswas, and A. Gopinath, "Matrix stiffness modulates mechanical interactions and promotes contact between motile cells," *Biomedicines*, vol. 9, no. 4, 2021.

[190] D. Boal, *Mechanics of the Cell*. Cambridge University Press, 2 ed., 2012.

[191] L. D. Landau and E. M. Lifshitz, *Theory of Elasticity*, vol. 7 of *Course of Theoretical Physics*. London: Pergamon Press, 1959.

[192] H. Wagner and H. Horner, "Elastic interaction and the phase transition in coherent metal-hydrogen systems," *Advances in Physics*, vol. 23, no. 4, pp. 587–637, 1974.

[193] H. Zabel and H. Peisl, "Sample-shape-dependent phase transition of hydrogen in niobium," *Physical Review Letters*, vol. 42, no. 8, p. 511, 1979.

[194] I. B. Bischofs and U. S. Schwarz, "Collective effects in cellular structure formation mediated by compliant environments: A monte carlo study," *Acta Biomaterialia*, vol. 2, no. 3, pp. 253–265, 2006.

[195] A.-K. Marel, M. Zorn, C. Klingner, R. Wedlich-Söldner, E. Frey, and J. O. Rädler, "Flow and diffusion in channel-guided cell migration," *Biophys. J.*, vol. 107, pp. 1054–1064, Sept. 2014.

[196] B. Ezhilan, R. Alonso-Matilla, and D. Saintillan, "On the distribution and swim pressure of run-and-tumble particles in confinement," *Journal of Fluid Mechanics*, vol. 781, 2015.

[197] J. Elgeti and G. Gompper, "Run-and-tumble dynamics of self-propelled particles in confinement," *EPL (Europhysics Letters)*, vol. 109, no. 5, p. 58003, 2015.

[198] W. Yan and J. F. Brady, "The force on a boundary in active matter," *Journal of Fluid Mechanics*, vol. 785, 2015.

[199] C. Wagner, M. Hagan, and A. Baskaran, "Steady-state distributions of ideal active brownian particles under confinement and forcing," *Journal of Statistical Mechanics: Theory and Experiment*, vol. 2017, p. 043203, 04 2017.

[200] A. Poncet, O. Bénichou, V. Démery, and D. Nishiguchi, "Pair correlation of dilute active brownian particles: From low-activity dipolar correction to high-activity algebraic depletion wings," *Physical Review E*, vol. 103, Jan. 2021.

[201] R. G. Winkler and G. Gompper, "The physics of active polymers and filaments," *The Journal of Chemical Physics*, vol. 153, no. 4, p. 040901, 2020.

[202] G. Volpe, S. Gigan, and G. Volpe, "Simulation of the active brownian motion of a microswimmer," *American Journal of Physics*, vol. 82, no. 7, pp. 659–664, 2014.

[203] G. A. Vliegenthart, A. Ravichandran, M. Ripoll, T. Auth, and G. Gompper, "Filamentous active matter: Band formation, bending, buckling, and defects," *Science advances*, vol. 6, no. 30, p. eaaw9975, 2020.

[204] M. P. Allen and D. J. Tildesley, *Computer simulation of liquids*. Oxford university press, 2017.

[205] H. R. Vutukuri, M. Lisicki, E. Lauga, and J. Vermant, "Light-switchable propulsion of active particles with reversible interactions," *Nature communications*, vol. 11, no. 1, pp. 1–9, 2020.

[206] H. R. Vutukuri, B. Bet, R. Van Roij, M. Dijkstra, and W. T. Huck, "Rational design and dynamics of self-propelled colloidal bead chains: from rotators to flagella," *Scientific reports*, vol. 7, no. 1, pp. 1–14, 2017.

[207] M. Puljiz, S. Huang, G. K. Auernhammer, and A. M. Menzel, "Forces on rigid inclusions in elastic media and resulting matrix-mediated interactions," *Phys. Rev. Lett.*, vol. 117, p. 238003, Nov 2016.

[208] R. Phillips, J. Kondev, and J. Theriot, *Physical Biology of the Cell*. New York: Garland Science, Taylor & Francis Group, November 2008.

[209] T. Eisenstecken, G. Gompper, and R. Winkler, "Conformational properties of active semiflexible polymers," *Polymers*, vol. 8, p. 304, Aug 2016.

[210] X. Liao, P. K. Purohit, and A. Gopinath, "Extensions of the worm-like-chain model to tethered active filaments under tension," *The Journal of Chemical Physics*, vol. 153, no. 19, p. 194901, 2020.

[211] T. Vicsek, A. Czirók, E. Ben-Jacob, I. Cohen, and O. Shochet, "Novel type of phase transition in a system of self-driven particles," *Physical review letters*, vol. 75, no. 6, p. 1226, 1995.

[212] G. Charras and E. Sahai, "Physical influences of the extracellular environment on cell migration," *Nature reviews Molecular cell biology*, vol. 15, no. 12, pp. 813–824, 2014.

[213] G. S. Redner, M. F. Hagan, and A. Baskaran, "Structure and dynamics of a phase-separating active colloidal fluid," *Biophysical Journal*, vol. 104, no. 2, p. 640a, 2013.

[214] D. Selmeczi, S. Mosler, P. H. Hagedorn, N. B. Larsen, and H. Flyvbjerg, "Cell motility as persistent random motion: theories from experiments," *Biophysical journal*, vol. 89, no. 2, pp. 912–931, 2005.

[215] U. S. Schwarz and S. A. Safran, "Physics of adherent cells," *Rev. Mod. Phys.*, vol. 85, no. 3, pp. 1327–1381, 2013.

[216] O. Chaudhuri, J. Cooper-White, P. A. Janmey, D. J. Mooney, and V. B. Shenoy, "Effects of extracellular matrix viscoelasticity on cellular behaviour," *Nature*, vol. 584, pp. 535–546, Aug 2020.

[217] D. Rüdiger, K. Kick, A. Goychuk, A. M. Vollmar, E. Frey, and S. Zahler, "Cell-based strain remodeling of a nonfibrous matrix as an organizing principle for vasculogenesis," *Cell Reports*, vol. 32, no. 6, p. 108015, 2020.

[218] P. S. Noerr, J. E. Zamora Alvarado, F. Golnaraghi, K. E. McCloskey, A. Gopinathan, and K. Dasbiswas, "Optimal mechanical interactions direct multicellular network formation on elastic substrates," *Proceedings of the National Academy of Sciences*, vol. 120, no. 45, p. e2301555120, 2023.

[219] J. Notbohm, S. Banerjee, K. J. Utuje, B. Gweon, H. Jang, Y. Park, J. Shin, J. P. Butler, J. J. Fredberg, and M. C. Marchetti, "Cellular contraction and polarization drive collective cellular motion," *Biophysical journal*, vol. 110, no. 12, pp. 2729–2738, 2016.

[220] A. Shellard and R. Mayor, "Durotaxis: the hard path from in vitro to in vivo," *Developmental cell*, vol. 56, no. 2, pp. 227–239, 2021.

[221] R. Sunyer and X. Trepat, "Durotaxis," *Current Biology*, vol. 30, no. 9, pp. R383–R387, 2020.

[222] M. Raab, J. Swift, P. D. P. Dingal, P. Shah, J.-W. Shin, and D. E. Discher, "Crawling from soft to stiff matrix polarizes the cytoskeleton and phosphoregulates myosin-ii heavy chain," *Journal of Cell Biology*, vol. 199, no. 4, pp. 669–683, 2012.

[223] B. Yeoman, G. Shatkin, P. Beri, A. Banisadr, P. Katira, and A. J. Engler, "Adhesion strength and contractility enable metastatic cells to become adurotactic," *Cell reports*, vol. 34, no. 10, p. 108816, 2021.

[224] J. Park, D.-H. Kim, H.-N. Kim, C. J. Wang, M. K. Kwak, E. Hur, K.-Y. Suh, S. S. An, and A. Levchenko, "Directed migration of cancer cells guided by the graded texture of the underlying matrix," *Nat. Mater.*, vol. 15, no. 7, p. 792, 2016.

[225] R. Sunyer, V. Conte, J. Escribano, A. Elosegui-Artola, A. Labernadie, L. Valon, D. Navajas, J. M. García-Aznar, J. J. Muñoz, P. Roca-Cusachs, *et al.*, "Collective cell durotaxis emerges from long-range intercellular force transmission," *Science*, vol. 353, no. 6304, pp. 1157–1161, 2016.

[226] A. Shellard and R. Mayor, "Collective durotaxis along a self-generated stiffness gradient in vivo," *Nature*, vol. 600, no. 7890, pp. 690–694, 2021.

[227] A. Isomursu, K.-Y. Park, J. Hou, B. Cheng, M. Mathieu, G. A. Shamsan, B. Fuller, J. Kasim, M. M. Mahmoodi, T. J. Lu, *et al.*, "Directed cell migration towards softer environments," *Nature materials*, vol. 21, no. 9, pp. 1081–1090, 2022.

[228] C. D. Hartman, B. C. Isenberg, S. G. Chua, and J. Y. Wong, "Vascular smooth muscle cell durotaxis depends on extracellular matrix composition," *Proc. Natl. Acad. Sci.*, vol. 113, pp. 11190–11195, oct 2016.

[229] G. Yu, J. Feng, H. Man, and H. Levine, "Phenomenological modeling of durotaxis," *Physical Review E*, vol. 96, no. 1, p. 010402, 2017.

[230] A. Zemel, F. Rehfeldt, A. E. X. Brown, D. E. Discher, and S. A. Safran, "Optimal matrix rigidity for stress-fibre polarization in stem cells," *Nature Physics*, vol. 6, pp. 468 –, Mar 2010.

[231] E. A. Novikova, M. Raab, D. E. Discher, and C. Storm, "Persistence-driven durotaxis: Generic, directed motility in rigidity gradients," *Physical review letters*, vol. 118, no. 7, p. 078103, 2017.

[232] P.-C. Chen, X.-Q. Feng, and B. Li, "Unified multiscale theory of cellular mechanical adaptations to substrate stiffness," *Biophysical Journal*, vol. 121, no. 18, pp. 3474–3485, 2022.

[233] M. Murrell, P. W. Oakes, M. Lenz, and M. L. Gardel, "Forcing cells into shape: the mechanics of actomyosin contractility," *Nature Reviews Molecular Cell Biology*, vol. 16, p. 486, Jul 2015. Review Article.

[234] A. L. Godeau, M. Leoni, J. Comelles, T. Guyomar, M. Lieb, H. Delanoë-Ayari, A. Ott, S. Harlepp, P. Sens, and D. Riveline, "3d single cell migration driven by temporal correlation between oscillating force dipoles," *Elife*, vol. 11, p. e71032, 2022.

[235] P. Sens, "Stick–slip model for actin-driven cell protrusions, cell polarization, and crawling," *Proceedings of the National Academy of Sciences*, vol. 117, no. 40, pp. 24670–24678, 2020.

[236] A. Carlsson, "Mechanisms of cell propulsion by active stresses," *New journal of physics*, vol. 13, no. 7, p. 073009, 2011.

[237] J. E. Ron, P. Monzo, N. C. Gauthier, R. Voituriez, and N. S. Gov, "One-dimensional cell motility patterns," *Phys. Rev. Res.*, vol. 2, p. 033237, Aug 2020.

[238] M. Caraglio and T. Franosch, "Analytic solution of an active brownian particle in a harmonic well," *Physical Review Letters*, vol. 129, no. 15, p. 158001, 2022.

[239] F. Di Trapani, T. Franosch, and M. Caraglio, "Active brownian particles in a circular disk with an absorbing boundary," *Physical Review E*, vol. 107, no. 6, p. 064123, 2023.

[240] D. B. Brückner, P. Ronceray, and C. P. Broedersz, "Inferring the dynamics of underdamped stochastic systems," *Phys. Rev. Lett.*, vol. 125, p. 058103, Jul 2020.

[241] P. Dieterich, R. Klages, R. Preuss, and A. Schwab, "Anomalous dynamics of cell migration," *Proceedings of the National Academy of Sciences*, vol. 105, no. 2, pp. 459–463, 2008.

[242] P.-H. Wu, A. Giri, S. X. Sun, and D. Wirtz, "Three-dimensional cell migration does not follow a random walk," *Proceedings of the National Academy of Sciences*, vol. 111, no. 11, pp. 3949–3954, 2014.

[243] L. Walpole, "An elastic singularity in joined half-spaces," *International journal of engineering science*, vol. 34, no. 6, pp. 629–638, 1996.

[244] Y. Li, Z. Hu, and C. Li, "New method for measuring poisson's ratio in polymer gels," *Journal of applied polymer science*, vol. 50, no. 6, pp. 1107–1111, 1993.

[245] Y.-G. Tao, W. K. den Otter, J. Dhont, and W. J. Briels, "Isotropic-nematic spinodals of rigid long thin rodlike colloids by event-driven brownian dynamics simulations," *The Journal of chemical physics*, vol. 124, no. 13, 2006.

[246] D. Heyes, "Translational and rotational diffusion of rod shaped molecules by molecular dynamics simulations," *The Journal of Chemical Physics*, vol. 150, no. 18, 2019.

[247] M. Doi and S. Edwards, "Dynamics of rod-like macromolecules in concentrated solution. part 1," *Journal of the Chemical Society, Faraday Transactions 2: Molecular and Chemical Physics*, vol. 74, pp. 560–570, 1978.

[248] H. H. Wensink, H. Löwen, M. Marechal, A. Härtel, R. Wittkowski, U. Zimmermann, A. Kaiser, and A. M. Menzel, "Differently shaped hard body colloids in confinement: From passive to active particles," *The European Physical Journal Special Topics*, vol. 222, pp. 3023–3037, 2013.

[249] C. G. Wagner, M. F. Hagan, and A. Baskaran, "Steady-state distributions of ideal active brownian particles under confinement and forcing," *Journal of Statistical Mechanics: Theory and Experiment*, vol. 2017, no. 4, p. 043203, 2017.

[250] Y. Fily, Y. Kafri, A. P. Solon, J. Tailleur, and A. Turner, "Mechanical pressure and momentum conservation in dry active matter," *Journal of Physics A: Mathematical and Theoretical*, vol. 51, no. 4, p. 044003, 2017.

[251] K. Drescher, J. Dunkel, L. H. Cisneros, S. Ganguly, and R. E. Goldstein, "Fluid dynamics and noise in bacterial cell–cell and cell–surface scattering," *Proceedings of the National Academy of Sciences*, vol. 108, no. 27, pp. 10940–10945, 2011.

[252] D. Lopez and E. Lauga, "Dynamics of swimming bacteria at complex interfaces," *Physics of Fluids*, vol. 26, p. 071902, 2014.

[253] J. Tailleur and M. Cates, "Sedimentation, trapping, and rectification of dilute bacteria," *EPL (Europhysics Letters)*, vol. 86, no. 6, p. 60002, 2009.

[254] A. P. Berke, L. Turner, H. C. Berg, and E. Lauga, "Hydrodynamic attraction of swimming microorganisms by surfaces," *Physical Review Letters*, vol. 101, no. 3, p. 038102, 2008.

[255] D. Smith, E. Gaffney, J. Blake, and J. Kirkman-Brown, "Human sperm accumulation near surfaces: a simulation study," *Journal of Fluid Mechanics*, vol. 621, pp. 289–320, 2009.

[256] D. Giacché, T. Ishikawa, and T. Yamaguchi, "Hydrodynamic entrapment of bacteria swimming near a solid surface," *Physical Review E*, vol. 82, no. 5, p. 056309, 2010.

[257] G. Li, J. Bensson, L. Nisimova, D. Munger, P. Mahautmr, J. X. Tang, M. R. Maxey, and Y. V. Brun, "Accumulation of swimming bacteria near a solid surface," *Physical Review E*, vol. 84, no. 4, p. 041932, 2011.

[258] H. C. Berg and L. Turner, "Chemotaxis of bacteria in glass capillary arrays. escherichia coli, motility, microchannel plate, and light scattering," *Biophysical Journal*, vol. 58, no. 4, pp. 919–930, 1990.

[259] E. Lauga, W. R. DiLuzio, G. M. Whitesides, and H. A. Stone, "Swimming in circles: motion of bacteria near solid boundaries," *Biophysical journal*, vol. 90, no. 2, pp. 400–412, 2006.

[260] L. Lemelle, J.-F. Palierne, E. Chatre, and C. Place, "Counterclockwise circular motion of bacteria swimming at the air-liquid interface," *Journal of bacteriology*, vol. 192, no. 23, pp. 6307–6308, 2010.

[261] A. E. Patteson, A. Gopinath, and P. E. Arratia, "Active colloids in complex fluids," *Current Opinion in Colloid & Interface Science*, vol. 21, pp. 86–96, 2016.

[262] K. Schaar, A. Zöttl, and H. Stark, "Detention times of microswimmers close to surfaces: Influence of hydrodynamic interactions and noise," *Phys. Rev. Lett.*, vol. 115, p. 038101, Jul 2015.

[263] H. A. Kramers, "Brownian motion in a field of force and the diffusion model of chemical reactions," *Physica*, vol. 7, no. 4, pp. 284–304, 1940.

[264] A. A. Ketebo, C. Park, J. Kim, M. Jun, and S. Park, "Probing mechanobiological role of filamin a in migration and invasion of human u87 glioblastoma cells using submicron soft pillars," *Nano Convergence*, vol. 8, no. 1, p. 19, 2021.

[265] R. S. Larson and E. J. Lightfoot, "Thermally activated escape from a lennard-jones potential well," *Physica A: Statistical Mechanics and its Applications*, vol. 149, no. 1-2, pp. 296–312, 1988.

[266] E. Woillez, Y. Zhao, Y. Kafri, V. Lecomte, and J. Tailleur, "Activated escape of a self-propelled particle from a metastable state," *Phys. Rev. Lett.*, vol. 122, no. 25, p. 258001, 2019.

[267] P. Maiuri, J.-F. Rupprecht, S. Wieser, V. Ruprecht, O. Bénichou, N. Carpi, M. Coppey, S. De Beco, N. Gov, C.-P. Heisenberg, *et al.*, "Actin flows mediate a universal coupling between cell speed and cell persistence," *Cell*, vol. 161, no. 2, pp. 374–386, 2015.

[268] C. Datt and G. J. Elfring, "Active particles in viscosity gradients," *Phys. Rev. Lett.*, vol. 123, p. 158006, Oct 2019.

[269] M. R. Stehnach, N. Waisbord, D. M. Walkama, and J. S. Guasto, "Viscophobic turning dictates microalgae transport in viscosity gradients," *Nature Physics*, vol. 17, no. 8, pp. 926–930, 2021.

[270] V. A. Shaik and G. J. Elfring, "Hydrodynamics of active particles in viscosity gradients," *Physical Review Fluids*, vol. 6, no. 10, p. 103103, 2021.

[271] S. Coppola and V. Kantsler, "Green algae scatter off sharp viscosity gradients," *Scientific reports*, vol. 11, no. 1, p. 399, 2021.

[272] M. Ghibaudo, A. Saez, L. Trichet, A. Xayaphoummine, J. Browaeys, P. Silberzan, A. Buguin, and B. Ladoux, "Traction forces and rigidity sensing regulate cell functions," *Soft Matter*, vol. 4, pp. 1836–1843, 2008.

[273] A. Zemel. private communication.

[274] L. Feld, L. Kellerman, A. Mukherjee, A. Livne, E. Bouchbinder, and H. Wolfenson, "Cellular contractile forces are nonmechanosensitive," *Science Advances*, vol. 6, no. 17, p. eaaz6997, 2020.

[275] D. Ben-Yaakov, R. Golkov, Y. Shokef, and S. A. Safran, "Response of adherent cells to mechanical perturbations of the surrounding matrix," *Soft Matter*, vol. 11, pp. 1412–1424, 2015.

[276] X. Yu, H. Wang, F. Ye, X. Wang, Q. Fan, and X. Xinpeng, "Biphasic curvature-dependence of cell migration inside microcylinders: persistent randomness versus directionality," *bioRxiv*, pp. 2022–12, 2022.

[277] D. P. Holmes, "Elasticity and stability of shape-shifting structures," *Current opinion in colloid & interface science*, vol. 40, pp. 118–137, 2019.

[278] I. Levin, R. Deegan, and E. Sharon, "Self-oscillating membranes: Chemomechanical sheets show autonomous periodic shape transformation," *Physical Review Letters*, vol. 125, no. 17, p. 178001, 2020.

[279] M. A. Dias, J. A. Hanna, and C. D. Santangelo, "Programmed buckling by controlled lateral swelling in a thin elastic sheet," *Physical Review E—Statistical, Nonlinear, and Soft Matter Physics*, vol. 84, no. 3, p. 036603, 2011.

[280] Y. Klein, E. Efrati, and E. Sharon, "Shaping of elastic sheets by prescription of non-euclidean metrics," *Science*, vol. 315, no. 5815, pp. 1116–1120, 2007.

[281] J. Kim, J. A. Hanna, M. Byun, C. D. Santangelo, and R. C. Hayward, "Designing responsive buckled surfaces by halftone gel lithography," *science*, vol. 335, no. 6073, pp. 1201–1205, 2012.

[282] E. Siéfert, E. Reyssat, J. Bico, and B. Roman, "Bio-inspired pneumatic shape-morphing elastomers," *Nature materials*, vol. 18, no. 1, pp. 24–28, 2019.

[283] S. Choudhary, G. Livne, S. Gat, and A. Bernheim-Groswasser, "The mechanics of (poro-) elastic contractile actomyosin networks as a model system of the cell cytoskeleton," *JoVE (Journal of Visualized Experiments)*, no. 193, p. e64377, 2023.

[284] M. Doi, "Gel dynamics," *Journal of the Physical Society of Japan*, vol. 78, no. 5, p. 052001, 2009.

[285] T. Vignaud, H. Ennomani, and M. Théry, "Polyacrylamide hydrogel micropatterning," in *Methods in cell biology*, vol. 120, pp. 93–116, Elsevier, 2014.

[286] N. Barber-Pérez, "Polyacrylamide stiffness-gradient hydrogels: A 2d culture system to study cell mechano-responsiveness to substrate stiffness," 2019.

[287] J. Nakanishi, Y. Kikuchi, T. Takarada, H. Nakayama, K. Yamaguchi, and M. Maeda, "Spatiotemporal control of cell adhesion on a self-assembled monolayer having a photocleavable protecting group," *Analytica chimica acta*, vol. 578, no. 1, pp. 100–104, 2006.

[288] G. Mahmud, C. J. Campbell, K. J. Bishop, Y. A. Komarova, O. Chaga, S. Soh, S. Huda, K. Kandere-Grzybowska, and B. A. Grzybowski, "Directing cell motions on micropatterned ratchets," *Nature physics*, vol. 5, no. 8, pp. 606–612, 2009.

[289] H. Mohammadi and C. A. McCulloch, "Impact of elastic and inelastic substrate behaviors on mechanosensation," *Soft Matter*, vol. 10, no. 3, pp. 408–420, 2014.

[290] M. Murrell, P. W. Oakes, M. Lenz, and M. L. Gardel, "Forcing cells into shape: the mechanics of actomyosin contractility," *Nature reviews Molecular cell biology*, vol. 16, no. 8, pp. 486–498, 2015.

[291] N. L. Dasanayake, P. J. Michalski, and A. E. Carlsson, "General mechanism of actomyosin contractility," *Physical review letters*, vol. 107, no. 11, p. 118101, 2011.

[292] R. De, A. Zemel, and S. A. Safran, "Dynamics of cell orientation," *Nature Physics*, vol. 3, no. 9, pp. 655–659, 2007.

[293] J. Ranft, M. Basan, J. Elgeti, J.-F. Joanny, J. Prost, and F. Jülicher, "Fluidization of tissues by cell division and apoptosis," *Proceedings of the National Academy of Sciences*, vol. 107, no. 49, pp. 20863–20868, 2010.